

An accurate and efficient framework for predictive insights into ionic surface chemistry

Benjamin X. Shi,[†] Andrew S. Rosen,[‡] Tobias Schäfer,[¶] Andreas Grüneis,[¶]
Venkat Kapil,^{†,§,||} Andrea Zen,^{⊥, #} and Angelos Michaelides^{*,†}

[†]*Yusuf Hamied Department of Chemistry, University of Cambridge, Lensfield Road,
Cambridge CB2 1EW, United Kingdom*

[‡]*Department of Chemical and Biological Engineering, Princeton University, Princeton, NJ
08540 USA*

[¶]*Institute for Theoretical Physics, TU Wien, Wiedner Hauptstraße 8-10/136, 1040
Vienna, Austria*

[§]*Department of Physics and Astronomy, University College London, 7-19 Gordon St,
London WC1H 0AH, UK*

^{||}*Thomas Young Centre and London Centre for Nanotechnology, 9 Gordon St, London
WC1H 0AH*

[⊥]*Dipartimento di Fisica Ettore Pancini, Università di Napoli Federico II, Monte S.
Angelo, I-80126 Napoli, Italy*

[#]*Department of Earth Sciences, University College London, Gower Street, London WC1E
6BT, United Kingdom*

E-mail: am452@cam.ac.uk

Abstract

Quantum-mechanical simulations can offer atomic-level insights into chemical processes on surfaces. This understanding is crucial for the rational design of new solid catalysts as well as materials to store energy and mitigate greenhouse gases. However, achieving the accuracy needed for reliable predictions has proven challenging. Density functional theory (DFT), the workhorse quantum-mechanical method, can often lead to inconsistent predictions, necessitating accurate methods from correlated wave-function theory (cWFT). However, the high computational demands and significant user intervention associated with cWFT have traditionally made it impractical to carry out for surfaces. In this work, we address this challenge, presenting an automated framework which leverages multilevel embedding approaches, to apply accurate cWFT methods to ionic surfaces with computational costs approaching DFT. With this framework, we have reproduced experimental adsorption enthalpies for a diverse set of 19 adsorbate–surface systems. Moreover, we resolve long-standing debates on the adsorption configuration of several systems, while offering valuable benchmarks to assess DFT. This framework is completely open-source, making it possible to now routinely apply cWFT to complex problems in ionic surface chemistry.

Introduction

Understanding the chemical processes occurring on surfaces is critical to applications ranging from the production of fuels via heterogeneous catalysis^{1,2} to the storage of energy³ and sequestration of greenhouse gases. The adsorption and desorption of molecules from surfaces is a crucial process within all of these applications, and the strength of this binding is dictated by the adsorption enthalpy H_{ads} , making it a fundamental quantity to accurately predict.⁴⁻⁷ For example, candidate materials for CO₂ or H₂ gas storage are screened based upon their H_{ads} value, often to within tight energetic windows⁸ (~ 150 meV). High accuracy on H_{ads} is also needed to compare the competitive adsorption between two molecular species, such as for

the separation of flue gases.⁹ Finally, H_{ads} is a necessary quantity within any (microkinetic) model of a surface chemical reaction, with an empirical dependence between the reaction rate and H_{ads} according to the well-established volcano plots.^{10–13}

The rational design of new materials for the above applications relies on an atomic-level understanding of surface processes, together with an accurate H_{ads} . Determining the adsorption configuration — the geometry a molecule adopts on a surface — is particularly important, as it underpins all subsequent processes.¹⁴ Quantum-mechanical simulation techniques can provide the atomic-level detail needed to study the adsorption configuration. They have become widely used to complement experimental techniques,^{15,16} where such detail is typically hard to obtain. However, achieving reliable agreement between theory and experiments in determining H_{ads} is challenging¹⁷ due to limitations/inaccuracies in the theoretical methods that are commonly employed and the frequent neglect of thermal contributions. Moreover, these inaccuracies can affect the predicted adsorption configuration, leading to incorrect identification of the most stable configuration, or a fortuitous match to experimental H_{ads} for a metastable configuration.

To extend simulations beyond just a tool to complement experiments, new techniques are needed that surpass the traditional cost–accuracy trade-off; they must achieve high accuracy on H_{ads} (rivalling experiments) while being fast enough to sample multiple adsorption sites and configurations to correctly identify the most stable configuration. Density functional theory (DFT) is the current workhorse technique, playing an important role in identifying the reactivity trends (e.g., Brønsted–Evans–Polanyi relationships^{18–22} and volcano plots^{10–13}) that now form pivotal tools for the *in silico* design of new solid catalysts.² Despite these successes, the density functional approximations (DFAs) to the exchange–correlation functional and dispersion interactions within DFT are not systematically improvable, presenting ongoing challenges^{23,24} in making reliable predictions.^{25,26} For example, 6 different adsorption configurations have been proposed by different DFT studies for NO adsorbed on the MgO(001) surface (see Fig. 1).

Correlated wave-function theory (cWFT) provides a systematically improvable hierarchy of methods, where coupled cluster (CC) theory with single, double and perturbative triple excitations²⁷ [CCSD(T)] is widely considered the method of choice. Its high cost and steep computational scaling, however, limits its direct application to adsorbate–surface systems. To bypass this cost, CCSD(T) is often applied within an embedding approach, where it is treated as either local fragments in periodic supercells^{28,29} or by approximating the surface as a finite embedded cluster.^{30–35} The latter embedded cluster approaches have demonstrated great success in reproducing experimental H_{ads} estimates, while new methods^{25,36,37} and approximations^{38–40} for the former are further enhancing its applicability.

The major limitation of embedded cluster approaches is the difficulty in generalising them to diverse sets of adsorbate—surface systems. Consequently, all studies until now have been mostly limited to one or two systems. There have been advances^{41–44} towards addressing these challenges — for example, the SKZCAM protocol^{43,44} by some of the authors provides systematic rubrics for applying embedded cluster approaches to any ionic crystal, surface termination, and molecule. However, tackling broad sets of adsorbate–surface systems or adsorption configurations – currently routine with DFT – still presents a major challenge as these embedding approaches remain complicated and cumbersome, requiring significant manual effort.⁴⁵ To make these tools usable by the broader community, they need to be streamlined, automatised and simplified into “black-box” tools, providing reliable insights from simple inputs (as illustrated in the top panel of Fig. 1).

In this work, we introduce the autoSKZCAM framework, which delivers CCSD(T)-quality predictions to general ionic surface chemistry problems at a cost and ease approaching DFT. With this framework, we have been able to reach unprecedented agreement to experimental H_{ads} for a set of 19 adsorbate–surface systems. These systems (visualised in Fig. 2 and Sec. S4 of the Supplementary Information) include a diverse array of molecules adsorbed onto MgO(001) as well as TiO₂ anatase(101) and rutile(110). Its low cost allows for multiple adsorption configurations of each system to be studied simultaneously, helping to resolve

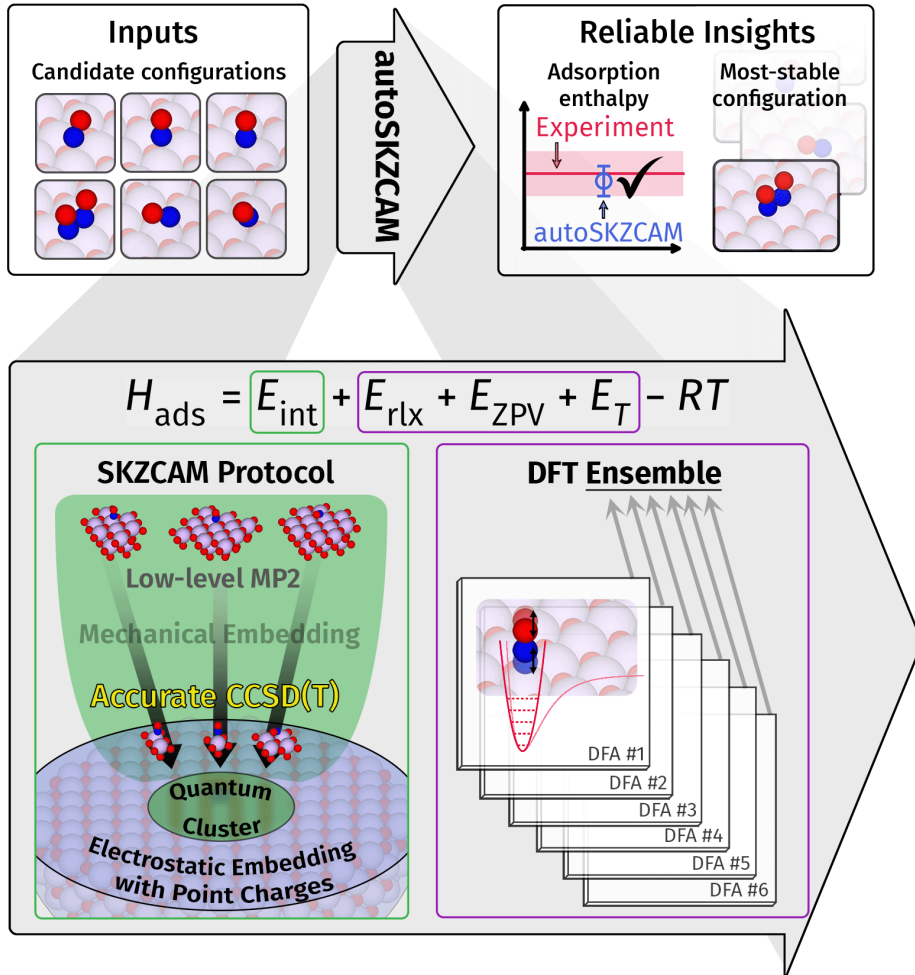


Figure 1: **Reliable insights into ionic surface chemistry with the autoSKZCAM framework.** Schematic description of the open-source autoSKZCAM framework. From a set of adsorbate–surface configurations, this framework can identify the most stable configuration and calculate an accurate adsorption enthalpy H_{ads} that reproduces experiment. It achieves high accuracy at low cost by partitioning H_{ads} via a divide-and-conquer scheme. The dominant contribution — the interaction energy E_{int} — is treated efficiently up to the “gold-standard” coupled cluster theory with single, double and perturbative triple excitations [CCSD(T)] level through the SKZCAM protocol. This protocol ensures low cost on E_{int} by employing a multilevel approach, where CCSD(T) is embedded within more affordable levels of theory such as second-order Møller-Plesset perturbation theory (MP2). The remaining relaxation energy E_{rlx} , zero-point vibrational energy E_{ZPV} and thermal contributions E_{T} are treated through an ensemble of 6 widely-used DFT density functional approximations to achieve an accurate (average) estimate with a corresponding error prediction.

long-standing debates between experiments and simulations on their adsorption configuration. Furthermore, it has provided valuable benchmarks for assessing the performance of DFAs in DFT, facilitating future advances in DFA development.

The autoSKZCAM framework automates the computation of an accurate yet low-cost H_{ads} , as summarised in the bottom panel of Fig. 1. It achieves these qualities by partitioning H_{ads} into separate contributions (discussed in the Methods and Sec. S3 of the Supplementary Information) that are addressed with appropriate techniques within a divide-and-conquer scheme. The principal contribution, the adsorbate–surface interaction energy E_{int} , is calculated efficiently up to the CCSD(T) level using the SKZCAM protocol.^{43,44,46} It has been automated within the present work, eliminating any manual intervention and enabling us to tackle a wide range of systems. Moreover, this automation has allowed CCSD(T) to be (mechanically) embedded within additional, more affordable, levels of theory via an ONIOM⁴⁷ procedure. This has reduced its cost by one order of magnitude (see Sec. S14 of the Supplementary Information), making it now competitive with periodic hybrid DFT. We show in Sec. S8 of the Supplementary Information that the remaining relaxation, zero-point vibrational and thermal contributions to H_{ads} can be estimated effectively with DFT by employing an ensemble of 6 widely-used density functional approximations. This entire computational framework is freely available on GitHub (upon acceptance of the manuscript) and we anticipate it will facilitate the exploration of more complex surface phenomena for future energy-relevant technologies.²

Results

Agreement across diverse systems

The 19 adsorbate–surface systems studied within this work are visualised in Fig. 2, where the H_{ads} computed by the autoSKZCAM framework is evaluated against experiment. There is complete agreement between experiment and autoSKZCAM on H_{ads} estimates (tabulated

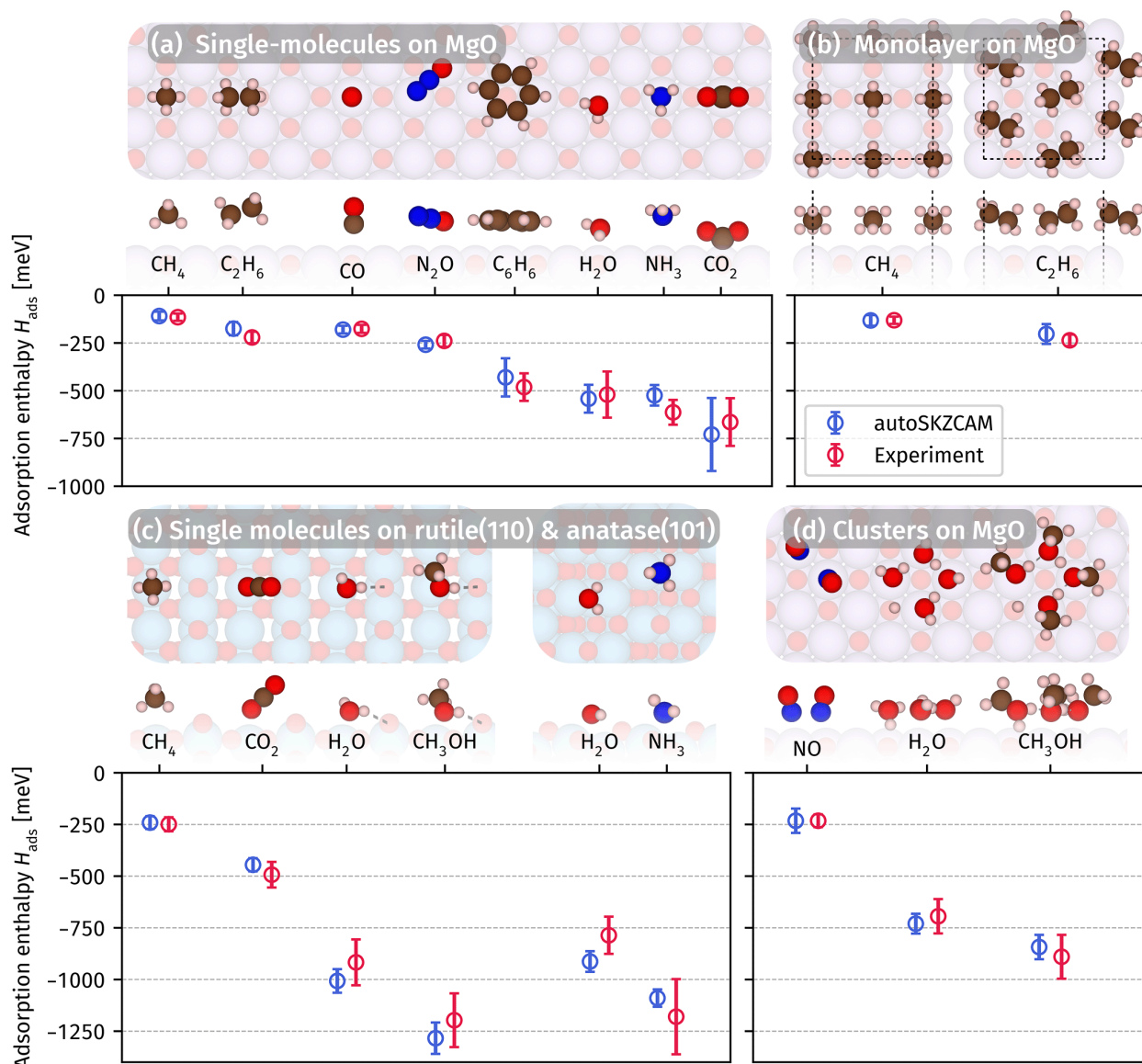


Figure 2: **Consensus with experiments across diverse systems.** A comparison of adsorption enthalpies computed with the autoSKZCAM framework against high-quality temperature programmed desorption experiments for a set of 19 adsorbate–surface combinations. These include (a) single molecules adsorbed on the MgO(001) surface, (b) monolayers adsorbed on MgO(001), (c) single molecules adsorbed on TiO₂ rutile(110) and anatase(101) as well as (d) clusters adsorbed on MgO(001). We discuss how we calculate the error bars (corresponding to 95% confidence intervals or more) on H_{ads} for the simulations and experiments (including references to the experimental data) in Secs. S9 and S11, respectively. A top and side view of the most stable geometry for each system is shown above each label, with C, H, N, O, Mg and Ti atoms corresponding to the brown, white, dark blue, red, purple and light blue spheres respectively.

in Sec. S9 of the Supplementary Information) for all studied systems, lying within their respective errors bars. Here, the error bars correspond to a 95% confidence interval on the experimental pre-exponential (ν) factor and a similar confidence interval calculated for the individual terms in the autoSKZCAM framework, as discussed in Secs. S11 and S9 of the Supplementary Information, respectively. This range of systems cover an H_{ads} of almost 1.5 eV, spanning weak physisorption to strong chemisorption and including a diverse set of molecules (CO, NO, N₂O, NH₃, H₂O, CO₂, CH₃OH, CH₄, C₂H₆ and C₆H₆) on important ionic surfaces [MgO(001) as well as TiO₂ anatase(101) and rutile(110)]. Besides the adsorption of small single molecules, some of which have been tackled before, we have also extended this work to monolayers [Fig. 2b] and to larger molecules such as C₆H₆ or molecular clusters of CH₃OH and H₂O [Fig. 2d].

The ability to study large systems, including molecular clusters on the surface, with the autoSKZCAM framework has been pivotal towards reproducing experiments. For example, we have studied several adsorption configurations of CH₃OH on MgO(001), including hydrogen (H-)bonded and partially dissociated clusters of CH₃OH. We find that agreement to experiment in Fig. 2 can only be obtained when considering partially dissociated clusters. As discussed in Sec. S1.1 of the Supplementary Information and in [Extended Data Fig. 1](#), other studied structures predict less stable adsorbates (i.e., a weaker absolute H_{ads}). We show in [Extended Data Fig. 2](#) that these insights are transferable to H₂O, which also forms partially dissociated clusters on MgO(001).

Reliable insights at the atomic-level

The automated nature and low cost of the autoSKZCAM framework enables a comprehensive exploration of the configurations the adsorbate can adopt in each adsorbate–surface system. Beyond H₂O and CH₃OH, we have used this framework to settle similar debates found within the literature on the adsorption configuration of N₂O, CO₂ and NO on MgO(001) as well as CO₂ on TiO₂ rutile(110). Here, inaccuracies in DFAs within DFT can lead to ambiguities

when determining the stable adsorption configuration through two possibilities: (1) the DFA predicts the wrong stable adsorption configuration; or (2) a metastable adsorption configuration fortuitously matches the experimental H_{ads} . The high accuracy of the autoSKZCAM framework ensures that the experimental H_{ads} is only reproduced when the correct stable adsorption configuration (corresponding to the most negative H_{ads}) has been identified.

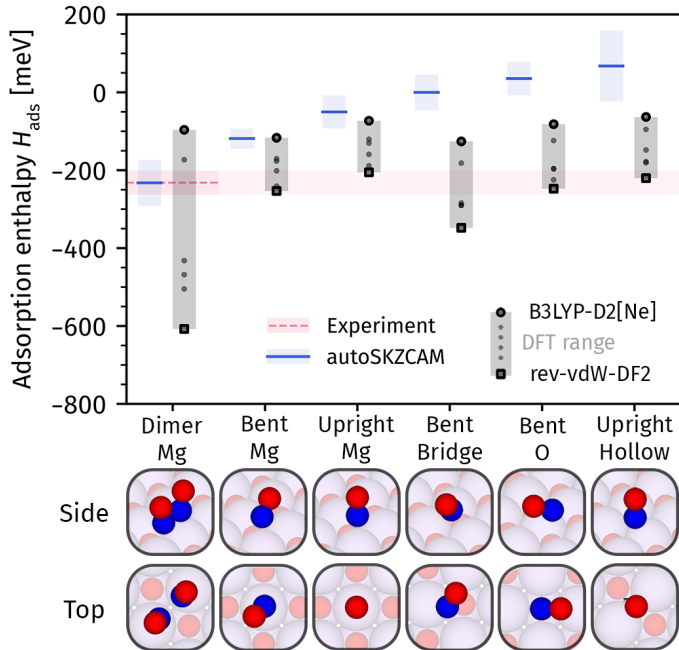


Figure 3: Correct identification of the NO on MgO(001) adsorption configuration. For NO on MgO(001), six adsorption configurations have been proposed: “Dimer Mg”, “Bent Mg”, “Upright Mg”, “Bent Bridge”, “Bent O” and “Upright Hollow”. These names reflect their orientation and binding sites on the surface. The adsorption enthalpy H_{ads} is calculated for each configuration with the autoSKZCAM framework and a set of 6 density functional approximations (DFAs) in DFT. The estimates from the 6 DFAs are plotted as a DFT “range” between the smallest and largest values. Experiments^{48,49} indicate that the Dimer Mg configuration is the most stable. The autoSKZCAM framework is the only method that correctly identifies this configuration while reproducing the experimental H_{ads} measurement by Wichtendahl *et al.*⁵⁰ Conservative error estimates (corresponding to a 95% confidence interval or more) are given for both experiment and autoSKZCAM, as discussed in Secs. S9 and S11, respectively. The DFAs used are: PBE-D2[Ne], revPBE-D4, vdW-DF2, rev-vdW-DF2, PBE0-D4 and B3LYP-D2[Ne], with B3LYP-D2[Ne] and rev-vdW-DF2 explicitly indicated, as these sit at either end of the DFT range. The autoSKZCAM and DFT estimates are tabulated in Sec. S1.3 of the Supplementary Information.

The ambiguities from utilising DFT are particularly evident in the adsorption of NO on

MgO(001), where different DFAs (and procedures) have led to the identification of multiple “stable” geometries, comprising 6 broad classes. In Fig. 3, we present H_{ads} estimates by several widely-used DFAs for these six adsorption configurations. For all six configurations, there are DFAs that yield H_{ads} values that agree with experiment. Notably, the rev-vdW-DF2 DFA⁵¹ predicts H_{ads} values that agree with experiments for the “Bent Mg”, “Upright Mg”, “Bent O” and “Upright Hollow” adsorption configurations. On the basis of such fortuitous agreement, prior studies (see Sec. S13 of the Supplementary Information) have mis-identified several of these configurations to be the most stable. On the other hand, the autoSKZCAM framework identifies the (covalently-bonded) dimer *cis*-(NO)₂ (dubbed “Dimer Mg”) configuration to be most stable, with an H_{ads} consistent with experiment while all other (monomer) configurations are predicted to be less stable by more than 80 meV. This prediction is commensurate with findings from Fourier-Transform Infrared Spectroscopy (FTIR)⁴⁸ and electron paramagnetic resonance⁴⁹ (EPR) experiments, both of which suggest that NO exists as a dimer on MgO(001), aside from a small number of monomers adsorbed on defect sites.

In many cases, debates on the most stable adsorption configuration cannot be resolved from experiments alone. For example, techniques like FTIR spectroscopy, low-energy electron diffraction (LEED), or X-ray and ultraviolet photoelectron spectroscopy (XPS and UPS) only provide indirect evidence. Moreover, while scanning tunneling microscopy (STM) offers real-space images, its resolution is often insufficient for definitive interpretation.⁵² The autoSKZCAM framework becomes particularly valuable within such contexts. Notably, both experiments^{53,54} and simulations^{55–58} have long-debated between a chemisorbed or physisorbed configuration [Extended Data Fig. 3 and Sec. S1.2 of the Supplementary Information] of CO₂ on MgO(001). With the autoSKZCAM framework, we show that it takes on a chemisorbed carbonate configuration in agreement with previous TPD measurements.^{54,59} Similarly, the adsorption of CO₂^{34,60} on TiO₂ rutile(110) [Extended Data Fig. 4 and Sec. S1.4 of the Supplementary Information] as well as N₂O⁶¹ on MgO(001) [Extended Data Fig. 5

and Sec. S1.5 of the Supplementary Information] have been debated to take on either a tilted or parallel geometry; the autoSKZCAM framework predicts the tilted geometry to be most stable for the former and the parallel geometry for the latter.

“Gold-standard” benchmarks

The accurate predictions from the autoSKZCAM framework for the systems studied in this work are particularly valuable as a benchmark dataset for non-covalent interactions, which are crucial for modelling the binding of adsorbates to surfaces. These interactions are physically reflected within the interaction energy E_{int} contribution to H_{ads} (see Methods), where it quantifies the strength of this binding. Previous studies^{46,62–64} have shown that DFAs struggle to consistently describe these interactions for adsorbate–surface systems and different DFAs can vary over a range exceeding 500 meV on E_{int} , even for a simple system like CO on MgO(001). Here, CCSD(T) is considered a widely-trusted approach for treating non-covalent interactions. However, while it has become common to generate reference datasets at the CCSD(T) level for small molecule interaction energies,^{65,66} it has not been possible for adsorbate–surface systems so far. These datasets are commonly used to e.g., parametrise the exchange–correlation functional or dispersion corrections in many modern DFAs. Their poor performance for adsorbate–surface systems arises in part from the lack of available references, particularly those involving metal oxides;⁶⁷ we can now address this gap with the autoSKZCAM framework.

In Fig. 4, a set of DFAs^{46,63} consisting of exchange–correlation functionals that span Jacob’s ladder, from the generalised gradient approximation (GGA) all the way up to the random phase approximation (RPA), have been compared against the autoSKZCAM E_{int} benchmarks; the values are tabulated in Sec. S2 of the Supplementary Information. No clear improvement in E_{int} is found moving up the rungs of Jacob’s ladder for the adsorbate–surface systems. In fact, two GGA-based DFAs (PBE-MBD/FI and rev-vdW-DF2) perform the best, with a mean absolute deviation (MAD) of 26 and 25 meV, within chemical accuracy

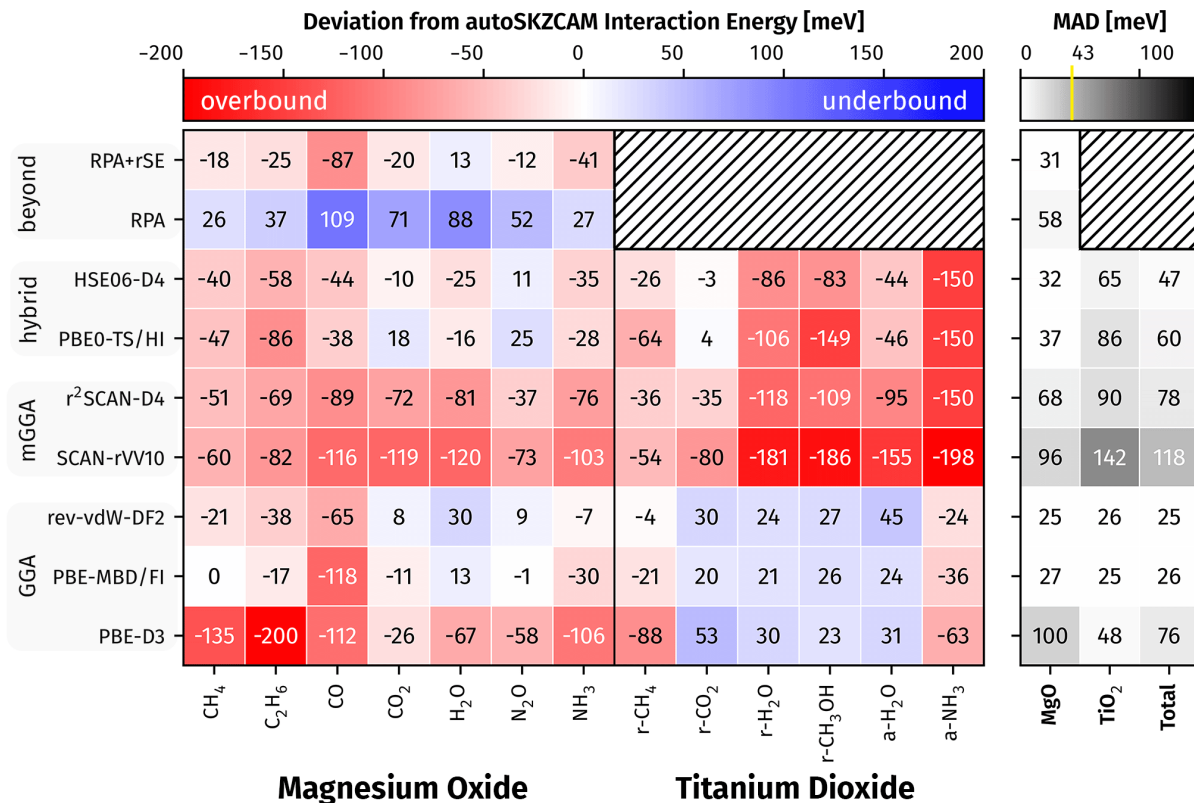


Figure 4: **A benchmark for lower-level theories.** The autoSKZCAM framework interaction energy benchmarks are used to assess a selection of density functional approximations along Jacob’s ladder as well as the random phase approximation. The deviation from the autoSKZCAM estimate is given as a colour map, with red and blue indicating overbinding and underbinding, respectively. We consider a range of molecules physisorbed on the MgO(001) and TiO₂ surfaces, where rutile(110) is indicated by ‘r-’ and anatase(101) is indicated by ‘a-’. The mean absolute deviations (MADs) across all of the systems, as well as the subsets involving the MgO and TiO₂ surfaces, are given in grey on the right panel. We indicate the typical ‘chemical accuracy’ of 43 meV in yellow on the colour bar. The autoSKZCAM and DFT interaction energies are tabulated in Sec. S2 of the Supplementary Information.

for the majority of systems. On the other hand, RPA — considered the current state-of-the-art method for surface chemistry — has a MAD of 58 meV for the MgO adsorbate–surface systems. These errors arise from a well-known systematic underbinding⁶⁸ of RPA, which is improved by incorporating renormalised singles corrections⁶⁹ (rSE), instead overbinding with an MAD of 31 meV. We expect these trends to persist for the TiO₂ surfaces although the higher cost of RPA has prevented its application to these systems.

These benchmarks provide particularly important insights towards designing improved

DFAs. For example, the PBE-D3^{70,71} with zero-damping, SCAN-rVV10,⁷² and r²SCAN-D4⁷³ DFAs are all found to significantly overbind E_{int} for systems involving MgO(001), with the latter two also overbinding for the TiO₂ surfaces. These observations are commensurate with previous findings, where the overbinding in PBE-D3 has been attributed to an overestimated Mg C_6 dispersion coefficient in the D3 dispersion correction.⁷⁴ SCAN and r²SCAN have recently been shown to overbind solids⁷⁵ and this work confirms that this overbinding persists for adsorbate–surface systems, with the rVV10 dispersion correction further exacerbating this overbinding.

Discussion

The agreement achieved in H_{ads} between experiment and the autoSKZCAM framework is not trivial. For example, we show in Fig. 5a and Sec. S13 of the Supplementary Information that DFT estimates collated from the literature can span a range of nearly 1000 meV for CO₂ adsorbed on MgO(001) and H₂O on TiO₂ rutile(110). Beyond the errors in E_{int} arising from the choice of DFA (as highlighted in Fig. 4), these errors also stem from the use of unconverged structural models in the embedded cluster or periodic slab approaches. Additionally, electronic structure parameters such as the basis set size, treatment of frozen cores, and pseudopotentials must be carefully controlled, with the majority of studies neglecting thermal and vibrational contributions to H_{ads} . These challenges become more pronounced for methods from cWFT, where ensuring converged electronic structure parameters or structural models are limited by their high computational cost. We highlight this challenge in Fig. 5a, where a range of 528 meV has been observed across cWFT based studies of H₂O on rutile(110), with similar discrepancies noted for CO on MgO(001).⁴⁴

Despite the challenges in applying cWFT methods like CCSD(T) to adsorbate–surface systems, there have been other successful applications within the literature besides this work. Notably, the collection of molecules adsorbed on MgO(001) as well as zeolites and metal–

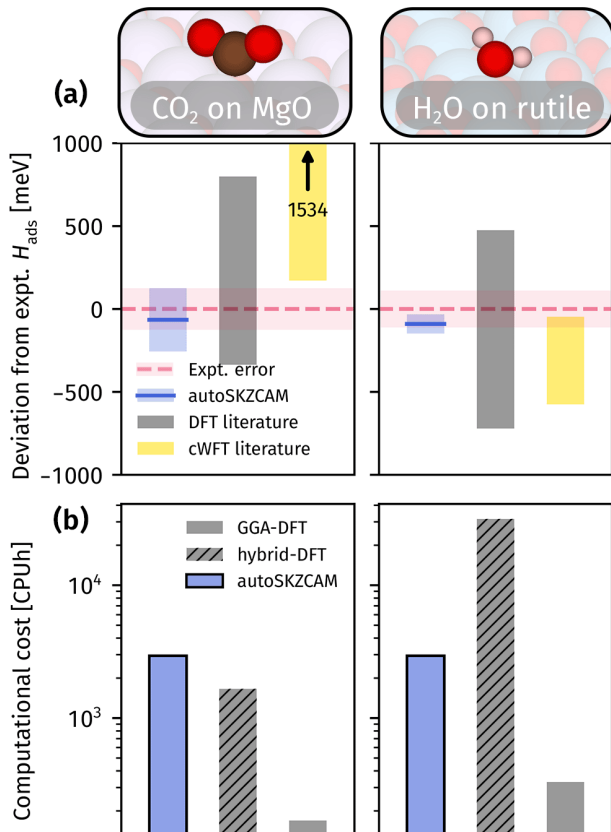


Figure 5: **High accuracy at comparable cost to periodic hybrid DFT.** For the chemisorbed CO₂ on MgO(001) and H₂O on TiO₂ rutile(110), we demonstrate the (a) excellent agreement to experimental TPD measurements^{54,76} for the autoSKZCAM framework relative to previous DFT (in grey) and cWFT (in yellow) literature, both of which are plotted as a range of values collated in Sec. S13 of the Supplementary Information. We show in (b) that its computational cost is competitive with periodic hybrid DFT. Conservative error estimates (corresponding to a 95% confidence interval or more) are given for both experiment and autoSKZCAM, as discussed in Secs. S9 and S11 of the Supplementary Information, respectively. The hardware and code to calculate the costs in CPU-hours is discussed in Sec. S14 of the Supplementary Information.

organic frameworks studied by Sauer and co-workers^{30–33} alongside the landmark study by Kubas *et al.*³⁴ tackling 5 molecules on the rutile(110) surface, both with an embedded cluster approach. More recently, this success has been extended towards periodic slab approaches with CCSD(T)^{28,29,39,40,44,77–80} thanks to new algorithmic and methodological developments. The key advance in the present study is the breadth, size and number of adsorbate–surface systems that can now be tackled, driven by the (1) low-cost, (2) general applicability, and (3) automated nature of the autoSKZCAM framework. Its low-cost is achieved by combining the

mechanical embedding approach of Sauer and co-workers⁸¹ with the electrostatic embedding procedure pioneered by Catlow and co-workers^{82–84} and Reuter *et al.*⁸⁵ It is made even more economical by combining CCSD(T) with new local approximations.^{86–88}

We highlight the low computational cost of the autoSKZCAM framework in Fig. 5b, where it is compared to periodic DFT – performed using sensible electronic structure settings⁸⁹ – with a hybrid and GGA DFA. The cost to perform the autoSKZCAM framework is competitive with periodic hybrid DFT, being around two times more expensive for CO₂ on MgO(001) while being six times cheaper for H₂O on TiO₂ rutile(110). Importantly, this cost does not change significantly with the increase in complexity from a MgO(001) to a TiO₂ rutile(110) surface as the embedding procedure ensures that the largest system (i.e., embedded cluster) tackled remains consistent in size across these surfaces. In Sec. S14 of the Supplementary Information, we also compare our autoSKZCAM framework costs for CO on MgO(001) to previous work. Its automation in the present work (as discussed in Sec. S6.6 of the Supplementary Information) has enabled further levels of mechanical embedding, which has led to an overall cost of ~ 600 CPUh to compute E_{int} for CO on MgO(001) with the autoSKZCAM framework. This is nearly two orders of magnitude lower than a previous (un-automated) application of the SKZCAM protocol⁴⁴ and an efficient periodic CCSD(T) calculation,^{39,44} while being more than three orders of magnitude cheaper than periodic quantum diffusion Monte Carlo.⁴⁴

Beyond the applications demonstrated so far, we discuss here the potential of the autoSKZCAM framework to validate experimental results. As shown in Fig. 2, it provides robust error estimates for H_{ads} that are lower than experimental uncertainties for the majority of systems. These experimental values were re-analysed from previous temperature programmed desorption (TPD) measurements, following Campbell and Sellers,⁶⁷ using more accurate system-specific⁹⁰ pre-exponential factors ν . The majority of the experimental error arises from uncertainties in ν with additional minor contributions discussed in Sec. S11 of the Supplementary Information. We show that using the original analysis procedure (set-

ting ν to a default value of 10^{13}) leads to H_{ads} values which are in worse agreement with autoSKZCAM, with a root mean squared deviation of 102 meV compared to 58 meV for the system-specific procedure. Going further, the autoSKZCAM framework can shed light on discrepancies between different temperature-programmed desorption experiments, as we have found for CO_2 on $\text{MgO}(001)$. Two measurements exist: one reports a weak H_{ads} characteristic of physisorption,⁵³ and the other reports a strong H_{ads} indicative of chemisorption.⁵⁴ For this particular case, our autoSKZCAM estimates agree with the chemisorption data but cannot replicate the physisorption results. In Sec. S1.2 of the Supplementary Information, we highlight inconsistencies in the physisorption experiment that cast doubt on these measurements. When these inconsistencies are accounted for, the experimental data aligns with our chemisorption estimates.

Conclusion

We have developed and implemented the autoSKZCAM framework to calculate accurate yet low cost adsorption enthalpies H_{ads} of molecules on ionic surfaces. This has enabled agreement to experimental measurements for a diverse set of 19 adsorbate–surface systems, beyond the accuracy of any density functional approximation considered, while being at a cost comparable to hybrid periodic DFT. We have revealed new insights into several of these systems, notably: CO_2 must bind on $\text{MgO}(001)$ in the long-debated chemisorbed state and that it can take on a tilted configuration on TiO_2 rutile(110), albeit close in stability to a horizontal parallel configuration; N_2O binds in a horizontal parallel fashion; NO exists as bound dimers on $\text{MgO}(001)$; and that CH_3OH and H_2O form partially dissociated H-bonded clusters on top of $\text{MgO}(001)$. In addition, we show that this dataset can be used to benchmark DFT exchange-correlation functionals and dispersion corrections, providing direct insights into their performance for adsorbate–surface systems.

This framework has been coded into an open-source package on Github (made avail-

able upon acceptance), making it a readily available tool to compute accurate reference data for adsorbate–surface systems to facilitate reliable surface chemistry studies (elaborated in Sec. S10 of the Supplementary Information). This reliability will be paramount in complementing experiments towards understanding important catalytic reaction processes, serving to unlock new directions for improving such processes. Furthermore, its automated nature means that it can serve as a standalone tool within a computational catalyst discovery pipeline to screen for new solid catalysts. Similarly, it can be used to provide large databases containing E_{int} benchmarks that can be used to directly parametrise improved (machine-learned) DFAs^{91,92} and electronic structure methods.

The main limitation of the the autoSKZCAM framework is that it currently only treats ionic surfaces. It will be important to develop new embedded cluster approaches that can treat transition metal surfaces^{35,93,94} and covalent materials like metal–organic frameworks (MOFs)^{95,96} and zeolites.^{81,97} The code and framework provided within the present work can be adapted in the future to accommodate such new approaches. Furthermore, it is desirable to go beyond a simple (local) harmonic description of H_{ads} to treat anharmonicities and non-localised phenomena (i.e., adsorption at high temperatures). Towards this end, there will be exciting prospects in integrating embedded cluster models with machine-learned interatomic potentials^{98,99} to extend the system sizes tackled and enable finite temperature effects to be incorporated.

Methods

The autoSKZCAM framework is developed and implemented within this work to serve as an automated tool for tackling problems in surface chemistry. For a given adsorption configuration, the autoSKZCAM framework will compute accurate (beyond-DFT) adsorption enthalpies H_{ads} at a low cost competitive with periodic hybrid DFT. Its low cost is achieved

by partitioning H_{ads} into several key contributions:⁸¹

$$H_{\text{ads}} = E_{\text{int}} + E_{\text{rlx}} + E_{\text{ZPV}} + E_{\text{T}} - RT, \quad (1)$$

that are treated separately with appropriate methods through a divide-and-conquer scheme. Here, the interaction energy E_{int} is defined as the energetic difference between the adsorbate–surface complex and the separate adsorbate and surface, both of which are fixed at their geometries in the complex. The relaxation energy E_{rlx} is the energy for the fixed adsorbate and surface to relax into their equilibrium geometries, while the zero-point vibrational and thermal contributions are given by E_{ZPV} and E_{T} respectively.

The interaction energy E_{int} is the dominant contribution to H_{ads} and there can be significant variations between chosen density functional approximations (DFAs) to DFT. This term is instead treated up to the CCSD(T) level efficiently through the SKZCAM protocol^{43,44,46} developed by Shi, Kapil, Zen, Chen, Alavi and Michaelides.⁴³ The remaining terms — E_{rlx} , E_{ZPV} and E_{T} — can be adequately treated using DFT, where we utilise an ensemble of 6 widely-used DFAs. When studying clusters or monolayers, there are additional terms for the lateral interaction energy between the molecules which are treated at the CCSD(T) level as discussed in Sec. S7 of the Supplementary Information. For chemisorbed CO_2 on $\text{MgO}(001)$, there is also an additional term (coming out of E_{rlx}) for the large conformational energy change in the CO_2 molecule. For the dissociated H_2O and CH_3OH clusters, we include a dissociation contribution E_{diss} which accounts for the energy change arising from dissociation of the parent molecularly adsorbed cluster.

The autoSKZCAM framework has been coded within an open-source package (to be released upon acceptance) on Github, making it freely accessible to all users, with examples and documentation provided within. It makes extensive use of the QuAcc workflow library,¹⁰⁰ which can be used to generate the relaxed adsorbate–surface geometries starting from just a molecule and crystal unit cell, as discussed in Sec. S10 of Supplementary Information. If

the adsorption configuration is not known, scripts are also provided to perform a random structure search to obtain candidate adsorption configurations.

Accurate interaction energies with the SKZCAM protocol

The most crucial component towards the accuracy and efficiency of the final H_{ads} from the autoSKZCAM framework is the CCSD(T) level E_{int} computed with the SKZCAM protocol. It addresses previous limitations in generalising embedded cluster approaches to different systems, defining systematic rubrics to generate a rapidly converging series of clusters – working for any ionic crystal, surface termination and molecule. By leveraging this smooth convergence, the bulk infinite-size limit E_{int} can be extrapolated from a set of clusters, as described in Sec. S6 of the Supplementary Information. This can be achieved efficiently by starting with the affordable second-order Møller-Plesset perturbation theory (MP2) to perform this (bulk) extrapolation with moderately sized clusters (<75 atoms). This MP2 prediction can then be elevated to the CCSD(T) level from smaller (<35 atom) clusters through an ONIOM-like⁴⁷ mechanical embedding approach. Specifically, we utilise new local approximations to CCSD(T), resulting in E_{int} estimates that are competitive with DFT in computational cost (see Sec. S14 of the Supplementary Information). Previously, this procedure would require significant user intervention to apply, but it has been carefully validated and automated within the present work. This automatisisation now facilitates routine application of CCSD(T) to calculate E_{int} of adsorbate–surface systems. Additionally, it has enabled a further lowering in computational cost by allowing for more levels (i.e., smaller basis sets or a bigger frozen core) to be part of the embedding, as discussed in Sec. S6.6 of the Supplementary Information.

The electrostatic embedding environment was constructed using py-Chemshell 20.0,⁸² setting formal point charges [i.e., Ti(4+), Mg(2+), O(2-)] in a 50 Å (60 Å) field around the quantum cluster center for the MgO (TiO₂) surface. A further region of effective core potentials was placed on the positive point charges within 4 Å (6 Å) of the quantum cluster

to prevent spurious charge leakage. MP2 was performed within ORCA 5.0.3¹⁰¹ with the resolution-of-identity approximation while CCSD(T) was performed within MRCC¹⁰² using the local natural orbital (LNO) approximation.^{86,103} A two-point (double-zeta/triple-zeta) complete basis set extrapolation,¹⁰⁴ together with counterpoise corrections, was used to calculate the MP2 and LNO-CCSD(T) E_{int} . Subsequent basis set and core-valence correlation contributions are added at the MP2 level, as discussed in Sec. S5 of the Supplementary Information.

Robust geometrical and vibrational contributions with an ensemble of DFAs

The remaining terms (i.e., E_{rlx} , E_{ZPV} and E_{T}) form a small overall contribution to H_{ads} that can be adequately treated with DFT. These terms are estimated by employing an ensemble^{105,106} of 6 widely-used DFAs of differing exchange-correlation functionals (up to hybrids) and dispersion corrections. The 6 DFAs used for MgO were PBE-D2[Ne], revPBE-D4, vdW-DF, rev-vdW-DF2, PBE0-D4, B3LYP-D2[Ne], where the [Ne] indicates the use of neon C_6 parameters for the Mg atoms. The TiO_2 surfaces used PBE-TS/HI, revPBE-D4, vdW-DF, rev-vdW-DF2, r²SCAN-rVV10, HSE06-D4. Through a simple averaging, this choice can provide robust estimates with corresponding 2σ standard deviations as an error measurement – typically much better than chemical accuracy (see Sec. S8 of the Supplementary Information). We discuss in Sec. S8.3 how this ensemble can be further used to assess inaccuracies from using a DFT geometry for the CCSD(T) treatment. As a result, this DFA ensemble allows for not only accurate H_{ads} to be obtained but also reliable error bars for comparison against experiments.

The DFT calculations were performed in the Vienna *ab-initio* simulations package (VASP) 6.3.0.^{107,108} Of the 13 systems involving MgO(001), we used a (4×4) supercell for all systems except for C_6H_6 , CH_3OH cluster and H_2O cluster, where a (8×8) supercell was used. The MgO surface slab consisted of 4 layers, with the bottom two layers fixed. The TiO_2

rutile(110) surface slab consisted of a (4×2) supercell with 5 tri-layers (and the bottom three fixed), while the anatase(101) surface slab consisted of a (3×1) supercell with 4 tri-layers and the bottom layer fixed. All surfaces incorporated 15 Å of vacuum with geometrical relaxation performed with a force convergence cutoff of 0.01 eV/Å. A plane-wave kinetic energy cutoff of 600 eV was used, which was reduced to 520 eV for the hybrid HSE06-D4 calculations on the TiO₂ surface systems. A $2\times 2\times 1$ Γ -centered Monkhorst-Pack k -point mesh was used for the MgO surface (reduced to only the Γ -point for the larger surface), $2\times 2\times 1$ mesh for the rutile(110) surface and $3\times 3\times 1$ mesh for anatase(101) surface. To calculate E_{ZPV} and E_T contributions, the contributions from individual vibrational modes were computed with the quasi rigid-rotor harmonic oscillator (quasi-RRHO) approximation.^{109,110} Further details, particularly the parameters for the benchmarks in Fig. 4, are given in Sec. S8.1 and Sec. S14 of the Supplementary Information.

Extended Data

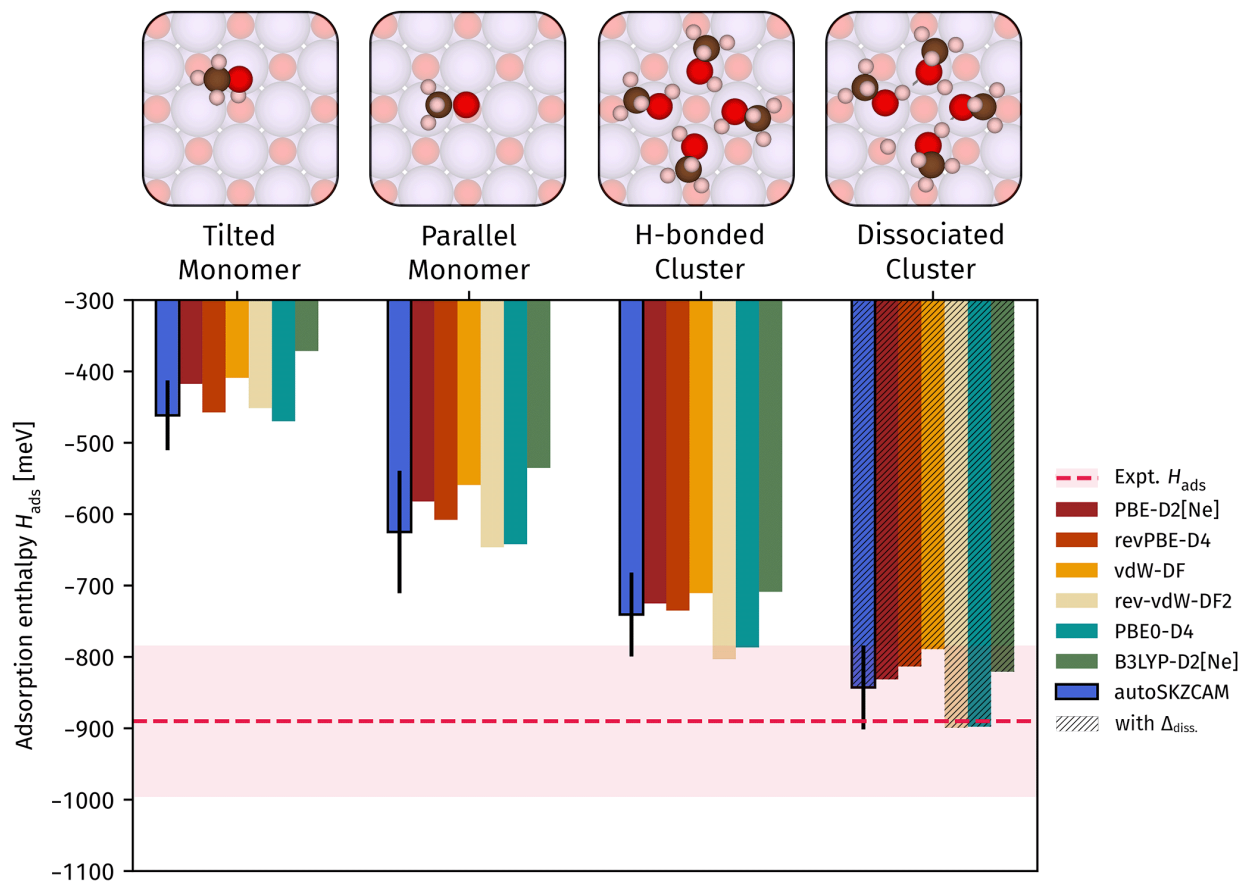


Figure Extended Data Fig. 1: **Stabilisation of CH₃OH clusters on MgO(001) through H-bonding and dissociation.** Adsorption enthalpy H_{ads} (per molecule) calculated with the autoSKZCAM framework and 6 different density functional approximations for CH₃OH on MgO(001). These are compared against TPD measurements by Günster *et al.*¹¹¹ We consider the tilted and parallel adsorption configuration of a single CH₃OH molecule on MgO(001) as well as a molecularly adsorbed and dissociated tetramer. The H_{ads} of the latter was computed by adding an additional term, E_{diss} , onto the molecularly adsorbed tetramer, as discussed in Sec. S8.5 of the Supplementary Information. Conservative error estimates (corresponding to a 95% confidence interval or more) are given for both experiment and autoSKZCAM, as discussed in Secs. S9 and S11 of the Supplementary Information, respectively.

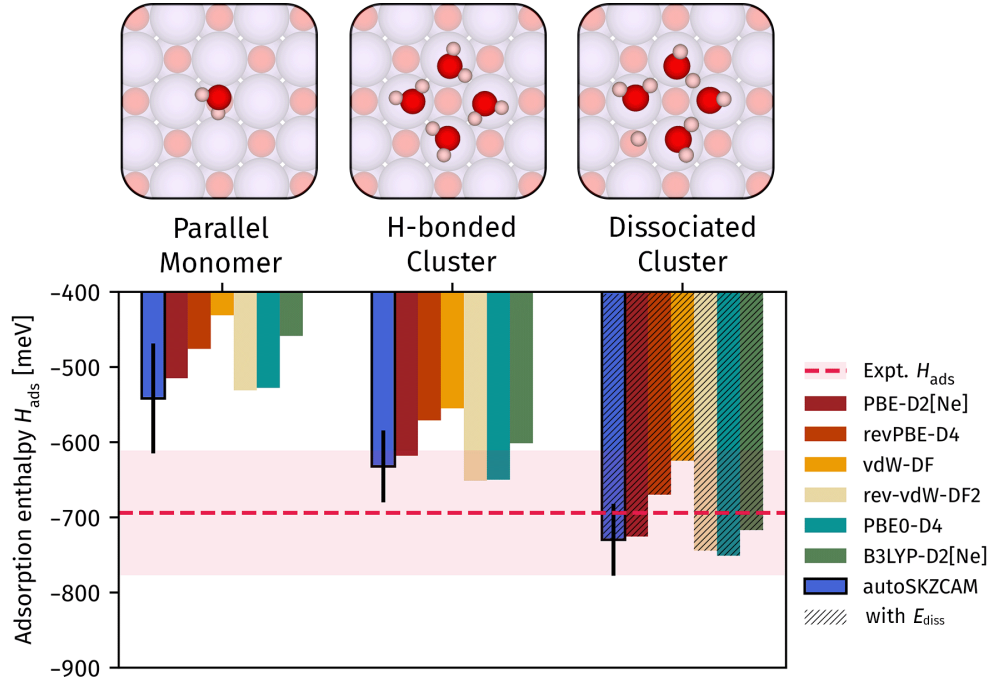


Figure Extended Data Fig. 2: **Stabilisation of H₂O clusters on MgO(001) through H-bonding and dissociation.** Adsorption enthalpy H_{ads} (per molecule) calculated with the autoSKZCAM framework and 6 different density functional approximations for H₂O on MgO(001). These are compared against TPD measurements by Stirniman *et al.*¹¹² We consider the adsorption of a single molecule, as well as a molecularly adsorbed and dissociated tetramer. The H_{ads} of the latter was computed by adding an additional term, E_{diss} , onto the molecularly adsorbed tetramer, as discussed in Sec. S8.5 of the Supplementary Information. Conservative error estimates (corresponding to a 95% confidence interval or more) are given for both experiment and autoSKZCAM, as discussed in Secs. S9 and S11 of the Supplementary Information, respectively.

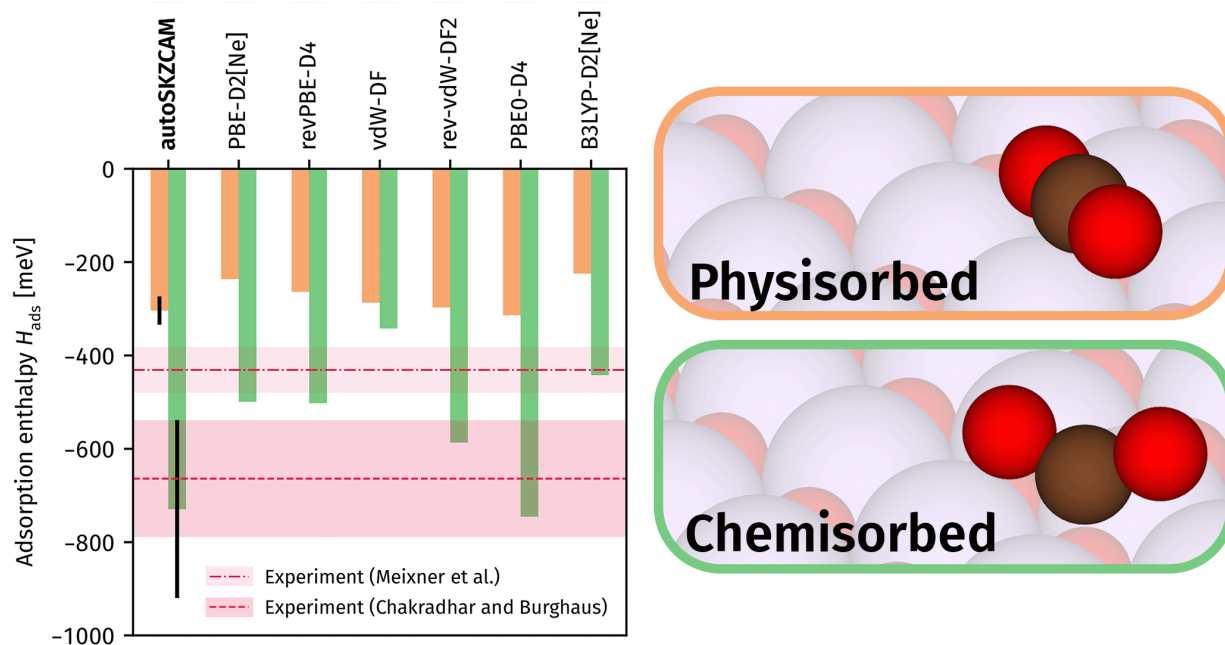


Figure Extended Data Fig. 3: **Resolving the chemisorbed state of CO₂ on MgO(001).** Adsorption enthalpy H_{ads} calculated with the autoSKZCAM framework and 6 different density functional approximations for the physisorbed (orange) and chemisorbed (green) state of CO₂ on MgO(001). These are compared against TPD measurements by Meixner *et al.*⁵³ and Chakradhar and Burghaus,⁵⁴ which propose a physisorbed and chemisorbed state, respectively. Conservative error estimates (corresponding to a 95% confidence interval or more) are given for both experiment and autoSKZCAM, as discussed in Secs. S9 and S11 of the Supplementary Information, respectively.

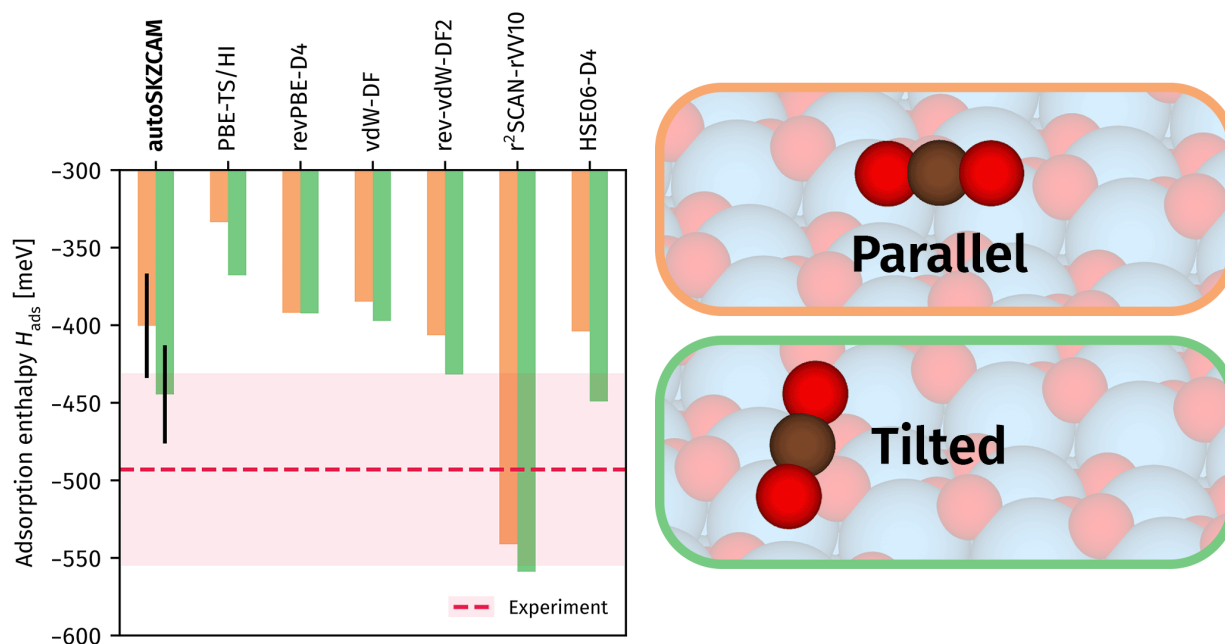


Figure Extended Data Fig. 4: **Preference towards the tilted configuration of CO₂ on the TiO₂ rutile(110).** Adsorption enthalpy H_{ads} calculated with the autoSKZCAM framework and 6 different density functional approximations for the parallel and tilted adsorption configuration of CO₂ on TiO₂ rutile(110). These are compared against TPD measurements by Thompson *et al.*¹¹³ Conservative error estimates (corresponding to a 95% confidence interval or more) are given for both experiment and autoSKZCAM, as discussed in Secs. S9 and S11 of the Supplementary Information, respectively.

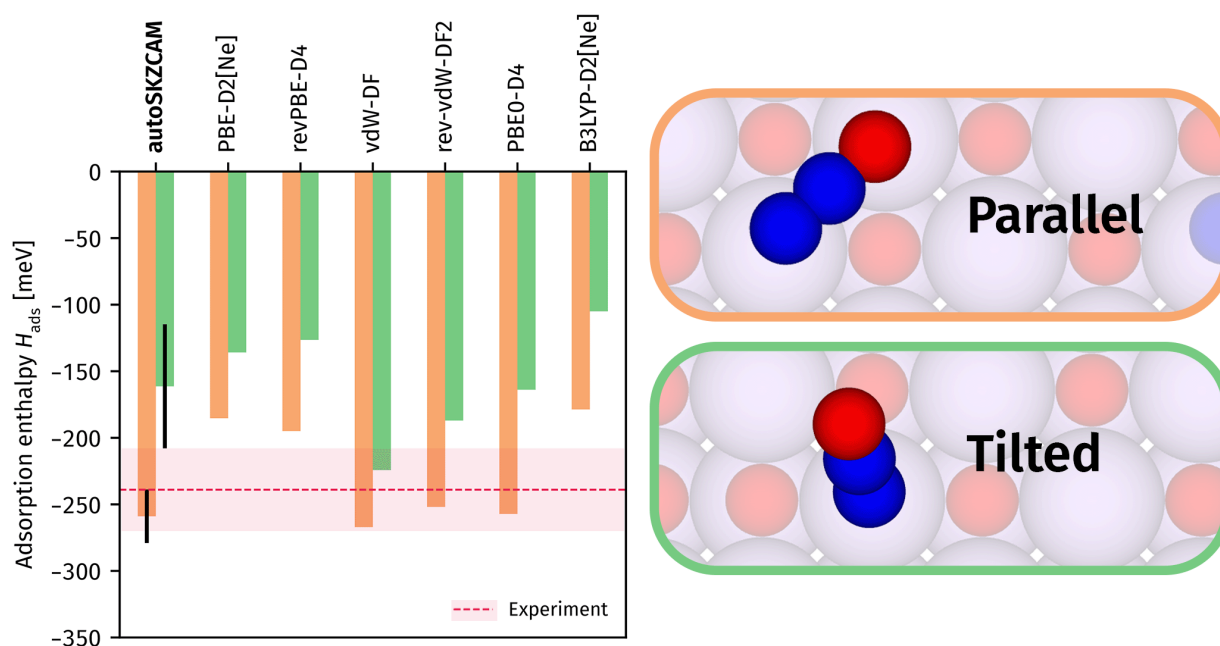


Figure Extended Data Fig. 5: **N₂O on MgO(001) adopts a parallel configuration.** Adsorption enthalpy H_{ads} calculated with the autoSKZCAM framework and 6 different density functional approximations for the parallel (orange) and tilted (green) adsorption configuration of N₂O on MgO(001). These are compared against TPD measurements by Lian *et al.*¹¹⁴ Conservative error estimates (corresponding to a 95% confidence interval or more) are given for both experiment and autoSKZCAM, as discussed in Secs. S9 and S11 of the Supplementary Information, respectively.

Acknowledgement

AZ acknowledges support from the European Union under the Next generation EU (projects 20222FXZ33 and P2022MC742). TS acknowledges support from the Austrian Science Fund (FWF) [DOI:10.55776/ESP335]. BXS acknowledges support from the EPSRC Doctoral Training Partnership (EP/T517847/1). AM acknowledges support from the European Union under the “n-AQUA” European Research Council project (Grant No. 101071937). The authors are grateful for: resources provided by the Cambridge Service for Data Driven Discovery (CSD3) operated by the University of Cambridge Research Computing Service (www.csd3.cam.ac.uk), provided by Dell EMC and Intel using Tier-2 funding from the Engineering and Physical Sciences Research Council (capital grant EP/P020259/1), and DiRAC funding from the Science and Technology Facilities Council (www.dirac.ac.uk); the Cirrus UK National Tier-2 HPC Service at EPCC (<http://www.cirrus.ac.uk>) funded by the University of Edinburgh and EPSRC (EP/P020267/1); the Vienna Scientific Cluster (VSC); computational resources granted by the UCL Myriad and Kathleen High Performance Computing Facility (Myriad@UCL and Kathleen@UCL), and associated support service; computational support from the UK Materials and Molecular Modelling Hub, which is partially funded by EPSRC (EP/P020194 and EP/T022213); and computational support from the UK national high performance computing service, ARCHER 2. Both the UK Materials and Molecular Modelling Hub and ARCHER 2 access was obtained via the UKCP consortium and funded by EPSRC grant ref EP/P022561/1.

Supporting Information Available

See the supplementary information for a detailed compilation of the obtained results as well as further data and analysis to support the points made throughout the text. The input and output files associated with this work and all analysis can be found on GitHub at [benshi97/Data_autoSKZCAM](https://github.com/benshi97/Data_autoSKZCAM) or viewed (and analysed) online on [Colab](https://colab.research.google.com/).

References

- (1) Greeley, J.; Jaramillo, T. F.; Bonde, J.; Chorkendorff, I.; Nørskov, J. K. Computational High-Throughput Screening of Electrocatalytic Materials for Hydrogen Evolution. *Nat. Mater.* **2006**, *5*, 909–913.
- (2) Nørskov, J. K.; Bligaard, T.; Rossmeisl, J.; Christensen, C. H. Towards the Computational Design of Solid Catalysts. *Nat. Chem.* **2009**, *1*, 37–46.
- (3) Jain, A.; Shin, Y.; Persson, K. A. Computational Predictions of Energy Materials Using Density Functional Theory. *Nat. Rev. Mater.* **2016**, *1*, 1–13.
- (4) Pablo-García, S.; Morandi, S.; Vargas-Hernández, R. A.; Jorner, K.; Ivković, Ž.; López, N.; Aspuru-Guzik, A. Fast Evaluation of the Adsorption Energy of Organic Molecules on Metals via Graph Neural Networks. *Nat. Comput. Sci.* **2023**, *3*, 433–442.
- (5) Gao, W.; Chen, Y.; Li, B.; Liu, S.-P.; Liu, X.; Jiang, Q. Determining the Adsorption Energies of Small Molecules with the Intrinsic Properties of Adsorbates and Substrates. *Nat. Commun.* **2020**, *11*, 1196.
- (6) Andersen, M.; Reuter, K. Adsorption Enthalpies for Catalysis Modeling through Machine-Learned Descriptors. *Acc. Chem. Res.* **2021**, *54*, 2741–2749.
- (7) Lan, J.; Palizhati, A.; Shuaibi, M.; Wood, B. M.; Wander, B.; Das, A.; Uyttendaele, M.; Zitnick, C. L.; Ulissi, Z. W. AdsorbML: A Leap in Efficiency for Adsorption Energy Calculations Using Generalizable Machine Learning Potentials. *npj Comput. Mater.* **2023**, *9*, 1–9.
- (8) Patel, H. A.; Byun, J.; Yavuz, C. T. Carbon Dioxide Capture Adsorbents: Chemistry and Methods. *ChemSusChem* **2017**, *10*, 1303–1317.
- (9) Rosen, A. S.; Mian, M. R.; Islamoglu, T.; Chen, H.; Farha, O. K.; Notestein, J. M.; Snurr, R. Q. Tuning the Redox Activity of Metal–Organic Frameworks for Enhanced,

- Selective O₂ Binding: Design Rules and Ambient Temperature O₂ Chemisorption in a Cobalt–Triazolate Framework. *J. Am. Chem. Soc.* **2020**, *142*, 4317–4328.
- (10) Bligaard, T.; Nørskov, J. K.; Dahl, S.; Matthiesen, J.; Christensen, C. H.; Sehested, J. The Brønsted–Evans–Polanyi Relation and the Volcano Curve in Heterogeneous Catalysis. *J. Catal.* **2004**, *224*, 206–217.
- (11) Falsig, H.; Hvolbæk, B.; Kristensen, I. S.; Jiang, T.; Bligaard, T.; Christensen, C. H.; Nørskov, J. K. Trends in the Catalytic CO Oxidation Activity of Nanoparticles. *Angew. Chem. Int. Ed.* **2008**, *47*, 4835–4839.
- (12) Cheng, J.; Hu, P. Utilization of the Three-Dimensional Volcano Surface To Understand the Chemistry of Multiphase Systems in Heterogeneous Catalysis. *J. Am. Chem. Soc.* **2008**, *130*, 10868–10869.
- (13) Montoya, J. H.; Seitz, L. C.; Chakhranont, P.; Vojvodic, A.; Jaramillo, T. F.; Nørskov, J. K. Materials for Solar Fuels and Chemicals. *Nat. Mater.* **2017**, *16*, 70–81.
- (14) Ertl, G. Elementary Steps in Heterogeneous Catalysis. *Angew. Chem. Int. Ed.* **1990**, *29*, 1219–1227.
- (15) Hammes-Schiffer, S.; Galli, G. Integration of Theory and Experiment in the Modelling of Heterogeneous Electrocatalysis. *Nat. Energy* **2021**, *6*, 700–705.
- (16) Seh, Z. W.; Kibsgaard, J.; Dickens, C. F.; Chorkendorff, I.; Nørskov, J. K.; Jaramillo, T. F. Combining Theory and Experiment in Electrocatalysis: Insights into Materials Design. *Science* **2017**, *355*, eaad4998.
- (17) Plata, R. E.; Singleton, D. A. A Case Study of the Mechanism of Alcohol-Mediated Morita Baylis–Hillman Reactions. The Importance of Experimental Observations. *J. Am. Chem. Soc.* **2015**, *137*, 3811–3826.

- (18) Nørskov, J. K.; Bligaard, T.; Logadottir, A.; Bahn, S.; Hansen, L. B.; Bollinger, M.; Benggaard, H.; Hammer, B.; Sljivancanin, Z.; Mavrikakis, M.; Xu, Y.; Dahl, S.; Jacobsen, C. J. H. Universality in Heterogeneous Catalysis. *J. Catal.* **2002**, *209*, 275–278.
- (19) Michaelides, A.; Liu, Z.-P.; Zhang, C. J.; Alavi, A.; King, D. A.; Hu, P. Identification of General Linear Relationships between Activation Energies and Enthalpy Changes for Dissociation Reactions at Surfaces. *J. Am. Chem. Soc.* **2003**, *125*, 3704–3705.
- (20) Abild-Pedersen, F.; Greeley, J.; Studt, F.; Rossmeisl, J.; Munter, T. R.; Moses, P. G.; Skúlason, E.; Bligaard, T.; Nørskov, J. K. Scaling Properties of Adsorption Energies for Hydrogen-Containing Molecules on Transition-Metal Surfaces. *Phys. Rev. Lett.* **2007**, *99*, 016105.
- (21) Calle-Vallejo, F.; Martínez, J. I.; García-Lastra, J. M.; Rossmeisl, J.; Koper, M. T. M. Physical and Chemical Nature of the Scaling Relations between Adsorption Energies of Atoms on Metal Surfaces. *Phys. Rev. Lett.* **2012**, *108*, 116103.
- (22) Lansford, J. L.; Mironenko, A. V.; Vlachos, D. G. Scaling Relationships and Theory for Vibrational Frequencies of Adsorbates on Transition Metal Surfaces. *Nat. Commun.* **2017**, *8*, 1842.
- (23) Ruzsinszky, A.; Perdew, J. P.; Csonka, G. I.; Vydrov, O. A.; Scuseria, G. E. Spurious Fractional Charge on Dissociated Atoms: Pervasive and Resilient Self-Interaction Error of Common Density Functionals. *J. Chem. Phys.* **2006**, *125*, 194112.
- (24) Mori-Sánchez, P.; Cohen, A. J.; Yang, W. Many-Electron Self-Interaction Error in Approximate Density Functionals. *J. Chem. Phys.* **2006**, *125*, 201102.
- (25) Schimka, L.; Harl, J.; Stroppa, A.; Grüneis, A.; Marsman, M.; Mittendorfer, F.; Kresse, G. Accurate Surface and Adsorption Energies from Many-Body Perturbation Theory. *Nat. Mater.* **2010**, *9*, 741–744.

- (26) Plessow, P. N.; Studt, F. How Accurately Do Approximate Density Functionals Predict Trends in Acidic Zeolite Catalysis? *J. Phys. Chem. Lett.* **2020**, *11*, 4305–4310.
- (27) Raghavachari, K.; Trucks, G. W.; Pople, J. A.; Head-Gordon, M. A Fifth-Order Perturbation Comparison of Electron Correlation Theories. *Chem. Phys. Lett.* **1989**, *157*, 479–483.
- (28) Schäfer, T.; Libisch, F.; Kresse, G.; Grüneis, A. Local Embedding of Coupled Cluster Theory into the Random Phase Approximation Using Plane Waves. *J. Chem. Phys.* **2021**, *154*, 011101.
- (29) Lau, B. T. G.; Knizia, G.; Berkelbach, T. C. Regional Embedding Enables High-Level Quantum Chemistry for Surface Science. *J. Phys. Chem. Lett.* **2021**, *12*, 1104–1109.
- (30) Tosoni, S.; Sauer, J. Accurate Quantum Chemical Energies for the Interaction of Hydrocarbons with Oxide Surfaces: CH₄/MgO(001). *Phys. Chem. Chem. Phys.* **2010**, *12*, 14330–14340.
- (31) Boese, A. D.; Sauer, J. Accurate Adsorption Energies of Small Molecules on Oxide Surfaces: CO–MgO(001). *Phys. Chem. Chem. Phys.* **2013**, *15*, 16481–16493.
- (32) Alessio, M.; Usvyat, D.; Sauer, J. Chemically Accurate Adsorption Energies: CO and H₂O on the MgO(001) Surface. *J. Chem. Theory Comput.* **2019**, *15*, 1329–1344.
- (33) Boese, A. D.; Sauer, J. Accurate Adsorption Energies for Small Molecules on Oxide Surfaces: CH₄/MgO(001) and C₂H₆/MgO(001). *J. Comp. Chem.* **2016**, *37*, 2374–2385.
- (34) Kubas, A.; Berger, D.; Oberhofer, H.; Maganas, D.; Reuter, K.; Neese, F. Surface Adsorption Energetics Studied with “Gold Standard” Wave-Function-Based Ab Initio Methods: Small-Molecule Binding to TiO₂(110). *J. Phys. Chem. Lett.* **2016**, *7*, 4207–4212.

- (35) Araujo, R. B.; Rodrigues, G. L. S.; dos Santos, E. C.; Pettersson, L. G. M. Adsorption Energies on Transition Metal Surfaces: Towards an Accurate and Balanced Description. *Nat. Commun.* **2022**, *13*, 6853.
- (36) Masios, N.; Irmeler, A.; Schäfer, T.; Grüneis, A. Averting the Infrared Catastrophe in the Gold Standard of Quantum Chemistry. *Phys. Rev. Lett.* **2023**, *131*, 186401.
- (37) Booth, G. H.; Grüneis, A.; Kresse, G.; Alavi, A. Towards an Exact Description of Electronic Wavefunctions in Real Solids. *Nature* **2013**, *493*, 365–370.
- (38) Mihm, T. N.; Schäfer, T.; Ramadugu, S. K.; Weiler, L.; Grüneis, A.; Shepherd, J. J. A Shortcut to the Thermodynamic Limit for Quantum Many-Body Calculations of Metals. *Nat. Comput. Sci.* **2021**, *1*, 801–808.
- (39) Ye, H.-Z.; Berkelbach, T. C. Adsorption and Vibrational Spectroscopy of CO on the Surface of MgO from Periodic Local Coupled-Cluster Theory. *Faraday Discuss.* **2024**,
- (40) Ye, H.-Z.; Berkelbach, T. C. Ab Initio Surface Chemistry with Chemical Accuracy. *arXiv:2309.14640* **2024**,
- (41) Dittmer, A.; Izsák, R.; Neese, F.; Maganas, D. Accurate Band Gap Predictions of Semiconductors in the Framework of the Similarity Transformed Equation of Motion Coupled Cluster Theory. *Inorg. Chem.* **2019**, *58*, 9303–9315.
- (42) Dittmer, A.; Stoychev, G. L.; Maganas, D.; Auer, A. A.; Neese, F. Computation of NMR Shielding Constants for Solids Using an Embedded Cluster Approach with DFT, Double-Hybrid DFT, and MP2. *J. Chem. Theory Comput.* **2020**, *16*, 6950–6967.
- (43) Shi, B. X.; Kapil, V.; Zen, A.; Chen, J.; Alavi, A.; Michaelides, A. General Embedded Cluster Protocol for Accurate Modeling of Oxygen Vacancies in Metal-Oxides. *J. Chem. Phys.* **2022**, *156*, 124704.

- (44) Shi, B. X.; Zen, A.; Kapil, V.; Nagy, P. R.; Grüneis, A.; Michaelides, A. Many-Body Methods for Surface Chemistry Come of Age: Achieving Consensus with Experiments. *J. Am. Chem. Soc.* **2023**, *145*, 25372–25381.
- (45) Kick, M.; Oberhofer, H. Towards a Transferable Design of Solid-State Embedding Models on the Example of a Rutile TiO₂ (110) Surface. *J. Chem. Phys.* **2019**, *151*, 184114.
- (46) Shi, B. X.; Wales, D. J.; Michaelides, A.; Myung, C. W. Going for Gold(-Standard): Attaining Coupled Cluster Accuracy in Oxide-Supported Nanoclusters. *J. Chem. Theory Comput.* **2024**, *20*, 5306–5316.
- (47) Chung, L. W.; Sameera, W. M. C.; Ramozzi, R.; Page, A. J.; Hatanaka, M.; Petrova, G. P.; Harris, T. V.; Li, X.; Ke, Z.; Liu, F.; Li, H.-B.; Ding, L.; Morokuma, K. The ONIOM Method and Its Applications. *Chem. Rev.* **2015**, *115*, 5678–5796.
- (48) Platero, E. E.; Scarano, D.; Spoto, G.; Zecchina, A. Dipole Coupling and Chemical Shifts of CO and NO Adsorbed on Oxides and Halides with Rock-Salt Structure. *Faraday Discuss. Chem. Soc.* **1985**, *80*, 183–193.
- (49) Di Valentin, C.; Pacchioni, G.; Chiesa, M.; Giamello, E.; Abbet, S.; Heiz, U. NO Monomers on MgO Powders and Thin Films. *J. Phys. Chem. B* **2002**, *106*, 1637–1645.
- (50) Wichtendahl, R.; Rodriguez-Rodrigo, M.; Härtel, U.; Kühlenbeck, H.; Freund, H.-J. Thermodesorption of CO and NO from Vacuum-Cleaved NiO(100) and MgO(100). *Phys. Status Solidi A* **1999**, *173*, 93–100.
- (51) Hamada, I. Van Der Waals Density Functional Made Accurate. *Phys. Rev. B* **2014**, *89*, 121103.

- (52) E. Hamlyn, R. C.; Mahapatra, M.; C. Grinter, D.; Xu, F.; Luo, S.; M. Palomino, R.; Kattel, S.; Waluyo, I.; Liu, P.; J. Stacchiola, D.; D. Senanayake, S.; A. Rodriguez, J. Imaging the Ordering of a Weakly Adsorbed Two-Dimensional Condensate: Ambient-Pressure Microscopy and Spectroscopy of CO₂ Molecules on Rutile TiO₂ (110). *Phys. Chem. Chem. Phys.* **2018**, *20*, 13122–13126.
- (53) Meixner, D. L.; Arthur, D. A.; George, S. M. Kinetics of Desorption, Adsorption, and Surface Diffusion of CO₂ on MgO(100). *Surf. Sci.* **1992**, *261*, 141–154.
- (54) Chakradhar, A.; Burghaus, U. Carbon Dioxide Adsorption on MgO(001)–CO₂ Kinetics and Dynamics. *Surf. Sci.* **2013**, *616*, 171–177.
- (55) Pacchioni, G.; Ricart, J. M.; Illas, F. Ab Initio Cluster Model Calculations on the Chemisorption of CO₂ and SO₂ Probe Molecules on MgO and CaO (100) Surfaces. A Theoretical Measure of Oxide Basicity. *J. Am. Chem. Soc.* **1994**, *116*, 10152–10158.
- (56) Jensen, M. B.; Pettersson, L. G. M.; Swang, O.; Olsbye, U. CO₂ Sorption on MgO and CaO Surfaces: A Comparative Quantum Chemical Cluster Study. *J. Phys. Chem. B* **2005**, *109*, 16774–16781.
- (57) Downing, C. A.; Sokol, A. A.; Catlow, C. R. A. The Reactivity of CO₂ on the MgO(100) Surface. *Phys. Chem. Chem. Phys.* **2013**, *16*, 184–195.
- (58) Mazheika, A.; Levchenko, S. V. Ni Substitutional Defects in Bulk and at the (001) Surface of MgO from First-Principles Calculations. *J. Phys. Chem. C* **2016**, *120*, 26934–26944.
- (59) Yanagisawa, Y.; Takaoka, K.; Yamabe, S.; Ito, T. Interaction of CO₂ with Magnesium Oxide Surfaces: A TPD, FTIR, and Cluster-Model Calculation Study. *J. Phys. Chem.* **1995**, *99*, 3704–3710.

- (60) Sorescu, D. C.; Lee, J.; Al-Saidi, W. A.; Jordan, K. D. CO₂ Adsorption on TiO₂(110) Rutile: Insight from Dispersion-Corrected Density Functional Theory Calculations and Scanning Tunneling Microscopy Experiments. *J. Chem. Phys.* **2011**, *134*, 104707.
- (61) Huesges, Z.; Müller, C.; Paulus, B.; Maschio, L. Dispersion Corrected DFT Calculations for the Adsorption of N₂O on MgO. *Surf. Sci.* **2014**, *627*, 11–15.
- (62) Wellendorff, J.; Silbaugh, T. L.; Garcia-Pintos, D.; Nørskov, J. K.; Bligaard, T.; Studt, F.; Campbell, C. T. A Benchmark Database for Adsorption Bond Energies to Transition Metal Surfaces and Comparison to Selected DFT Functionals. *Surf. Sci.* **2015**, *640*, 36–44.
- (63) R. Rehak, F.; Piccini, G.; Alessio, M.; Sauer, J. Including Dispersion in Density Functional Theory for Adsorption on Flat Oxide Surfaces, in Metal–Organic Frameworks and in Acidic Zeolites. *Phys. Chem. Chem. Phys.* **2020**, *22*, 7577–7585.
- (64) Caldeweyher, E.; Mewes, J.-M.; Ehlert, S.; Grimme, S. Extension and Evaluation of the D4 London-dispersion Model for Periodic Systems. *Phys. Chem. Chem. Phys.* **2020**, *22*, 8499–8512.
- (65) Řezáč, J.; Riley, K. E.; Hobza, P. S66: A Well-balanced Database of Benchmark Interaction Energies Relevant to Biomolecular Structures. *J. Chem. Theory Comput.* **2011**, *7*, 2427–2438.
- (66) Donchev, A. G.; Taube, A. G.; Decolvenaere, E.; Hargus, C.; McGibbon, R. T.; Law, K.-H.; Gregersen, B. A.; Li, J.-L.; Palmo, K.; Siva, K.; Bergdorf, M.; Klepeis, J. L.; Shaw, D. E. Quantum Chemical Benchmark Databases of Gold-Standard Dimer Interaction Energies. *Sci. Data* **2021**, *8*, 55.
- (67) Campbell, C. T.; Sellers, J. R. V. Enthalpies and Entropies of Adsorption on Well-Defined Oxide Surfaces: Experimental Measurements. *Chem. Rev.* **2013**, *113*, 4106–4135.

- (68) Ren, X.; Tkatchenko, A.; Rinke, P.; Scheffler, M. Beyond the Random-Phase Approximation for the Electron Correlation Energy: The Importance of Single Excitations. *Phys. Rev. Lett.* **2011**, *106*, 153003.
- (69) Klimeš, J.; Kaltak, M.; Maggio, E.; Kresse, G. Singles Correlation Energy Contributions in Solids. *J. Chem. Phys.* **2015**, *143*, 102816.
- (70) Perdew, J. P.; Burke, K.; Ernzerhof, M. Generalized Gradient Approximation Made Simple. *Phys. Rev. Lett.* **1996**, *77*, 3865–3868.
- (71) Grimme, S.; Antony, J.; Ehrlich, S.; Krieg, H. A Consistent and Accurate Ab Initio Parametrization of Density Functional Dispersion Correction (DFT-D) for the 94 Elements H-Pu. *J. Chem. Phys.* **2010**, *132*, 154104.
- (72) Ning, J.; Kothakonda, M.; Furness, J. W.; Kaplan, A. D.; Ehlert, S.; Brandenburg, J. G.; Perdew, J. P.; Sun, J. Workhorse Minimally Empirical Dispersion-Corrected Density Functional with Tests for Weakly Bound Systems: r²SCAN+rVV10. *Phys. Rev. B* **2022**, *106*, 075422.
- (73) Ehlert, S.; Huniar, U.; Ning, J.; Furness, J. W.; Sun, J.; Kaplan, A. D.; Perdew, J. P.; Brandenburg, J. G. r²SCAN-D4: Dispersion Corrected Meta-Generalized Gradient Approximation for General Chemical Applications. *J. Chem. Phys.* **2021**, *154*, 061101.
- (74) Ehrlich, S.; Moellmann, J.; Reckien, W.; Bredow, T.; Grimme, S. System-Dependent Dispersion Coefficients for the DFT-D3 Treatment of Adsorption Processes on Ionic Surfaces. *ChemPhysChem* **2011**, *12*, 3414–3420.
- (75) Kothakonda, M.; Kaplan, A. D.; Isaacs, E. B.; Bartel, C. J.; Furness, J. W.; Ning, J.; Wolverton, C.; Perdew, J. P.; Sun, J. Testing the r²SCAN Density Functional for the Thermodynamic Stability of Solids with and without a van Der Waals Correction. *ACS Mater. Au* **2023**, *3*, 102–111.

- (76) Dohnálek, Z.; Kim, J.; Bondarchuk, O.; White, J. M.; Kay, B. D. Physisorption of N₂, O₂, and CO on Fully Oxidized TiO₂(110). *J. Phys. Chem. B* **2006**, *110*, 6229–6235.
- (77) Al-Hamdani, Y. S.; Rossi, M.; Alfè, D.; Tsatsoulis, T.; Ramberger, B.; Brandenburg, J. G.; Zen, A.; Kresse, G.; Grüneis, A.; Tkatchenko, A.; Michaelides, A. Properties of the Water to Boron Nitride Interaction: From Zero to Two Dimensions with Benchmark Accuracy. *J. Chem. Phys.* **2017**, *147*, 044710.
- (78) Tsatsoulis, T.; Sakong, S.; Groß, A.; Grüneis, A. Reaction Energetics of Hydrogen on Si(100) Surface: A Periodic Many-Electron Theory Study. *J. Chem. Phys.* **2018**, *149*, 244105.
- (79) Brandenburg, J. G.; Zen, A.; Fitzner, M.; Ramberger, B.; Kresse, G.; Tsatsoulis, T.; Grüneis, A.; Michaelides, A.; Alfè, D. Physisorption of Water on Graphene: Subchemical Accuracy from Many-Body Electronic Structure Methods. *J. Phys. Chem. Lett.* **2019**, *10*, 358–368.
- (80) Schäfer, T.; Gallo, A.; Irmeler, A.; Hummel, F.; Grüneis, A. Surface Science Using Coupled Cluster Theory via Local Wannier Functions and In-RPA-embedding: The Case of Water on Graphitic Carbon Nitride. *J. Chem. Phys.* **2021**, *155*, 244103.
- (81) Sauer, J. Ab Initio Calculations for Molecule–Surface Interactions with Chemical Accuracy. *Acc. Chem. Res.* **2019**, *52*, 3502–3510.
- (82) Lu, Y. et al. Multiscale QM/MM Modelling of Catalytic Systems with ChemShell. *Phys. Chem. Chem. Phys.* **2023**, *25*, 21816–21835.
- (83) Buckeridge, J.; Butler, K. T.; Catlow, C. R. A.; Logsdail, A. J.; Scanlon, D. O.; Shevlin, S. A.; Woodley, S. M.; Sokol, A. A.; Walsh, A. Polymorph Engineering of TiO₂: Demonstrating How Absolute Reference Potentials Are Determined by Local Coordination. *Chem. Mater.* **2015**, *27*, 3844–3851.

- (84) Scanlon, D. O.; Dunnill, C. W.; Buckeridge, J.; Shevlin, S. A.; Logsdail, A. J.; Woodley, S. M.; Catlow, C. R. A.; Powell, M. J.; Palgrave, R. G.; Parkin, I. P.; Watson, G. W.; Keal, T. W.; Sherwood, P.; Walsh, A.; Sokol, A. A. Band Alignment of Rutile and Anatase TiO₂. *Nat. Mater.* **2013**, *12*, 798–801.
- (85) Berger, D.; Oberhofer, H.; Reuter, K. First-Principles Embedded-Cluster Calculations of the Neutral and Charged Oxygen Vacancy at the Rutile TiO₂(110) Surface. *Phys. Rev. B* **2015**, *92*, 075308.
- (86) Nagy, P. R.; Kállay, M. Approaching the Basis Set Limit of CCSD(T) Energies for Large Molecules with Local Natural Orbital Coupled-Cluster Methods. *J. Chem. Theory Comput.* **2019**, *15*, 5275–5298.
- (87) Riplinger, C.; Neese, F. An Efficient and near Linear Scaling Pair Natural Orbital Based Local Coupled Cluster Method. *J. Chem. Phys.* **2013**, *138*, 034106.
- (88) Ma, Q.; Werner, H.-J. Explicitly Correlated Local Coupled-Cluster Methods Using Pair Natural Orbitals. *Wiley Interdiscip. Rev.: Comput. Mol. Sci.* **2018**, *8*, e1371.
- (89) Jain, A.; Ong, S. P.; Hautier, G.; Chen, W.; Richards, W. D.; Dacek, S.; Cholia, S.; Gunter, D.; Skinner, D.; Ceder, G.; Persson, K. A. Commentary: The Materials Project: A Materials Genome Approach to Accelerating Materials Innovation. *APL Mater.* **2013**, *1*, 011002.
- (90) Campbell, C. T.; Sellers, J. R. V. The Entropies of Adsorbed Molecules. *J. Am. Chem. Soc.* **2012**, *134*, 18109–18115.
- (91) Kirkpatrick, J. et al. Pushing the Frontiers of Density Functionals by Solving the Fractional Electron Problem. *Science* **2021**, *374*, 1385–1389.
- (92) Bystrom, K.; Kozinsky, B. CIDER: An Expressive, Nonlocal Feature Set for Ma-

- chine Learning Density Functionals with Exact Constraints. *J. Chem. Theory Comput.* **2022**, *18*, 2180–2192.
- (93) Sheldon, C.; Paier, J.; Usvyat, D.; Sauer, J. Hybrid RPA:DFT Approach for Adsorption on Transition Metal Surfaces: Methane and Ethane on Platinum (111). *J. Chem. Theory Comput.* **2024**, *20*, 2219–2227.
- (94) Carbone, J. P.; Irmeler, A.; Gallo, A.; Schäfer, T.; Benschoten, W. Z. V.; Shepherd, J. J.; Grüneis, A. CO Adsorption on Pt(111) Studied by Periodic Coupled Cluster Theory. *Faraday Discuss.* **2024**,
- (95) Sillar, K.; Hofmann, A.; Sauer, J. Ab Initio Study of Hydrogen Adsorption in MOF-5. *J. Am. Chem. Soc.* **2009**, *131*, 4143–4150.
- (96) Sillar, K.; Sauer, J. Ab Initio Prediction of Adsorption Isotherms for Small Molecules in Metal–Organic Frameworks: The Effect of Lateral Interactions for Methane/CPO-27-Mg. *J. Am. Chem. Soc.* **2012**, *134*, 18354–18365.
- (97) Berger, F.; Rybicki, M.; Sauer, J. Adsorption and Cracking of Propane by Zeolites of Different Pore Size. *J. Catal.* **2021**, *395*, 117–128.
- (98) Daru, J.; Forbert, H.; Behler, J.; Marx, D. Coupled Cluster Molecular Dynamics of Condensed Phase Systems Enabled by Machine Learning Potentials: Liquid Water Benchmark. *Phys. Rev. Lett.* **2022**, *129*, 226001.
- (99) Chen, M. S.; Lee, J.; Ye, H.-Z.; Berkelbach, T. C.; Reichman, D. R.; Markland, T. E. Data-Efficient Machine Learning Potentials from Transfer Learning of Periodic Correlated Electronic Structure Methods: Liquid Water at AFQMC, CCSD, and CCSD(T) Accuracy. *J. Chem. Theory Comput.* **2023**, *19*, 4510–4519.
- (100) Rosen, A. S. Quacc – The Quantum Accelerator: <https://zenodo.org/records/13921187>. Zenodo, 2024.

- (101) Neese, F.; Wennmohs, F.; Becker, U.; Riplinger, C. The ORCA Quantum Chemistry Program Package. *J. Chem. Phys.* **2020**, *152*, 224108.
- (102) Kállay, M. et al. The MRCC Program System: Accurate Quantum Chemistry from Water to Proteins. *J. Chem. Phys.* **2020**, *152*, 074107.
- (103) Nagy, P. R.; Samu, G.; Kállay, M. Optimization of the Linear-Scaling Local Natural Orbital CCSD(T) Method: Improved Algorithm and Benchmark Applications. *J. Chem. Theory Comput.* **2018**, *14*, 4193–4215.
- (104) Neese, F.; Valeev, E. F. Revisiting the Atomic Natural Orbital Approach for Basis Sets: Robust Systematic Basis Sets for Explicitly Correlated and Conventional Correlated *Ab Initio* Methods? *J. Chem. Theory Comput.* **2011**, *7*, 33–43.
- (105) Wellendorff, J.; Lundgaard, K. T.; Møgelhøj, A.; Petzold, V.; Landis, D. D.; Nørskov, J. K.; Bligaard, T.; Jacobsen, K. W. Density Functionals for Surface Science: Exchange-correlation Model Development with Bayesian Error Estimation. *Phys. Rev. B* **2012**, *85*, 235149.
- (106) Rui, Y.; Chen, Y.; Ivanova, E.; Grabowski, I.; Dral, P. O. The Best DFT Functional Is the Ensemble of Functionals. 2024.
- (107) Kresse, G.; Furthmüller, J. Efficiency of Ab-Initio Total Energy Calculations for Metals and Semiconductors Using a Plane-Wave Basis Set. *Comput. Mater. Sci.* **1996**, *6*, 15–50.
- (108) Kresse, G.; Furthmüller, J. Efficient Iterative Schemes for Ab Initio Total-Energy Calculations Using a Plane-Wave Basis Set. *Phys. Rev. B* **1996**, *54*, 11169–11186.
- (109) Grimme, S. Supramolecular Binding Thermodynamics by Dispersion-Corrected Density Functional Theory. *Chem. - Eur. J.* **2012**, *18*, 9955–9964.

- (110) Li, Y.-P.; Gomes, J.; Mallikarjun Sharada, S.; Bell, A. T.; Head-Gordon, M. Improved Force-Field Parameters for QM/MM Simulations of the Energies of Adsorption for Molecules in Zeolites and a Free Rotor Correction to the Rigid Rotor Harmonic Oscillator Model for Adsorption Enthalpies. *J. Phys. Chem. C* **2015**, *119*, 1840–1850.
- (111) Günster, J.; Liu, G.; Stultz, J.; Goodman, D. W. Interaction of Methanol and Water on MgO(100) Studied by Ultraviolet Photoelectron and Metastable Impact Electron Spectroscopies. *J. Chem. Phys.* **1999**, *110*, 2558–2565.
- (112) Stirniman, M. J.; Huang, C.; Scott Smith, R.; Joyce, S. A.; Kay, B. D. The Adsorption and Desorption of Water on Single Crystal MgO(100): The Role of Surface Defects. *J. Chem. Phys.* **1996**, *105*, 1295–1298.
- (113) Thompson, T. L.; Diwald, O.; Yates, J. T. CO₂ as a Probe for Monitoring the Surface Defects on TiO₂(110) Temperature-Programmed Desorption. *J. Phys. Chem. B* **2003**, *107*, 11700–11704.
- (114) Lian, J. C.; Kieseritzky, E.; Gonchar, A.; Sterrer, M.; Rocker, J.; Gao, H.-J.; Risse, T. N₂O Adsorption on the Surface of MgO(001) Thin Films: An Infrared and TPD Study. *J. Phys. Chem. C* **2010**, *114*, 3148–3151.

Supplementary Information for:
An accurate and efficient framework for predictive insights into ionic surface chemistry

Benjamin X. Shi,¹ Andrew S. Rosen,² Tobias Schäfer,³ Andreas Grüneis,³ Venkat Kapil,^{1,4,5} Andrea Zen,^{6,7} and Angelos Michaelides¹

¹*Yusuf Hamied Department of Chemistry, University of Cambridge,
Lensfield Road, Cambridge CB2 1EW, United Kingdom*

²*Department of Chemical and Biological Engineering,
Princeton University, Princeton, NJ 08540 USA*

³*Institute for Theoretical Physics, TU Wien,
Wiedner Hauptstraße 8-10/136, 1040 Vienna, Austria*

⁴*Department of Physics and Astronomy, University College London,
7-19 Gordon St, London WC1H 0AH, UK*

⁵*Thomas Young Centre and London Centre for Nanotechnology, 9 Gordon St, London WC1H 0AH*

⁶*Dipartimento di Fisica Ettore Pancini, Università di
Napoli Federico II, Monte S. Angelo, I-80126 Napoli, Italy*

⁷*Department of Earth Sciences, University College London,
Gower Street, London WC1E 6BT, United Kingdom*

(Dated: December 24, 2024)

CONTENTS

| | |
|--------------------------------------------------------------------------------------------|----|
| Part I: Additional results and discussion | 7 |
| S1. Insights into adsorption configuration | 8 |
| S1.1. Cluster CH ₃ OH and H ₂ O on MgO(001) | 8 |
| S1.2. CO ₂ on MgO(001) | 10 |
| S1.3. NO on MgO(001) | 11 |
| S1.4. CO ₂ on TiO ₂ rutile(110) | 12 |
| S1.5. N ₂ O on MgO(001) | 14 |
| S1.6. Previously debated systems | 14 |
| S2. A benchmark dataset for non-covalent interactions of adsorbate–surface systems | 16 |
| S2.1. Computational details for the DFA benchmark | 17 |
| Part II: Supporting data | 18 |
| S3. The approach to calculating the adsorption enthalpy | 19 |
| S4. The adsorbate–surface complexes studied in this work | 20 |
| S5. Computational details for correlated wave-function theory | 23 |
| S6. Interaction energies computed with the SKZCAM protocol | 24 |
| S6.1. Generating a systematic series of clusters within electrostatic embedding | 25 |
| S6.2. Extrapolating towards the bulk limit with the series of clusters | 27 |
| S6.3. Multilevel Δ CC contribution through mechanical embedding with small clusters | 37 |

| | |
|-------------------------------------------------------------------------------------------------------------------------|----|
| S6.4. Further multilevel contributions for basis set and semi-core electron correlation | 40 |
| S6.5. The final E_{int} estimates and their error bars | 43 |
| S6.6. Improvements to SKZCAM protocol in present work | 45 |
| S7. Contributions for the cohesive and conformational energy from cWFT in selected systems | 46 |
| S7.1. Conformational energy of the chemisorbed CO_2 on $\text{MgO}(001)$ | 46 |
| S7.2. Cohesive energy in CH_4 and C_2H_6 monolayers on $\text{MgO}(001)$ | 48 |
| S7.3. Cohesive and dissociation energy in H_2O and CH_3OH clusters on $\text{MgO}(001)$ | 51 |
| S7.4. Cohesive energy of NO dimer on $\text{MgO}(001)$ | 53 |
| S8. Geometry relaxation and enthalpic contributions from a DFT ensemble | 55 |
| S8.1. Computational details for periodic density functional theory | 55 |
| S8.2. The relaxation energy | 57 |
| S8.3. Estimating geometrical errors | 59 |
| S8.4. Zero-point vibrational and enthalpic contributions | 66 |
| S8.5. Dissociation energy for the H_2O and CH_3OH clusters | 68 |
| S9. Final autoSKZCAM estimates | 69 |
| S9.1. Validating autoSKZCAM error estimates | 71 |
| S10. Automation of the autoSKZCAM framework | 72 |
| S10.1. QuAcc computational workflow details | 72 |
| S10.2. Automated SKZCAM protocol | 74 |
| S11. Analysing experimental estimates and techniques | 75 |

| | |
|------------------------------------------------------------------------|----|
| | 4 |
| S12. Comparison of H_{ads} between autoSKZCAM and experiments | 79 |
| S13. Previous computational literature | 82 |
| S14. Benchmarking the cost of the autoSKZCAM framework | 84 |
| References | 86 |

We provide additional supporting data as well as contextual information to the main text here. All output files are provided on [Github \[195\]](#), with a corresponding Jupyter Notebook file that analyses all of the data. This data can also be viewed and analysed on the browser with [Google Colab](#).

Within this supplementary data, we start by providing more detail on two key developments of this work:

- Firstly, we discuss the atomic-level insights into the adsorption configuration for several of the studied systems in Sec. [S1](#), discussing the prior literature and how autoSKZCAM helps to resolve previous discrepancies.
- The other key output of this work is the CCSD(T)-level dataset of references on the interaction energy for the set of adsorbate–surface system studied within this work, provided in Sec. [S2](#). We expect that this will serve as a useful benchmark tool for assessing the performance of newly developed density functional approximations as well as approximate correlated wave-function methods.

In the second part to the supplementary information, we provide more elaborate details and concrete numbers to support the claims made within the main text:

- We discuss the approach we take towards computing the adsorption enthalpy in Sec. [S3](#) which forms the basis of the autoSKZCAM framework developed within the present work.
- We show the adsorbate–surface complexes studied within this work in Sec. [S4](#).
- We give the details of the correlated wave-function methods [MP2 and CCSD(T)] used in this work in Sec. [S5](#).
- We describe the SKZCAM protocol – used to calculate the interaction energy contribution to the adsorption enthalpy – in Sec. [S6](#). The set of clusters generated by this protocol and the MP2 and CCSD(T) estimates for each cluster are also provided.
- We discuss additional contributions calculated at the CCSD(T)-level, such as conformational energy and cohesive energy (for the clusters and monolayers) contributions to the final adsorption enthalpy in Sec. [S7](#).

- We describe how the remaining contributions to the adsorption enthalpy – geometrical relaxation, zero-point vibrational and thermal – are calculated using an ensemble of density functional approximations in Sec. [S8](#).
- We provide the final adsorption enthalpy estimates made with the autoSKZCAM framework in Sec. [S9](#) and make some additional validation tests on its reliability in Sec. [S9.1](#).
- We describe how the autoSKZCAM framework has been automated using the QuAcc computational materials science workflow library in Sec. [S10](#).
- We describe how we analyse accurate experimental adsorption enthalpies with reliable error bars in Sec. [S11](#).
- The final autoSKZCAM adsorption enthalpy estimates are compared to experiments in Sec. [S12](#).
- These estimates are further compared to previous literature in Sec. [S13](#).
- Finally, we benchmark and highlight the low-cost of the autoSKZCAM framework relative to DFT in Sec. [S14](#).

Part I: Further insights and discussion

S1. INSIGHTS INTO ADSORPTION CONFIGURATION

We now discuss specific subset of systems within the 19 studied adsorbate–surface systems (see Sec. S4 where there have been debates on the adsorption configuration. In particular, we apply the autoSKZCAM framework to compute H_{ads} for each of these systems and show that the lowest energy configuration has an H_{ads} that agrees with experiment; with all other configurations predicted to be less stable with an H_{ads} that cannot reproduce experiment.

S1.1. Cluster CH₃OH and H₂O on MgO(001)

For both CH₃OH and H₂O on MgO(001), we have observed that it is necessary to account for H-bonded clustering of the molecules on the surface together with partial dissociation of the cluster to achieve agreement on H_{ads} with experiments. In Fig. S1, we compare the H_{ads} with the revPBE-D4 [197, 198] density functional approximation (DFA) for several adsorption configurations of CH₃OH on MgO(001), involving a single molecule up to clusters adsorbed on the surface. This DFA was chosen because it can successfully reproduce autoSKZCAM estimates in Extended Data Fig. 1 and 2 of the main text. For single molecules, we considered both a tilted [199, 200] and parallel [201, 202] adsorption configuration. These have been proposed within previous literature and we find that the tilted configuration is more stable, albeit unable to reproduce experiment. This hints at missing contributions found in e.g., H-bonded and dissociated clusters. For the H-bonded clusters, we have considered the lowest-energy, as discovered through a random structure search, geometries for the dimer, trimer and tetramer, while dissociation is induced by moving an H-atom onto a nearby O atom. There is significant stabilisation for the H-bonded tetramer of CH₃OH relative to the dimer or trimer, as it can form a complete H-bonded network commensurate with the underlying geometry of the MgO(001) surface. However, this is still insufficient for reproduce the experimental H_{ads} . There is further stabilisation when dissociation is induced. While dissociation is isoenergetic (to within 2 meV) to the molecular form for the dimer, there is stabilisation of 43 meV for the trimer, which goes up to 78 meV for the tetramer. This stabilisation brings the dissociated tetramer H_{ads} into agreement with experiments. Such stabilisation upon dissociation has also been observed for clusters of H₂O, where we find that dissociation stabilises the H₂O tetramer by 81 meV (Extended Data Fig. 2 of the main text), which would bring the autoSKZCAM estimate into excellent agreement with experiment.

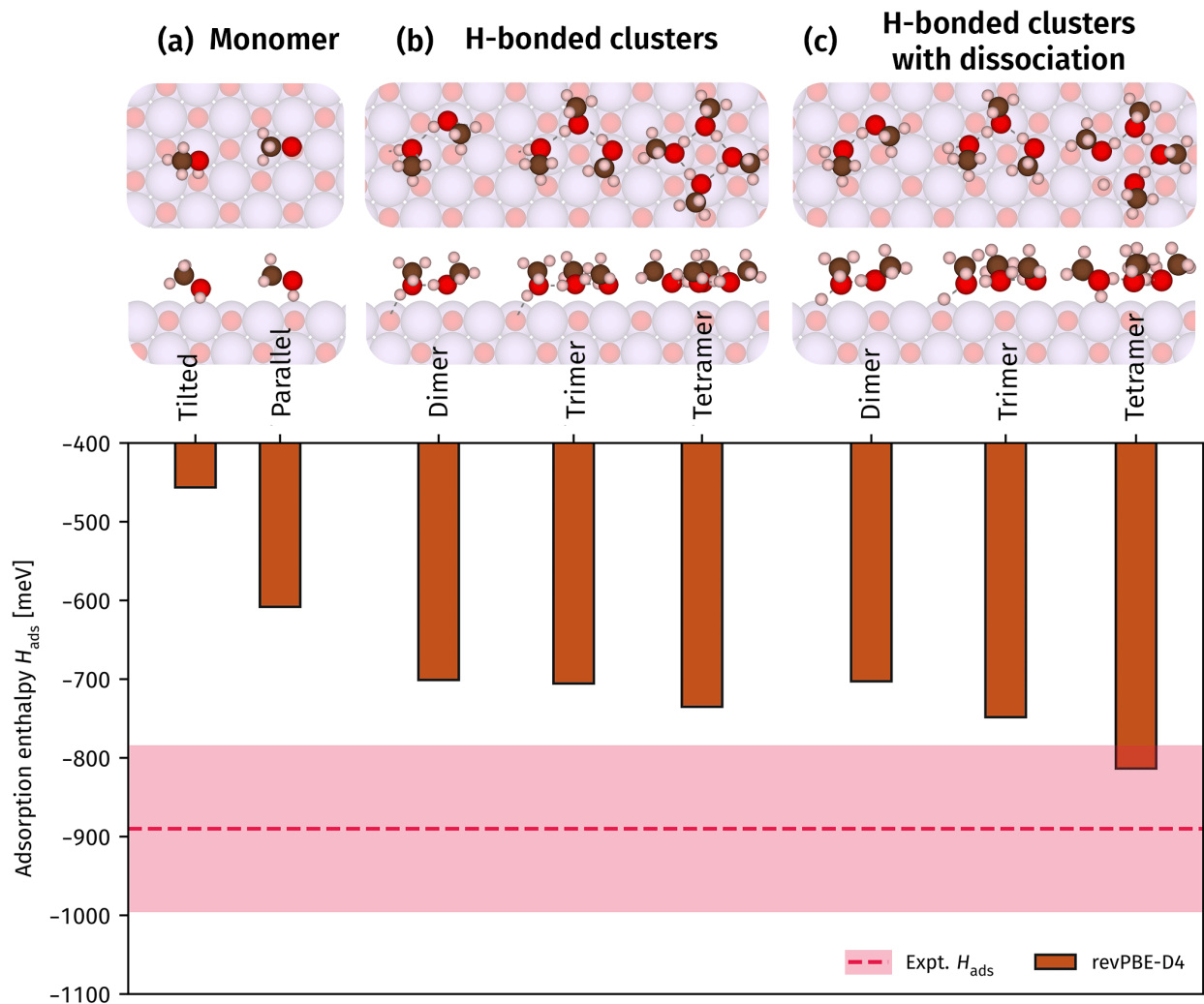


FIG. S1. Comparison of the H_{ads} (per molecule) calculated with the revPBE-D4 functional for the adsorption of (a) monomer CH_3OH on $\text{MgO}(001)$, (b) H-bonded clusters and (c) H-bonded CH_3OH cluster with partial dissociation. We consider the lowest energy dimer, trimer and tetramer adsorption configurations. These are compared against experimental TPD measurements by Günster *et al.* [196]. Conservative error estimates (corresponding to a 95% confidence interval or more) are given for both experiment and autoSKZCAM, as discussed in Secs. S9 and S11, respectively.

In Extended Data Figs. 1 and 2 of the main text, we plot the H_{ads} for H_2O and CH_3OH on $\text{MgO}(001)$ for the monomer and tetramer configurations using the autoSKZCAM framework and a set of density functional approximations. As discussed in Sec. S8.5, we predict the H_{ads} for the dissociated form of the tetramer by using the DFT ensemble to calculate E_{diss} – the stabilisation energy to form the dissociated cluster from the (molecular) H-bonded cluster. This enables excellent agreement to experimental H_{ads} for both H_2O and CH_3OH .

Our insights are in agreement with experimental evidence, which suggests that even at low

coverage limits, CH₃OH molecules will form 2D islands [203]. In particular, we suggest that these 2D islands contain H-bonded networks together with partial dissociation. It should be noted that while an H_{ads} value was obtained for a single-monomer of H₂O in Refs. 204, 205, this was done by subtracting the lateral interactions (including both H-bonding and partial dissociation) of a 2D monolayer of water from the monolayer H_{ads} of H₂O. Physically, we expect a similar behaviour for H₂O molecules to cluster on the MgO(001) surface, even at the low coverage limits.

S1.2. CO₂ on MgO(001)

The adsorption of CO₂ on MgO has been the subject of many theoretical and experimental studies over the years. These have largely revolved around a physisorbed or chemisorbed (‘monodentate’) state. Within experiments, early work by Meixner *et al.* [206] used laser-induced thermal desorption experiments to predict an H_{ads} of -431 meV, which was attributed to a physisorbed state due to its low (absolute) value. However, a TPD experiment by Chakradhar and Burghaus [207] came to an estimate of -664 meV on H_{ads} and attributed this to the formation of surface carbonates (i.e., chemisorption) as confirmed via XPS, with no evidence of a physisorbed state. On the simulations front, there are several studies which have found the chemisorbed state to be completely unstable [208, 209], predicting a physisorbed state [210–213], while many have also predicted a chemisorbed state to show significant stability [214–216].

We use the autoSKZCAM framework to calculate the H_{ads} for both the physisorbed and chemisorbed structure in Extended Data Fig. 3 of the main text. We find that the autoSKZCAM framework comes into good agreement with the experiment of Chakradhar and Burghaus [207] for the chemisorbed state while it does not come into agreement for the physisorbed state. The DFAs all predict the chemisorbed state to be more stable than the physisorbed state by more than 200 meV, except for vdW-DF, where the differences are less than 30 meV. It can be seen that while the chemisorbed state are all predicted correctly, most of the DFAs are unable to reach agreement with experiment. Similarly, most DFAs are unable to match with the experiment by Meixner *et al.* for the physisorbed state. This points towards potential errors within the original measurements by Meixner *et al.*. For example, Chakradhar and Burghaus have surmised that the temperature reading (~ 120 K) of Meixner *et al.* was ‘un-calibrated’ as the low desorption temperatures do not agree with previous TPD measurements [217, 218] including their own (~ 230 K). In fact, data by Meixner *et al.* indicates a ‘lack of surface mobility’ of the CO₂ which points towards a chemisorbed

state. If the measurements by Meixner *et al.* were re-analysed with a desorption temperature of 230 K, their experiment would predict H_{ads} of -826 ± 94 meV, in good agreement with our autoSKZCAM predictions. Beyond previous TPD measurements, there has been significant recent interest in MgO for CO₂ storage [219, 220], with the chemisorbed state now supported with new evidence from NMR experiments [221, 222].

S1.3. NO on MgO(001)

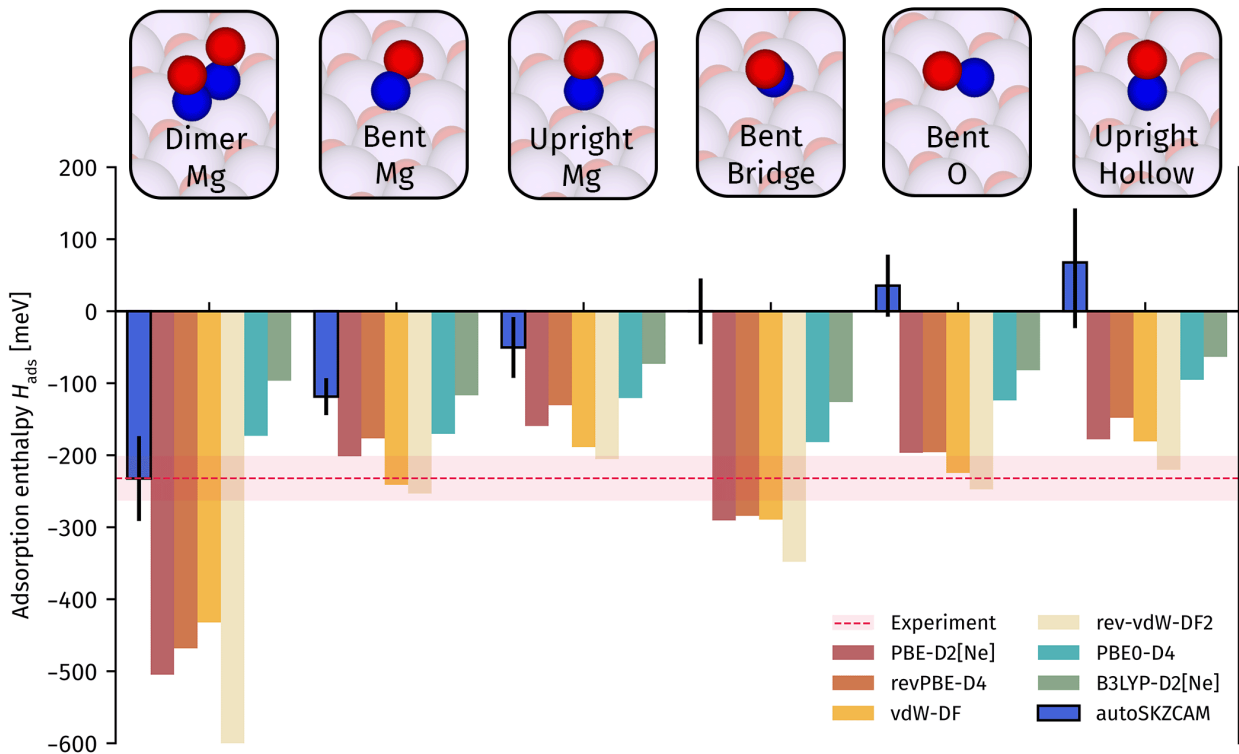


FIG. S2. Comparison of H_{ads} (per molecule) calculated with the autoSKZCAM framework and several DFAs (from the ensemble) for the various adsorption configurations of NO on the MgO(001) surface. These are compared against experimental TPD measurements by Wichtendahl *et al.* [223]. Conservative error estimates (corresponding to a 95% confidence interval or more) are given for both experiment and autoSKZCAM, as discussed in Secs. S9 and S11, respectively.

The adsorption of nitric oxide on the MgO(001) surface has been widely studied by both experiments and computational simulations. Within the computational literature, a wide range of adsorption configurations have been proposed, which we show in Fig. 3 of the main text. For each given geometry, most studies (see Table S29) employing DFT have found E_{ads} in a range in agreement with the experimental H_{ads} estimate [223]. In particular, most studies have looked at

TABLE S1. Comparison between autoSKZCAM and 6 DFAs in their predicted H_{ads} (in meV) for the different configurations of NO on MgO(001). The experimental H_{ads} is -232 ± 31 meV.

| | autoSKZCAM | PBE-D2[Ne] | revPBE-D4 | vdW-DF | rev-vdW-DF2 | PBE0-D4 | B3LYP-D2[Ne] |
|-----------------|---------------|--------------|--------------|--------------|--------------|--------------|--------------|
| Dimer | -232 ± 59 | -505 ± 5 | -468 ± 5 | -432 ± 5 | -607 ± 5 | -173 ± 5 | -96 ± 5 |
| Bent-Mg | -119 ± 26 | -201 ± 3 | -177 ± 3 | -241 ± 3 | -253 ± 3 | -170 ± 3 | -117 ± 3 |
| Vertical-Mg | -50 ± 42 | -159 ± 3 | -130 ± 3 | -189 ± 3 | -205 ± 3 | -120 ± 3 | -73 ± 3 |
| Bent-Bridge | 0 ± 46 | -291 ± 5 | -284 ± 5 | -289 ± 5 | -348 ± 5 | -182 ± 5 | -126 ± 5 |
| Bent-O | 35 ± 43 | -197 ± 3 | -196 ± 3 | -225 ± 3 | -247 ± 3 | -124 ± 3 | -82 ± 3 |
| Vertical-Hollow | 68 ± 91 | -178 ± 6 | -148 ± 6 | -181 ± 6 | -220 ± 6 | -95 ± 6 | -63 ± 6 |

the adsorption of monomers on the surface. On the other hand, experiments have largely pointed towards the absence of monomers on the surface. For example, EPR [224] indicates that only 0.5% of sites contained NO monomers (bonded mostly to defects), with FTIR [225] showing that most NO species exist as a closed-shell diamagnetic *cis*-(NO)₂ species, hereafter dubbed the NO dimer.

In Fig. S2, we have studied all proposed (monomer and dimer) geometries of NO on the MgO(001) surface with the autoSKZCAM framework and the ensemble of DFAs (providing specific values in Table S1). We find that the monomer species are not as stable as many DFAs predict, being 100 meV higher in H_{ads} than the NO dimer. On top of being the configuration with the lowest H_{ads} , the autoSKZCAM framework also predicts an H_{ads} which reproduces experiment, coming into agreement with previous experimental evidence that NO exists in its *cis*-(NO)₂ geometry on top of the MgO surface. In addition, our estimates show that monomers are unlikely to exist on the terrace sites at low temperatures, with only the NO dimer expected to form.

S1.4. CO₂ on TiO₂ rutile(110)

The adsorption of CO₂ on TiO₂ rutile(110) has been the subject of many theoretical and experimental studies over the years. Besides one study [226], the majority of computational simulations have demonstrated CO₂ on TiO₂ rutile(110) to take on a tilted geometry on top of the surface. Similarly, barring one experiment, the majority of experiments have pointed towards a tilted geometry on the rutile(110) surface. A study by Sorescu *et al.* [227] found that a simulated STM

image of the parallel configuration was more consistent with experimental STM images. However, a later study with some of the original authors showed a preference for a tilted geometry [228] which rotates about the z -axis to diffuse across the TiO₂ rutile(110) surface. This was later confirmed by further independent studies with STM [229] and FTIR [230].

In Extended Data Fig. 4, we have compared the H_{ads} computed with the autoSKZCAM framework (and several DFAs) against experiment for the parallel and tilted geometry. We find that the tilted geometry is more stable than the parallel geometry by 45 meV, albeit with some overlap in their error bars. With the tilted geometry, we are able to reach agreement with experiment, providing strong evidence that it is the expected geometry on the TiO₂ rutile(110) surface, although the small energy difference with the parallel state suggests that under normal temperatures, it can easily move into this metastable state, commensurate with its easy diffusion observed in experiments. We find that all of the DFAs also predict a more stable tilted geometry, although revPBE-D4 predicts the two geometries to be nearly isoenergetic with a 0.3 meV difference.

Our work has also allowed us to re-examine some of the previous experimental and computational work that have claimed a more stable parallel adsorption configuration. The experiment of Sorescu *et al.* [227] with STM had indicated a more consistent agreement towards a parallel geometry. However, this is in disagreement with later STM studies and recent work [231] have actually simulated the STM images of a tilted, parallel and vertical geometry of CO₂ on rutile(110). The differences between the simulated STM images were found to be minor between the adsorption configurations and in fact, the low resolution of STM (in general) meant that they found the vertical geometry to be most consistent, in disagreement with Sorescu *et al.*, and found to be the least stable configuration from their simulations [231]. This overall suggests that STM does not have the resolution to discern the geometry of CO₂ on rutile(110). The computational simulation by Kubas *et al.* [226] was the only work we found which predicted a parallel geometry to be lower in energy than the tilted geometry, using not only DFT but also DLPNO-CCSD(T) In Table S2, we show that the surface model which they used - an embedded cluster approach - differs significantly from previous DFT simulations as well as our simulations. Specifically, we have compared PBE-D3 predictions using their embedded cluster model with periodic slab models from two previous DFT simulations as well as our own periodic DFT calculations. All the slab calculations come into agreement that the tilted geometry is between 18 meV to 37 meV more stable than the parallel geometry, while Kubas *et al.* predicts it to be less stable by 49 meV. In fact, all their functionals have predicted an unstable parallel geometry, while our autoSKZCAM framework calculations as

TABLE S2. Comparison of the E_{ads} of the CO_2 on TiO_2 rutile(110) adsorption configurations from previous DFT studies using PBE-D3 (with zero-damping).

| | Parallel | Tilted | Δ |
|-----------------------|----------|--------|----------|
| Sorescu et al. [232] | -371 | -389 | -18 |
| Kubas et al. [226] | -446 | -397 | 49 |
| Dohnalek et al. [229] | -420 | -450 | -30 |
| This work | -345 | -382 | -37 |

well as periodic DFT calculations all suggest a tilted geometry.

S1.5. N_2O on $\text{MgO}(001)$

N_2O on $\text{MgO}(001)$ is an example of a system that has been very sparsely studied within previous computational simulations, with Scagnelli *et al.* [233] predicting no binding for a geometry with O pointing towards the Mg atom on the MgO surface, while Huesges *et al.* [234] found a tilted geometry with either N or O pointing towards the Mg atom on the MgO surface that are roughly isoenergetic (to within 10 meV). With our DFT ensemble, we find that the tilted geometry with the O pointing towards the Mg atom relaxes to a geometry close to parallel to the surface, such that both N and O close to an Mg atom. This was confirmed through an additional random structure search, which did not find a tilted O-down geometry. Thus, we compare the parallel configuration with a (N-down) tilted configuration in Extended Data Fig. 5. Both the autoSKZCAM framework and the 6 studied DFAs predict the parallel configuration to be the lowest in energy, with autoSKZCAM coming into agreement with the experimental H_{ads} . The variation between DFAs is relatively small (within 70 meV), with four of the six DFAs lying within the experimental H_{ads} error bars.

S1.6. Previously debated systems

Most of the other systems within this work have got geometries that are now well-resolved, however some of these systems were previously topics of debate and we briefly mention some of these systems. For example, it was previously debated whether the CO molecule adsorbs with

the C or O atom pointing towards the Mg atom within early simulations [235] but this was later understood to arise from errors with using Hartree-Fock theory with a small basis set [236]. Another system which has been previously under debate is the arrangement of the alkane monolayers on the MgO(001) surface. In particular, for methane, it was not known whether the molecules take up a dipod or tripod [237, 238] configuration, containing two and three H atoms pointing downwards respectively. Furthermore, there were questions whether the methane molecules were rotated with respect to its neighbours [239]. Both of these questions were resolved through a combination of experiments [240, 241] and theory [239, 242]. Similarly, the ethane monolayer has been determined by LEED [243–245] to take its current configuration in Fig. S4, which is in agreement with work by Alessio *et al.* [246]. As seen in Fig. 2 of the main text, we are able to achieve excellent agreement to experiment on the H_{ads} for both alkane monolayers on MgO.

S2. A BENCHMARK DATASET FOR NON-COVALENT INTERACTIONS OF ADSORBATE–SURFACE SYSTEMS

We have highlighted in Fig. 4 of the main text the possibility to use the numbers generated by the autoSKZCAM framework to benchmark the performance of density functional approximations for adsorbate–surface systems – currently sorely lacking [247]. Specifically, the final E_{int} estimates used in Fig. 4 of the main text are given in Table S3. This forms a database covering a range of adsorbate–surface interactions on three prototypical ionic surfaces. The availability of such databases [248, 249] have been pivotal towards calibrating the performance of modern density functional approximations. The poor performance of many sophisticated (hybrid) DFAs in Fig. 4 of the main text can be attributed to the lack of adsorbate–surface benchmarks to calibrate them. The corresponding geometries used to calculate E_{int} are available in the Github repository [195] at: https://github.com/benshi97/Data_autoSKZCAM/tree/master/Data/Miscellaneous/DFT_Comparison/Geometries for comparison to the benchmark values in Table S3.

TABLE S3. Comparison of E_{int} (in meV) from a set of DFAs against autoSKZCAM estimates.

| | CH ₄ on MgO(001) | C ₂ H ₆ on MgO(001) | CO on MgO(001) | Physisorbed CO ₂ on MgO(001) | Monomer H ₂ O on MgO(001) | Parallel N ₂ O on MgO(001) | NH ₃ on MgO(001) | CH ₄ on TiO ₂ rutile(110) | Tilted CO ₂ on TiO ₂ rutile(110) | H ₂ O on TiO ₂ rutile(110) | CH ₃ OH on TiO ₂ rutile(110) | H ₂ O on TiO ₂ anatase(101) | NH ₃ on TiO ₂ anatase(101) |
|------------------------|-----------------------------|-------------------------------------------|----------------|-----------------------------------------|--------------------------------------|---------------------------------------|-----------------------------|-------------------------------------------------|--------------------------------------------------------|--------------------------------------------------|----------------------------------------------------|---------------------------------------------------|--------------------------------------------------|
| autoSKZCAM | -122 | -175 | -207 | -308 | -703 | -256 | -657 | -269 | -493 | -1310 | -1634 | -1208 | -1377 |
| RPA+rSE | -141 | -200 | -294 | -328 | -689 | -269 | -698 | - | - | - | - | - | - |
| RPA | -96 | -137 | -98 | -236 | -614 | -204 | -630 | - | - | - | - | - | - |
| HSE06-D4 | -162 | -233 | -252 | -319 | -728 | -245 | -692 | -295 | -496 | -1397 | -1718 | -1252 | -1528 |
| PBE0-TS/HI | -169 | -262 | -245 | -289 | -719 | -231 | -686 | -333 | -489 | -1417 | -1784 | -1254 | -1528 |
| r ² SCAN-D4 | -173 | -244 | -296 | -380 | -784 | -294 | -734 | -306 | -528 | -1429 | -1743 | -1303 | -1527 |
| SCAN-rVV10 | -182 | -257 | -323 | -427 | -823 | -329 | -761 | -323 | -573 | -1492 | -1821 | -1363 | -1576 |
| rev-vdW-DF2 | -144 | -213 | -272 | -299 | -672 | -246 | -665 | -273 | -462 | -1286 | -1607 | -1163 | -1402 |
| PBE-MBD/FI | -121 | -192 | -325 | -319 | -689 | -258 | -687 | -291 | -472 | -1289 | -1608 | -1183 | -1414 |
| PBE-D3 | -257 | -375 | -320 | -334 | -770 | -314 | -764 | -357 | -439 | -1280 | -1611 | -1176 | -1441 |

S2.1. Computational details for the DFA benchmark

We have compared a set of 8 DFAs against the E_{int} calculated by the SKZCAM protocol in Sec. S6. This was performed for a set of adsorbate–surface systems which cover an E_{int} of over 1.6 eV, providing a stringent test of the DFA. Discussion of the performance of these methods can be found in the main text and we describe the computational details here.

The same k -point grids were used as those in Table S17. The GGA and meta-GGA calculations were performed with a 1000 eV energy cutoff together with small core (Ti_{sv} and Mg_{sv}) PAW potentials together with hard C, H, N and O PAW potentials. The hybrid DFT calculations were performed with the Ti_{pv} and Mg_{pv} PAW potentials with standard C, H, N and O PAW potentials with an energy cutoff of 600 eV. A correction for errors (typically less than 10 meV) in the PAW potential was calculated at the GGA (PBE-TS/HI for PBE0-TS/HI and PBE-D4 for HSE06-D4) level. The random phase approximation (RPA) calculations were performed in VASP with an energy cutoff of 550 eV and a cutoff of 366 eV for the response function, using the same k -point grid as the DFT calculations. Using PBE orbitals, we calculated RPA and RPA+rSE [250] energies for MgO(001) in a (4×4) supercell with a 2×2×1 k -point mesh. The calculations employed VASP’s low-scaling implementation [251] with a plane-wave cutoff of 550 eV and a 12-point frequency grid. The complete basis set limit was estimated via the built-in extrapolation technique. We used the GW variants of the Mg_{sv}, C, H, N and O PAW potentials.

Part II: Supporting data

S3. THE APPROACH TO CALCULATING THE ADSORPTION ENTHALPY

The adsorption enthalpy H_{ads} is the central quantity in surface chemistry. It represents the enthalpy released when a molecule binds to a surface, giving a physical description for the strength of this binding. Adsorption and desorption represents primary processes within any chemical reaction happening on a surface and as such, H_{ads} is a key quantity that can control the reaction rate, as empirically shown by the Sabatier principle [252].

The standard path towards computing H_{ads} starts from E_{ads} – the adsorption energy under static conditions (i.e., zero temperature and pressure) – and adds contributions for the zero-point vibrational (ZPV) energies E_{ZPV} and vibrational temperature contributions E_{T} alongside an RT term for the work done due to pressure [253]:

$$H_{\text{ads}} = E_{\text{ads}} + E_{\text{ZPV}} + E_{\text{T}} - RT. \quad (1)$$

E_{ads} can be obtained from the total energy calculations from e.g., standard correlated wave-function theory (cWFT) and DFT calculations. It is defined as the difference between the energy of the adsorbate–surface complex and the energies of the gas-phase molecule (M) and the pristine surface (S), all in their equilibrium geometries. E_{ZPV} and E_{T} can be obtained from vibrational energies by considering a Taylor expansion of the potential energy surface (PES) around the energetically most stable equilibrium structure. This approach assumes that the molecules are localised within a potential well to one specific adsorption site. More challenging cases may require incorporating anharmonic effects, models that sample more adsorption sites or to perform global molecular dynamics to obtain ensemble averages [254]: $H_{\text{ads}} = \langle H_{\text{MS}} \rangle - \langle H_{\text{M}} \rangle - \langle H_{\text{S}} \rangle$. However, for most surface phenomena, these effects are not expected to contribute significantly to the adsorption enthalpy, especially at lower temperatures.

Within this work, we make a further breakdown of E_{ads} into a contribution from the interaction energy E_{int} and the geometric relaxation energy E_{rlx} :

$$E_{\text{ads}} = E_{\text{int}} + E_{\text{rlx}}. \quad (2)$$

The former aims to obtain only the interaction between the molecule and surface and is defined as the difference between the energy of the adsorbate–surface complex against the energies of the molecule (M//MS) and surface (M//S) constrained to their geometry in the complex. The latter accounts for the geometric relaxation of the molecule and surface in the complex from their

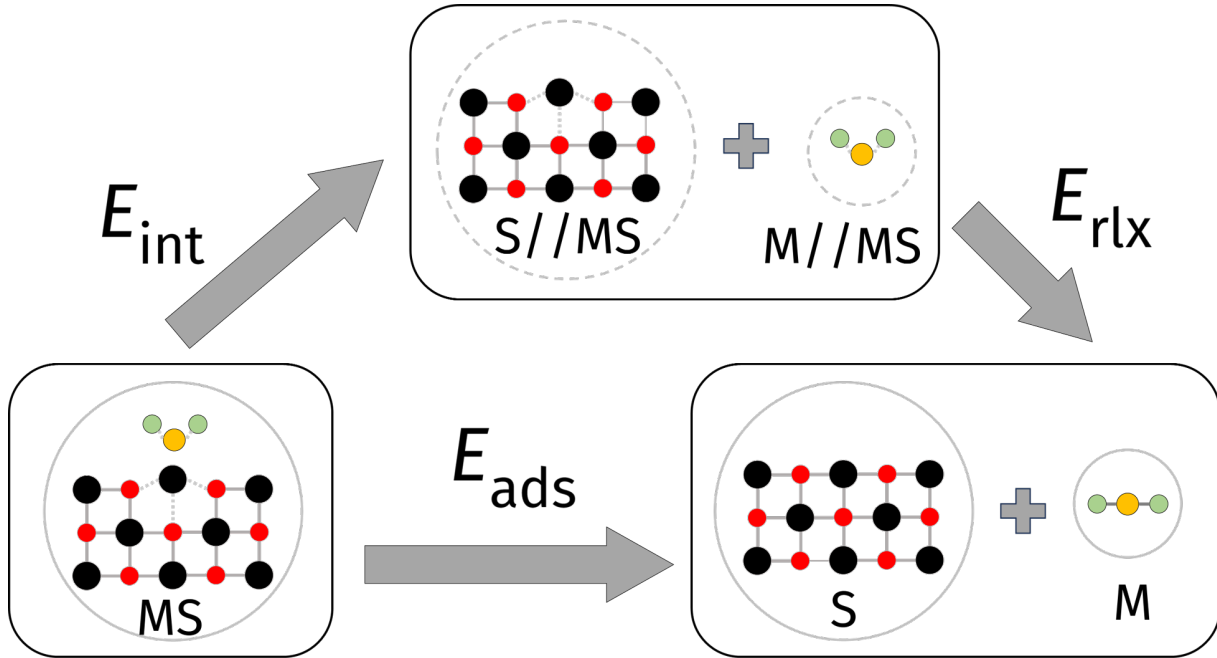


FIG. S3. The physical description of the adsorption energy E_{ads} in terms of the total energy of the adsorbate–surface complex (MS), pristine surface (S) and gas-phase molecule (M) in their equilibrium positions. This can be further broken down in a thermodynamic cycle into an interaction energy E_{int} contribution, defined as the energetic difference between MS against M and S fixed to their geometries in MS (i.e., M//MS and S//MS respectively), followed by a relaxation term E_{rlx} bring these two systems into their equilibrium geometries. The circles represent a single system/calculation, with a dashed-line circle indicating a geometry fixed to that found in the adsorbate–surface complex while a line circle indicates an equilibrium geometry.

respective equilibrium positions:

$$E_{\text{rlx}} = E_{\text{M//MS}} - E_{\text{M}} + E_{\text{S//MS}} - E_{\text{S}} \quad (3)$$

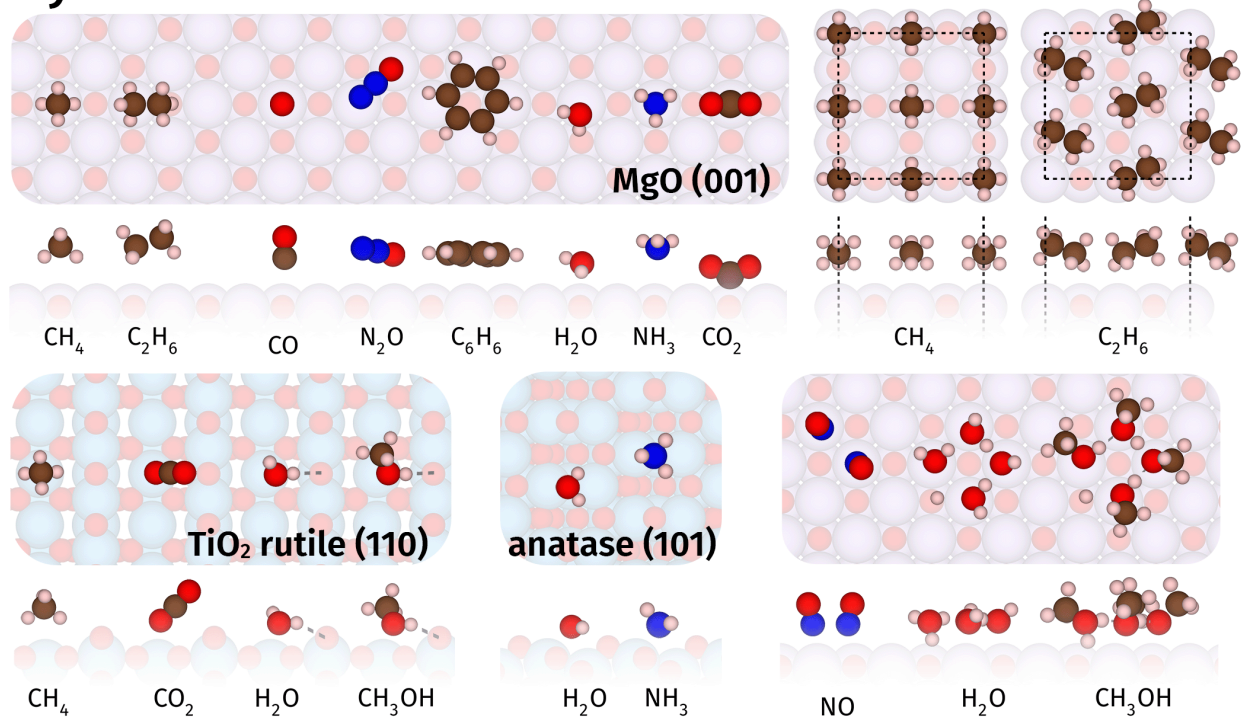
Within the subsequent sections, we will discuss how these individual terms are tackled to obtain an accurate H_{ads} that can match experimental accuracy, leading to the new insights and benchmarks in Secs. S1 and S2.

S4. THE ADSORBATE–SURFACE COMPLEXES STUDIED IN THIS WORK

Within this work, we have studied 19 adsorbate–surface systems in total, considering several adsorption configurations (29 in total) to obtain new insights into their binding mechanism as shown in Fig. S4. The systems consists of several molecular adsorbates of technological relevance (CO,

NO, N₂O, NH₃, H₂O, CO₂, CH₃OH, CH₄, C₂H₆ and C₆H₆). The adsorption of these molecules have been considered on the MgO(001) surface and on both the TiO₂ anatase(101) and rutile(110) surfaces, all of which have important potential technological applications. For example TiO₂ has been under heavy investigation for the photocatalytic conversion of H₂O to hydrogen [255, 256], while MgO is being investigated to be used as an adsorbent of harmful CO₂ [219] and NO_x [257] gases. These systems have been chosen because high quality experimental estimates [258] exist for their adsorption enthalpy, with open questions on their adsorption mechanism. Some of these systems have also been well-studied with computational simulations, namely density functional theory (DFT), with there often being discrepancies in the predicted binding mechanism (see Sec.S1, which we will resolve with the reliable accuracy afforded by the autoSKZCAM framework). Only a handful have been studied with accurate methods from correlated wave-function theory (cWFT) and our ability to tackle the diverse range of systems (oftentimes much larger or more complex than studied by cWFT before) have been enabled by the general/automated nature and low-cost of the autoSKZCAM framework.

Systems Studied



Insights Obtained

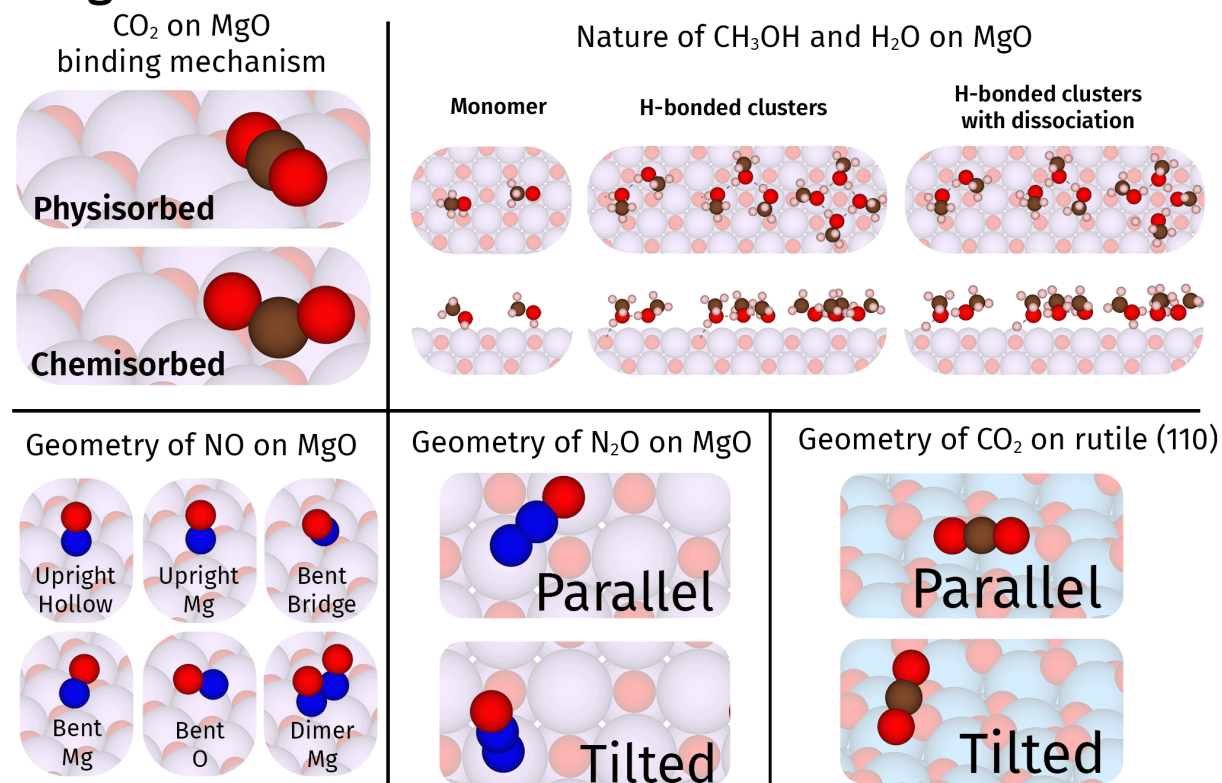


FIG. S4. The adsorbate–surface systems that we study within this work. There are 19 adsorbate–surface systems in total. For several of these systems, we have examined multiple competing adsorption configurations to reveal new atomic-level insights on how the molecules bind onto the surface.

S5. COMPUTATIONAL DETAILS FOR CORRELATED WAVE-FUNCTION THEORY

The ability to reach an accurate E_{int} and ultimately H_{ads} value which agrees with experiments rests upon employing methods from correlated wave-function theory (cWFT). Specifically, we make use of two levels of theory: second-order Møller-Plesset perturbation theory (MP2) [259] and coupled cluster theory with single, double, and perturbative triple excitations [CCSD(T)] [260]. We leverage the developments within two efficient quantum chemistry codes, ORCA 5.0.3 [261] and MRCC 2023 [262], to perform our cWFT calculations. Here, the MP2 calculations were performed with the ORCA program using the resolution-of-identity approximation. We leverage the developments in efficient local approximations to CCSD(T) - specifically the local natural orbital (LNO) [263, 264] approximation in MRCC and the domain-based local pair natural orbital (DLPNO) [265–268] approximation in ORCA. The former was used for the majority of CCSD(T) calculations while the latter was used for treating the open-shell NO monomers adsorbed on MgO.

We have used the Dunning family [269] of correlation consistent basis sets, where aug-cc-pVXZ are used on the non-metal (C, H, N, O) atoms, with X represent its size in terms of double (DZ), triple (TZ) or quadruple (QZ) zeta. For the metal cations (Mg and Ti), we do not include augmentation and use either the cc-pVXZ or cc-pwCVXZ basis sets alongside an associated treatment of correlation from semicore electrons on the metal cations. The former treats only valence (i.e., $3s^2$ or $3d^24s^2$) electrons while the latter includes weighted core-valence basis functions [270] to incorporate sub-valence s and p electron contributions to the electron correlation treatment [271]. The combinations that we specifically compute for E_{int} will be shortened to: aVDZ, aV(DZ/TZ), aV(TZ/QZ), awCVDZ, awCV(DZ/TZ), awCV(TZ/QZ). Here, the ‘a’ in front indicates that there is an augmentation treatment (only on the non-metal atoms), while the inclusion of wC indicates the use of core-valence basis sets on the metal atoms. Those with (DZ/TZ) or (TZ/QZ) involve a two-point complete basis set (CBS) extrapolation, using parameters taken from Neese and Valeev [272], for the enclosed pair of basis functions.

We use the def2-QZVPP-RI-JK auxiliary basis function for density-fitting/resolution-of-identity Hartree-Fock (HF) computations, and the RI auxiliary basis sets from Weigend [273, 274] corresponding to the AO basis sets for subsequent cWFT calculations. For the metal atoms, where RI basis functions were not available, we generated automatic auxiliary basis functions using the approach of Stoychev *et al.* [275, 276]. The interaction energy calculations all employed counterpoise corrections to overcome basis set superposition errors. We used `TightPNO` settings for the DLPNO-

CCSD(T) treatment in ORCA and `tight` LNO thresholds together with setting `bpedo=0.99999` for improved correlation energy capture in MRCC. The corresponding DLPNO-MP2 and LMP2 estimates with the same settings were used when calculating the ΔCC quantity.

S6. INTERACTION ENERGIES COMPUTED WITH THE SKZCAM PROTOCOL

The interaction energy E_{int} forms the majority of the contribution towards H_{ads} , making it an important quantity to get right. It is also the key term where a method which goes beyond DFT is needed to reach a reliable level of accuracy. As we show in Fig. 4 of the main text, E_{int} can vary by more than 300 meV across popular DFAs, while we will show in Section S8 that these errors are smaller (on average lower than 20 meV) for the other terms in Eq. 1. CCSD(T) is the method of choice for computing E_{int} , however studies with CCSD(T) for adsorbate–surface systems is sparse and limited due to its steep scaling [260] with system size. This makes it quickly intractable for studying surfaces – typically involve large system sizes. We have developed the SKZCAM protocol in Refs. 277 and 278 to address the challenge of applying CCSD(T) to obtain the E_{int} of surface systems. On top of achieving high accuracy at a low cost, one of the key advancements of the SKZCAM protocol is that it can be generalised and automated to study molecules adsorbed on any (ionic) surface termination and adsorption site. Within this work, we have capitalised on these qualities by automating the entire SKZCAM protocol to obtain E_{int} (and indeed the overall autoSKZCAM framework to obtain H_{ads}), as described in Sec. S10. These developments have enabled the unprecedented set of systems which we study within this work.

With only the adsorbate–surface geometry as input, the SKZCAM protocol can provide an accurate E_{int} . There are four major steps towards achieving this (illustrated in Fig. S5), starting with (a) constructing an electrostatic embedding environment, (b) generating the (embedded) clusters and (c) extrapolating E_{int} to the bulk limit at the lower-level second-order Møller-Plesset perturbation theory before (d) elevating E_{int} to the CCSD(T) level with a ΔCC contribution through mechanical embedding. We will describe each of these steps in the next few sub-sections, providing tables with the contributions towards the final E_{int} .

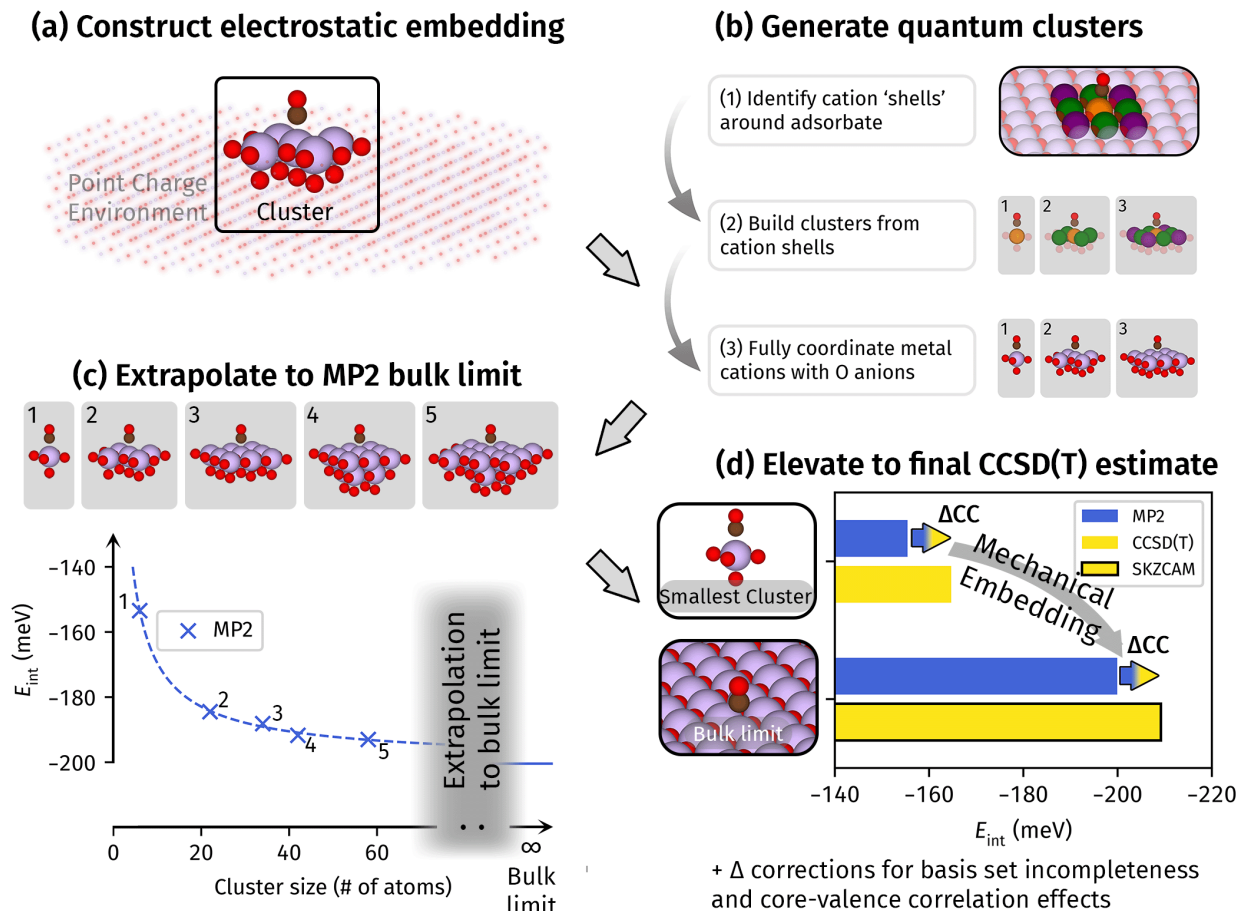


FIG. S5. Schematic of the SKZCAM protocol to calculate E_{int} . It is a general protocol which starts by (a) generating the electrostatic embedding environment, followed by (b) creating the series of systematically converging clusters. From these clusters, the (c) MP2 bulk limit can be obtained through extrapolation. Finally, we reach the CCSD(T) estimate by adding a ΔCC correction (from the smallest cluster) onto this MP2 bulk limit.

S6.1. Generating a systematic series of clusters within electrostatic embedding

The SKZCAM protocol models the surface through an electrostatic embedding scheme [279], where a (quantum) cluster that has been cleaved out of the surface is coupled to an environment that represents the interactions arising from the atoms outside the cluster. This environment consists of point charges placed at the positions of the metal cations and oxygen anions, taking formal values of +4 and +2 for Ti and Mg respectively, while taking a value of -2 for O. We have used the py-ChemShell 2020 package [280] to generate the embedding environment, placing point charges within a hemisphere (of radius `radius_cluster`=50 Å for TiO₂ and 60 Å for MgO surfaces, respectively) around the adsorbate molecule, with a further set of (fitting) point charges placed (`bq_layer`=6 Å)

on the outer edge to reproduce the Madelung potential within (`radius_active=`)40Å the adsorbate. Subsequently, after cleaving the quantum cluster, capped effective core potentials (ECP) are placed on positive (metal cation) point charges within a radius of `cutoff_boundary=`6Å and 4Å for the TiO₂ and 60 Å for MgO surfaces, respectively, to prevent spurious charge leakage.

With the electrostatic embedding environment created, the key remaining question is how to design the quantum cluster with particular attention required on controlling its size. High-level methods from cWFT, such as CCSD(T), can quickly become intractable for larger clusters while small clusters are not typically converged towards the bulk (infinite size) limit. The SKZCAM protocol provides a set of rubrics - hence its description as a ‘protocol’ - to automatically generate a set of small clusters [as shown in part (b) of Fig. S5]. It involves a simple two-step process, whereby cation metal shells (from e.g., a radial distribution function around the adsorbate molecule) are used to progressively build up the metal cations in clusters of growing size. This is followed by fully coordinating the metal cations with O anions to complete each cluster. The first step is intuitive since it is expected that atoms closer to the adsorbate contribute most significantly to E_{int} while we have found that convergence of properties such as vacancy formation energies [277] and adsorption energies [278] become significantly faster when the metal cations are fully coordinated by O anions in the second step to prevent any dangling bonds on the metal cations.

In Fig. S6, we highlight the set of clusters generated by the SKZCAM protocol for the MgO(001), TiO₂ rutile(110) and anatase(101) surfaces respectively. Based on the rubrics explained above, the generated clusters will be adapted to be efficient and centered around each specific adsorbate–surface system. For the MgO(001) surface, there are three different sets of clusters which will be generated based on the adsorption site - an ‘Mg-centered’, ‘O-centered’ or ‘Hollow-centered’ cluster. The adsorbate–surface systems for the rutile(110) and anatase(101) surfaces have their adsorbates all centred on the Ti-site, so only one set of unique clusters ended up being generated for each of the system.

We specifically show the first 9 clusters generated by the SKZCAM protocol (although clusters up to arbitrary size can be created). We find that only the first 7 clusters are required to reach accurate estimates of E_{int} , so only the first 7 clusters were used for the MgO(001) surface as described in the subsequent sections. For the clusters used in the TiO₂ rutile(110) and anatase(101) surfaces, we find that the first two clusters (dubbed ‘-2’ and ‘-1’ clusters) were too small to provide sensible E_{int} values, instead starting the SKZCAM protocol from the third cluster onwards (dubbed ‘1’, ‘2’, ‘3’, ..., ‘7’)

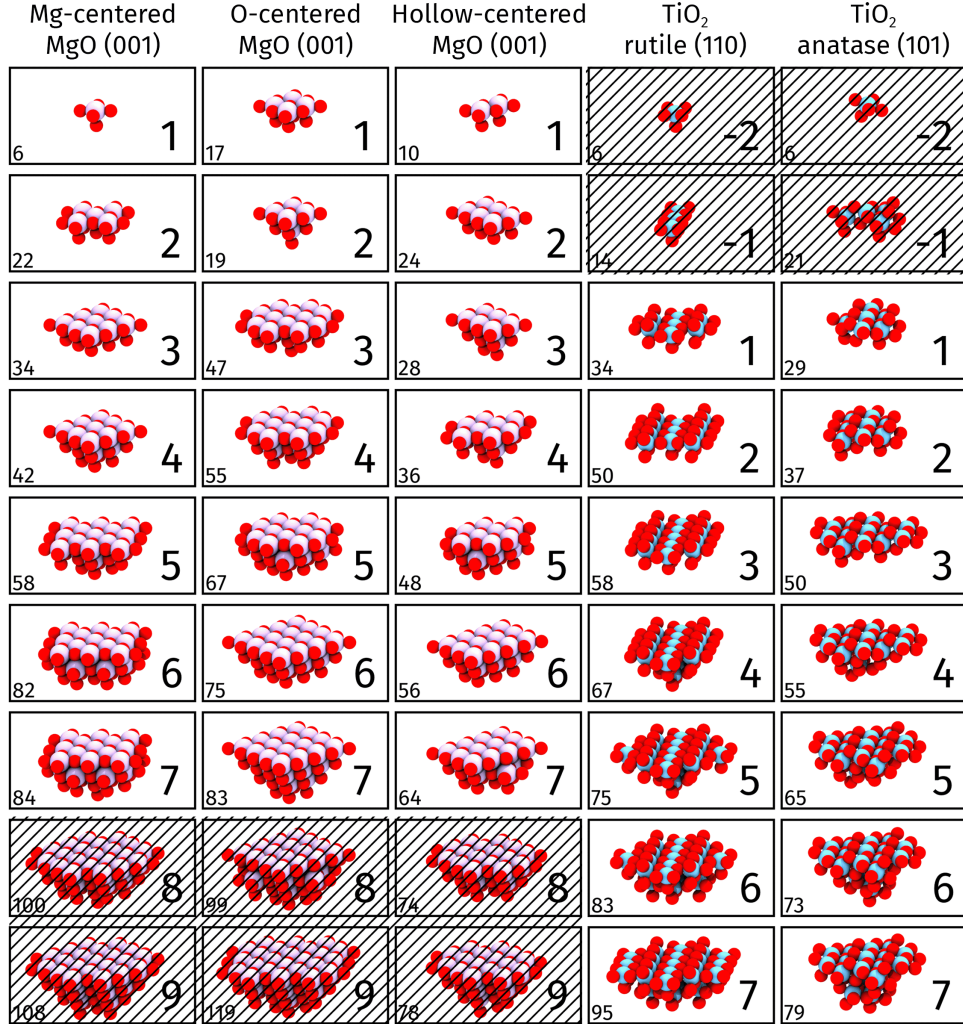


FIG. S6. The series of clusters generated by the SKZCAM protocol for the systems studied within this work. We have generated the first 9 clusters from the SKZCAM protocol and shade in hatched lines those which we do not study within this work, as explained within the text.

S6.2. Extrapolating towards the bulk limit with the series of clusters

The series of clusters generated by the SKZCAM protocol achieves several qualities that can be exploited to reach the CCSD(T) bulk limit accurately and efficient, which we discuss in this section and the next. One of the key properties is that there is a smooth and fast convergence of E_{int} with cluster size (as a function of the number of atoms N in the cluster). For the MgO surfaces, we use this smooth convergence to extrapolate towards the bulk limit $E_{\text{int}}^{\text{bulk}}$, using a formula of the form:

$$E_{\text{int}}(N) = E_{\text{int}}^{\text{bulk}} + \frac{A}{N}, \quad (4)$$

where A and $E_{\text{int}}^{\text{bulk}}$ can be obtained by fitting E_{int} to the series of clusters. This formula was inspired by the N^{-1} scaling of finite-effects observed in cWFT methods [281] and the dependence of E_{int}

on a pairwise dispersive additive interaction is N^{-2} , which has been verified for H_2O adsorption on the 2D hBN surface [282, 283]. Regardless of the formula, given the systematic convergence of E_{int} to $E_{\text{int}}^{\text{bulk}}$, we expect to reach the correct extrapolated value once sufficient number of clusters are included within the extrapolation. As a rule of thumb, we find that fits involving the first 5 clusters from the SKZCAM protocol are sufficient at reaching a converged estimate to within 5 meV, which we observe for most of the systems (see Table S4). The largest cluster may involve sizes up to 70 atoms, and while this size may be too large for CCSD(T), it can be affordably tackled with MP2 at the complete basis set (CBS) limit using a two-point extrapolation with the double-zeta (DZ) and triple-zeta (TZ) basis sets. Furthermore, we can estimate the error on this fit by using MP2 with the smaller DZ basis set to observe how $E_{\text{int}}^{\text{bulk}}$ changes as more clusters are included. We have specifically estimated the error of our CBS(DZ/TZ) estimate of $E_{\text{int}}^{\text{bulk}}$ with the fifth cluster from the SKZCAM protocol by finding its maximum deviation at the DZ level when compared to incorporating 6 or 7 clusters in the fit.

For both the TiO_2 surfaces, we find that the convergence is not as smooth as with the MgO surface, with E_{int} oscillating as a function of cluster size. Such behaviour is reminiscent of the odd-even oscillations common to TiO_2 studies [284] and what we observed for oxygen vacancy formation energies [277]. For these systems, we simply set $E_{\text{int}}^{\text{bulk}}$ to be the E_{int} value from the fifth cluster, and set the error bar to the maximum deviation observed with respect to larger clusters with the DZ basis set. We find errors that are typically below 20 meV for most of the studied TiO_2 adsorbate–surface systems, with only the H_2O and CH_3OH molecules on rutile(110) leading to slightly larger errors that are still within 40 meV.

TABLE S4: E_{int} (in meV) of the clusters generated by the SKZCAM protocol for the 19 adsorbate–surface systems and their studied adsorption configurations. The type of clusters used is given within the brackets and the corresponding size for each cluster is provided in Figure S6.

| CH ₄ on MgO(001) (Mg-centered) | 1 | 2 | 3 | 4 | 5 | 6 | 7 |
|-------------------------------------------------------------------|------|------|------|------|------|------|------|
| E_{int} MP2 awCVDZ | -25 | -55 | -62 | -65 | -69 | -72 | -73 |
| $E_{\text{int}}^{\text{bulk}}$ MP2 awCVDZ | - | - | - | -70 | -71 | -72 | -73 |
| E_{int} MP2 CBS(awCVDZ/awCVTZ) | -71 | -96 | -101 | -103 | -105 | - | - |
| $E_{\text{int}}^{\text{bulk}}$ MP2 CBS(awCVDZ/awCVTZ) | - | - | - | -107 | -108 | - | - |
| E_{int} MP2 CBS(awCVTZ/awCVQZ) | -68 | -95 | -99 | - | - | - | - |
| E_{int} LMP2 CBS(awCVDZ/awCVTZ) | -70 | -91 | -93 | - | - | - | - |
| E_{int} LNO-CCSD(T) CBS(awCVDZ/awCVTZ) | -86 | -107 | -109 | - | - | - | - |
| Monolayer CH ₄ on MgO(001) (Mg-centered) | 1 | 2 | 3 | 4 | 5 | 6 | 7 |
| E_{int} MP2 awCVDZ | -24 | -54 | -62 | -64 | -68 | -71 | -73 |
| $E_{\text{int}}^{\text{bulk}}$ MP2 awCVDZ | - | - | - | -69 | -70 | -72 | -73 |
| E_{int} MP2 CBS(awCVDZ/awCVTZ) | -70 | -95 | -100 | -102 | -104 | - | - |
| $E_{\text{int}}^{\text{bulk}}$ MP2 CBS(awCVDZ/awCVTZ) | - | - | - | -106 | -107 | - | - |
| E_{int} MP2 CBS(awCVTZ/awCVQZ) | -67 | -94 | -98 | - | - | - | - |
| E_{int} LMP2 CBS(awCVDZ/awCVTZ) | -69 | -90 | -94 | - | - | - | - |
| E_{int} LNO-CCSD(T) CBS(awCVDZ/awCVTZ) | -85 | -106 | -110 | - | - | - | - |
| C ₂ H ₆ on MgO(001) (Mg-centered) | 1 | 2 | 3 | 4 | 5 | 6 | 7 |
| E_{int} MP2 awCVDZ | -30 | -79 | -93 | -97 | -104 | -108 | -110 |
| $E_{\text{int}}^{\text{bulk}}$ MP2 awCVDZ | - | - | - | -105 | -107 | -109 | -110 |
| E_{int} MP2 CBS(awCVDZ/awCVTZ) | -90 | -136 | -146 | -149 | -153 | - | - |
| $E_{\text{int}}^{\text{bulk}}$ MP2 CBS(awCVDZ/awCVTZ) | - | - | - | -157 | -158 | - | - |
| E_{int} MP2 CBS(awCVTZ/awCVQZ) | -87 | -133 | -141 | - | - | - | - |
| E_{int} LMP2 CBS(awCVDZ/awCVTZ) | -92 | -131 | -140 | - | - | - | - |
| E_{int} LNO-CCSD(T) CBS(awCVDZ/awCVTZ) | -112 | -151 | -160 | - | - | - | - |
| Monolayer C ₂ H ₆ on MgO(001) (Mg-centered) | 1 | 2 | 3 | 4 | 5 | 6 | 7 |
| E_{int} MP2 awCVDZ | -21 | -71 | -86 | -89 | -96 | -101 | -102 |
| $E_{\text{int}}^{\text{bulk}}$ MP2 awCVDZ | - | - | - | -98 | -100 | -102 | -103 |
| E_{int} MP2 CBS(awCVDZ/awCVTZ) | -73 | -121 | -131 | -134 | -139 | - | - |
| $E_{\text{int}}^{\text{bulk}}$ MP2 CBS(awCVDZ/awCVTZ) | - | - | - | -142 | -144 | - | - |
| E_{int} MP2 CBS(awCVTZ/awCVQZ) | -71 | -118 | -127 | - | - | - | - |
| E_{int} LMP2 CBS(awCVDZ/awCVTZ) | -72 | -115 | -124 | - | - | - | - |
| E_{int} LNO-CCSD(T) CBS(awCVDZ/awCVTZ) | -91 | -135 | -144 | - | - | - | - |

Continued on next page

TABLE S4: (continued)

| CO on MgO(001) (Mg-centered) | 1 | 2 | 3 | 4 | 5 | 6 | 7 |
|---------------------------------------------------------|------|------|------|------|------|------|------|
| E_{int} MP2 awCVDZ | -47 | -100 | -111 | -117 | -122 | -127 | -128 |
| $E_{\text{int}}^{\text{bulk}}$ MP2 awCVDZ | - | - | - | -125 | -127 | -128 | -129 |
| E_{int} MP2 CBS(awCVDZ/awCVTZ) | -155 | -184 | -192 | -195 | -197 | - | - |
| $E_{\text{int}}^{\text{bulk}}$ MP2 CBS(awCVDZ/awCVTZ) | - | - | - | -199 | -200 | - | - |
| E_{int} MP2 CBS(awCVTZ/awCVQZ) | -155 | -186 | -189 | - | - | - | - |
| E_{int} LMP2 CBS(awCVDZ/awCVTZ) | -153 | -183 | -185 | - | - | - | - |
| E_{int} LNO-CCSD(T) CBS(awCVDZ/awCVTZ) | -160 | -190 | -194 | - | - | - | - |
| C ₆ H ₆ on MgO(001) (O-centered) | 1 | 2 | 3 | 4 | 5 | 6 | 7 |
| E_{int} MP2 awCVDZ | -197 | -203 | -305 | -313 | -322 | -330 | -335 |
| $E_{\text{int}}^{\text{bulk}}$ MP2 awCVDZ | - | - | - | -367 | -367 | -368 | -369 |
| E_{int} MP2 CBS(awCVDZ/awCVTZ) | -338 | -344 | -414 | -422 | -428 | - | - |
| $E_{\text{int}}^{\text{bulk}}$ MP2 CBS(awCVDZ/awCVTZ) | - | - | - | -460 | -460 | - | - |
| E_{int} MP2 CBS(awCVTZ/awCVQZ) | -354 | -359 | -416 | - | - | - | - |
| E_{int} LMP2 CBS(awCVDZ/awCVTZ) | -335 | -340 | -404 | - | - | - | - |
| E_{int} LNO-CCSD(T) CBS(awCVDZ/awCVTZ) | -311 | -316 | -379 | - | - | - | - |
| Parallel N ₂ O on MgO(001) (Hollow-centered) | 1 | 2 | 3 | 4 | 5 | 6 | 7 |
| E_{int} MP2 awCVDZ | -143 | -175 | -179 | -185 | -188 | -193 | -195 |
| $E_{\text{int}}^{\text{bulk}}$ MP2 awCVDZ | - | - | - | -200 | -200 | -201 | -202 |
| E_{int} MP2 CBS(awCVDZ/awCVTZ) | -206 | -229 | -232 | -238 | -242 | - | - |
| $E_{\text{int}}^{\text{bulk}}$ MP2 CBS(awCVDZ/awCVTZ) | - | - | - | -248 | -249 | - | - |
| E_{int} MP2 CBS(awCVTZ/awCVQZ) | -207 | -231 | -230 | - | - | - | - |
| E_{int} LMP2 CBS(awCVDZ/awCVTZ) | -203 | -225 | -226 | - | - | - | - |
| E_{int} LNO-CCSD(T) CBS(awCVDZ/awCVTZ) | -209 | -231 | -233 | - | - | - | - |
| Tilted N ₂ O on MgO(001) (Mg-centered) | 1 | 2 | 3 | 4 | 5 | 6 | 7 |
| E_{int} MP2 awCVDZ | -44 | -98 | -111 | -116 | -122 | -126 | -129 |
| $E_{\text{int}}^{\text{bulk}}$ MP2 awCVDZ | - | - | - | -125 | -127 | -128 | -130 |
| E_{int} MP2 CBS(awCVDZ/awCVTZ) | -122 | -159 | -168 | -172 | -175 | - | - |
| $E_{\text{int}}^{\text{bulk}}$ MP2 CBS(awCVDZ/awCVTZ) | - | - | - | -178 | -179 | - | - |
| E_{int} MP2 CBS(awCVTZ/awCVQZ) | -129 | -165 | -171 | - | - | - | - |
| E_{int} LMP2 CBS(awCVDZ/awCVTZ) | -120 | -155 | -159 | - | - | - | - |
| E_{int} LNO-CCSD(T) CBS(awCVDZ/awCVTZ) | -104 | -139 | -144 | - | - | - | - |
| Vertical-Hollow NO on MgO(001) (Hollow-centered) | 1 | 2 | 3 | 4 | 5 | 6 | 7 |

Continued on next page

TABLE S4: (continued)

| | | | | | | | |
|---------------------------------------------------|------|------|------|------|------|------|------|
| E_{int} MP2 aVDZ | -159 | -177 | -183 | -185 | -186 | -185 | -186 |
| $E_{\text{int}}^{\text{bulk}}$ MP2 aVDZ | - | - | - | -194 | -194 | -193 | -192 |
| E_{int} MP2 CBS(aVDZ/aVTZ) | -224 | -236 | -233 | -240 | -241 | - | - |
| $E_{\text{int}}^{\text{bulk}}$ MP2 CBS(aVDZ/aVTZ) | - | - | - | -243 | -244 | - | - |
| E_{int} MP2 CBS(awCVDZ/awCVTZ) | -242 | -259 | -257 | - | - | - | - |
| E_{int} MP2 CBS(aVTZ/aVQZ) | -213 | -227 | -225 | - | - | - | - |
| E_{int} DLPNO-MP2 CBS(aVDZ/aVTZ) | -219 | - | - | - | - | - | - |
| E_{int} DLPNO-CCSD(T) CBS(aVDZ/aVTZ) | 71 | - | - | - | - | - | - |
| Vertical-Mg NO on MgO(001) (Mg-centered) | 1 | 2 | 3 | 4 | 5 | 6 | 7 |
| E_{int} MP2 aVDZ | 135 | 94 | 91 | 86 | 82 | 80 | 77 |
| $E_{\text{int}}^{\text{bulk}}$ MP2 aVDZ | - | - | - | 79 | 78 | 78 | 77 |
| E_{int} MP2 CBS(aVDZ/aVTZ) | 65 | 35 | 33 | 33 | 30 | - | - |
| $E_{\text{int}}^{\text{bulk}}$ MP2 CBS(aVDZ/aVTZ) | - | - | - | 26 | 26 | - | - |
| E_{int} MP2 CBS(awCVDZ/awCVTZ) | 43 | 9 | 5 | - | - | - | - |
| E_{int} MP2 CBS(aVTZ/aVQZ) | 67 | 42 | 41 | - | - | - | - |
| E_{int} DLPNO-MP2 CBS(aVDZ/aVTZ) | 64 | - | - | - | - | - | - |
| E_{int} DLPNO-CCSD(T) CBS(aVDZ/aVTZ) | -4 | - | - | - | - | - | - |
| Bent-Bridge NO on MgO(001) (Mg-centered) | 1 | 2 | 3 | 4 | 5 | 6 | 7 |
| E_{int} MP2 aVDZ | -460 | -486 | -494 | -503 | -505 | -507 | -510 |
| $E_{\text{int}}^{\text{bulk}}$ MP2 aVDZ | - | - | - | -503 | -505 | -507 | -508 |
| E_{int} MP2 CBS(aVDZ/aVTZ) | -620 | -649 | -654 | -656 | -658 | - | - |
| $E_{\text{int}}^{\text{bulk}}$ MP2 CBS(aVDZ/aVTZ) | - | - | - | -661 | -661 | - | - |
| E_{int} MP2 CBS(awCVDZ/awCVTZ) | -639 | -675 | -682 | - | - | - | - |
| E_{int} MP2 CBS(aVTZ/aVQZ) | -618 | -654 | -658 | - | - | - | - |
| E_{int} DLPNO-MP2 CBS(aVDZ/aVTZ) | -620 | - | - | - | - | - | - |
| E_{int} DLPNO-CCSD(T) CBS(aVDZ/aVTZ) | 6 | - | - | - | - | - | - |
| Bent-Mg NO on MgO(001) (Mg-centered) | 1 | 2 | 3 | 4 | 5 | 6 | 7 |
| E_{int} MP2 aVDZ | 52 | 9 | 5 | 2 | -2 | -4 | -7 |
| $E_{\text{int}}^{\text{bulk}}$ MP2 aVDZ | - | - | - | -6 | -7 | -7 | -8 |
| E_{int} MP2 CBS(aVDZ/aVTZ) | -15 | -43 | -46 | -47 | -50 | - | - |
| $E_{\text{int}}^{\text{bulk}}$ MP2 CBS(aVDZ/aVTZ) | - | - | - | -53 | -53 | - | - |
| E_{int} MP2 CBS(awCVDZ/awCVTZ) | -37 | -70 | -75 | - | - | - | - |
| E_{int} MP2 CBS(aVTZ/aVQZ) | -17 | -42 | -44 | - | - | - | - |
| E_{int} DLPNO-MP2 CBS(aVDZ/aVTZ) | -14 | - | - | - | - | - | - |

Continued on next page

TABLE S4: (continued)

| | | | | | | | |
|-------------------------------------------------------|------|------|------|------|------|------|------|
| E_{int} DLPNO-CCSD(T) CBS(aVDZ/aVTZ) | -62 | - | - | - | - | - | - |
| Bent-O NO on MgO(001) (O-centered) | 1 | 2 | 3 | 4 | 5 | 6 | 7 |
| E_{int} MP2 aVDZ | -496 | -500 | -502 | -502 | -504 | -503 | -503 |
| $E_{\text{int}}^{\text{bulk}}$ MP2 aVDZ | - | - | - | -505 | -506 | -505 | -505 |
| E_{int} MP2 CBS(aVDZ/aVTZ) | -640 | -641 | -643 | -645 | -646 | - | - |
| $E_{\text{int}}^{\text{bulk}}$ MP2 CBS(aVDZ/aVTZ) | - | - | - | -646 | -647 | - | - |
| E_{int} MP2 CBS(awCVDZ/awCVTZ) | -649 | -656 | -661 | - | - | - | - |
| E_{int} MP2 CBS(aVTZ/aVQZ) | -639 | -638 | -648 | - | - | - | - |
| E_{int} DLPNO-MP2 CBS(aVDZ/aVTZ) | -630 | - | - | - | - | - | - |
| E_{int} DLPNO-CCSD(T) CBS(aVDZ/aVTZ) | 29 | - | - | - | - | - | - |
| Dimer NO on MgO(001) (Hollow-centered) | 1 | 2 | 3 | 4 | 5 | 6 | 7 |
| E_{int} MP2 awCVDZ | -138 | -172 | -177 | -184 | -188 | -191 | -193 |
| $E_{\text{int}}^{\text{bulk}}$ MP2 awCVDZ | - | - | - | -200 | -200 | -201 | -202 |
| E_{int} MP2 CBS(awCVDZ/awCVTZ) | -222 | -244 | -246 | -251 | -253 | - | - |
| $E_{\text{int}}^{\text{bulk}}$ MP2 CBS(awCVDZ/awCVTZ) | - | - | - | -261 | -261 | - | - |
| E_{int} MP2 CBS(awCVTZ/awCVQZ) | -226 | -246 | -246 | - | - | - | - |
| E_{int} LMP2 CBS(awCVDZ/awCVTZ) | -217 | -239 | - | - | - | - | - |
| E_{int} LNO-CCSD(T) CBS(awCVDZ/awCVTZ) | -199 | -222 | - | - | - | - | - |
| Monomer H ₂ O on MgO(001) (Mg-centered) | 1 | 2 | 3 | 4 | 5 | 6 | 7 |
| E_{int} MP2 awCVDZ | -514 | -542 | -546 | -552 | -556 | -559 | -559 |
| $E_{\text{int}}^{\text{bulk}}$ MP2 awCVDZ | - | - | - | -555 | -557 | -558 | -559 |
| E_{int} MP2 CBS(awCVDZ/awCVTZ) | -641 | -667 | -671 | -671 | -674 | - | - |
| $E_{\text{int}}^{\text{bulk}}$ MP2 CBS(awCVDZ/awCVTZ) | - | - | - | -677 | -677 | - | - |
| E_{int} MP2 CBS(awCVTZ/awCVQZ) | -641 | -670 | -668 | - | - | - | - |
| E_{int} LMP2 CBS(awCVDZ/awCVTZ) | -639 | -663 | -664 | - | - | - | - |
| E_{int} LNO-CCSD(T) CBS(awCVDZ/awCVTZ) | -665 | -688 | -689 | - | - | - | - |
| Tetramer H ₂ O on MgO(001) (O-centered) | 1 | 2 | 3 | 4 | 5 | 6 | 7 |
| E_{int} MP2 awCVDZ | -296 | -299 | -333 | -335 | -339 | -344 | -347 |
| $E_{\text{int}}^{\text{bulk}}$ MP2 awCVDZ | - | - | - | -354 | -354 | -355 | -357 |
| E_{int} MP2 CBS(awCVDZ/awCVTZ) | -392 | -394 | -409 | -412 | -414 | - | - |
| $E_{\text{int}}^{\text{bulk}}$ MP2 CBS(awCVDZ/awCVTZ) | - | - | - | -420 | -421 | - | - |
| E_{int} MP2 CBS(awCVTZ/awCVQZ) | -411 | -412 | -418 | - | - | - | - |
| E_{int} LMP2 CBS(awCVDZ/awCVTZ) | -390 | -392 | -407 | - | - | - | - |
| E_{int} LNO-CCSD(T) CBS(awCVDZ/awCVTZ) | -417 | -419 | -434 | - | - | - | - |

Continued on next page

TABLE S4: (continued)

| Tilted CH ₃ OH on MgO(001) (Mg-centered) | 1 | 2 | 3 | 4 | 5 | 6 | 7 |
|-----------------------------------------------------------|------|------|------|------|------|------|------|
| E_{int} MP2 awCVDZ | -569 | -603 | -613 | -619 | -625 | -630 | -632 |
| $E_{\text{int}}^{\text{bulk}}$ MP2 awCVDZ | - | - | - | -623 | -625 | -628 | -629 |
| E_{int} MP2 CBS(awCVDZ/awCVTZ) | -703 | -745 | -754 | -756 | -760 | - | - |
| $E_{\text{int}}^{\text{bulk}}$ MP2 CBS(awCVDZ/awCVTZ) | - | - | - | -764 | -765 | - | - |
| E_{int} MP2 CBS(awCVTZ/awCVQZ) | -704 | -749 | -752 | - | - | - | - |
| E_{int} LMP2 CBS(awCVDZ/awCVTZ) | -701 | -739 | -746 | - | - | - | - |
| E_{int} LNO-CCSD(T) CBS(awCVDZ/awCVTZ) | -723 | -759 | -768 | - | - | - | - |
| Parallel CH ₃ OH on MgO(001) (Mg-centered) | 1 | 2 | 3 | 4 | 5 | 6 | 7 |
| E_{int} MP2 awCVDZ | -395 | -424 | -423 | -429 | -427 | -429 | -428 |
| $E_{\text{int}}^{\text{bulk}}$ MP2 awCVDZ | - | - | - | -433 | -432 | -432 | -432 |
| E_{int} MP2 CBS(awCVDZ/awCVTZ) | -443 | -493 | -499 | -496 | -499 | - | - |
| $E_{\text{int}}^{\text{bulk}}$ MP2 CBS(awCVDZ/awCVTZ) | - | - | - | -509 | -508 | - | - |
| E_{int} MP2 CBS(awCVTZ/awCVQZ) | -426 | -474 | -481 | - | - | - | - |
| E_{int} LMP2 CBS(awCVDZ/awCVTZ) | -442 | -488 | -491 | - | - | - | - |
| E_{int} LNO-CCSD(T) CBS(awCVDZ/awCVTZ) | -458 | -505 | -507 | - | - | - | - |
| Tetramer CH ₃ OH on MgO(001) (O-centered) | 1 | 2 | 3 | 4 | 5 | 6 | 7 |
| E_{int} MP2 awCVDZ | -320 | -323 | -370 | -373 | -378 | -386 | -389 |
| $E_{\text{int}}^{\text{bulk}}$ MP2 awCVDZ | - | - | - | -399 | -399 | -401 | -403 |
| E_{int} MP2 CBS(awCVDZ/awCVTZ) | -423 | -425 | -451 | -455 | -457 | - | - |
| $E_{\text{int}}^{\text{bulk}}$ MP2 CBS(awCVDZ/awCVTZ) | - | - | - | -469 | -469 | - | - |
| E_{int} MP2 CBS(awCVTZ/awCVQZ) | -440 | -443 | -462 | - | - | - | - |
| E_{int} LMP2 CBS(awCVDZ/awCVTZ) | -420 | -422 | -449 | - | - | - | - |
| E_{int} LNO-CCSD(T) CBS(awCVDZ/awCVTZ) | -447 | -449 | -476 | - | - | - | - |
| NH ₃ on MgO(001) (Mg-centered) | 1 | 2 | 3 | 4 | 5 | 6 | 7 |
| E_{int} MP2 awCVDZ | -377 | -449 | -475 | -482 | -493 | -500 | -501 |
| $E_{\text{int}}^{\text{bulk}}$ MP2 awCVDZ | - | - | - | -492 | -497 | -500 | -502 |
| E_{int} MP2 CBS(awCVDZ/awCVTZ) | -551 | -582 | -602 | -606 | -608 | - | - |
| $E_{\text{int}}^{\text{bulk}}$ MP2 CBS(awCVDZ/awCVTZ) | - | - | - | -608 | -610 | - | - |
| E_{int} MP2 CBS(awCVTZ/awCVQZ) | -570 | -602 | -611 | - | - | - | - |
| E_{int} LMP2 CBS(awCVDZ/awCVTZ) | -547 | -580 | -599 | - | - | - | - |
| E_{int} LNO-CCSD(T) CBS(awCVDZ/awCVTZ) | -578 | -610 | -630 | - | - | - | - |
| Physisorbed CO ₂ on MgO(001) (Hollow-centered) | 1 | 2 | 3 | 4 | 5 | 6 | 7 |

Continued on next page

TABLE S4: (continued)

| | | | | | | | |
|----------------------------------------------------------|-------|-------|-------|-------|-------|-------|-------|
| E_{int} MP2 awCVDZ | -147 | -180 | -184 | -186 | -188 | -189 | -192 |
| $E_{\text{int}}^{\text{bulk}}$ MP2 awCVDZ | - | - | - | -202 | -201 | -200 | -200 |
| E_{int} MP2 CBS(awCVDZ/awCVTZ) | -240 | -264 | -265 | -269 | -272 | - | - |
| $E_{\text{int}}^{\text{bulk}}$ MP2 CBS(awCVDZ/awCVTZ) | - | - | - | -280 | -280 | - | - |
| E_{int} MP2 CBS(awCVTZ/awCVQZ) | -239 | -262 | -261 | - | - | - | - |
| E_{int} LMP2 CBS(awCVDZ/awCVTZ) | -237 | -258 | -261 | - | - | - | - |
| E_{int} LNO-CCSD(T) CBS(awCVDZ/awCVTZ) | -267 | -288 | -293 | - | - | - | - |
| Chemisorbed CO ₂ on MgO(001) (O-centered) | 1 | 2 | 3 | 4 | 5 | 6 | 7 |
| E_{int} MP2 awCVDZ | -2843 | -2857 | -2760 | -2767 | -2774 | -2754 | -2743 |
| $E_{\text{int}}^{\text{bulk}}$ MP2 awCVDZ | - | - | - | -2767 | -2774 | -2754 | -2743 |
| E_{int} MP2 CBS(awCVDZ/awCVTZ) | -3334 | -3332 | -3292 | -3295 | -3309 | - | - |
| $E_{\text{int}}^{\text{bulk}}$ MP2 CBS(awCVDZ/awCVTZ) | - | - | - | -3295 | -3309 | - | - |
| E_{int} MP2 CBS(awCVTZ/awCVQZ) | -3311 | -3301 | -3272 | - | - | - | - |
| E_{int} LMP2 CBS(awCVDZ/awCVTZ) | -3330 | -3328 | -3283 | - | - | - | - |
| E_{int} LNO-CCSD(T) CBS(awCVDZ/awCVTZ) | -3548 | -3547 | -3506 | - | - | - | - |
| CH ₄ on TiO ₂ rutile(110) | 1 | 2 | 3 | 4 | 5 | 6 | 7 |
| E_{int} MP2 aVDZ | -219 | -202 | -208 | -208 | -211 | -210 | -213 |
| $E_{\text{int}}^{\text{bulk}}$ MP2 aVDZ | - | - | - | -208 | -211 | -210 | -213 |
| E_{int} MP2 CBS(aVDZ/aVTZ) | -282 | -262 | -267 | -265 | -267 | - | - |
| $E_{\text{int}}^{\text{bulk}}$ MP2 CBS(aVDZ/aVTZ) | - | - | - | -265 | -267 | - | - |
| E_{int} MP2 CBS(aVTZ/aVQZ) | -281 | -261 | - | - | - | - | - |
| E_{int} MP2 CBS(awCVTZ/awCVQZ) | -283 | -263 | - | - | - | - | - |
| E_{int} LMP2 CBS(aVDZ/aVTZ) | -282 | -263 | - | - | - | - | - |
| E_{int} LNO-CCSD(T) CBS(aVDZ/aVTZ) | -283 | -263 | - | - | - | - | - |
| Parallel CO ₂ on TiO ₂ rutile(110) | 1 | 2 | 3 | 4 | 5 | 6 | 7 |
| E_{int} MP2 aVDZ | -337 | -315 | -320 | -323 | -327 | -326 | -331 |
| $E_{\text{int}}^{\text{bulk}}$ MP2 aVDZ | - | - | - | -323 | -327 | -326 | -331 |
| E_{int} MP2 CBS(aVDZ/aVTZ) | -425 | -401 | -405 | -405 | -408 | - | - |
| $E_{\text{int}}^{\text{bulk}}$ MP2 CBS(aVDZ/aVTZ) | - | - | - | -405 | -408 | - | - |
| E_{int} MP2 CBS(aVTZ/aVQZ) | -425 | -404 | - | - | - | - | - |
| E_{int} MP2 CBS(awCVTZ/awCVQZ) | -433 | -411 | - | - | - | - | - |
| E_{int} LMP2 CBS(aVDZ/aVTZ) | -421 | -398 | - | - | - | - | - |
| E_{int} LNO-CCSD(T) CBS(aVDZ/aVTZ) | -413 | -393 | - | - | - | - | - |
| Tilted CO ₂ on TiO ₂ rutile(110) | 1 | 2 | 3 | 4 | 5 | 6 | 7 |

Continued on next page

TABLE S4: (continued)

| | | | | | | | |
|----------------------------------------------------|-------|-------|-------|-------|-------|-------|-------|
| E_{int} MP2 aVDZ | -441 | -390 | -401 | -395 | -399 | -392 | -396 |
| $E_{\text{int}}^{\text{bulk}}$ MP2 aVDZ | - | - | - | -395 | -399 | -392 | -396 |
| E_{int} MP2 CBS(aVDZ/aVTZ) | -521 | -467 | -476 | -468 | -470 | - | - |
| $E_{\text{int}}^{\text{bulk}}$ MP2 CBS(aVDZ/aVTZ) | - | - | - | -468 | -470 | - | - |
| E_{int} MP2 CBS(aVTZ/aVQZ) | -527 | -475 | - | - | - | - | - |
| E_{int} MP2 CBS(awCVTZ/awCVQZ) | -519 | -466 | - | - | - | - | - |
| E_{int} LMP2 CBS(aVDZ/aVTZ) | -516 | -461 | - | - | - | - | - |
| E_{int} LNO-CCSD(T) CBS(aVDZ/aVTZ) | -539 | -486 | - | - | - | - | - |
| H ₂ O on TiO ₂ rutile(110) | 1 | 2 | 3 | 4 | 5 | 6 | 7 |
| E_{int} MP2 aVDZ | -1256 | -1141 | -1161 | -1139 | -1146 | -1113 | -1119 |
| $E_{\text{int}}^{\text{bulk}}$ MP2 aVDZ | - | - | - | -1139 | -1146 | -1113 | -1119 |
| E_{int} MP2 CBS(aVDZ/aVTZ) | -1420 | -1304 | -1319 | -1292 | -1299 | - | - |
| $E_{\text{int}}^{\text{bulk}}$ MP2 CBS(aVDZ/aVTZ) | - | - | - | -1292 | -1299 | - | - |
| E_{int} MP2 CBS(aVTZ/aVQZ) | -1436 | -1324 | - | - | - | - | - |
| E_{int} MP2 CBS(awCVTZ/awCVQZ) | -1399 | -1280 | - | - | - | - | - |
| E_{int} LMP2 CBS(aVDZ/aVTZ) | -1418 | -1301 | - | - | - | - | - |
| E_{int} LNO-CCSD(T) CBS(aVDZ/aVTZ) | -1447 | -1340 | - | - | - | - | - |
| CH ₃ OH on TiO ₂ rutile(110) | 1 | 2 | 3 | 4 | 5 | 6 | 7 |
| E_{int} MP2 aVDZ | -1555 | -1427 | -1451 | -1433 | -1441 | -1405 | -1413 |
| $E_{\text{int}}^{\text{bulk}}$ MP2 aVDZ | - | - | - | -1433 | -1441 | -1405 | -1413 |
| E_{int} MP2 CBS(aVDZ/aVTZ) | -1752 | -1622 | -1641 | -1616 | -1624 | - | - |
| $E_{\text{int}}^{\text{bulk}}$ MP2 CBS(aVDZ/aVTZ) | - | - | - | -1616 | -1624 | - | - |
| E_{int} MP2 CBS(aVTZ/aVQZ) | -1768 | -1643 | - | - | - | - | - |
| E_{int} MP2 CBS(awCVTZ/awCVQZ) | -1741 | -1608 | - | - | - | - | - |
| E_{int} LMP2 CBS(aVDZ/aVTZ) | -1748 | -1617 | - | - | - | - | - |
| E_{int} LNO-CCSD(T) CBS(aVDZ/aVTZ) | -1767 | -1644 | - | - | - | - | - |
| H ₂ O on TiO ₂ anatase(101) | 1 | 2 | 3 | 4 | 5 | 6 | 7 |
| E_{int} MP2 aVDZ | -1273 | -1266 | -1118 | -1107 | -1074 | -1061 | -1059 |
| $E_{\text{int}}^{\text{bulk}}$ MP2 aVDZ | - | - | - | -1107 | -1074 | -1061 | -1059 |
| E_{int} MP2 CBS(aVDZ/aVTZ) | -1406 | -1396 | -1249 | -1236 | -1202 | - | - |
| $E_{\text{int}}^{\text{bulk}}$ MP2 CBS(aVDZ/aVTZ) | - | - | - | -1236 | -1202 | - | - |
| E_{int} MP2 CBS(aVTZ/aVQZ) | -1407 | -1399 | - | - | - | - | - |
| E_{int} MP2 CBS(awCVTZ/awCVQZ) | -1394 | -1384 | - | - | - | - | - |
| E_{int} LMP2 CBS(aVDZ/aVTZ) | -1401 | -1391 | - | - | - | - | - |

Continued on next page

TABLE S4: (continued)

| | | | | | | | |
|---------------------------------------------------|-------|-------|-------|-------|-------|-------|-------|
| E_{int} LNO-CCSD(T) CBS(aVDZ/aVTZ) | -1419 | -1409 | - | - | - | - | - |
| NH ₃ on TiO ₂ anatase(101) | 1 | 2 | 3 | 4 | 5 | 6 | 7 |
| E_{int} MP2 aVDZ | -1348 | -1333 | -1272 | -1262 | -1223 | -1209 | -1206 |
| $E_{\text{int}}^{\text{bulk}}$ MP2 aVDZ | - | - | - | -1262 | -1223 | -1209 | -1206 |
| E_{int} MP2 CBS(aVDZ/aVTZ) | -1511 | -1491 | -1422 | -1410 | -1368 | - | - |
| $E_{\text{int}}^{\text{bulk}}$ MP2 CBS(aVDZ/aVTZ) | - | - | - | -1410 | -1368 | - | - |
| E_{int} MP2 CBS(aVTZ/aVQZ) | -1523 | -1506 | - | - | - | - | - |
| E_{int} MP2 CBS(awCVTZ/awCVQZ) | -1511 | -1492 | - | - | - | - | - |
| E_{int} LMP2 CBS(aVDZ/aVTZ) | -1506 | -1485 | - | - | - | - | - |
| E_{int} LNO-CCSD(T) CBS(aVDZ/aVTZ) | -1514 | -1493 | - | - | - | - | - |

S6.3. Multilevel Δ CC contribution through mechanical embedding with small clusters

Another quality of the quantum clusters generated by the SKZCAM protocol is that the difference between methods from cWFT, namely CCSD(T) and MP2, is relatively independent of the chosen cluster size. Thus, from the small affordable quantum clusters generated by the SKZCAM protocol, one can obtain a Δ CC contribution which can be used to elevate the MP2 bulk limit effectively up to the CCSD(T) bulk limit. This mechanical embedding procedure is based upon Morokuma’s ONIOM method [285] as well as the hybrid high-level:low-level approach of Sauer [253]. For each of the studied adsorbate–surface systems and adsorption configurations, we perform local CCSD(T) calculations up to the third SKZCAM cluster (where possible) as shown in Table S5. We set Δ CC to be the average of the three cluster, with its error taken to be the maximum deviation from the mean. We find that the deviations are very small; being 1 meV or less for most of the systems involving the MgO surface and TiO₂ anatase surface, while this error is typically below 5 meV for the TiO₂ rutile surface systems.

It should be noted that within this Δ CC contribution, there are also errors arising from using a local approximation for the CCSD(T) treatment. In Table S6, we have performed canonical CBS(DZ/TZ) CCSD(T) on the smallest cluster (corresponding to cluster ‘-2’ for the TiO₂ clusters) for a selection of adsorbate–surface systems. Together with the canonical MP2 estimate we have already computed for these clusters, we compare these against the LNO-CCSD(T) and local-MP2 (LMP2) estimates of E_{int} . It can be seen that the errors in LMP2 and LNO-CCSD(T) are all below 5 meV, attesting to the accuracy of our final Δ CC contribution (using LNO-CCSD(T) and LMP2), where Δ CC itself has an MAD of 3 meV from the canonical Δ CC for this selection of systems. The final error which we compute for our Δ CC contribution is the root squared sum of the error from the mechanical embedding procedure and 5 meV for the maximum observed error from using the local approximation.

TABLE S5. Comparison of the ΔCC values for the clusters generated from SKZCAM protocol for all of the studied systems. The mean is calculated from the set of clusters used, with the error being the maximum deviation from the mean.

| Cluster System | 1 | 2 | 3 | Mean | Error |
|----------------------------------------------------------|------|------|------|------|-------|
| CH ₄ on MgO(001) | -15 | -16 | -16 | -16 | 0 |
| Monolayer CH ₄ on MgO(001) | -15 | -16 | -16 | -16 | 0 |
| C ₂ H ₆ on MgO(001) | -20 | -20 | -20 | -20 | 0 |
| Monolayer C ₂ H ₆ on MgO(001) | -19 | -19 | -20 | -20 | 1 |
| CO on MgO(001) | -7 | -7 | -9 | -8 | 1 |
| C ₆ H ₆ on MgO(001) | 24 | 24 | 25 | 24 | 1 |
| Parallel N ₂ O on MgO(001) | -6 | -7 | -7 | -6 | 1 |
| Tilted N ₂ O on MgO(001) | 17 | 16 | 16 | 16 | 1 |
| Vertical-Hollow NO on MgO(001) | 289 | - | - | 289 | 0 |
| Vertical-Mg NO on MgO(001) | -68 | - | - | -68 | 0 |
| Bent-Bridge NO on MgO(001) | 626 | - | - | 626 | 0 |
| Bent-Mg NO on MgO(001) | -48 | - | - | -48 | 0 |
| Bent-O NO on MgO(001) | 659 | - | - | 659 | 0 |
| Dimer NO on MgO(001) | 18 | 17 | - | 18 | 1 |
| Monomer H ₂ O on MgO(001) | -26 | -25 | -26 | -25 | 0 |
| Tetramer H ₂ O on MgO(001) | -27 | -27 | -27 | -27 | 0 |
| Tilted CH ₃ OH on MgO(001) | -22 | -21 | -22 | -21 | 1 |
| Parallel CH ₃ OH on MgO(001) | -16 | -17 | -17 | -17 | 0 |
| Tetramer CH ₃ OH on MgO(001) | -27 | -27 | -27 | -27 | 0 |
| NH ₃ on MgO(001) | -31 | -30 | -31 | -31 | 1 |
| Physisorbed CO ₂ on MgO(001) | -30 | -31 | -32 | -31 | 1 |
| Chemisorbed CO ₂ on MgO(001) | -218 | -219 | -224 | -220 | 4 |
| CH ₄ on TiO ₂ rutile(110) | -1 | 0 | - | -1 | 1 |
| Parallel CO ₂ on TiO ₂ rutile(110) | 8 | 5 | - | 7 | 2 |
| Tilted CO ₂ on TiO ₂ rutile(110) | -23 | -24 | - | -24 | 1 |
| H ₂ O on TiO ₂ rutile(110) | -29 | -39 | - | -34 | 5 |
| CH ₃ OH on TiO ₂ rutile(110) | -19 | -27 | - | -23 | 4 |
| H ₂ O on TiO ₂ anatase(101) | -18 | -18 | - | -18 | 0 |
| NH ₃ on TiO ₂ anatase(101) | -8 | -8 | - | -8 | 0 |

TABLE S6. Comparing canonical (C-)MP2, canonical CCSD(T) and canonical Δ CC (in meV) against their local variants (i.e., LMP2, LNO-CCSD(T), L- Δ CC). This was compared for the first cluster generated by the SKZCAM protocol for the specific MgO adsorption site in Fig. S6, while it corresponds to cluster ‘-2’ for the TiO₂ surfaces.

| | C-MP2 | L-MP2 | L-MP2 Error | C-CCSD(T) | LNO-CCSD(T) | LNO-CCSD(T) Error | C-DeltaCC | (L-)DeltaCC | (L-)DeltaCC Error |
|----------------------------------------------------------|-------|-------|-------------|-----------|-------------|-------------------|-----------|-------------|-------------------|
| CH ₄ on MgO(001) | -71 | -70 | 0 | -91 | -86 | 5 | -20 | -15 | 4 |
| C ₂ H ₆ on MgO(001) | -90 | -92 | 2 | -116 | -112 | 4 | -26 | -20 | 6 |
| CO on MgO(001) | -155 | -153 | 2 | -165 | -160 | 5 | -9 | -7 | 3 |
| Parallel N ₂ O on MgO(001) | -206 | -203 | 2 | -215 | -209 | 6 | -9 | -6 | 3 |
| Tilted N ₂ O on MgO(001) | -122 | -120 | 2 | -107 | -104 | 4 | 15 | 17 | 2 |
| Dimer NO on MgO(001) | -222 | -217 | 5 | -205 | -199 | 6 | 17 | 18 | 2 |
| Monomer H ₂ O on MgO(001) | -641 | -639 | 2 | -670 | -665 | 5 | -29 | -26 | 3 |
| Tilted CH ₃ OH on MgO(001) | -703 | -701 | 2 | -729 | -723 | 7 | -27 | -22 | 5 |
| Parallel CH ₃ OH on MgO(001) | -443 | -442 | 1 | -466 | -458 | 8 | -23 | -16 | 6 |
| NH ₃ on MgO(001) | -551 | -547 | 4 | -583 | -578 | 5 | -32 | -31 | 1 |
| Physisorbed CO ₂ on MgO(001) | -240 | -237 | 3 | -265 | -267 | 2 | -25 | -30 | 5 |
| CH ₄ on TiO ₂ rutile(110) | -395 | -395 | 0 | -398 | -394 | 5 | -3 | 2 | 4 |
| Parallel CO ₂ on TiO ₂ rutile(110) | -454 | -451 | 3 | -467 | -463 | 4 | -13 | -12 | 1 |
| Tilted CO ₂ on TiO ₂ rutile(110) | -830 | -828 | 3 | -851 | -850 | 0 | -20 | -23 | 2 |
| H ₂ O on TiO ₂ rutile(110) | -2469 | -2466 | 3 | -2477 | -2477 | 0 | -9 | -12 | 3 |
| CH ₃ OH on TiO ₂ rutile(110) | -2921 | -2916 | 5 | -2922 | -2921 | 1 | -1 | -5 | 4 |
| H ₂ O on TiO ₂ anatase(101) | -1874 | -1871 | 3 | -1896 | -1895 | 1 | -22 | -23 | 1 |
| NH ₃ on TiO ₂ anatase(101) | -1801 | -1799 | 3 | -1822 | -1824 | 3 | -20 | -26 | 5 |
| MAD | 0 | 0 | 3 | 0 | 0 | 4 | 0 | 0 | 3 |

S6.4. Further multilevel contributions for basis set and semi-core electron correlation

Besides the Δ_{CC} contribution, it is possible to make further multilevel contributions (especially now that it has been automated in Section S10) in the vein of Pople’s ‘model chemistry’ [286]. This lowers the cost of reaching an accurate estimate as these contributions (e.g., basis set size or frozen core treatment) need to only be evaluated on the small affordable clusters generated by the SKZCAM protocol. Specifically we consider further contributions to: (1) fix our basis set extrapolation treatment to more accurately reach the basis set limit and (2) incorporate electron correlation contributions beyond the valence electrons from semi-core electrons. Adding these contributions can lower the cost as it means that we can use cheaper settings (i.e., smaller basis sets while correlating only valence electrons) in the $E_{\text{int}}^{\text{bulk}}$ and Δ_{CC} calculations. For the adsorbate–surface systems involving the TiO_2 surfaces and the open-shell NO monomers on the MgO surface, we have computed the MP2 $E_{\text{int}}^{\text{bulk}}$ and Δ_{CC} with semi-core electrons (i.e., 2s2p on Mg or 3s3p on Ti) frozen in the correlation treatment. This has been particularly important towards making tackling these systems, involving more electrons or requiring unrestricted MP2/CCSD(T), more affordable. We use a Δ_{core} contribution to account for these missing effects at the MP2 level from the smaller and more affordable clusters of the SKZCAM protocol (up to cluster 3). The Δ_{core} contributions are shown in Table S7. We take the mean of the clusters as our final Δ_{core} estimate and use the maximum deviation from the mean as the error. The maximum deviation are all below 5 meV.

For all of the adsorbate–surface systems, we add a further Δ_{basis} contribution which corrects for potential errors in our extrapolation treatment to reach the complete basis set limit; we used a two-point CBS(aVDZ/aVTZ) or CBS(awCDZ/awCVTZ) extrapolation. This contribution is calculated by considering the difference between the more accurate CBS(aVTZ/aVQZ) or CBS(awCVTZ/awCVQZ) extrapolation treatment with the CBS(aVDZ/aVTZ) or CBS(awCVDZ/awCVTZ) extrapolation treatment for the smallest clusters. The calculated Δ_{basis} contributions for the SKZCAM protocol clusters are shown in Table S8. We take the mean of the clusters as our final Δ_{basis} estimate and use the maximum deviation from the mean as the error, with most systems having errors below 5 meV, besides the larger systems (e.g., C_6H_6 and the tetramers on MgO(001)), where deviations may go up to 10 meV.

Both Δ_{core} and Δ_{basis} are important contributions which enable our final H_{ads} estimate to better match experiments while maintaining a low cost, with contributions up to 40 meV for the former

TABLE S7. Comparison of the Δ_{core} values for the clusters generated from SKZCAM protocol for all of the studied systems. The mean is calculated from the set of clusters used, with the error being the maximum deviation from the mean.

| Cluster | 1 | 2 | 3 | Mean | Error |
|----------------------------------------------------------|-----|-----|-----|------|-------|
| Vertical-Hollow NO on MgO(001) | -18 | -24 | -24 | -22 | 4 |
| Vertical-Mg NO on MgO(001) | -22 | -26 | -28 | -25 | 3 |
| Bent-Bridge NO on MgO(001) | -19 | -26 | -28 | -24 | 5 |
| Bent-Mg NO on MgO(001) | -22 | -27 | -29 | -26 | 3 |
| Bent-O NO on MgO(001) | -9 | -15 | -18 | -14 | 5 |
| CH ₄ on TiO ₂ rutile(110) | -2 | -3 | - | -2 | 0 |
| Parallel CO ₂ on TiO ₂ rutile(110) | -8 | -7 | - | -7 | 0 |
| Tilted CO ₂ on TiO ₂ rutile(110) | 8 | 10 | - | 9 | 1 |
| H ₂ O on TiO ₂ rutile(110) | 37 | 44 | - | 41 | 4 |
| CH ₃ OH on TiO ₂ rutile(110) | 28 | 35 | - | 31 | 4 |
| H ₂ O on TiO ₂ anatase(101) | 13 | 15 | - | 14 | 1 |
| NH ₃ on TiO ₂ anatase(101) | 13 | 14 | - | 13 | 1 |

and 13 meV in the latter.

TABLE S8. Comparison of the Δ_{basis} values for the clusters generated from SKZCAM protocol for all of the studied systems. The mean is calculated from the set of clusters used, with the error being the maximum deviation from the mean.

| Cluster System | 1 | 2 | 3 | Mean | Error |
|----------------------------------------------------------|-----|-----|-----|------|-------|
| CH ₄ on MgO(001) | 3 | 0 | 2 | 2 | 1 |
| Monolayer CH ₄ on MgO(001) | 3 | 1 | 2 | 2 | 1 |
| C ₂ H ₆ on MgO(001) | 3 | 3 | 4 | 3 | 1 |
| Monolayer C ₂ H ₆ on MgO(001) | 2 | 2 | 4 | 3 | 1 |
| CO on MgO(001) | 0 | -1 | 3 | 1 | 2 |
| C ₆ H ₆ on MgO(001) | -15 | -15 | -2 | -11 | 9 |
| Parallel N ₂ O on MgO(001) | -2 | -2 | 2 | -1 | 2 |
| Tilted N ₂ O on MgO(001) | -6 | -6 | -3 | -5 | 2 |
| Vertical-Hollow NO on MgO(001) | 10 | 8 | 8 | 9 | 1 |
| Vertical-Mg NO on MgO(001) | 2 | 7 | 8 | 5 | 4 |
| Bent-Bridge NO on MgO(001) | 2 | -5 | -4 | -2 | 4 |
| Bent-Mg NO on MgO(001) | -2 | 2 | 2 | 1 | 3 |
| Bent-O NO on MgO(001) | 1 | 2 | -6 | -1 | 5 |
| Dimer NO on MgO(001) | -4 | -3 | -1 | -2 | 2 |
| Monomer H ₂ O on MgO(001) | 0 | -3 | 3 | 0 | 3 |
| Tetramer H ₂ O on MgO(001) | -19 | -18 | -9 | -15 | 6 |
| Tilted CH ₃ OH on MgO(001) | -1 | -3 | 2 | -1 | 3 |
| Parallel CH ₃ OH on MgO(001) | 17 | 19 | 18 | 18 | 1 |
| Tetramer CH ₃ OH on MgO(001) | -18 | -18 | -11 | -16 | 4 |
| NH ₃ on MgO(001) | -19 | -20 | -9 | -16 | 7 |
| Physisorbed CO ₂ on MgO(001) | 1 | 2 | 4 | 3 | 2 |
| Chemisorbed CO ₂ on MgO(001) | 23 | 32 | 20 | 25 | 7 |
| CH ₄ on TiO ₂ rutile(110) | 1 | 1 | - | 1 | 0 |
| Parallel CO ₂ on TiO ₂ rutile(110) | -1 | -3 | - | -2 | 1 |
| Tilted CO ₂ on TiO ₂ rutile(110) | -6 | -8 | - | -7 | 1 |
| H ₂ O on TiO ₂ rutile(110) | -16 | -20 | - | -18 | 2 |
| CH ₃ OH on TiO ₂ rutile(110) | -16 | -21 | - | -19 | 2 |
| H ₂ O on TiO ₂ anatase(101) | 0 | -3 | - | -2 | 1 |
| NH ₃ on TiO ₂ anatase(101) | -13 | -15 | - | -14 | 1 |

S6.5. The final E_{int} estimates and their error bars

To summarise the above sections, the final CCSD(T) interaction energy bulk-limit estimate, $E_{\text{int}}^{\text{CCSD(T)}}$, is given as the sum of the following contributions:

$$E_{\text{int}}^{\text{bulk CCSD(T)}} = E_{\text{int}}^{\text{bulk MP2}} + \Delta_{\text{basis}} + \Delta_{\text{core}} + \Delta_{\text{CC}}. \quad (5)$$

The contributions are shown in Table S9 for all of the adsorbate–surface systems studied within this work. The series of clusters generated by the SKZCAM protocol provides a straightforward means to estimate the error from each of these contributions. For $E_{\text{int}}^{\text{bulk MP2}}$, we calculate the error in this term by finding the maximum deviation when a larger set of clusters are used to extrapolate $E_{\text{int}}^{\text{bulk MP2}}$ (with only the awCVDZ/aVDZ basis set) for the systems with the MgO surface (barring the chemisorbed CO₂ system). For the TiO₂ rutile(110) and anatase(101) surfaces, as well as the chemisorbed CO₂ on MgO(001), the larger clusters are used to estimate the maximum deviation. For Δ_{CC} , Δ_{basis} and Δ_{core} , we estimate the error by taking the maximum deviation from the mean of the clusters used to calculate these terms. The final error on $E_{\text{int}}^{\text{bulk CCSD(T)}}$ is the root squared sum of the errors from each of these terms. It can be seen in Table S9 that the errors are typically below 10 meV for all of the MgO adsorbate–surface systems, with some of the TiO₂ adsorbate–surface systems having a larger error, but all are within chemical accuracy of 43 meV.

TABLE S9. Final E_{int} values (in meV) for the systems studied in this work. We show the individual terms which make up these final E_{int} values and also give final MP2, CCSD and CCSD(T) estimates, where the latter two are obtained by adding the ΔCC values to the final MP2 E_{int} value.

| System | $E_{\text{int}}^{\text{bulk MP2}}$ | $\Delta\text{CC} [\text{CCSD(T)}]$ | $\Delta\text{CC} [\text{CCSD}]$ | Δ_{basis} | Δ_{core} | $E_{\text{int}}^{\text{autoSKZCAM}} [\text{MP2}]$ | $E_{\text{int}}^{\text{autoSKZCAM}} [\text{CCSD}]$ | $E_{\text{int}}^{\text{autoSKZCAM}} [\text{CCSD(T)}]$ |
|----------------------------------------------------------|------------------------------------|------------------------------------|---------------------------------|-------------------------|------------------------|---------------------------------------------------|----------------------------------------------------|-------------------------------------------------------|
| CH ₄ on MgO(001) | -108 ± 2 | -16 ± 0 | 18 ± 7 | 2 ± 1 | 0 ± 0 | -106 ± 2 | -88 ± 7 | -122 ± 2 |
| Monolayer CH ₄ on MgO(001) | -107 ± 2 | -16 ± 0 | 18 ± 7 | 2 ± 1 | 0 ± 0 | -105 ± 3 | -87 ± 7 | -121 ± 3 |
| C ₂ H ₆ on MgO(001) | -158 ± 3 | -20 ± 0 | 32 ± 13 | 3 ± 1 | 0 ± 0 | -155 ± 4 | -122 ± 14 | -175 ± 4 |
| Monolayer C ₂ H ₆ on MgO(001) | -144 ± 3 | -20 ± 1 | 29 ± 13 | 3 ± 1 | 0 ± 0 | -141 ± 3 | -112 ± 13 | -161 ± 3 |
| CO on MgO(001) | -200 ± 3 | -8 ± 1 | 33 ± 8 | 1 ± 2 | 0 ± 0 | -199 ± 3 | -166 ± 9 | -207 ± 4 |
| C ₆ H ₆ on MgO(001) | -460 ± 2 | 24 ± 1 | 164 ± 24 | -11 ± 9 | 0 ± 0 | -470 ± 9 | -307 ± 26 | -446 ± 9 |
| Parallel N ₂ O on MgO(001) | -249 ± 2 | -6 ± 1 | 40 ± 6 | -1 ± 2 | 0 ± 0 | -250 ± 3 | -210 ± 7 | -256 ± 3 |
| Tilted N ₂ O on MgO(001) | -179 ± 3 | 16 ± 1 | 64 ± 11 | -5 ± 2 | 0 ± 0 | -184 ± 4 | -120 ± 11 | -168 ± 4 |
| Vertical-Hollow NO on MgO(001) | -244 ± 1 | 289 ± 0 | 334 ± 0 | 9 ± 1 | -22 ± 4 | -257 ± 4 | 76 ± 4 | 32 ± 4 |
| Vertical-Mg NO on MgO(001) | 26 ± 2 | -68 ± 0 | -49 ± 0 | 5 ± 4 | -25 ± 3 | 6 ± 5 | -43 ± 5 | -62 ± 5 |
| Bent-Bridge NO on MgO(001) | -661 ± 3 | 626 ± 0 | 693 ± 0 | -2 ± 4 | -24 ± 5 | -688 ± 8 | 6 ± 8 | -62 ± 8 |
| Bent-Mg NO on MgO(001) | -53 ± 1 | -48 ± 0 | -23 ± 0 | 1 ± 3 | -26 ± 3 | -78 ± 5 | -102 ± 5 | -126 ± 5 |
| Bent-O NO on MgO(001) | -647 ± 0 | 659 ± 0 | 720 ± 0 | -1 ± 5 | -14 ± 5 | -661 ± 7 | 59 ± 7 | -3 ± 7 |
| Dimer NO on MgO(001) | -261 ± 2 | 18 ± 1 | 67 ± 5 | -2 ± 2 | 0 ± 0 | -263 ± 2 | -197 ± 5 | -246 ± 3 |
| Monomer H ₂ O on MgO(001) | -677 ± 2 | -25 ± 0 | 22 ± 9 | 0 ± 3 | 0 ± 0 | -677 ± 4 | -655 ± 10 | -703 ± 4 |
| Tetramer H ₂ O on MgO(001) | -421 ± 3 | -27 ± 0 | 3 ± 7 | -15 ± 6 | 0 ± 0 | -436 ± 7 | -433 ± 10 | -463 ± 7 |
| Tilted CH ₃ OH on MgO(001) | -765 ± 4 | -21 ± 1 | 45 ± 14 | -1 ± 3 | 0 ± 0 | -765 ± 5 | -720 ± 14 | -787 ± 5 |
| Parallel CH ₃ OH on MgO(001) | -508 ± 1 | -17 ± 0 | 50 ± 10 | 18 ± 1 | 0 ± 0 | -490 ± 1 | -440 ± 10 | -506 ± 1 |
| Tetramer CH ₃ OH on MgO(001) | -469 ± 4 | -27 ± 0 | 18 ± 10 | -16 ± 4 | 0 ± 0 | -485 ± 6 | -466 ± 12 | -511 ± 6 |
| NH ₃ on MgO(001) | -610 ± 5 | -31 ± 1 | 9 ± 16 | -16 ± 7 | 0 ± 0 | -626 ± 9 | -618 ± 18 | -657 ± 9 |
| Physisorbed CO ₂ on MgO(001) | -280 ± 1 | -31 ± 1 | 21 ± 7 | 3 ± 2 | 0 ± 0 | -277 ± 2 | -256 ± 7 | -308 ± 2 |
| Chemisorbed CO ₂ on MgO(001) | -3309 ± 32 | -220 ± 4 | -447 ± 7 | 25 ± 7 | 0 ± 0 | -3284 ± 32 | -3731 ± 33 | -3504 ± 32 |
| CH ₄ on TiO ₂ rutile(110) | -267 ± 2 | -1 ± 1 | 53 ± 0 | 1 ± 0 | -2 ± 0 | -268 ± 2 | -216 ± 2 | -269 ± 2 |
| Parallel CO ₂ on TiO ₂ rutile(110) | -408 ± 4 | 7 ± 2 | 71 ± 1 | -2 ± 1 | -7 ± 0 | -417 ± 4 | -346 ± 4 | -410 ± 5 |
| Tilted CO ₂ on TiO ₂ rutile(110) | -470 ± 6 | -24 ± 1 | 8 ± 1 | -7 ± 1 | 9 ± 1 | -469 ± 7 | -460 ± 7 | -493 ± 7 |
| H ₂ O on TiO ₂ rutile(110) | -1299 ± 33 | -34 ± 5 | -68 ± 6 | -18 ± 2 | 41 ± 4 | -1276 ± 33 | -1344 ± 34 | -1310 ± 33 |
| CH ₃ OH on TiO ₂ rutile(110) | -1624 ± 36 | -23 ± 4 | -31 ± 5 | -19 ± 2 | 31 ± 4 | -1612 ± 36 | -1642 ± 37 | -1634 ± 37 |
| H ₂ O on TiO ₂ anatase(101) | -1202 ± 15 | -18 ± 0 | -32 ± 0 | -2 ± 1 | 14 ± 1 | -1190 ± 16 | -1222 ± 16 | -1208 ± 16 |
| NH ₃ on TiO ₂ anatase(101) | -1368 ± 18 | -8 ± 0 | -35 ± 1 | -14 ± 1 | 13 ± 1 | -1369 ± 18 | -1404 ± 18 | -1377 ± 18 |

S6.6. Improvements to SKZCAM protocol in present work

We highlight here that because the SKZCAM protocol has been automatized in the present work (described in Sec. S10), it has allowed for a significant lowering of computational cost compared to previous applications of the SKZCAM protocol [278, 287]. The improvements are as follows:

1. More intermediate layers in the ONIOM mechanical embedding treatment. For example, we have added the Δ_{basis} and Δ_{core} terms to the final E_{int} , enabling cheaper calculations of ΔCC and $E_{\text{int}}^{\text{bulk MP2}}$ – the two dominant contributions to the overall computational cost – including only valence, no longer requiring semicore, electrons in the correlation treatment (due to Δ_{core}) and a smaller basis set treatment (due to Δ_{basis}).
2. The use of multiple different codes that are efficient for different types of calculations. We can utilise the ORCA code to perform highly efficient MP2 calculations [261] while still leveraging the LNO-CCSD(T) implementation [263, 264] in MRCC. Previously, we were limited towards only using one code due to the additional manual overhead.

Overall, these improvements enable significant lowering of costs. To put these improvements into context, our previous simulation [278] of the CO on MgO(001) required around 20,000 CPUh to perform while these improvements enable a cost to be lowered by two orders of magnitude to around 600 CPUh. Without these improvements, the application to the TiO₂ surface systems would have been largely unfeasible as well.

S7. CONTRIBUTIONS FOR THE COHESIVE AND CONFORMATIONAL ENERGY FROM CWFT IN SELECTED SYSTEMS

For the adsorption of monomers on the MgO surface, the definition of E_{int} has been defined in Fig. S3, where its difference with the adsorption energy E_{ads} is the energy to relax the monomer molecule and surface from their geometries in the adsorbate–surface complex to their equilibrium geometry, given by the quantity E_{rlx} . When computing the adsorption energy of clusters and the monolayers on the MgO(001) surface, there are additional contributions towards E_{ads} arising from the cohesive energy E_{coh} (or lateral interaction) that binds the molecules together. In general, E_{rlx} does not form a large contribution towards E_{ads} , with E_{int} being the dominant contribution, oftentimes more than 80% of H_{ads} . This is one of the reasons why we have computed E_{rlx} with DFT. However, it is not the case for systems where the molecule undergoes significant conformational changes (due to e.g., charge transfer). This is specifically the case for the chemisorbed CO_2 on MgO(001), where there is a large energy change of almost ~ 2 eV to bring the CO_2 from its bent geometry back into its linear geometry. This large conformational energy change E_{conf} is a quantity that is highly sensitive to the DFA. As such, for this system, we have computed E_{conf} with CCSD(T) - a negligible overall computational cost for the CO_2 molecule. We elaborate further on the value of these terms in the next sections.

S7.1. Conformational energy of the chemisorbed CO_2 on MgO(001)

As illustrated in Fig. S7, for the chemisorbed CO_2 on MgO(001), we have effectively broken up the original E_{rlx} , containing the relaxation energy for both the molecule and surface, such that it only pertains to the surface, with E_{conf} corresponding to the relaxation energy for the molecule. The importance of this contribution is shown in Table S10 where the conformational energy change is predicted by several DFAs (as well as MP2, CCSD) and find that they can differ by more than 300 meV from CCSD(T). These are well-known effects arising from the delocalisation error inherent in most DFAs [288]. The canonical MP2, CCSD and CCSD(T) calculations were performed in MRCC with the CBS(aVTZ/aVQZ) basis set treatment.

TABLE S10. Comparison of the E_{conf} values (in meV) for chemisorbed CO_2 chemisorbed on MgO for several DFAs as well as MP2, CCSD and CCSD(T).

| | E_{conf} [meV] |
|--------------|-------------------------|
| PBE-D2[Ne] | 1841 |
| revPBE-D4 | 1797 |
| vdW-DF | 1763 |
| rev-vdW-DF2 | 1836 |
| PBE0-D4 | 2153 |
| B3LYP-D2[Ne] | 2075 |
| MP2 | 2045 |
| CCSD | 2304 |
| CCSD(T) | 2094 |

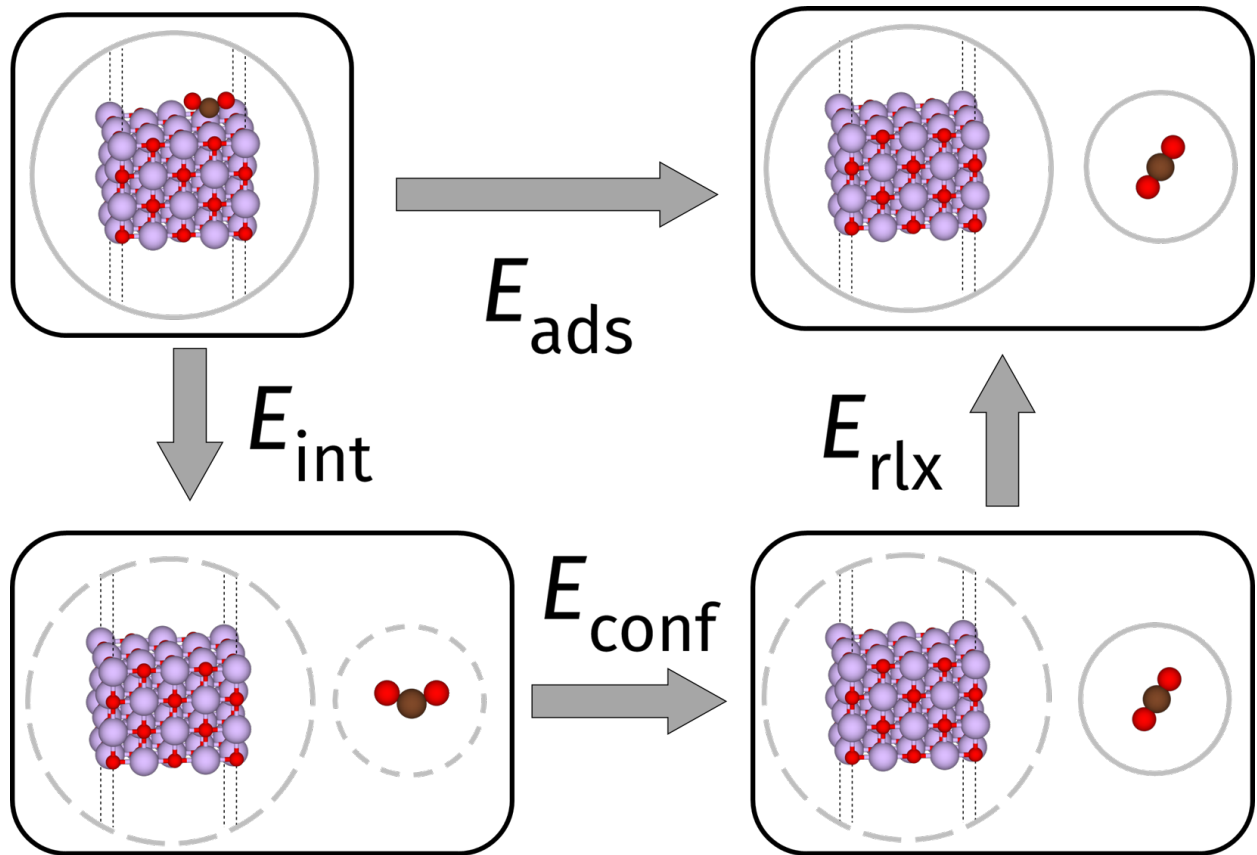


FIG. S7. The contributions to the adsorption energy E_{ads} for the chemisorbed CO_2 on MgO(001). Beyond the interaction energy E_{int} , there is E_{conf} - the relaxation energy to return the molecule in its geometry within the adsorbate-surface complex to its equilibrium geometry, leaving E_{rlx} to be the relaxation energy to bring the surface (at the geometry of the adsorbate-surface complex) into its equilibrium geometry. The circles represent a single system/calculation, with a dashed circle indicating a geometry fixed to that found in the adsorbate-surface complex while a line circle indicates an equilibrium geometry.

S7.2. Cohesive energy in CH₄ and C₂H₆ monolayers on MgO(001)

As illustrated in Fig. S8 for monolayer CH₄ on MgO(001), the E_{coh} cohesive energy term corresponds to the energetic contribution to E_{ads} arising from the lateral interactions of the molecules on the surface, with E_{int} corresponding to the interaction energy of the individual molecules (as monomers) on the MgO surface. The choice to compute E_{coh} and E_{int} separately, as opposed to computing their sum: $E_{\text{int}}^{\text{ML}}$ directly is because the SKZCAM protocol, as an embedding approach, can only calculate E_{int} for localised phenomena such as the adsorption of monomers. Practically, E_{coh} is computed by first computing E_{int} and subtracting it from $E_{\text{int}}^{\text{ML}}$. The computed E_{coh} is shown in Table S11 and it can be seen that across the different functionals, it can vary by over 40 meV, clearly requiring the need to go beyond DFT to treat this interaction.

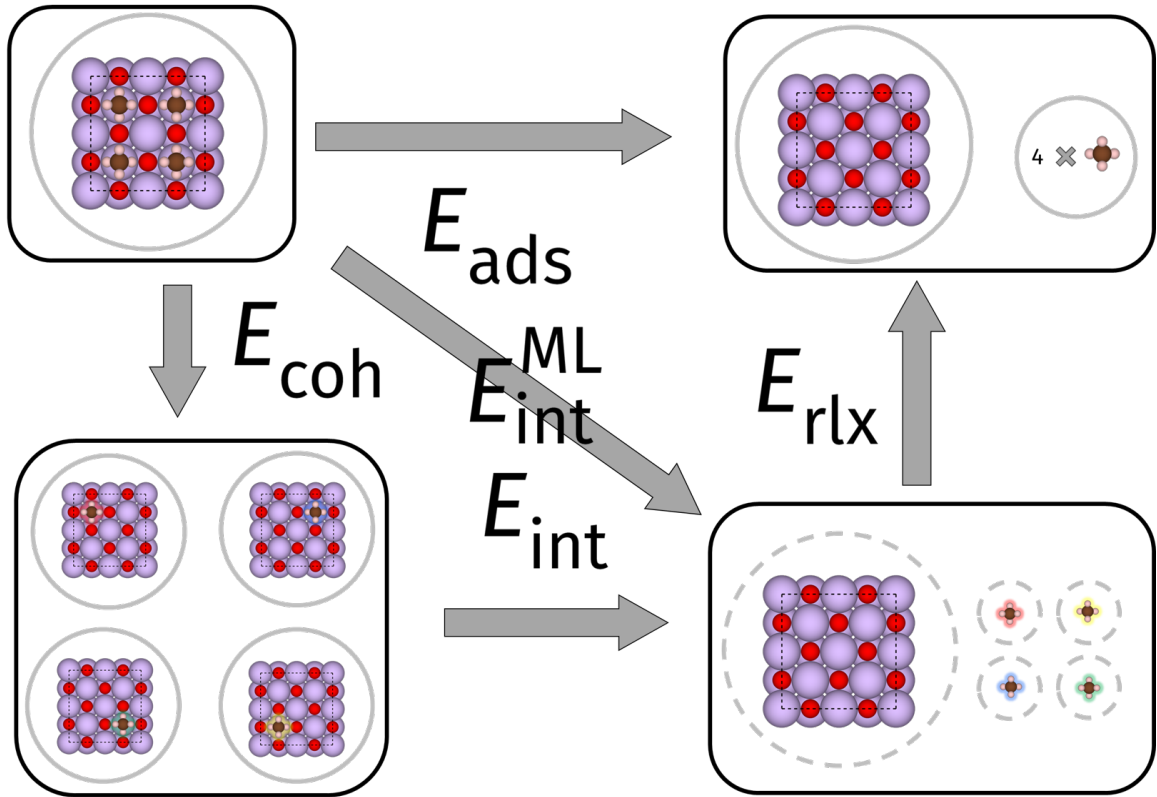


FIG. S8. The contributions to the adsorption energy E_{ads} for the monolayer CH₄ on MgO(001). Here, the E_{rlx} contribution remains the same as in Fig. S3. There is now an additional cohesive energy E_{coh} term which represents the lateral interactions between the molecules within the monolayer (in the presence of the MgO surface). Under this definition, the interaction energy E_{int} is calculated by treating the four molecules of the monolayer as individual monomers on the MgO(001) surface. The circles represent a single system/calculation, with a dashed circle indicating a geometry fixed to that found in the adsorbate–surface complex while a line circle indicates an equilibrium geometry.

TABLE S11. Table showcasing how the final CCSD(T)-quality E_{coh} (in meV) is computed. CCSD(T) (and other WFT methods) is used to compute the two-body (2B) contribution to the many-body expansion of the $E_{\text{coh}}^{\text{gas}}$ - the cohesive energy of the alkane monolayer in the absence of the MgO surface. This contribution is used to correct the 2B contribution to $E_{\text{coh}}^{\text{gas}}$ for revPBE-D4 (i.e., it is used to account for 3B and beyond contributions). Finally, we reach the final E_{coh} by incorporating the effect of the MgO surface at the revPBE-D4 level (i.e., the difference between E_{coh} and $E_{\text{coh}}^{\text{gas}}$).

| | CH ₄ Monolayer | | | C ₂ H ₆ Monolayer | | |
|--------------|----------------------------------|-------------------------------|------------------|-----------------------------------------|-------------------------------|------------------|
| | $E_{\text{coh}}^{2\text{B gas}}$ | $E_{\text{coh}}^{\text{gas}}$ | E_{coh} | $E_{\text{coh}}^{2\text{B gas}}$ | $E_{\text{coh}}^{\text{gas}}$ | E_{coh} |
| PBE-D2[Ne] | - | -53 | -40 | - | -125 | -106 |
| revPBE-D4 | -46 | -42 | -31 | -79 | -62 | -48 |
| vdW-DF | - | -72 | -58 | - | -88 | -67 |
| rev-vdW-DF2 | - | -40 | -43 | - | -69 | -83 |
| PBE0-D4 | - | -43 | -34 | - | -77 | -64 |
| B3LYP-D2[Ne] | - | -39 | -37 | - | -124 | -124 |
| MP2 | -15 | -11 | - | -58 | -41 | -27 |
| CCSD | -33 | -29 | -18 | -59 | -43 | -29 |
| CCSD(T) | -40 | -37 | -25 | -92 | -75 | -61 |

It is not directly possible to elevate E_{coh} up to CCSD(T) quality as it involves (minor effects) arising from the presence of the MgO surface. Instead, we have to consider the cohesive energy $E_{\text{coh}}^{\text{gas}}$ of monolayer in the absence of the surface (i.e., in the gas phase). Specifically, it is possible to make a many-body expansion of $E_{\text{coh}}^{\text{gas}}$, incorporating 2-body (2B) contributions (see Fig. S9 and beyond). As we show for revPBE-D4, the 2B contribution ($E_{\text{coh}}^{2\text{B gas}}$) makes up the most dominant contribution of $E_{\text{coh}}^{\text{gas}}$, differing by 4 meV and 17 meV for the CH₄ and C₂H₆ monolayers respectively. We have computed the CCSD(T) $E_{\text{coh}}^{2\text{B gas}}$ contribution and from this, we can correct this (major) part of $E_{\text{coh}}^{\text{gas}}$ and subsequently E_{coh} . We also make use of the frozen-natural orbital (FNO) approximation to speed up these calculations. The treatment has been performed before by Alessio *et al.* [246] and Tosoni *et al.* [242] and we come in excellent agreement; differences could arise from differing geometries or CCSD(T) being more accurate than MP2.

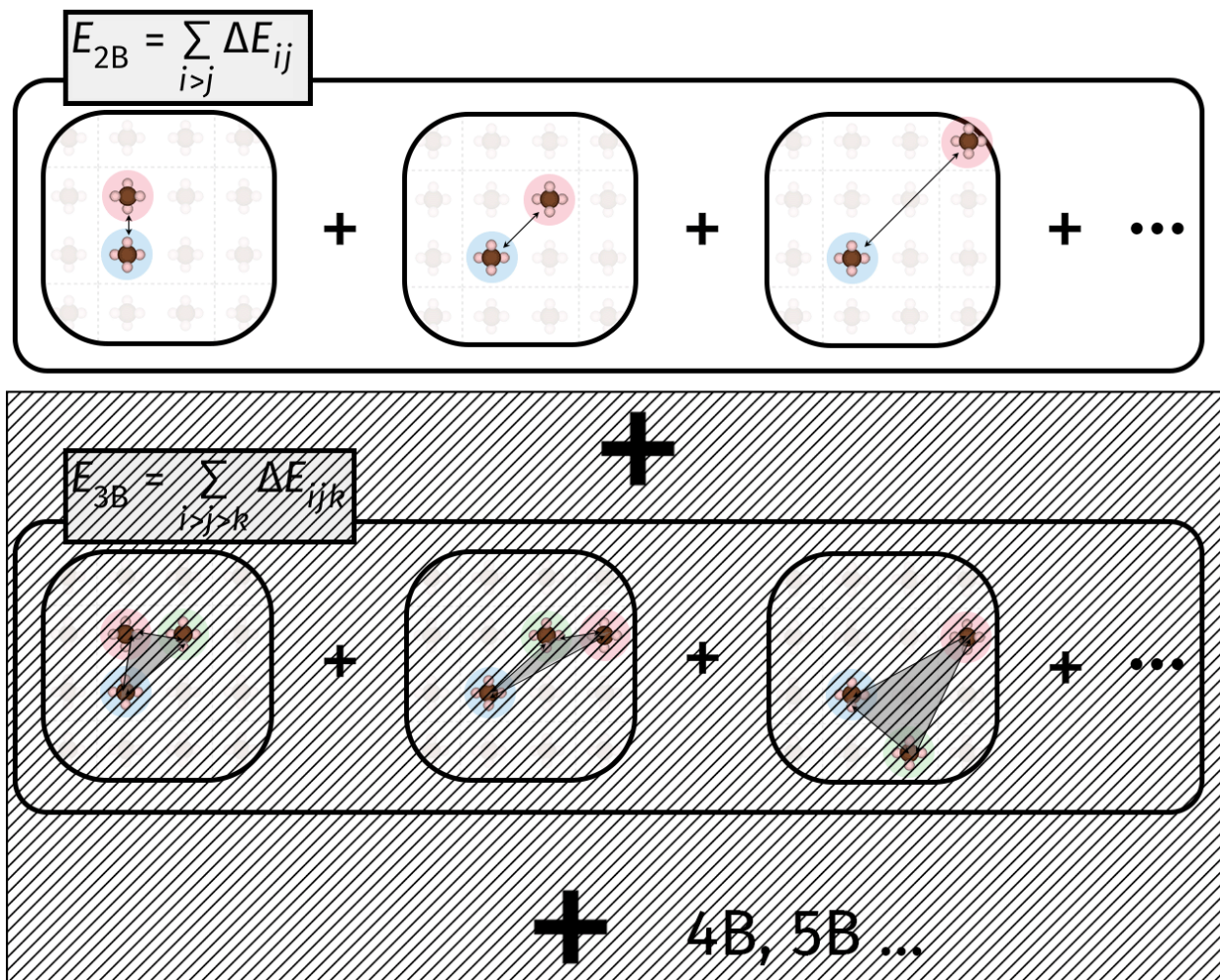


FIG. S9. Showcasing the many-body expansion to obtain $E_{\text{coh}}^{\text{gas}}$ of alkane monolayers (using CH_4 as an example). We compute the 2B contribution at the CCSD(T) level and treat the higher-body contributions with revPBE-D4.

S7.3. Cohesive and dissociation energy in H₂O and CH₃OH clusters on MgO(001)

For the (non-dissociated) molecular H₂O and CH₃OH clusters on MgO(001), we partition the E_{ads} into contributions from E_{int} , E_{rlx} and E_{coh} , as seen in Fig. S10. Here, E_{int} is defined to be the interaction energy required to remove the entire cluster from the surface, taking the cluster to be the ‘molecule’. The cohesive energy is then the binding energy to break the cluster into its separate molecules, all within the gas phase and having their geometries fixed to that within the cluster-surface complex. Finally E_{rlx} is the energy to relax the molecules and surface into their equilibrium geometries.

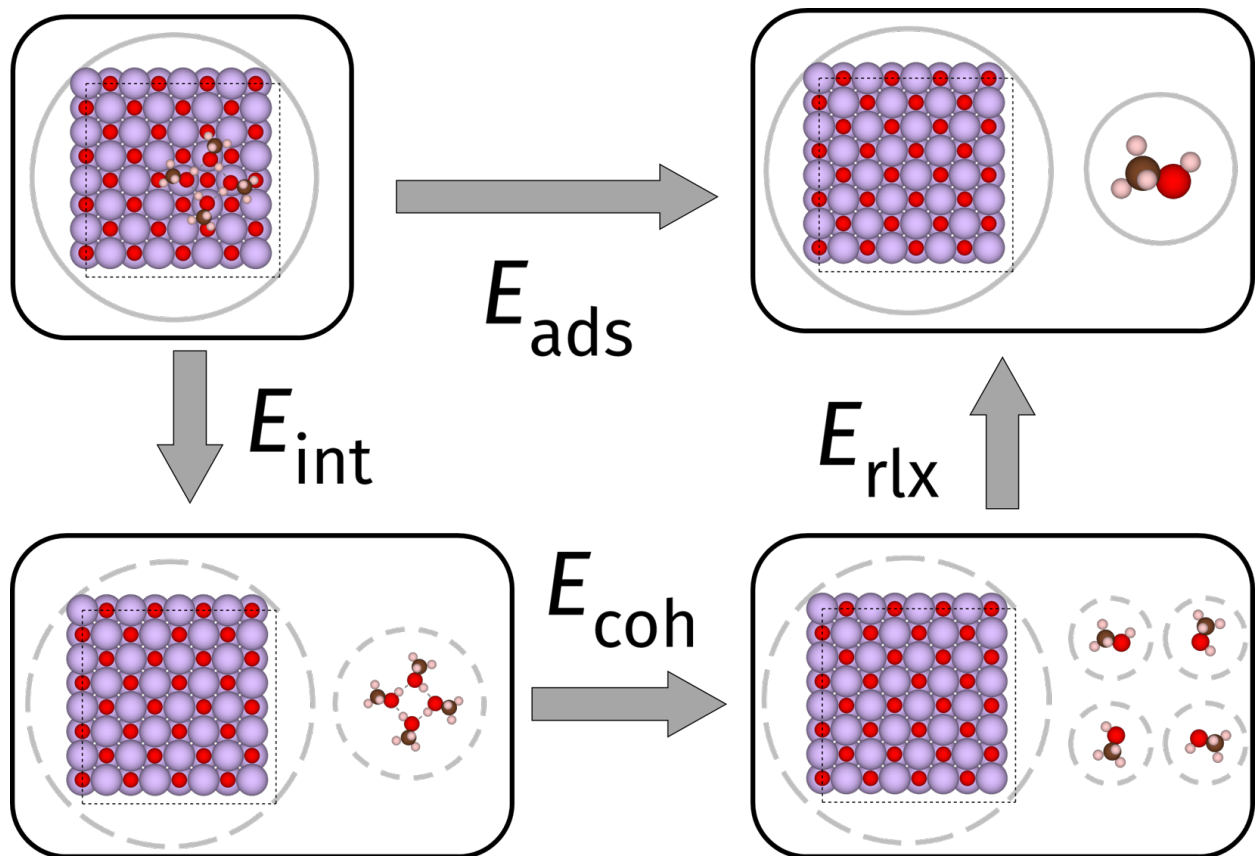


FIG. S10. The contributions to the adsorption energy E_{ads} for the tetramer CH₃OH cluster on MgO(001). Here, the E_{rlx} contribution remains the same as in Fig. S3. There is now an additional cohesive energy E_{coh} term which represents the lateral interactions between the molecules within the cluster (in the gas phase). Under this definition, the interaction energy E_{int} is calculated by treating the cluster as a single ‘molecule’ that first desorbs from the surface. The circles represent a single system/calculation, with a dashed circle indicating a geometry fixed to that found in the adsorbate–surface complex while a line circle indicates an equilibrium geometry.

The cohesive energy is computed for the revPBE-D4 geometry for the ensemble of DFAs as well

TABLE S12. Comparison between several DFAs, MP2 and CCSD against CCSD(T) for the cohesive energy E_{coh} per monomer (in meV) of the tetramer CH_3OH and H_2O cluster.

| | CH_3OH | H_2O |
|--------------|------------------------|----------------------|
| PBE-D2[Ne] | -380 | -309 |
| revPBE-D4 | -328 | -261 |
| vdW-DF | -291 | -240 |
| rev-vdW-DF2 | -357 | -289 |
| PBE0-D4 | -367 | -302 |
| B3LYP-D2[Ne] | -371 | -303 |
| MP2 | -341 | -276 |
| CCSD | -311 | -269 |
| CCSD(T) | -336 | -281 |

as MP2, CCSD and CCSD(T) in Table S12. There is a range of 90 meV and 70 meV between the DFAs, highlighting the need to move towards CCSD(T) for high accuracy.

To calculate the adsorption energy E_{ads} of the partially dissociated clusters of H_2O and CH_3OH on $\text{MgO}(001)$, we compute an additional term E_{diss} which accounts for the energy difference/stabilisation between the molecularly adsorbed and partially-dissociated forms of the H_2O and CH_3OH tetramers (see Fig. S11). We use the revPBE-D4 geometry of the molecular and partially-dissociated forms and have computed this energy using the ensemble of DFAs, as shown in Sec. S8.5.

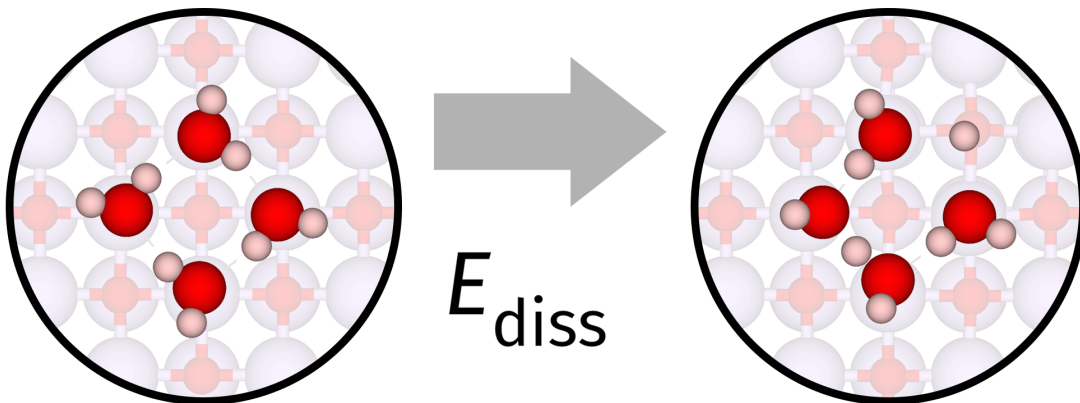


FIG. S11. The dissociation energy E_{diss} is defined as the energetic stabilisation to form a dissociated cluster from the original molecularly adsorbed cluster. We use the H_2O tetramer cluster as the example.

S7.4. Cohesive energy of NO dimer on MgO(001)

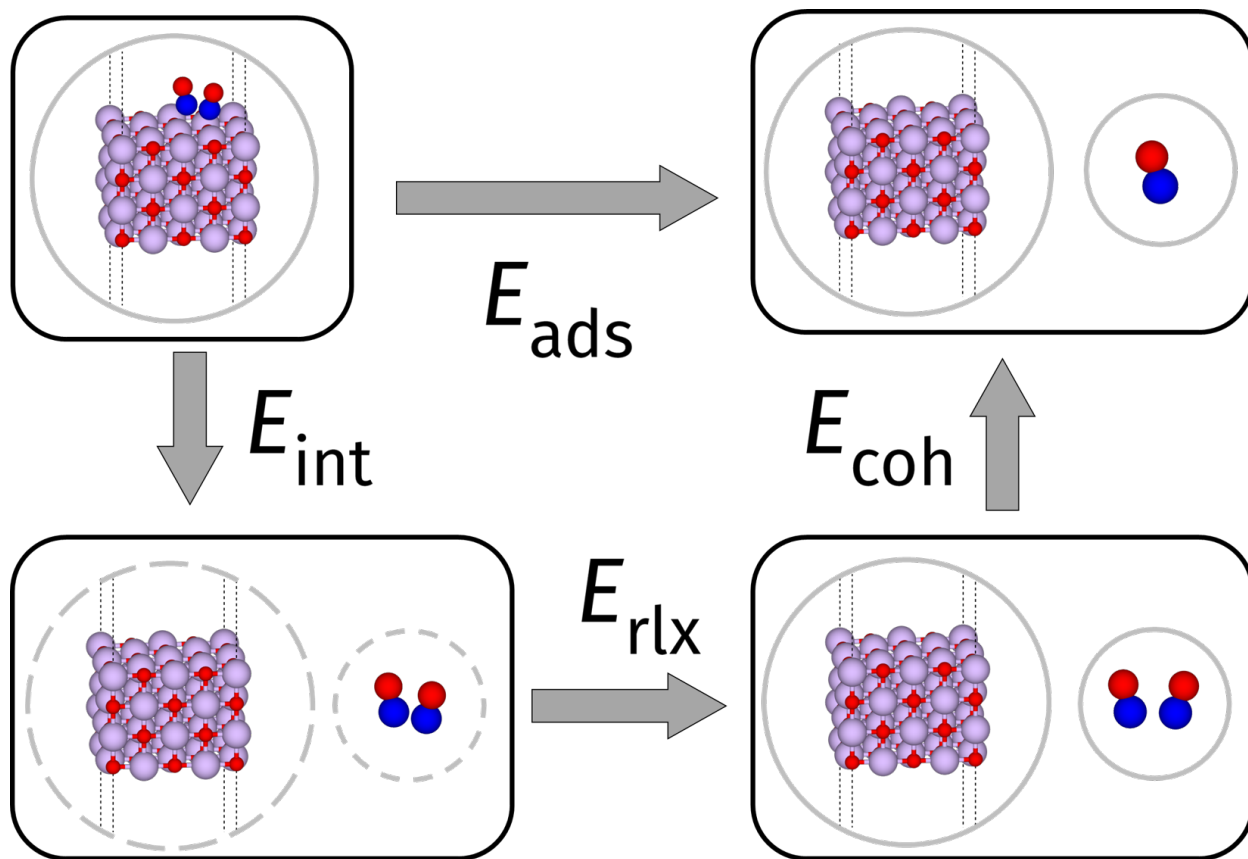


FIG. S12. The contributions to the adsorption energy E_{ads} for the NO dimer on MgO(001). Here, the interaction energy E_{int} is calculated by treating the dimer as a single ‘molecule’ that first desorbs from the surface. Then, E_{rlx} represents the relaxation energy for the surface into its equilibrium geometry and the dimer into its equilibrium geometry (as a dimer). The cohesive energy E_{coh} term which represents the binding energy to bring the dimer to two separate monomers, all in their equilibrium geometry. The circles represent a single system/calculation, with a dashed circle indicating a geometry fixed to that found in the adsorbate–surface complex while a line circle indicates an equilibrium geometry.

As illustrated in Fig. S12, the contributions to the E_{ads} of the NO dimer on MgO(001) differ slightly from those of the H₂O and CH₃OH tetramers. The definition of E_{int} remains the same, treating the dimer as the ‘molecule’. However, the relaxation energy E_{rlx} now pertains to the energy to bring the dimer from its geometry in the dimer-surface complex into its equilibrium geometry (together with the surface) and E_{coh} now represents the binding energy of the dimer against the separate monomers. This new definition of E_{coh} was chosen because the binding energy of the NO dimer is a well-studied topic both with experiments [289, 290] and computational simulations [291, 292], with a complete summary of previous work found in Ref. 293.

TABLE S13. Comparison of experiment and MRMP2 against several DFAs and CCSD(T) for the cohesive energy E_{coh} per monomer (in meV) of the NO dimer.

| Method | E_{coh} [meV] |
|--------------------|------------------------|
| PBE-D2[Ne] | -239 |
| revPBE-D4 | -192 |
| vdW-DF | -160 |
| rev-vdW-DF2 | -281 |
| PBE0-D4 | 53 |
| B3LYP-D2[Ne] | 63 |
| CCSD(T) [294] | -22 |
| Experiment [293] | -61 to -82 |
| MRMP2(18,14) [293] | -75 |

As a multireference problem, DFT has trouble with getting E_{coh} right, clearly seen in Table S13 where there is an 344 meV range in E_{coh} across the DFAs that we have studied. Relative to the experimental E_{coh} window of -61 to -82 meV per monomer (or 121–165 meV in terms of binding energy), CCSD(T) has been shown to underbind this quantity with a value of -22 meV. Previous work with multireference second-order perturbation theory (MRMP2) using a large (18,14) active space have demonstrated much better agreement [293] with an E_{coh} of -75 meV. One of the advantages of the partitioning of the E_{ads} in Fig. S12 is that we have broken down E_{ads} into various contributions which can be tackled with different methods. Specifically, E_{int} can be reliably treated with CCSD(T), while E_{rlx} can be treated with DFT and E_{coh} can be treated with multireference methods. This allows us to use the previously computed MRMP2 value [293] of E_{coh} in our final E_{ads} and H_{ads} .

S8. GEOMETRY RELAXATION AND ENTHALPIC CONTRIBUTIONS FROM A DFT ENSEMBLE

The autoSKZCAM framework extends the accurate E_{int} computed with the SKZCAM protocol towards computing an accurate H_{ads} estimate that can be compared directly with experiments. The aim is to make the calculation of H_{ads} affordable and to decrease the number of CCSD(T)-level calculations required, especially on the contributions where it isn't needed. Specifically, the autoSKZCAM framework uses DFT to compute the remaining geometrical relaxation E_{rlx} , zero-point vibrational E_{ZPV} and temperature E_{T} contributions to enable the calculation of H_{ads} within Eqs. 1 and 2. These terms make overall small contributions to the final H_{ads} , thus errors due to the approximate nature of DFT are not expected to alter the numbers significantly. Furthermore, these are quantities that do not depend on the absolute value of the potential energy surface (as in the case of E_{int}) but on 'relative' changes around the minima to e.g., compute vibrational frequencies or relaxation energies, where DFT can perform accurately for.

To ensure reliable estimates with error bars, we use an ensemble/set of density functional approximations (DFAs). For MgO, we used the 6 high-accuracy DFAs within the ensemble: PBE-D2[Ne] [242, 295], revPBE-D4 [197, 198], vdW-DF [296], rev-vdW-DF2 [297], PBE0-D4 [198, 298] and B3LYP-D2[Ne] [242, 299], where[Ne] denotes that the Neon D2 parameters [300] have been used on the Mg atom [242], or subsets of them as we discuss later. For the TiO₂ systems, we used the: PBE-TS/Hi [295, 301], revPBE-D4, vdW-DF, rev-vdw-DF2, r²SCAN-rVV10 [302] and HSE06-D4 [198, 303] functionals. These DFAs were chosen because they are generally expected to perform well for their respective surfaces for both E_{int} and unit cell lattice parameters (see Tables S14, S15 and S16 for the MgO, TiO₂ rutile(110) and anatase(101) surfaces respectively), allowing us to probe a sensible range of values as close as possible to the true answer. The use of an ensemble of DFAs allows us to take averages for improved estimates and to give error estimates on E_{rlx} and E_{ZPV} and E_{T} which we will discuss in Section S8.3 and S8.4 respectively. Their specific computational details are provided in Section S8.1.

S8.1. Computational details for periodic density functional theory

Periodic DFT were performed with the Vienna *Ab-Initio* Simulation Package 6.3.0 [306, 307] (VASP). For each of the three surfaces, we used an ensemble of 6 DFAs to calculate the terms

TABLE S14. Lattice parameter (in Å) and H₂O E_{int} for MgO(001) obtained from the DFT ensemble. These are compared to experiment [304] for the lattice parameter and the autoSKZCAM E_{int} .

| | Lattice Parameter a | H ₂ O E_{int} |
|--------------|---------------------|-----------------------------------|
| PBE-D2[Ne] | 4.234 | -693 |
| revPBE-D4 | 4.220 | -637 |
| vdW-DF | 4.273 | -567 |
| rev-vdW-DF2 | 4.220 | -711 |
| PBE0-D4 | 4.175 | -695 |
| B3LYP-D2[Ne] | 4.202 | -618 |
| Reference | 4.214 | -702 |

TABLE S15. Lattice parameter (in Å) and H₂O E_{int} for TiO₂ rutile(110) obtained from the DFT ensemble. These are compared to experiment [305] for the lattice parameter and the autoSKZCAM E_{int} .

| | Lattice Parameter a | Lattice Parameter c | H ₂ O E_{int} |
|---------------------------|---------------------|---------------------|-----------------------------------|
| PBE-TS/HI | 4.611 | 2.970 | -1282 |
| revPBE-D4 | 4.598 | 2.958 | -1214 |
| vdW-DF | 4.685 | 2.995 | -1026 |
| rev-vdW-DF2 | 4.618 | 2.961 | -1344 |
| r ² SCAN-rVV10 | 4.590 | 2.957 | -1552 |
| HSE06-D4 | 4.559 | 2.940 | -1410 |
| Reference | 4.587 | 2.954 | -1310 |

that make up H_{ads} . The electronic structure parameters [k -point grid, energy cutoff and projected augmented wave (PAW) potentials] are provided in Table S17. An energy cutoff of 600 eV was used for most of the DFAs, although this was reduced to 520 eV for the hybrid HSE06-D4 calculations on the TiO₂ surface systems. For the HSE06-D4 calculation relaxations, we lower its cost by using a reduced Γ -point grid (via NKRED) for the exact exchange contribution to the total energy and use a 18 electron core PAW potential on the Ti atoms. A Γ -centered k -point mesh was used in all the systems, with the k -point grids chosen to converge E_{int} to 1 meV.

The three surfaces used to model the adsorbate–surface systems are shown in Fig. S13. For the MgO system, we perform calculations on a 4 layer slab, where the bottom two layers are fixed. The majority of systems used a 4×4, with an 8×8 supercell used for C₆H₆ and the CH₃OH and H₂O clusters. The 2×2×1 k -point grid used with the 4×4 supercell was reduced to a Γ -point grid for the 8×8 supercell. The TiO₂ rutile(110) surface slab consisted of a p(4×2) supercell with 5

TABLE S16. Lattice parameter (in Å) and H₂O E_{int} for TiO₂ anatase(101) obtained from the DFT ensemble. These are compared to experiment [305] for the lattice parameter and the autoSKZCAM E_{int} .

| | Lattice Parameter a | Lattice Parameter c | H ₂ O E_{int} |
|---------------------------|---------------------|---------------------|-----------------------------------|
| PBE-TS/HI | 3.789 | 9.659 | -1095 |
| revPBE-D4 | 3.790 | 9.548 | -1096 |
| vdW-DF | 3.839 | 9.767 | -917 |
| rev-vdW-DF2 | 3.798 | 9.590 | -1179 |
| r ² SCAN-rVV10 | 3.785 | 9.531 | -1392 |
| HSE06-D4 | 3.751 | 9.540 | -1224 |
| Reference | 3.782 | 9.502 | -1207 |

tri-layers (and the bottom three fixed), while the anatase(101) surface slab consisted of a (3×1) supercell with 4 tri-layers and the bottom layer fixed. All surfaces incorporated 15Å of vacuum and were generated through a geometrical relaxation performed with a force convergence cutoff of 0.01 eV/Å. Subsequently, a molecule was added onto the surface and relaxed with the same force convergence cutoff. Vibrational frequency calculations were performed for a subset of the DFT ensemble (see Section S8.4) using a finite-differences approach with POTIM=0.01Å displacements, one in the positive and negative direction along the three Cartesian directions (i.e., NFREE=2). The self-consistent field cycles were set to an energy convergence of 10⁻⁸ eV for the vibrational frequency calculations, with 10⁻⁷ eV as standard for geometry optimisations.

S8.2. The relaxation energy

For the adsorption of monomers on the surfaces, the relaxation energy E_{rlx} is defined as the energy change when the surface and molecule are relaxed from their geometry in the adsorbate-surface complex to their equilibrium geometries. This definition persists for the tetramer CH₃OH and H₂O clusters and the monolayer alkanes on MgO(001), where the individual monomers in the cluster or monolayer are compared to their equilibrium geometries in the gas-phase. For the NO dimer, this definition slightly changes to be the energy change from the dimer on the MgO(001) surface to the dimer’s equilibrium geometry for reasons discussed in Section S7.4. For the chemisorbed CO₂ on the MgO(001) surface, E_{rlx} now only corresponds to the relaxation of the surface, with the relaxation of the molecule encapsulated in the E_{conf} term that is treated at the CCSD(T) level, discussed in Section S7.1. The result is that E_{rlx} is a small quantity relative

TABLE S17. DFT parameters used for the three different surfaces. The parameters for hybrids are also different from those for the metaGGA, GGA and vdW-inclusive functionals, grouped as (meta)GGA in the table. The number of layers in parentheses indicates the number of layers fixed at the bottom of the slab. The k -points in parenthesis indicates the k -point mesh used for the exact exchange potential. We used the PBE version 54 set of PAW potentials for all the calculations.

| | MgO(001) | | TiO ₂ rutile(110) | | TiO ₂ anatase(101) | |
|---------------------|-----------------|-----------------|------------------------------|---------------|-------------------------------|---------------|
| | (meta)GGA | hybrid | (meta)GGA | hybrid | (meta)GGA | hybrid |
| Supercell Size | 4×4 | 4×4 | p(4×2) | p(4×2) | 3×1 | 3×1 |
| Number of Layers | 4(2) | 4(2) | 5(3) O-Ti-O | 5(2) O-Ti-O | 8(2) O-Ti-O layers | 8(2) O-Ti-O |
| k -point Mesh | 2×2×1 | 2×2×1(2×2×1) | 2×2×1 | 2×2×1(1×1×1) | 3×3×1 | 3×3×1(1×1×1) |
| Energy cutoff | 600 | 600 | 600 | 520 | 600 | 520 |
| Vacuum | 15 | 15 | 15 | 13 | 15 | 13 |
| Metal PAW potential | Mg-pv (4e core) | Mg-pv (4e core) | Ti-pv (12e core) | Ti (18e core) | Ti-pv (12e core) | Ti (18e core) |

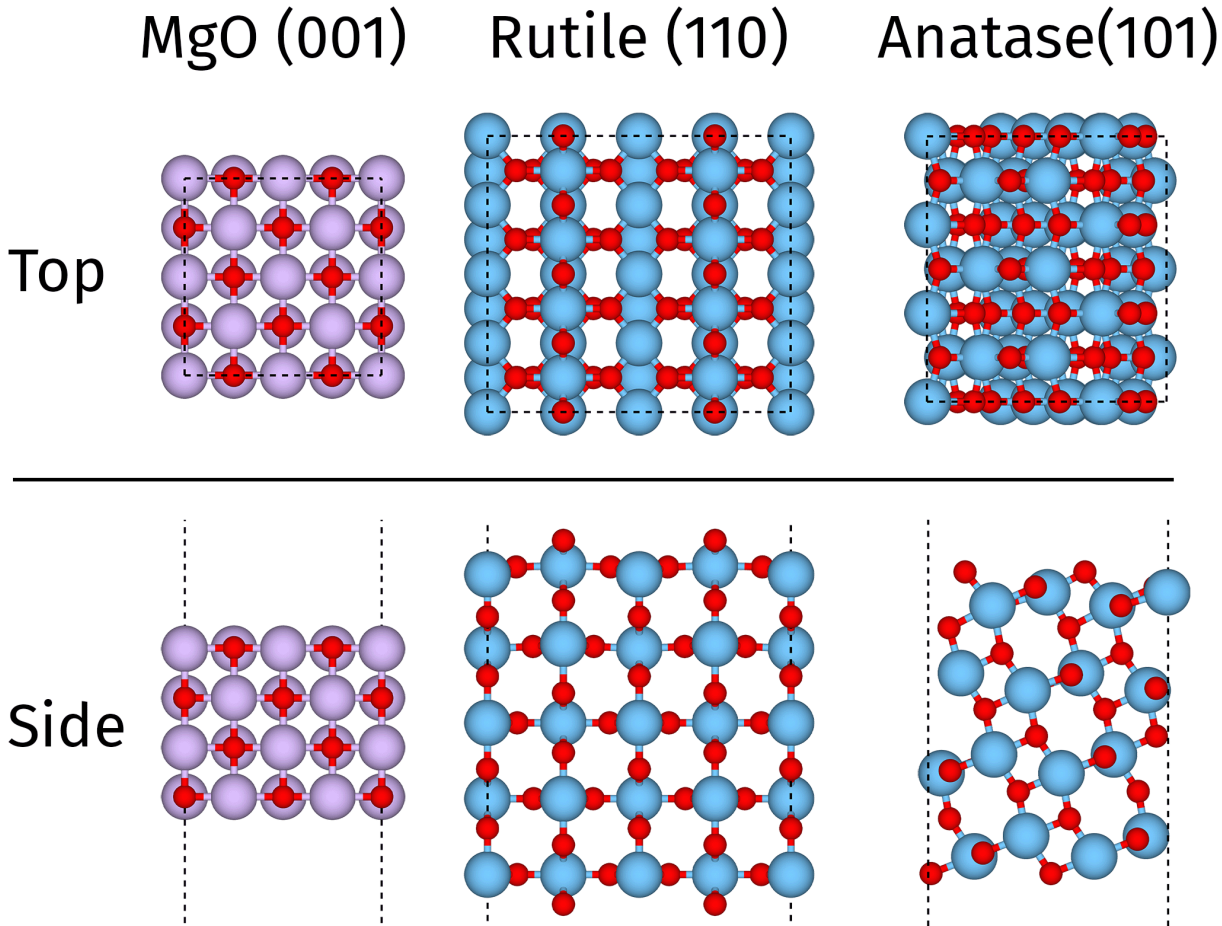


FIG. S13. Top and side views for the MgO(001), TiO₂ rutile(110) and TiO₂ anatase(101) surfaces.

to the overall E_{ads} , as we show for the DFT ensemble in Tables S18 and S19 for the MgO and TiO₂ surfaces respectively. As discussed in the next section, we use revPBE-D4 to generate the adsorbate–surface geometries, and hence use the E_{rlx} term generated by this DFA. For the NO dimer system, we have opted to use the geometry and E_{rlx} from B3LYP-D2[Ne] as revPBE-D4 strongly overestimates the binding of the NO dimer.

S8.3. Estimating geometrical errors

Obtaining energy gradients (for e.g., forces) is challenging with methods from cWFT such as CCSD(T) and even for codes where this is possible, it would be highly expensive. As such, it is common to use geometries generated by a lower level of theory such as DFT. There is thus an error in the resulting E_{ads} that arises from the use of a DFT geometry. Besides this geometrical error in E_{ads} , there is also an additional error because we use DFT to calculate E_{rlx} in Eq. 2; specifically

with the DFA used to generate the geometry. There is an additional error associated with using this DFT value of E_{rlx} and we aim to capture the combination of these two errors within an error term dubbed ϵ_{geom} .

This ϵ_{geom} error can be estimated from the ensemble of DFAs. The application of a method, whether another DFA or one from cWFT, on the revPBE-D4 geometry can be denoted as Method//revPBE-D4 and the resulting approximate adsorption energy $E_{\text{ads}}^{\text{approx}}$ can be defined as:

$$\begin{aligned}
 E_{\text{ads}}^{\text{approx}}[\text{Method//revPBE-D4}] = & E_{\text{int}}[\text{Method//revPBE-D4}] + \\
 & E_{\text{rlx}}[\text{revPBE-D4//revPBE-D4}] + \\
 & (E_{\text{coh}}[\text{Method//revPBE-D4}] + E_{\text{conf}}[\text{Method//revPBE-D4}]),
 \end{aligned}
 \tag{6}$$

where E_{coh} and E_{conf} are included for the systems that have those terms, discussed in Section S7. The true adsorption energy $E_{\text{ads}}^{\text{true}}$ corresponds to the E_{ads} evaluated with the method with its corresponding geometry (i.e., Method//Method) and it is the quantity that we ultimately aim to approximate with $E_{\text{ads}}^{\text{approx}}$.

We chose revPBE-D4 as the functional to generate the geometries for subsequent E_{int} with the SKZCAM protocol because we find that it provides a low error on $E_{\text{ads}}^{\text{approx}}$ relative to $E_{\text{ads}}^{\text{true}}$ when evaluated across the other functionals in the ensemble. In Fig. S14, we have compared the 6 DFAs within the ensemble for their performance in reproducing $E_{\text{ads}}^{\text{true}}$. The chosen systems highlight a range of binding and surfaces and revPBE-D4 performs well across all the adsorbate–surface systems, with an MAD that are all less than 5% of $E_{\text{ads}}^{\text{true}}$. We note that the only system where we have chosen not to use the revPBE-D4 geometry is NO dimer as a hybrid such as B3LYP-D2[Ne] predicts the correct ground state and does not strongly overbind its cohesive energy E_{coh} like the GGAs [293].

In Tables S18 and S19, we have computed $E_{\text{ads}}^{\text{approx}}$ (including the corresponding E_{int}) and $E_{\text{ads}}^{\text{true}}$ across the entire DFT ensemble for the monomers adsorbed on MgO(001) and TiO₂ surfaces respectively. We take ϵ_{geom} to be 2 times the root mean squared error (2RMSE) of $E_{\text{ads}}^{\text{approx}}$ against $E_{\text{ads}}^{\text{true}}$ for the DFAs in the ensemble, excluding revPBE-D4 (which should have no error by definition). Assuming an even/normal distribution around $E_{\text{ads}}^{\text{true}}$ from using the revPBE-D4 geometry for $E_{\text{ads}}^{\text{approx}}$, this error choice gives a 95% confidence interval on the final estimate.

We also compute this error for the monolayer and clusters on MgO in Table S20, where an

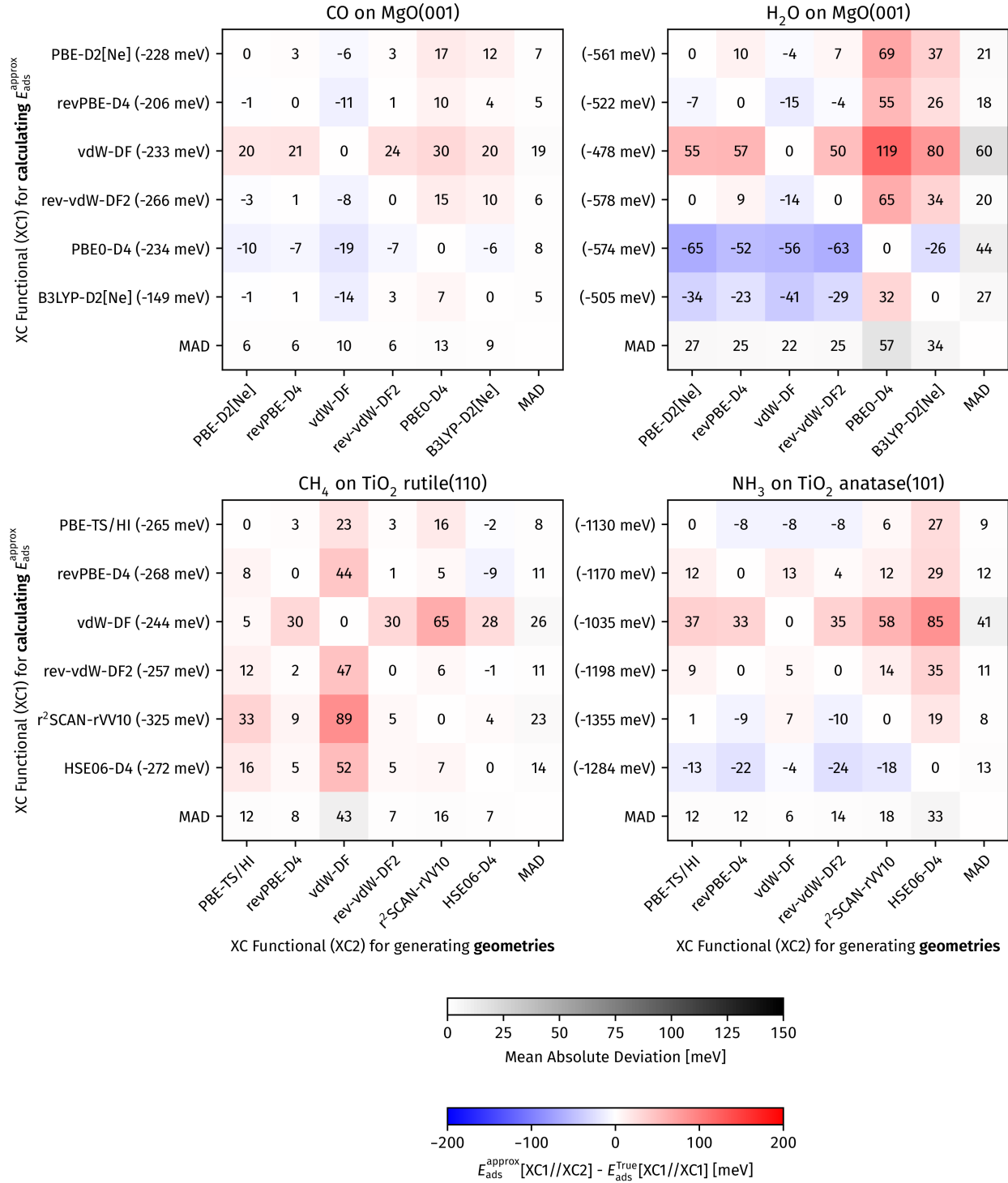


FIG. S14. Estimating the errors for using geometries generated by a DFA. The CO on MgO(001), H₂O on MgO(001), CH₄ on TiO₂ rutile(110) and NH₃ on TiO₂ anatase(101) adsorbate–surface systems were used as illustration. For the geometry generated by each DFA (on the x-axis), an approximate $E_{\text{ads}}^{\text{approx}}$ is calculated for the DFT ensemble along each column as defined in Eq. 6. This is compared to the true $E_{\text{ads}}^{\text{true}}$ from using the corresponding geometry of each DFA. The difference between $E_{\text{ads}}^{\text{approx}}$ and $E_{\text{ads}}^{\text{true}}$ is plotted, with a corresponding mean absolute deviation for each DFA’s geometry is given in the bottom row.

additional cohesive energy term E_{coh} has evaluated with the corresponding DFA on the revPBE-D4 geometry. Table S20 also includes chemisorbed CO_2 on $\text{MgO}(001)$, where there is an additional E_{conf} term to estimate $E_{\text{ads}}^{\text{approx}}$ and obtain ϵ_{geom} .

TABLE S18: For the monomers on the $\text{MgO}(001)$ surface, we estimate the errors for using the revPBE-D4 geometry and E_{rlx} in the final E_{ads} of the autoSKZCAM protocol using an ensemble of 6 different DFAs. The errors are calculated as the difference between the true $E_{\text{ads}}^{\text{true}}$ (using the appropriate DFA) and the approximated $E_{\text{ads}}^{\text{approx}}$ using the revPBE-D4 geometry and E_{rlx} .

| | | CH_4 | C_2H_6 | CO | C_6H_6 | Parallel N_2O | Tilted N_2O | Vertical-Hollow NO | Vertical-Mg NO | Bent-Bridge NO | Bent-Mg NO | Bent-O NO | Monomer H_2O | Tilted CH_3OH | Parallel CH_3OH | NH_3 | Physisorbed CO_2 |
|-------------|----------------------------------|---------------|------------------------|-------------|------------------------|-------------------------------|-----------------------------|-----------------------------|-------------------------|-------------------------|---------------------|--------------------|------------------------------|-------------------------------|---------------------------------|---------------|---------------------------|
| PBE-D2[Ne] | E_{int} | -115 | -157 | -233 | -278 | -180 | -137 | -263 | -170 | -353 | -207 | -242 | -666 | -735 | -460 | -617 | -238 |
| | E_{rlx} | 2 | 1 | 8 | 26 | 3 | 10 | 29 | 9 | 51 | 6 | 39 | 114 | 145 | 46 | 89 | 14 |
| | $E_{\text{ads}}^{\text{approx}}$ | -114 | -156 | -224 | -252 | -177 | -127 | -234 | -161 | -302 | -201 | -203 | -552 | -590 | -414 | -528 | -225 |
| | $E_{\text{ads}}^{\text{true}}$ | -115 | -158 | -228 | -261 | -179 | -132 | -184 | -162 | -301 | -203 | -196 | -561 | -599 | -417 | -540 | -227 |
| | Error | 2 | 2 | 3 | 9 | 2 | 5 | -50 | 1 | -1 | 2 | -7 | 10 | 9 | 3 | 12 | 2 |
| revPBE-D4 | E_{int} | -143 | -219 | -215 | -565 | -192 | -133 | -184 | -142 | -346 | -184 | -234 | -637 | -770 | -502 | -636 | -268 |
| | E_{rlx} | 2 | 1 | 8 | 26 | 3 | 10 | 29 | 9 | 51 | 6 | 39 | 114 | 145 | 46 | 89 | 14 |
| | $E_{\text{ads}}^{\text{approx}}$ | -142 | -218 | -206 | -538 | -189 | -123 | -154 | -133 | -294 | -178 | -195 | -522 | -625 | -457 | -547 | -254 |
| | $E_{\text{ads}}^{\text{true}}$ | -142 | -218 | -206 | -538 | -189 | -123 | -154 | -133 | -294 | -178 | -195 | -522 | -625 | -457 | -547 | -254 |
| | Error | 0 | 0 | 0 | 0 | 0 | 0 | 0 | 0 | 0 | 0 | 0 | 0 | 0 | 0 | 0 | 0 |
| vdW-DF | E_{int} | -137 | -197 | -221 | -391 | -246 | -181 | -174 | -179 | -306 | -227 | -221 | -535 | -643 | -405 | -590 | -258 |
| | E_{rlx} | 2 | 1 | 8 | 26 | 3 | 10 | 29 | 9 | 51 | 6 | 39 | 114 | 145 | 46 | 89 | 14 |
| | $E_{\text{ads}}^{\text{approx}}$ | -135 | -196 | -212 | -365 | -242 | -171 | -145 | -170 | -255 | -221 | -182 | -421 | -498 | -360 | -502 | -245 |
| | $E_{\text{ads}}^{\text{true}}$ | -156 | -233 | -233 | -466 | -261 | -220 | -187 | -191 | -300 | -243 | -224 | -478 | -576 | -408 | -543 | -277 |
| | Error | 21 | 37 | 21 | 101 | 19 | 50 | 42 | 21 | 45 | 22 | 42 | 57 | 78 | 48 | 41 | 33 |
| rev-vdW-DF2 | E_{int} | -141 | -207 | -273 | -460 | -247 | -192 | -293 | -254 | -411 | -260 | -290 | -683 | -794 | -490 | -671 | -303 |
| | E_{rlx} | 2 | 1 | 8 | 26 | 3 | 10 | 29 | 9 | 51 | 6 | 39 | 114 | 145 | 46 | 89 | 14 |
| | $E_{\text{ads}}^{\text{approx}}$ | -140 | -206 | -265 | -433 | -244 | -182 | -264 | -245 | -360 | -254 | -251 | -568 | -649 | -444 | -583 | -289 |
| | $E_{\text{ads}}^{\text{true}}$ | -140 | -207 | -266 | -449 | -246 | -183 | -227 | -208 | -358 | -255 | -247 | -578 | -663 | -451 | -584 | -288 |
| | Error | 0 | 1 | 1 | 16 | 2 | 1 | -37 | -37 | -2 | 0 | -5 | 9 | 14 | 6 | 1 | -2 |
| PBE0-D4 | E_{int} | -159 | -227 | -250 | -523 | -246 | -166 | -103 | -126 | -259 | -171 | -167 | -741 | -853 | -536 | -701 | -325 |
| | E_{rlx} | 2 | 1 | 8 | 26 | 3 | 10 | 29 | 9 | 51 | 6 | 39 | 114 | 145 | 46 | 89 | 14 |
| | $E_{\text{ads}}^{\text{approx}}$ | -158 | -226 | -241 | -497 | -243 | -156 | -74 | -117 | -208 | -165 | -128 | -626 | -708 | -491 | -613 | -312 |
| | $E_{\text{ads}}^{\text{true}}$ | -158 | -229 | -234 | -521 | -251 | -160 | -102 | -123 | -192 | -172 | -123 | -574 | -659 | -469 | -576 | -304 |

Continued on next page

TABLE S18: (continued)

| Error | 0 | 4 | -7 | 24 | 8 | 4 | 28 | 6 | -16 | 6 | -5 | -52 | -49 | -22 | -37 | -7 | |
|--------------|----------------------------------|-----|------|------|------|------|------|-----|-----|------|------|------|------|------|------|------|------|
| B3LYP-D2[Ne] | E_{int} | -89 | -127 | -156 | -210 | -168 | -98 | -37 | -66 | -171 | -108 | -100 | -643 | -714 | -427 | -599 | -230 |
| | E_{rlx} | 2 | 1 | 8 | 26 | 3 | 10 | 29 | 9 | 51 | 6 | 39 | 114 | 145 | 46 | 89 | 14 |
| | $E_{\text{ads}}^{\text{approx}}$ | -87 | -126 | -148 | -184 | -164 | -88 | -7 | -57 | -120 | -102 | -61 | -528 | -569 | -382 | -510 | -216 |
| | $E_{\text{ads}}^{\text{true}}$ | -88 | -131 | -149 | -219 | -173 | -101 | -70 | -76 | -136 | -118 | -81 | -505 | -552 | -371 | -492 | -215 |
| | Error | 1 | 5 | 1 | 35 | 8 | 13 | 62 | 18 | 16 | 16 | 20 | -23 | -17 | -11 | -18 | -1 |
| 2RMSE | 19 | 34 | 20 | 100 | 20 | 46 | 91 | 42 | 45 | 25 | 42 | 73 | 85 | 49 | 53 | 30 | |

TABLE S19: For the monomers on the TiO_2 rutile(110) and anatase(101) surfaces, we estimate the errors for using the revPBE-D4 geometry and E_{rlx} in the final E_{ads} of the autoSKZCAM protocol using an ensemble of 6 different DFAs. The errors are calculated as the difference between the true $E_{\text{ads}}^{\text{true}}$ (using the appropriate DFA) and the approximated $E_{\text{ads}}^{\text{approx}}$ using the revPBE-D4 geometry and E_{rlx} .

| | | CH_4 on TiO_2 rutile(110) | Parallel CO_2 on TiO_2 rutile(110) | Tilted CO_2 on TiO_2 rutile(110) | H_2O on TiO_2 rutile(110) | CH_3OH on TiO_2 rutile(110) | H_2O on TiO_2 anatase(101) | NH_3 on TiO_2 anatase(101) |
|-----------|----------------------------------|---------------------------------------------|------------------------------------------------------|----------------------------------------------------|----------------------------------------------------|------------------------------------------------------|-----------------------------------------------------|----------------------------------------------|
| PBE-TS/HI | E_{int} | -283 | -333 | -400 | -1236 | -1560 | -1108 | -1351 |
| | E_{rlx} | 22 | 14 | 50 | 238 | 302 | 225 | 212 |
| | $E_{\text{ads}}^{\text{approx}}$ | -262 | -318 | -350 | -998 | -1258 | -883 | -1138 |
| | $E_{\text{ads}}^{\text{true}}$ | -265 | -329 | -366 | -988 | -1231 | -860 | -1130 |
| | Error | -3 | -11 | -16 | 10 | 27 | 23 | 8 |
| revPBE-D4 | E_{int} | -289 | -402 | -441 | -1214 | -1549 | -1096 | -1382 |
| | E_{rlx} | 22 | 14 | 50 | 238 | 302 | 225 | 212 |
| | $E_{\text{ads}}^{\text{approx}}$ | -268 | -388 | -390 | -976 | -1247 | -871 | -1170 |
| | $E_{\text{ads}}^{\text{true}}$ | -268 | -388 | -390 | -976 | -1247 | -871 | -1170 |
| | Error | 0 | 0 | 0 | 0 | 0 | 0 | 0 |
| vdW-DF | E_{int} | -235 | -366 | -437 | -1080 | -1370 | -969 | -1214 |
| | E_{rlx} | 22 | 14 | 50 | 238 | 302 | 225 | 212 |
| | $E_{\text{ads}}^{\text{approx}}$ | -214 | -352 | -387 | -841 | -1068 | -744 | -1002 |
| | $E_{\text{ads}}^{\text{true}}$ | -244 | -381 | -395 | -849 | -1090 | -759 | -1035 |
| | Error | -30 | -28 | -8 | -8 | -23 | -15 | -33 |

Continued on next page

TABLE S19: (continued)

| | | | | | | | | |
|------------------------|----------------------------------|------|------|------|-------|-------|-------|-------|
| rev-vdW-DF2 | E_{int} | -276 | -409 | -472 | -1300 | -1619 | -1171 | -1410 |
| | E_{rlx} | 22 | 14 | 50 | 238 | 302 | 225 | 212 |
| | $E_{\text{ads}}^{\text{approx}}$ | -255 | -395 | -422 | -1062 | -1317 | -946 | -1198 |
| | $E_{\text{ads}}^{\text{true}}$ | -257 | -402 | -430 | -1050 | -1312 | -933 | -1198 |
| | Error | -2 | -7 | -7 | 12 | 5 | 13 | 0 |
| $r^2\text{SCAN-rVV10}$ | E_{int} | -338 | -533 | -584 | -1501 | -1832 | -1367 | -1577 |
| | E_{rlx} | 22 | 14 | 50 | 238 | 302 | 225 | 212 |
| | $E_{\text{ads}}^{\text{approx}}$ | -316 | -519 | -533 | -1263 | -1529 | -1142 | -1364 |
| | $E_{\text{ads}}^{\text{true}}$ | -325 | -537 | -557 | -1232 | -1491 | -1124 | -1355 |
| | Error | -9 | -18 | -23 | 31 | 39 | 18 | 9 |
| HSE06-D4 | E_{int} | -288 | -406 | -481 | -1368 | -1688 | -1229 | -1518 |
| | E_{rlx} | 22 | 14 | 50 | 238 | 302 | 225 | 212 |
| | $E_{\text{ads}}^{\text{approx}}$ | -267 | -392 | -431 | -1130 | -1386 | -1004 | -1306 |
| | $E_{\text{ads}}^{\text{true}}$ | -272 | -400 | -447 | -1092 | -1333 | -967 | -1284 |
| | Error | -5 | -8 | -16 | 38 | 52 | 36 | 22 |
| 2RMSE | 29 | 33 | 31 | 46 | 66 | 45 | 37 | |

TABLE S20: For the clusters and monolayer systems as well as chemisorbed CO_2 on $\text{MgO}(001)$ surface, we estimate the errors for using the DFT geometry and E_{rlx} in the final E_{ads} of the autoSKZCAM protocol using an ensemble of 6 different DFAs. The errors are calculated as the difference between the true $E_{\text{ads}}^{\text{true}}$ (using the appropriate DFA) and the approximated $E_{\text{ads}}^{\text{approx}}$ using the revPBE-D4 geometry and E_{rlx} . For the NO dimer, this is done with respect to the B3LYP-D2[N2] geometry and E_{rlx} . There is an additional cohesive energy E_{coh} term for the monolayer and cluster systems. For the chemisorbed CO_2 , there is an additional conformational energy E_{conf} term.

| | Monolayer CH_4 | Monolayer C_2H_6 | Dimer NO | Tetramer H_2O | Tetramer CH_3OH | Chemisorbed CO_2 |
|---------------------------------------|-------------------------|----------------------------------|----------|-------------------------------|---------------------------------|---------------------------|
| E_{int} | -114 | -142 | -340 | -397 | -416 | -2993 |
| E_{rlx} | 1 | 4 | 26 | 52 | 68 | 663 |
| E_{coh} or E_{conf} | -40 | -106 | -234 | -309 | -380 | 1841 |
| $E_{\text{ads}}^{\text{approx}}$ | -153 | -245 | -548 | -654 | -729 | -489 |
| $E_{\text{ads}}^{\text{true}}$ | -153 | -248 | -551 | -660 | -733 | -518 |
| Error | 0 | -3 | -3 | -6 | -5 | -29 |

Continued on next page

TABLE S20: (continued)

| | | | | | | | |
|--------------|---------------------------------------|------|------|------|------|------|-------|
| revPBE-D4 | E_{int} | -142 | -207 | -351 | -404 | -483 | -2981 |
| | E_{rlx} | 1 | 4 | 26 | 52 | 68 | 663 |
| | E_{coh} or E_{conf} | -31 | -48 | -186 | -261 | -328 | 1797 |
| | $E_{\text{ads}}^{\text{approx}}$ | -171 | -251 | -511 | -613 | -743 | -521 |
| | $E_{\text{ads}}^{\text{true}}$ | -171 | -251 | -514 | -613 | -743 | -521 |
| | Error | 0 | 0 | -3 | 0 | 0 | 0 |
| vdW-DF | E_{int} | -136 | -200 | -337 | -376 | -447 | -2638 |
| | E_{rlx} | 1 | 4 | 26 | 52 | 68 | 663 |
| | E_{coh} or E_{conf} | -58 | -67 | -145 | -240 | -291 | 1763 |
| | $E_{\text{ads}}^{\text{approx}}$ | -192 | -263 | -457 | -564 | -670 | -212 |
| | $E_{\text{ads}}^{\text{true}}$ | -219 | -319 | -478 | -597 | -719 | -361 |
| | Error | -27 | -55 | -21 | -33 | -48 | -149 |
| rev-vdW-DF2 | E_{int} | -140 | -197 | -398 | -452 | -519 | -3082 |
| | E_{rlx} | 1 | 4 | 26 | 52 | 68 | 663 |
| | E_{coh} or E_{conf} | -43 | -83 | -276 | -289 | -357 | 1836 |
| | $E_{\text{ads}}^{\text{approx}}$ | -181 | -277 | -648 | -689 | -809 | -583 |
| | $E_{\text{ads}}^{\text{true}}$ | -182 | -282 | -654 | -693 | -811 | -605 |
| | Error | -1 | -5 | -5 | -4 | -2 | -21 |
| PBE0-D4 | E_{int} | -158 | -211 | -290 | -465 | -526 | -3713 |
| | E_{rlx} | 1 | 4 | 26 | 52 | 68 | 663 |
| | E_{coh} or E_{conf} | -34 | -64 | 62 | -302 | -367 | 2153 |
| | $E_{\text{ads}}^{\text{approx}}$ | -191 | -271 | -202 | -715 | -825 | -898 |
| | $E_{\text{ads}}^{\text{true}}$ | -193 | -274 | -219 | -692 | -795 | -764 |
| | Error | -3 | -2 | -17 | 23 | 30 | 134 |
| B3LYP-D2[Ne] | E_{int} | -87 | -111 | -231 | -400 | -429 | -3250 |
| | E_{rlx} | 1 | 4 | 26 | 52 | 68 | 663 |
| | E_{coh} or E_{conf} | -37 | -124 | 63 | -303 | -371 | 2075 |
| | $E_{\text{ads}}^{\text{approx}}$ | -124 | -231 | -143 | -651 | -732 | -512 |
| | $E_{\text{ads}}^{\text{true}}$ | -127 | -238 | -143 | -643 | -717 | -460 |
| | Error | -4 | -7 | 0 | 8 | 16 | 52 |
| 2RMSE | | 25 | 50 | 25 | 38 | 53 | 188 |

In general, we find that ϵ_{geom} is relatively small, being less than 40 meV for the majority of systems. For the monomers on MgO, the ϵ_{geom} range is between 20–100 meV, while this error range lowers to 29–66 meV for the TiO₂ surfaces. We find that this geometrical error is particularly dependent on the strength of the binding, going from 20 meV for CO on MgO - a system with weak

physisorption to 66 meV for CH₃OH on TiO₂ rutile(110), a system with much stronger adsorption behaviour. In particular, the largest error is found for the chemisorbed CO₂ system with a value of 188 meV, arising from the large change to the surface and molecule electronic structure and geometry due to charge transfer.

S8.4. Zero-point vibrational and enthalpic contributions

The DFT ensemble was also used to calculate the zero-point vibrational E_{ZPV} and thermal E_T contributions to the adsorption enthalpy H_{ads} . As both E_{ZPV} and E_T can be computed from vibrational modes, we will particular discuss overall enthalpic contributions: $\Delta H = E_{ZPV} + E_T - RT$, to add onto E_{ads} to make H_{ads} . We utilised the rigid-rotor quasi-harmonic approximation (quasi-RRHO) to compute these terms based on the vibrational frequencies computed by DFT. These were first proposed by Grimme *et al.* [308] for entropies and then adapted for enthalpies by Li *et al.* [309]. Within the simple rigid-rotor harmonic oscillator (RRHO) models, the contribution of each vibrational mode i with frequency ν_i contributes $V_i^{RRHO} = \frac{1}{2}h\nu_i + \frac{h\nu_i}{1+e^{h\nu_i/k_B T}}$ to ΔH (including the contribution to E_{ZPV} in the first term and E_T in the second term). One deficiency of this model is that it is wrong for the zero-frequency (translation + rotation) modes as it predicts a $k_B T$ contribution to ΔH rather than $\frac{1}{2}k_B T$. The quasi-RRHO fixes this issue by creating an interpolation between the RRHO model and the free rotor model (whereby each mode contributes $\frac{1}{2}k_B T$) at low frequencies:

$$V_i^{\text{quasi-RRHO}} = \omega(\nu_i) \times V_i^{\text{RRHO}} + (1 - \omega(\nu_i)) \times \frac{1}{2}k_B T, \quad (7)$$

$$\omega(\nu_i) = \frac{1}{1 + (\nu_0/\nu_i)^4} \quad (8)$$

where we have set the interpolation to start at around $\nu_0 = 100 \text{ cm}^{-1}$.

We have calculated the vibrational frequencies of the molecule (both on the surface and in the gas-phase) to calculate the ΔH contribution to H_{ads} . This is shown in Table S21, where we have computed E_{ZPV} , E_T and ΔH using four DFAs from the ensemble. For the MgO surface, the four DFAs were: XC 1 = PBE-D2[Ne], XC 2 = revPBE-D4, XC 3 = vdW-DF, XC 4 = rev-vdW-DF2. For the TiO₂ surfaces, the DFAs selected were: XC 1 = PBE-TS/HI, XC 2 = revPBE-D4, XC 3 = vdW-DF, XC 4 = rev-vdW-DF2. The final ΔH contribution was taken to be the average of the four functionals with the error estimated to be the 2σ standard deviation of the four estimates to ensure 95% confidence interval in the estimate. It can be seen that the ΔH contribution, relative

TABLE S21. The zero-point vibrational energy (E_{ZPV}), thermal energy (E_{therm}), and overall enthalpy (ΔH) contributions (in meV) to the adsorption enthalpy for all studied systems using an ensemble of 4 different DFAs. The errors are calculated as the 2σ standard deviation of the ΔH values for the 4 DFAs.

| | | | | | | | | | | | | | | | | | | | | | | | | | | | | | |
|-------------------|----|----|----|----|-----|-----|----|----|----|----|----|----|----|-----|-----|-----|-----|-----|-----|-----|-----|----|-----|-----|-----|-----|-----|-----|-----|
| Temperature [K] | 47 | 47 | 75 | 61 | 162 | 77 | 80 | 80 | 80 | 80 | 80 | 80 | 80 | 203 | 235 | 286 | 286 | 286 | 160 | 120 | 230 | 85 | 177 | 177 | 303 | 370 | 257 | 410 | |
| RT [meV] | 4 | 4 | 6 | 5 | 14 | 7 | 7 | 7 | 7 | 7 | 7 | 7 | 7 | 17 | 20 | 25 | 25 | 25 | 14 | 10 | 20 | 7 | 15 | 15 | 26 | 32 | 22 | 35 | |
| E_{ZPV} [XC 1] | 29 | 29 | 12 | 17 | 31 | 1 | 3 | 18 | 13 | 23 | 11 | 10 | 63 | 84 | 98 | 36 | 22 | 61 | 72 | 2 | 47 | 17 | 7 | 9 | 110 | 68 | 113 | 111 | |
| E_T [XC 1] | -5 | -5 | -2 | -4 | -6 | 2 | -1 | 0 | -5 | -3 | -6 | -3 | -4 | -10 | -22 | -19 | 3 | 1 | 1 | -13 | 0 | -8 | -3 | 3 | 3 | -18 | 10 | -18 | -2 |
| ΔH [XC 1] | 20 | 20 | 3 | 7 | 20 | -12 | -6 | -4 | 7 | 3 | 10 | 1 | 0 | 47 | 45 | 58 | 14 | -1 | 38 | 46 | -8 | 19 | 6 | -5 | -3 | 66 | 46 | 73 | 74 |
| E_{ZPV} [XC 2] | 23 | 28 | 13 | 37 | 28 | 9 | 2 | 6 | 22 | 14 | 26 | 13 | 11 | 64 | 85 | 100 | 38 | 24 | 63 | 72 | 1 | 47 | 25 | 9 | 12 | 111 | 74 | 112 | 115 |
| E_T [XC 2] | -4 | -5 | -2 | -5 | -5 | 2 | -1 | -1 | -5 | -4 | -6 | -3 | -4 | -10 | -21 | -19 | 3 | 1 | 1 | -12 | 0 | -8 | -4 | 3 | 3 | -15 | 9 | -15 | 1 |
| ΔH [XC 2] | 15 | 20 | 4 | 26 | 18 | -3 | -5 | -2 | 10 | 4 | 12 | 3 | 0 | 47 | 47 | 61 | 17 | 0 | 39 | 46 | -9 | 19 | 13 | -3 | 0 | 69 | 51 | 75 | 80 |
| E_{ZPV} [XC 3] | 10 | 10 | 0 | 28 | 28 | -1 | 0 | 12 | 10 | 18 | 9 | 7 | 58 | 84 | 97 | 41 | 24 | 62 | 69 | -2 | 44 | 6 | 5 | 7 | 96 | 71 | 90 | 105 | |
| E_T [XC 3] | -2 | -2 | 0 | -5 | -5 | 2 | 0 | 0 | -3 | -3 | -5 | -2 | -3 | -9 | -18 | -16 | 5 | 1 | 5 | -12 | 1 | -8 | -1 | 3 | 3 | -7 | 13 | -9 | 3 |
| ΔH [XC 3] | 3 | 4 | -7 | 17 | 17 | -14 | -7 | -7 | 2 | 0 | 6 | 0 | -3 | 42 | 48 | 60 | 21 | 1 | 43 | 43 | -11 | 16 | -3 | -7 | -5 | 63 | 52 | 59 | 72 |
| E_{ZPV} [XC 4] | 15 | 17 | 4 | 22 | 32 | -1 | 1 | 4 | 19 | 14 | 25 | 12 | 10 | 65 | 85 | 100 | 37 | 21 | 61 | 68 | 0 | 48 | 19 | 11 | 13 | 108 | 67 | 107 | 107 |
| E_T [XC 4] | -4 | -4 | -1 | -5 | -6 | 2 | -1 | 0 | -5 | -4 | -6 | -3 | -4 | -10 | -21 | -20 | 3 | 1 | 0 | -13 | 0 | -9 | -5 | 3 | 3 | -17 | 9 | -15 | 0 |
| ΔH [XC 4] | 8 | 8 | -4 | 10 | 21 | -13 | -6 | -3 | 7 | 4 | 12 | 2 | 0 | 48 | 46 | 60 | 15 | -3 | 37 | 42 | -10 | 19 | 7 | -2 | 0 | 64 | 44 | 70 | 71 |
| Final ΔH | 11 | 13 | -1 | 15 | 19 | -10 | -6 | -4 | 7 | 2 | 10 | 1 | -1 | 46 | 47 | 60 | 17 | -1 | 39 | 44 | -10 | 18 | 6 | -4 | -2 | 65 | 48 | 69 | 75 |
| Error | 13 | 14 | 10 | 14 | 3 | 9 | 1 | 4 | 6 | 3 | 5 | 3 | 3 | 5 | 3 | 2 | 6 | 3 | 5 | 3 | 2 | 2 | 11 | 4 | 4 | 5 | 7 | 13 | 7 |

TABLE S22. Comparing the effect of only the molecule vibrational degrees of freedom and the inclusion of surface degrees of freedom on the enthalpy (ΔH) contribution (in meV) to the adsorption enthalpy for a select few molecules adsorbed on MgO(001). ΔH is calculated as the mean from an ensemble of 4 DFAs (neglecting the hybrid DFAs) with 2σ error included.

| | CO | H ₂ O Monomer | CO ₂ Physisorbed | CO ₂ Chemisorbed |
|------------------|--------|--------------------------|-----------------------------|-----------------------------|
| Molecule | 19 ± 6 | 47 ± 5 | -10 ± 5 | 18 ± 5 |
| Molecule+Surface | 19 ± 1 | 48 ± 5 | -8 ± 2 | 31 ± 3 |

to E_{ads} is overall small to H_{ads} , ranging from -10 to 75 meV. Moreover the error estimates are also small, ranging from 1 to 15 meV.

We expect nuclear quantum [310] contributions to ΔH to be small while anharmonic effects can have a potential effect for weakly binding molecules such as CH₄ on MgO(001) [311]. This effect is well-captured by the error bar, where CH₄ on MgO(001) gives a larger error bar on ΔH than the stronger binding systems. Another source of error is the freezing of surface vibrational modes when calculating ΔH . In Table S22, we have calculated ΔH for a select number of systems which include the surface degrees of freedom in the top two layers of MgO(001). Overall, there is negligible change of maximum 2 meV for the majority of systems. The only system where there is a significant effect is for chemisorbed CO₂ where it changes from 18 ± 5 meV to 31 ± 5 meV, due to changes in the surface electronic structure from charge transfer. In our final H_{ads} analysis, we will include the surface degrees of freedom for CO₂ on MgO(001) only, while neglecting it for all other systems.

S8.5. Dissociation energy for the H₂O and CH₃OH clusters

As discussed in Sec. S1.1, we use the autoSKZCAM framework to obtain the adsorption enthalpy for a molecularly adsorbed (tetramer) cluster of CH₃OH and H₂O. The lowest energy geometry involves partial dissociation of the CH₃OH and H₂O clusters. In our final H_{ads} for these two systems, we compute an additional term E_{diss} which accounts for the (electronic) energetic stabilisation to form the partially dissociated cluster. This is performed using the DFT ensem-

TABLE S23. The dissociation energy E_{diss} (in meV) for the CH₃OH and H₂O tetramer calculated for the DFT ensemble. This is defined as the energy difference between the dissociated and molecular configurations of the tetramer.

| | CH ₃ OH Tetramer | H ₂ O Tetramer |
|--------------|-----------------------------|---------------------------|
| PBE-D2[Ne] | -76 | -89 |
| revPBE-D4 | -78 | -81 |
| vdW-DF | -48 | -52 |
| rev-vdW-DF2 | -65 | -75 |
| PBE0-D4 | -80 | -83 |
| B3LYP-D2[Ne] | -81 | -98 |
| Average | -71 | -80 |
| Error | 24 | 29 |
| Final | -71 ± 24 | -79 ± 29 |

ble – using the revPBE-D4 geometry – shown in Table S23 for the 6 DFAs, where we obtain an average and calculate the error as the 2σ standard deviation. We have also computed the enthalpic difference (-31 meV and -18 meV for H₂O and CH₃OH) between the dissociated and molecular configurations (with geometries taken from revPBE-D4) and added this contribution to the original ΔH calculated for the molecular configuration in Table S21; this leads to a final ΔH of 42 ± 2 meV and 8 ± 5 meV for the dissociated configuration of H₂O and CH₃OH respectively, as shown in Table S24.

S9. FINAL AUTOSKZCAM ESTIMATES

In Table S24, we show the terms which make up the final E_{ads} and H_{ads} estimates in our autoSKZCAM framework. Robust error bars have been estimated which aim to encapsulate the major sources of errors (to at least a 95% confidence interval) within this estimate with respect to a fully converged CCSD(T) estimate. The $E_{\text{int}}^{\text{SKZCAM}}$ error estimate covers the potential finite-size errors from utilising the SKZCAM protocol in Sec. S6, while ϵ_{geom} (discussed in Sec. S8) covers the error from computing $E_{\text{rlx}}^{\text{DFT}}$ with DFT and the error from using a DFT geometry in all the individual terms of E_{ads} . We reach a final error estimate as the root squared sum of the errors within the individual terms. As seen in Table S24, ϵ_{geom} is in general the largest source of error out of all of the terms and serves as the major term to target for future improvements.

TABLE S24. A summary of the terms which make up the final autoSKZCAM E_{ads} and H_{ads} estimate (in meV). Here, the final E_{ads} value is the sum of $E_{\text{int}}^{\text{SKZCAM}}$, $E_{\text{rlx}}^{\text{DFT}}$, $E_{\text{coh}}^{\text{CCSD(T)}}$ and $E_{\text{conf}}^{\text{CCSD(T)}}$ values, where the last two terms are only included for systems where they are calculated in Sec. S7. The errors due to $E_{\text{rlx}}^{\text{DFT}}$ and from using the revPBE-D4 geometry for all the E_{ads} terms is encapsulated in ϵ_{geom} from an ensemble of DFAs. An additional ΔH term is also calculated, further calculated from a DFT ensemble.

| | $E_{\text{int}}^{\text{SKZCAM}}$ | $E_{\text{rlx}}^{\text{DFT}}$ | $E_{\text{coh}}^{\text{CCSD(T)}}$ | $E_{\text{conf}}^{\text{CCSD(T)}}$ | ϵ_{geom} | $E_{\text{diss.}}^{\text{DFT}}$ | $E_{\text{ads}}^{\text{autoSKZCAM}}$ | ΔH^{DFT} | $H_{\text{ads}}^{\text{autoSKZCAM}}$ |
|----------------------------------------------------------|----------------------------------|-------------------------------|-----------------------------------|------------------------------------|--------------------------|---------------------------------|--------------------------------------|-------------------------|--------------------------------------|
| CH ₄ on MgO(001) | -122 ± 2 | 2 | - | - | 19 | - | -120 ± 19 | 11 ± 13 | -109 ± 23 |
| Monolayer CH ₄ on MgO(001) | -121 ± 3 | 1 | -25 | - | 25 | - | -145 ± 25 | 13 ± 14 | -132 ± 28 |
| C ₂ H ₆ on MgO(001) | -175 ± 4 | 1 | - | - | 34 | - | -174 ± 34 | -1 ± 10 | -175 ± 35 |
| Monolayer C ₂ H ₆ on MgO(001) | -161 ± 3 | 4 | -61 | - | 50 | - | -218 ± 50 | 15 ± 14 | -203 ± 52 |
| CO on MgO(001) | -207 ± 4 | 8 | - | - | 20 | - | -198 ± 20 | 19 ± 3 | -180 ± 20 |
| C ₆ H ₆ on MgO(001) | -446 ± 9 | 26 | - | - | 100 | - | -420 ± 100 | -10 ± 9 | -430 ± 100 |
| Parallel N ₂ O on MgO(001) | -256 ± 3 | 3 | - | - | 20 | - | -253 ± 20 | -6 ± 1 | -259 ± 20 |
| Tilted N ₂ O on MgO(001) | -168 ± 4 | 10 | - | - | 46 | - | -157 ± 46 | -4 ± 4 | -161 ± 47 |
| Vertical-Hollow NO on MgO(001) | 32 ± 4 | 29 | - | - | 91 | - | 61 ± 91 | 7 ± 6 | 68 ± 91 |
| Vertical-Mg NO on MgO(001) | -62 ± 5 | 9 | - | - | 42 | - | -53 ± 42 | 2 ± 3 | -50 ± 42 |
| Bent-Bridge NO on MgO(001) | -62 ± 8 | 51 | - | - | 45 | - | -10 ± 45 | 10 ± 5 | 0 ± 46 |
| Bent-Mg NO on MgO(001) | -126 ± 5 | 6 | - | - | 25 | - | -120 ± 26 | 1 ± 3 | -119 ± 26 |
| Bent-O NO on MgO(001) | -3 ± 7 | 39 | - | - | 42 | - | 36 ± 43 | -1 ± 3 | 35 ± 43 |
| Dimer NO on MgO(001) | -246 ± 3 | 42 | -75 | - | 59 | - | -278 ± 59 | 46 ± 5 | -232 ± 59 |
| Monomer H ₂ O on MgO(001) | -703 ± 4 | 114 | - | - | 73 | - | -588 ± 73 | 47 ± 3 | -542 ± 73 |
| Dissociated Tetramer H ₂ O on MgO(001) | -463 ± 7 | 52 | -281 | - | 38 | -80 ± 29 | -772 ± 48 | 42 ± 2 | -730 ± 48 |
| Tilted CH ₃ OH on MgO(001) | -787 ± 5 | 145 | - | - | 85 | - | -642 ± 86 | 17 ± 6 | -625 ± 86 |
| Parallel CH ₃ OH on MgO(001) | -506 ± 1 | 46 | - | - | 49 | - | -461 ± 49 | -1 ± 3 | -461 ± 49 |
| Dissociated Tetramer CH ₃ OH on MgO(001) | -511 ± 6 | 68 | -336 | - | 53 | -71 ± 24 | -851 ± 59 | 8 ± 5 | -843 ± 59 |
| NH ₃ on MgO(001) | -657 ± 9 | 89 | - | - | 53 | - | -568 ± 53 | 44 ± 3 | -524 ± 54 |
| Physisorbed CO ₂ on MgO(001) | -308 ± 2 | 14 | - | - | 30 | - | -294 ± 30 | -10 ± 2 | -304 ± 30 |
| Chemisorbed CO ₂ on MgO(001) | -3504 ± 32 | 663 | - | 2094 | 188 | - | -747 ± 191 | 18 ± 2 | -729 ± 191 |
| CH ₄ on TiO ₂ rutile(110) | -269 ± 2 | 22 | - | - | 29 | - | -247 ± 29 | 6 ± 11 | -241 ± 31 |
| Parallel CO ₂ on TiO ₂ rutile(110) | -410 ± 5 | 14 | - | - | 33 | - | -396 ± 33 | -4 ± 4 | -400 ± 34 |
| Tilted CO ₂ on TiO ₂ rutile(110) | -493 ± 7 | 50 | - | - | 31 | - | -442 ± 31 | -2 ± 4 | -445 ± 32 |
| H ₂ O on TiO ₂ rutile(110) | -1310 ± 33 | 238 | - | - | 46 | - | -1072 ± 57 | 65 ± 5 | -1007 ± 57 |
| CH ₃ OH on TiO ₂ rutile(110) | -1634 ± 37 | 302 | - | - | 66 | - | -1332 ± 76 | 48 ± 7 | -1284 ± 76 |
| H ₂ O on TiO ₂ anatase(101) | -1208 ± 16 | 225 | - | - | 45 | - | -983 ± 48 | 69 ± 13 | -913 ± 50 |
| NH ₃ on TiO ₂ anatase(101) | -1377 ± 18 | 212 | - | - | 37 | - | -1165 ± 41 | 75 ± 7 | -1090 ± 42 |

S9.1. Validating autoSKZCAM error estimates

Besides being accurate and low-cost, one of the highlights of the autoSKZCAM framework are the additional steps we have taken to quantify the major error contributions to the final H_{ads} estimate. In this section, we highlight the effectiveness of our chosen procedure for estimating errors, using the chemisorbed CO_2 on $\text{MgO}(001)$ as an example due to the relatively large estimated error bars for this system. As seen in Table S24, the major source of error comes from ϵ_{geom} – the error for utilising DFT to generate the geometry to calculate the adsorption energy E_{ads} , encapsulating the interaction energy E_{int} , relaxation energy E_{rlx} and additional terms (e.g., E_{coh} and E_{conf}). To understand how well our error estimates cover the errors from utilising DFT to generate the geometry, we have calculated H_{ads} with the autoSKZCAM framework using the geometries from the 6 different density functional approximations in the DFT ensemble in Table S25. Our final H_{ads} estimate (in Table S24) of -729 ± 191 meV covers a range from -538 ,meV to -920 meV. The actual range of values for using the six different DFAs goes from -599 meV for PBE0-D4 to -840 ,meV for vdW-DF. There is overall a faithful (and conservative) representation of the range of possible values of H_{ads} in Table S25, with no values lying outside this error bar.

TABLE S25. Final H_{ads} (in meV) for CO_2 chemisorbed on MgO using various DFAs as the geometry within the subsequent autoSKZCAM framework treatment. The final H_{ads} is the sum of $E_{\text{int}}^{\text{MP2,bulk}}$, Δ_{CC} , Δ_{basis} , $E_{\text{rlx}}^{\text{DFT}}$, $E_{\text{conf}}^{\text{CCSD(T)}}$ and ΔH^{DFT} terms as described in Sec. S8.

| | $E_{\text{int}}^{\text{MP2,bulk}}$ | Δ_{CC} | Δ_{basis} | $E_{\text{rlx}}^{\text{DFT}}$ | $E_{\text{conf}}^{\text{CCSD(T)}}$ | ΔH^{DFT} | $H_{\text{ads}}^{\text{final}}$ |
|--------------|------------------------------------|----------------------|-------------------------|-------------------------------|------------------------------------|-------------------------|---------------------------------|
| PBE-D2[Ne] | -3358 | -225 | 24 | 693 | 2085 | 18 | -763 |
| revPBE-D4 | -3309 | -220 | 25 | 663 | 2094 | 18 | -729 |
| vdW-DF | -3457 | -228 | 23 | 704 | 2100 | 18 | -840 |
| rev-vdW-DF2 | -3296 | -223 | 24 | 676 | 2055 | 18 | -746 |
| PBE0-D4 | -3223 | -224 | 24 | 773 | 2033 | 18 | -599 |
| B3LYP-D2[Ne] | -3338 | -227 | 24 | 810 | 2029 | 18 | -685 |

S10. AUTOMATION OF THE AUTOSKZCAM FRAMEWORK

The autoSKZCAM framework is freely available and open-source on Github (to be shared upon acceptance of the manuscript). We have developed a set of functions that automates the entire SKZCAM protocol to generate the clusters and inputs to obtain an accurate interaction energy E_{int} . The remaining contributions to the adsorption enthalpy is calculated with the DFT ensemble and this can involve a significant number of calculations/book-keeping. We make extensive use of the QuAcc computational materials science workflow library [312] to manage these calculations. All of this can be achieved within a single Jupyter Notebook, requiring very little user intervention.

S10.1. QuAcc computational workflow details

The QuAcc workflow library contains (user-defined) ‘recipes’ that represent specific tasks (i.e., calculating the static energy or performing a geometry optimisation) and ‘flows’ which represent workflows that combine these recipes to e.g., generate slabs from the bulk or make an adsorbed surface geometry. This allows for a seamless process to study surfaces that can be efficiently dispatched to any computing environment. We make use of many of the pre-existing recipes and flows within QuAcc and as part of this work, we have also developed new recipes and flows to enable calculations using a DFT ensemble (or arbitrary number of DFAs).

In the left panel of Fig. S15, we highlight the processes executed within QuAcc to calculate the DFT ensemble contributions to H_{ads} . Starting from a unit cell, the `bulk_to_slab_flow` will generate the necessary surface termination and relax the surface to its equilibrium geometry. Subsequently, the adsorbate is added onto the surface within the `slab_to_ads_flow` to generate the relaxed adsorbate–surface complex. Currently the flow accepts placing the adsorbates on the “on-top”, “bridge”, “hollow” and “subsurface” sites if the position of the molecule is known or expected to follow chemical intuition. We also provide a short function to perform random structure search to produce starting geometries that can be relaxed to identify unbiased low-energy adsorbate–surface adsorption configurations.

From the candidate adsorbate–surface structure(s), the QuAcc workflow will then submit a series of `static_job` calculations which aims to calculate E_{ads} , E_{int} and E_{rlx} across the ensemble of DFAs. In particular, it will calculate both $E_{\text{ads}}^{\text{true}}$ and $E_{\text{ads}}^{\text{approx}}$ (see Section S8) to estimate the error with using a DFT geometry for E_{ads} . Subsequently the vibrational frequencies of the molecule

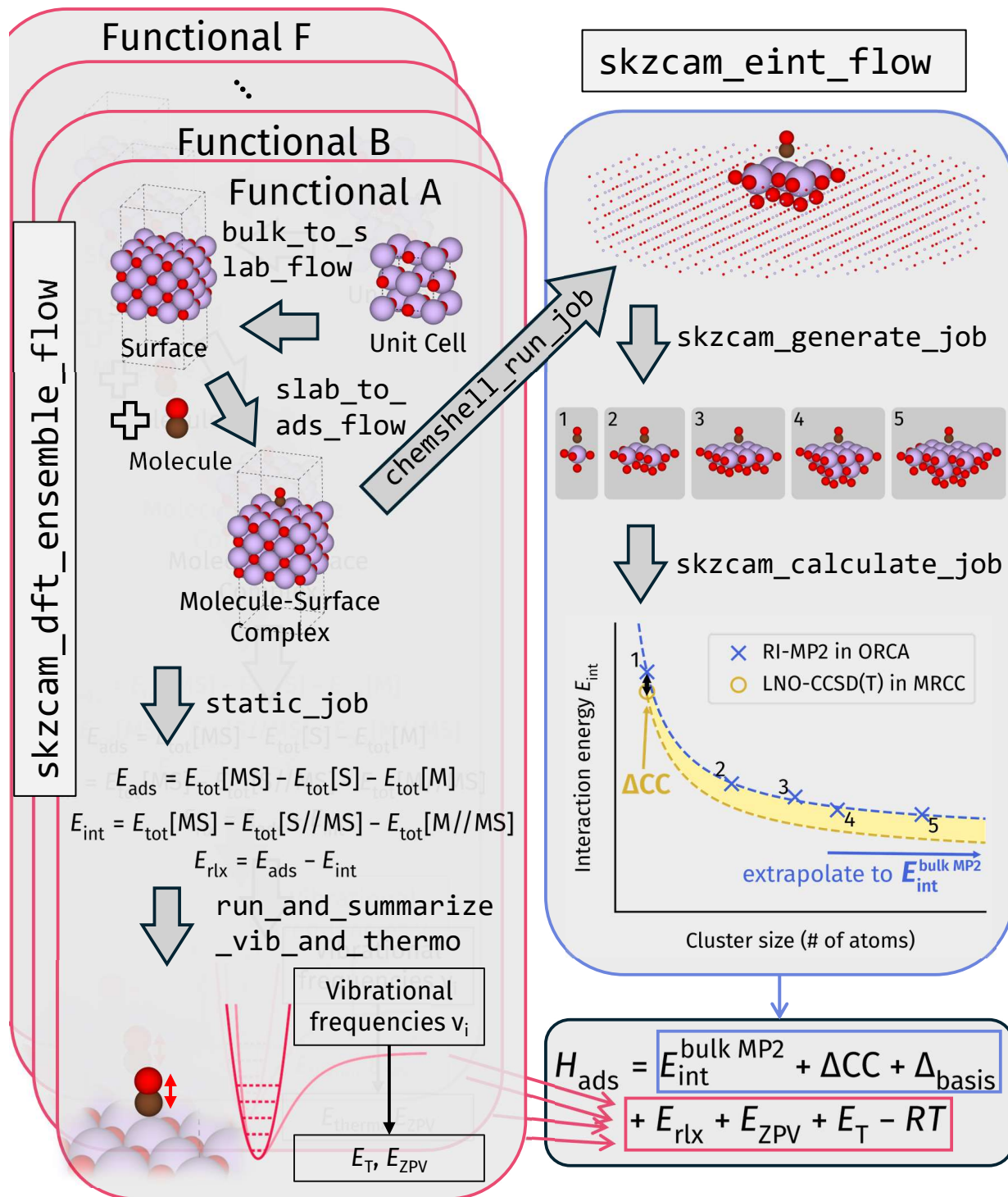


FIG. S15. The computational workflow for reaching an accurate and low-cost H_{ads} using the autoSKZ-CAM framework. It makes heavy use of the QuAcc computational materials science workflow library [312]. We make use of pre-existing ‘flows’ to generate the adsorbate–surface complex for the density functional approximations within the DFT ensemble and to subsequently calculate E_{ads} , E_{int} and E_{rlx} as well as E_{ZPV} and E_T . We have developed new Python modules to generate the series of clusters and inputs necessary to calculate a CCSD(T)-quality E_{int} with the SKZCAM protocol. The inputs can be either submitted directly on a computing cluster or managed through QuAcc. These terms are all combined to reach the final H_{ads} estimate.

(on the surface and in the gas-phase) are calculated in order to determine E_{ZPV} and E_T across the DFT ensemble.

S10.2. Automated SKZCAM protocol

One of the key developments within the present work is the automatization of the SKZCAM protocol, which significantly lowers its cost and requires almost no user intervention to operate. From an adsorbate-surface structure, either generated by the one of the DFAs in the DFT ensemble or taken from the literature, it will generate all of the inputs necessary to come to a final estimate of the E_{int} , with the choice of several (ONIOM) embedding layers within an intuitive interface.

We have developed a set of Python modules which runs through the key steps of the SKZCAM protocol. Firstly, it interfaces with the py-ChemShell [280] program to generate the necessary point charge environment using the `chemshell_run_job`. The generate output (a `pun` file) is then read and used to generate the set of embedded clusters with `skzcam_calculate_job`. This will generate the appropriate set of inputs (for the different levels of theory, basis set sizes and frozen core treatments, described in Sec. S6) that define all the individual calculations that need to be performed. At present, these inputs can be generated for either ORCA [261] or MRCC [262]. The inputs can be copied to the computing cluster of choice for the calculations to be performed. Alternatively, one can make use of the QuAcc computational workflow library to directly manage and submit the jobs. Once the MP2 and CCSD(T) calculations are complete, we provide analysis scripts to calculate the MP2 bulk limit $E_{\text{int}}^{\text{bulk MP2}}$, Δ_{CC} contribution and further contributions for basis set Δ_{basis} and core contributions Δ_{core} .

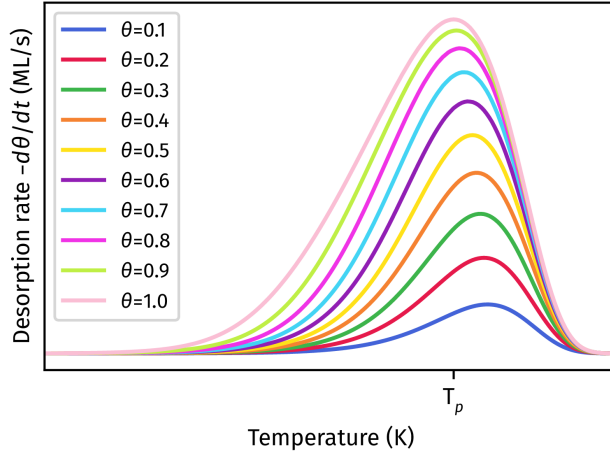


FIG. S16. A schematic of a typical temperature programmed desorption spectra as a function of concentration θ . Created with tools provided within Ref. 314.

S11. ANALYSING EXPERIMENTAL ESTIMATES AND TECHNIQUES

Experimental techniques can obtain the adsorption enthalpy H_{ads} through methods such as single crystal adsorption calorimetry (SCAC), equilibrium adsorption isotherms (EAI) and temperature programmed desorption (TPD) experiments [258, 313]. SCAC are considered to provide the most reliable measurements of H_{ads} while EAI provides a straightforward means for measuring this quantity for reversible adsorption-desorption experiments using the Clausius-Clapeyron expression. Despite requiring more analysis than the other two methods, TPD experiments are by far the most common technique for measuring H_{ads} for metal-oxide surfaces [258] due to the simplicity and ready availability of TPD equipment.

In TPD experiments, the surface with preadsorbed molecules is heated at a constant heating rate. The rate of appearance of the gas desorbing from the surface is then monitored using a mass spectrometer. The desorption rate is measured as a function of the temperature to create plots such as shown in Fig. S16. The central equation for first order desorption TPD spectra is an Arrhenius type relationship which relates the desorption rate $-\frac{d\theta}{dt}$ to the activation energy E_d for desorption:

$$-\frac{d\theta}{dt} = \nu\theta \exp\left(-\frac{E_d}{RT_p}\right), \quad (9)$$

where ν is the pre-exponential factor, θ is the concentration and T_p is the temperature where the desorption rate is a maximum. One can then obtain E_d by inverting this first-order Wigner-Polanyi

equation:

$$E_d(\theta) = -RT_p \ln\left(-\frac{d\theta}{dt}/(\nu\theta)\right). \quad (10)$$

From TPD curves plotted at various surface concentrations, the value of E_d and ν can also be obtained by finding the best fit to simulated TPDs. The errors on $\log(\nu)$ with this approach can be of the order of ± 2 [315].

The simplest method to determine E_d is through the Redhead equation [316], which relates the heating rate β and T_p to E_d by the following equation:

$$\frac{E_d}{RT_p^2} = \left(\frac{\nu}{\beta}\right) \exp\left(-\frac{E_d}{RT_p}\right), \quad (11)$$

Here, T_p and β are known but ν is normally estimated to be 10^{13} . Rearranging the equation and taking an empirical linear relationship between E_d and T_p gives the following relationship:

$$E_d = RT_p \ln\left(\frac{\nu T_p}{\beta} - 3.64\right). \quad (12)$$

Thus, a ten order of magnitude change in ν is expected to change E_d by $\sim \ln(10)RT_p = 2.3RT_p$.

When matching experiments with theory, there can be three sources of discrepancy. The major source of error arises in the prescribed value of ν in the determination of E_d from the TPD spectra. This is not known but it can span between $\log(\nu) = 12$ and $\log(\nu) = 19$ [317] and most experiments will simply set $\log(\nu) = 13$, which can introduce large errors. Recently, Sellers and Campbell [317] have demonstrated a relationship between the entropy of the gas when adsorbed on a surface and in the gas phase, which has allowed for predictions of $\log(\nu)$ to a 2σ standard deviation of ~ 1.72 . The majority of experiments are taken from Campbell and Sellers [258], with H_{ads} using the predicted values of ν . We perform re-analysis of E_d with the predicted ν for systems not included within their work, indicated by systems where $\log(\nu) = 13.0 \rightarrow \dots$ in Table S26. Second, there is also an error in E_d as it is not directly equal to H_{ads} . E_d is an activation energy, but its relationship to H_{ads} has differed between different studies. For example, the collection of experimental estimates [242, 253, 318, 319] re-analysed by Sauer and co-workers has used the relationship:

$$H_{\text{ads}} = -E_d + RT_p, \quad (13)$$

to compare to experiments, following on the approximate relation between the enthalpy and activation energy of reaction barriers [320]. On the other hand, the collection of work by Campbell [258, 321] and co-workers as well as others [322] have used the relationship:

$$H_{\text{ads}} = -E_d - \frac{1}{2}RT_p, \quad (14)$$

which was derived from relating the isosteric heat of adsorption (the negative of H_{ads}) from SCAC experiments to E_{d} in Ref. 323. In this work we opt to set H_{ads} to $-E_{\text{d}}$, and add an RT_p error contribution to account for the two potential directions which H_{ads} can point to with respect to E_{d} . The final source of error arises in differences in the concentration between simulation and experiment. For most work, for example from the re-analysis by Campbell and Sellers, a concentration dependence of E_{d} is provided and we opt to take the smallest concentration for the adsorption of monomers, while we take the highest concentration for the monolayers. For the clusters, we aim to take the average of the low and high concentration. We add the error bars as half the difference between the low and high concentration for the clusters. At the end, the final estimate of H_{ads} will have its error be the root squared sum of these three sources of errors.

TABLE S26. Experimental adsorption enthalpies (in meV) for the systems studied within this work.

| Surface | Adsorbate | Temperature | $\log(\nu)$ | H_{ads} (meV) | Error | Details |
|-------------------------------|-----------------------------------------|-------------|-------------------|------------------------|-------|--------------------------------------------------------------------------------------------------------------------------------------------------------------------------------------------------------------------------------------------------------------|
| MgO(001) | CH ₄ | 47 | 13.1 ± 2.0 | -115 | 19 | Dilute limit E_d estimate by Tait <i>et al.</i> [324, 325]. |
| MgO(001) | C ₂ H ₆ | 75 | 14.9 ± 2.0 | -221 | 30 | Dilute limit E_d estimate by Tait <i>et al.</i> [324, 325]. |
| MgO(001) | CO | 61 | 13.8 ± 1.6 | -176 | 21 | Average of the H_{ads} re-analysis by C&S for Refs. 315 and 223 at low coverage, with 0.5RT removed. |
| MgO(001) | N ₂ O | 77 | 13.0 → 14.0 ± 2.0 | -239 | 31 | E_d measured by Lian <i>et al.</i> [326] with subsequent conversion to H_{ads} . |
| MgO(001) | C ₆ H ₆ | 161.5 | 15.1 ± 1.6 | -481 | 72 | Average taken of H_{ads} re-analyzed by C&S between low and high coverage in Ref. 327, with 0.5RT removed. |
| MgO(001) | H ₂ O | 203 | - | -520 | 121 | H_{ads} from Ferry <i>et al.</i> [204, 205, 319] estimated by subtracting lateral molecule-molecule interactions (-35.1 ± 9.6 kJ/mol) from the H_{ads} of H ₂ O monolayer on MgO, both obtained from LEED adsorption isotherms. |
| MgO(001) | NH ₃ | 160 | 13.0 → 14.0 ± 2.0 | -613 | 65 | E_d measurement from Arthur <i>et al.</i> [328] with subsequent conversion to H_{ads} . |
| MgO(001) | Physisorbed CO ₂ | 120 | 13.0 → 14.0 ± 2.0 | -431 | 49 | E_d measurement from Meixner <i>et al.</i> [206] with subsequent conversion to H_{ads} . |
| MgO(001) | Chemisorbed CO ₂ | 230 | 13.0 → 14.0 ± 2.0 | -664 | 125 | E_d measurement from Chakradhar and Burghaus [207] as the average of the α and β peaks with subsequent conversion to H_{ads} . |
| MgO(001) | Monolayer CH ₄ | 47 | 13.1 ± 2.0 | -131 | 19 | Monolayer E_d estimate by Tait <i>et al.</i> [324, 325]. |
| MgO(001) | Monolayer C ₂ H ₆ | 75 | 14.9 ± 2.0 | -236 | 30 | Monolayer E_d estimate by Tait <i>et al.</i> [324, 325]. |
| MgO(001) | Cluster NO | 79.5 | 14.0 ± 1.6 | -232 | 31 | Average taken of H_{ads} re-analyzed by C&S between low and high coverage in Ref. 223, with 0.5RT removed. |
| MgO(001) | Cluster H ₂ O | 235 | 14.5 ± 1.6 | -694 | 83 | H_{ads} re-analysis by C&S for Ref. 329, with 0.5RT removed. |
| MgO(001) | Cluster CH ₃ OH | 285.5 | 15.3 ± 1.6 | -890 | 106 | H_{ads} re-analysis by C&S for Ref. 196, with 0.5RT removed. |
| TiO ₂ rutile(110) | CH ₄ | 85 | 14.9 ± 2.0 | -249 | 34 | Low-coverage estimate of E_d by Chen <i>et al.</i> [330] with subsequent conversion to H_{ads} . |
| TiO ₂ rutile(110) | CO ₂ | 177 | 13.6 ± 2.0 | -493 | 62 | H_{ads} re-analysis by C&S for Ref. 331, with 0.5RT removed. |
| TiO ₂ rutile(110) | H ₂ O | 303 | 14.7 ± 1.6 | -917 | 111 | Average taken of H_{ads} re-analysis by C&S for Refs. 332 and 333 in low coverage limit |
| TiO ₂ rutile(110) | CH ₃ OH | 370 | 15.5 ± 1.6 | -1197 | 130 | H_{ads} re-analysis by C&S for Ref. 334, with 0.5RT removed. |
| TiO ₂ anatase(101) | H ₂ O | 257 | 14.6 ± 1.6 | -786 | 90 | H_{ads} re-analysis by C&S for Ref. 335, with 0.5RT removed. |
| TiO ₂ anatase(101) | NH ₃ | 410 | 13.3 ± 2.0 | -1180 | 182 | E_d estimate taken from Koust <i>et al.</i> [336] at the lowest studied coverage with subsequent conversion to H_{ads} , with 0.5RT removed. |

S12. COMPARISON OF H_{ads} BETWEEN AUTOSKZCAM AND EXPERIMENTS

With the autoSKZCAM approach, we have computed a final H_{ads} that aims to reach CCSD(T) quality. The error bars have been designed to capture the major sources of error to at least a 95% confidence interval: (1) finite size errors for calculating E_{int} with the SKZCAM protocol, (2) errors for using a DFT geometry and DFT E_{rlx} and (3) errors from using DFT to calculate zero-point vibrational and temperature contributions. Similarly, we have also analysed experimental TPD experiments to obtain H_{ads} estimates with reliable error bars that account for: (1) errors in the ν estimate, (2) errors between the measured Arrhenius activation energy and H_{ads} and (3) errors arising from concentration dependence.

We compare the autoSKZCAM predicted H_{ads} with experiment in Table S27. In particular, we calculate Δ_{min} , the smallest (absolute) deviation between autoSKZCAM and experiment within the limits of their error bars. If $\Delta_{\text{min}} = 0$, we expect the two estimates to be indistinguishable and to agree within their respective error bars. For all of the systems, we find the autoSKZCAM protocol to be indistinguishable from experiments.

In general, we find that the error bars from the autoSKZCAM framework are lower than experiment. For both the autoSKZCAM framework and experiment, the error bars increase when H_{ads} increases. For experiments, this arises because the errors are typically a function of RT_p and stronger binding correlates with a higher T_p . On the other hand, for the autoSKZCAM protocol, the errors rest mostly on ϵ_{geom} - the error arising from using a DFT geometry. A stronger binding typically means that the molecule has a stronger effect on the surface (electronic structure), hence leading to larger changes (and in turn E_{rlx}) to the geometry of the surface.

For several of the systems: CO_2 , N_2O , NO , H_2O , CH_3OH on $\text{MgO}(001)$ and CO_2 on TiO_2 rutile(110), we have studied multiple geometries using the autoSKZCAM framework in Section S1 and show in Table S27 the structure with the most negative H_{ads} value - the stable geometry we expect will be observed within experiments. Similarly, some systems have had several experimental H_{ads} estimates. For most of these systems, the experimental H_{ads} have agreed, barring CO_2 on $\text{MgO}(001)$, where two experiments have given H_{ads} that differ by more than 300 meV with one [206] suggesting a physisorbed structure while the other [207] predicting a chemisorbed structure. Our autoSKZCAM estimates have helped to shed further light on the discrepancies between these two experiments and provide evidence for the accuracy of one over the other, as discussed in Section S1.2.

TABLE S27. Comparison of the experimental and autoSKZCAM H_{ads} values (in meV) for the systems studied in this work. The Δ_{min} column shows the minimum difference between the experimental H_{ads} value and the autoSKZCAM H_{ads} value accounting for their error bars.

| System | Expt. H_{ads} | Expt. ϵ | autoSKZCAM H_{ads} | autoSKZCAM ϵ | Δ_{min} |
|--------------------------------------------------------|------------------------|------------------|-----------------------------|-----------------------|-----------------------|
| CH ₄ on MgO(001) | -115 | 19 | -109 | 23 | 0 |
| C ₂ H ₆ on MgO(001) | -221 | 30 | -175 | 35 | 0 |
| CO on MgO(001) | -176 | 21 | -180 | 20 | 0 |
| Parallel N ₂ O on MgO(001) | -239 | 31 | -259 | 20 | 0 |
| C ₆ H ₆ on MgO(001) | -481 | 72 | -430 | 100 | 0 |
| Monomer H ₂ O on MgO(001) | -520 | 121 | -542 | 73 | 0 |
| NH ₃ on MgO(001) | -613 | 65 | -524 | 54 | 0 |
| Chemisorbed CO ₂ on MgO(001) | -664 | 125 | -729 | 191 | 0 |
| Monolayer CH ₄ on MgO(001) | -131 | 19 | -132 | 28 | 0 |
| Monolayer C ₂ H ₆ on MgO(001) | -236 | 30 | -203 | 52 | 0 |
| Dimer NO on MgO(001) | -232 | 31 | -232 | 59 | 0 |
| Dissociated Tetramer H ₂ O on MgO(001) | -694 | 83 | -730 | 48 | 0 |
| Dissociated Tetramer CH ₃ OH on MgO(001) | -890 | 106 | -843 | 59 | 0 |
| CH ₄ on TiO ₂ rutile(110) | -249 | 34 | -241 | 31 | 0 |
| Tilted CO ₂ on TiO ₂ rutile(110) | -493 | 62 | -445 | 32 | 0 |
| H ₂ O on TiO ₂ rutile(110) | -917 | 111 | -1007 | 57 | 0 |
| CH ₃ OH on TiO ₂ rutile(110) | -1197 | 130 | -1284 | 76 | 0 |
| H ₂ O on TiO ₂ anatase(101) | -786 | 90 | -913 | 50 | 0 |
| NH ₃ on TiO ₂ anatase(101) | -1180 | 182 | -1090 | 42 | 0 |

We show in Table S28 the importance of correct analysis of experimental results, where the RMSD is increased from 58 meV to 102 meV when going from the system-specific ν approach suggested by Campbell and Sellers [258] to the standard approach of using $\nu = 10^{13}$.

TABLE S28. Comparison of the experimental H_{ads} values in meV with the autoSKZCAM H_{ads} values for the systems studied in this work. The H_{ads} values are compared with the re-analysed values in Table S26 and the values obtained by using the conventional $\log(\nu) = 13$ in temperature programmed desorption (TPD) experiments. The root mean squared deviation (RMSD) is also calculated against the autoSKZCAM H_{ads} values.

| System | autoSKZCAM | Experiment (Table S1) | Experiment ($\nu=10^{13}$) |
|--------------------------------------------------------|------------|-----------------------|------------------------------|
| CH ₄ on MgO(001) | -109 ± 23 | -115 | -114 |
| C ₂ H ₆ on MgO(001) | -175 ± 35 | -221 | -192 |
| CO on MgO(001) | -180 ± 20 | -176 | -166 |
| Parallel N ₂ O on MgO(001) | -259 ± 20 | -239 | -223 |
| C ₆ H ₆ on MgO(001) | -430 ± 100 | -481 | -413 |
| Monomer H ₂ O on MgO(001) | -542 ± 73 | -520 | -520 |
| NH ₃ on MgO(001) | -524 ± 54 | -613 | -581 |
| Chemisorbed CO ₂ on MgO(001) | -729 ± 191 | -664 | -618 |
| Monolayer CH ₄ on MgO(001) | -132 ± 28 | -131 | -130 |
| Monolayer C ₂ H ₆ on MgO(001) | -203 ± 52 | -236 | -207 |
| Dimer NO on MgO(001) | -232 ± 59 | -232 | -216 |
| Dissociated Tetramer H ₂ O on MgO(001) | -730 ± 48 | -694 | -624 |
| Dissociated Tetramer CH ₃ OH on MgO(001) | -843 ± 59 | -890 | -759 |
| CH ₄ on TiO ₂ rutile(110) | -241 ± 31 | -249 | -216 |
| Tilted CO ₂ on TiO ₂ rutile(110) | -445 ± 32 | -493 | -471 |
| H ₂ O on TiO ₂ rutile(110) | -1007 ± 57 | -917 | -814 |
| CH ₃ OH on TiO ₂ rutile(110) | -1284 ± 76 | -1197 | -1013 |
| H ₂ O on TiO ₂ anatase(101) | -913 ± 50 | -786 | -704 |
| NH ₃ on TiO ₂ anatase(101) | -1090 ± 42 | -1180 | -1155 |
| RMSD | | 58 | 102 |

S13. PREVIOUS COMPUTATIONAL LITERATURE

Many of the adsorbate–surface systems within this work have been studied before by both DFT and cWFT. In particular, owing to its affordable nature and popularity, DFT has been widely used, providing several predictions for each system and we have collated some of this previous literature in Table S29. Much of the early work in the late 1990’s and early 2000’s have utilised embedded cluster calculations (often with hybrid functionals such as B3LYP), with the current DFT workhorse being planewave periodic codes. For each system, we observe quite significant deviations across the DFT literature, varying by over 300 meV for most systems. These variations largely arise from differences in the exchange–correlation functional but even for the same functional, predictions can significantly vary due to differences in the basis set and pseudopotential treatment, which are discussed within each cited literature.

Importantly, for some of these systems, even the predicted adsorption configuration of the adsorbate is not known and different studies may suggest different geometries. For example, whether CO₂ adopts a chemisorbed (bent) or physisorbed (linear) geometry on the MgO(001) has been under debate, with studies which point towards either. Similarly, the a myriad of geometries have been predicted for NO on MgO(001) by different studies, many of which cite agreement to experiment. With DFT, this agreement can be fortuitous many times due to errors in the surface model, DFA, electronic structures or neglect of thermal contributions. These discrepancies have highlighted the need for accurate approaches such as autoSKZCAM framework that can predict the correct geometries (with H_{ads} that match experiments) that get the right answers for the right reasons; we highlight its success in predicting the ground-state configuration for several systems in Section S1.

While less common, calculations with cWFT have also been applied before to a selection of the studied systems and we highlight these previous work (and the method used) in Table S29. As we showed in Fig. 2 of the main text, the deviations between methods from cWFT can be significant (to as large as 500 meV for some systems). These deviations can arise from errors in the method used and also from electronic structure parameters; methods from cWFT are severely affected by basis set and surface model, as has been discussed extensively for CO on MgO(001) in Ref. 278. Overall, these deviations highlight the need for going to a high level of theory, namely CCSD(T) and accurate surface models; all of which has been achieved within the autoSKZCAM framework.

TABLE S29. Compilation of E_{ads} values (in meV) of previous density functional theory (DFT) and correlated wave-function theory (cWFT) literature for the systems studied within this work.

| System | DFT | WFT |
|-----------------------------------------------------|-------------------------------------------------------------------------------------------------------------------------------------------------------------|----------------------------------------------------------------------------------------------------------------------------------------------------------------|
| CH ₄ on MgO(001) | -50 [337], 2 [238], 17 [338], -300 [213], -120 [216], -152 [311] | -134 [MP2+ΔCC] [339] |
| C ₂ H ₆ on MgO(001) | -127 [339], -154 [339] | -196 [MP2+ΔCC] [339] |
| CO on MgO(001) | -9 to -282 [340], -175 to -408 [341] | -207 [LNO-CCSD(T)] [342], -199 [LNO-CCSD(T)] [278], -230 [MP2+ΔCC] [246], 70 [CCSD(T)] [216], -398 [CCSD] [343], -72 [RPA@PBE] [344], -310 [RPA@PBE+rSE] [344] |
| N ₂ O on MgO(001) | -258 [234], >0 [233], -137 [234] | |
| C ₆ H ₆ on MgO(001) | -20 [337] | |
| Monomer H ₂ O on MgO(001) | -342 [345], -500 [346], -340 [347], -422 to 667 [348] | -574 [ΔCC] [246], -480 [DMC] [349], -608 [RPA@PBE+rSE] [344], -492 [RPA@PBE] [344] |
| NH ₃ on MgO(001) | -668 [350], -867 [351] | -608 [PCT] [352] |
| CO ₂ on MgO(001) | Chemisorbed: -1000 [213], 135 [209], -680 [215], -640 [216], -380 [214], Physisorbed: -320 [353], -90 [212], -126 [211], -120 [213] | Chemisorbed: 870 [MP2] [208], -494 [RPA@PBE] [This work], -340 [MP2] [210] |
| NO on MgO(001) | Hollow: -312 [354], Bent-Mg: -520 [355], Upright-Mg: -260 [356], -297 [357], Bent-O: -464 [358], -312 [359, 360], Dimer: -40 [224], Bent-Bridge: -150 [362] | Bent-Mg: 29 [RPA@PBE] [344], -360 [RPA@PBE+rSE] [344] |
| Cluster CH ₃ OH on MgO(001) | -718 [363], -466 [364], -640 [365], -508 [199] | -964 [200], -598 [MP2] [201] |
| Cluster H ₂ O on MgO(001) | -610 [366], -592 [367], -720 [368] | |
| Monolayer CH ₄ on MgO(001) | -18 [239, 369], -124 to -353 [341] | -79 [PCI-80] [238], -138 [MP2+ΔCC] [242], -145 [MP2+ΔCC] [246], -87 [RPA@PBE] [344], -140 [RPA@PBE+rSE] [344] |
| Monolayer C ₂ H ₆ on MgO(001) | -234 to -568 [341] | -242 [MP2+ΔCC] [246] |
| CH ₄ on TiO ₂ rutile(110) | -48 to -412 [226], -360 [371] | -408 [CCSD(T)] [226] |
| CO ₂ on TiO ₂ rutile(110) | -95 to -559 [226], -640 [372] | -542 [CCSD(T)] [226] |
| H ₂ O on TiO ₂ rutile(110) | -442 to -950 [226], -840 [373], 1032 [232] | -1638 [374], -1492 [MP2] [375], -984 [DLPNO-CCSD(T)] [226], -964 [LNO-CCSD(T)] [376], -1390 [CCSD] [377] |
| CH ₃ OH on TiO ₂ rutile(110) | -468 to -1145 [226], -1490 [378], -760 [380] | -1234 [379], -1106 [DLPNO-CCSD(T)] [226] |
| H ₂ O on TiO ₂ anatase(101) | -740 [381], -650 [382], -1088 [383], -977 [384] | -1170 [DLPNO-CCSD(T)] [385] |
| NH ₃ on TiO ₂ anatase(101) | -1200 [336], -1113 [383], 1193 [387] | -1153 [386], - |

S14. BENCHMARKING THE COST OF THE AUTOSKZCAM FRAMEWORK

We perform an analysis of the cost for computing the interaction energy E_{int} from the autoSKZCAM framework against a GGA-based (PBE-D3) and hybrid-based (PBE0-TS/HI) DFA. In both cases, we have attempted to make the calculations efficient to the best of our abilities. For example, for periodic hybrid calculations, we make use of the Adaptively Compressed Exchange Operator [388] and use an initial wave-function coming from the GGA calculation to enable efficient self-consistent field (SCF) energy convergence to the cutoff of 10^{-5} eV (looser than our standard settings in Sec. S8.1). We also use a smaller energy cutoff of 520 eV for both the GGA and hybrid DFT calculations. The cost for the autoSKZCAM framework is the sum of all the individual contributions to E_{int} outlined in Table S4, with the same corresponding computational details described in Sec. S5. The efficiency of the autoSKZCAM framework calculations for CO₂ on MgO(001) is further enhanced by performing both MP2 and CCSD(T) calculations using the aVXZ basis sets rather than awCVXZ and only treating the valence electrons in the correlation treatment. A further Δ_{core} contribution is calculated by performing additional CBS(awCVTZ/awCVQZ) calculations for the first three clusters generated by the SKZCAM protocol, commensurate with the procedure used for H₂O on TiO₂ rutile(110). The costs in CPU-hours (CPUh) to perform both periodic DFT and autoSKZCAM calculations were assessed on 2.1 GHz, 18-core Intel Xeon E5-2695 (Broadwell) series processors on the Cirrus high-performance computing (HPC) cluster [<https://www.cirrus.ac.uk/>]. The costs are compared in Table S30 for CO₂ on MgO(001) and H₂O on TiO₂ rutile(110).

TABLE S30. Computational cost in CPU hours for the periodic DFT, both a GGA (PBE-D3) and hybrid (PBE0-TS/HI), compared to autoSKZCAM for the CO₂ on MgO(001) and H₂O on TiO₂ rutile(110) adsorbate–surface systems. Details of these calculations are described in the text.

| | GGA | hybrid | autoSKZCAM |
|--------------------------------------------------|-----|--------|------------|
| CO ₂ on MgO(001) | 169 | 1657 | 2944 |
| H ₂ O on TiO ₂ rutile(110) | 330 | 31517 | 6703 |

We find that the cost with the autoSKZCAM framework for CO₂ on MgO(001) is slightly higher (less than 2 times) than hybrid DFT, which is in turn an order of magnitude more expensive than the GGA calculation. However, when moving towards the more complex H₂O on TiO₂ rutile(110), the cost of the autoSKZCAM framework becomes significantly cheaper (by almost 5 times) than the periodic hybrid DFT calculation. The GGA calculation remains an order of magnitude cheaper

than the autoSKZCAM framework for this system. It should be highlighted that the cost moving from CO₂ on MgO(001) to H₂O on TiO₂ rutile(110) does not change significantly (less than 3 times increase) for the autoSKZCAM framework, while there is more than an order of magnitude change for hybrid DFT. This feature of the autoSKZCAM framework arises because the size of the clusters selected by the SKZCAM protocol (described in Sec. S6.1) does not depend on the complexity of the surface, and should remain similar in size between different types of surfaces since it's based on radial cutoffs.

It is also useful to highlight the cost of the autoSKZCAM framework in relation to previous high-level calculations. In particular, CO on MgO(001) has been the prototypical surface system for cWFT methods, as highlighted in Ref. 278. We gather previous estimates in Table S31; these should be taken as rough estimates as they were all performed on different computing systems. Out of all of these previous works, the autoSKZCAM is by far the cheapest, with a cost of ~ 600 CPUh. This is improved over the previous SKZCAM protocol calculations due to the described improvements in Sec. S6.6. Ye and Berkelbach previously performed periodic LNO-CCSD(T) calculations for this system and arrived at a cost of $\sim 18,000$ CPUh. Compared to this, periodic CCSD(T) (without the LNO approximation) was shown to take $\sim 200,000$ CPUh to perform in Ref. 278, with periodic DMC being even more costly at $\sim 1,000,000$ CPUh. In the present study, the RPA calculations took $\sim 4,000$ CPUh, relatively comparable to hybrid DFT at $\sim 1,000$ CPUh.

TABLE S31. Rough computational cost in CPU hours for several methods from correlated wave-function theory applied to CO on MgO(001). Details are provided in their respective references. As a guide, hybrid DFT costs $\sim 1,000$ CPUh [278] for this system.

| Method | Cost [CPUh] |
|-----------------------------------------|----------------|
| autoSKZCAM framework (This work) | ~ 600 |
| RPA (This work) | ~ 4000 |
| Periodic LNO-CCSD(T) [342] | ~ 18000 |
| Cluster CCSD(T) [278] [SKZCAM protocol] | ~ 20000 |
| Periodic CCSD(T) [278] | ~ 200000 |
| Periodic DMC [278] | ~ 1000000 |

-
- [1] Shi, B. X. Research data supporting: An accurate and efficient framework for predictive insights into ionic surface chemistry. https://github.com/benshi97/Data_autoSKZCAM (2024).
- [2] Günster, J., Liu, G., Stultz, J. & Goodman, D. W. Interaction of methanol and water on MgO(100) studied by ultraviolet photoelectron and metastable impact electron spectroscopies. *J. Chem. Phys.* **110**, 2558–2565 (1999).
- [3] Zhang, Y. & Yang, W. Comment on “Generalized Gradient Approximation Made Simple”. *Phys. Rev. Lett.* **80**, 890–890 (1998).
- [4] Caldeweyher, E. *et al.* A generally applicable atomic-charge dependent London dispersion correction. *J. Chem. Phys.* **150**, 154122 (2019).
- [5] Petitjean, H. *et al.* Quantitative Investigation of MgO Brønsted Basicity: DFT, IR, and Calorimetry Study of Methanol Adsorption. *J. Phys. Chem. C* **114**, 3008–3016 (2010).
- [6] A. Sainna, M. *et al.* A combined periodic DFT and QM/MM approach to understand the radical mechanism of the catalytic production of methanol from glycerol. *Faraday Discuss.* **229**, 108–130 (2021).
- [7] Branda, M. M., Peralta, J. E., Castellani, N. J. & Contreras, R. H. Theoretical study of charge transfer interactions in methanol adsorbed on magnesium oxide. *Surf. Sci.* **504**, 235–243 (2002).
- [8] Trabelsi, M. *et al.* Thermodynamic and structural study of methanol thin films adsorbed on MgO(100). *Surf. Sci.* **566–568**, 789–793 (2004).
- [9] Rudberg, J. & Foster, M. Adsorption of Methanol on the MgO(100) Surface: An Infrared Study at Room Temperature. *J. Phys. Chem. B* **108**, 18311–18317 (2004).
- [10] Ferry, D. *et al.* The properties of a two-dimensional water layer on MgO(001). *Surf. Sci.* **377–379**, 634–638 (1997).
- [11] Ferry, D. *et al.* Water monolayers on MgO(100): Structural investigations by LEED experiments, tensor LEED dynamical analysis and potential calculations. *Surf. Sci.* **409**, 101–116 (1998).
- [12] Meixner, D. L., Arthur, D. A. & George, S. M. Kinetics of desorption, adsorption, and surface diffusion of CO₂ on MgO(100). *Surf. Sci.* **261**, 141–154 (1992).
- [13] Chakradhar, A. & Burghaus, U. Carbon dioxide adsorption on MgO(001)–CO₂ kinetics and dynamics. *Surf. Sci.* **616**, 171–177 (2013).
- [14] Pacchioni, G., Ricart, J. M. & Illas, F. Ab Initio Cluster Model Calculations on the Chemisorption of CO₂ and SO₂ Probe Molecules on MgO and CaO (100) Surfaces. A Theoretical Measure of Oxide Basicity. *J. Am. Chem. Soc.* **116**, 10152–10158 (1994).
- [15] Jensen, M. B., Pettersson, L. G. M., Swang, O. & Olsbye, U. CO₂ Sorption on MgO and CaO Surfaces: A Comparative Quantum Chemical Cluster Study. *J. Phys. Chem. B* **109**, 16774–16781 (2005).
- [16] Pacchioni, G. Physisorbed and chemisorbed CO₂ at surface and step sites of the MgO(100) surface. *Surf. Sci.* **281**, 207–219 (1993).

- [17] Hammami, R., Dhouib, A., Fernandez, S. & Minot, C. CO₂ adsorption on (001) surfaces of metal monoxides with rock-salt structure. *Catal. Today* **139**, 227–233 (2008).
- [18] Cornu, D., Guesmi, H., Krafft, J.-M. & Lauron-Pernot, H. Lewis Acido-Basic Interactions between CO₂ and MgO Surface: DFT and DRIFT Approaches. *J. Phys. Chem. C* **116**, 6645–6654 (2012).
- [19] Manae, M. A., Dheer, L., Rai, S., Shetty, S. & Waghmare, U. V. Activation of CO₂ and CH₄ on MgO surfaces: Mechanistic insights from first-principles theory. *Phys. Chem. Chem. Phys.* **24**, 1415–1423 (2022).
- [20] Baltrusaitis, J., Hatch, C. & Orlando, R. Periodic DFT Study of Acidic Trace Atmospheric Gas Molecule Adsorption on Ca- and Fe-Doped MgO(001) Surface Basic Sites. *J. Phys. Chem. A* **116**, 7950–7958 (2012).
- [21] Downing, C. A., Sokol, A. A. & Catlow, C. R. A. The reactivity of CO₂ on the MgO(100) surface. *Phys. Chem. Chem. Phys.* **16**, 184–195 (2013).
- [22] Mazheika, A. & Levchenko, S. V. Ni Substitutional Defects in Bulk and at the (001) Surface of MgO from First-Principles Calculations. *J. Phys. Chem. C* **120**, 26934–26944 (2016).
- [23] Yanagisawa, Y., Takaoka, K., Yamabe, S. & Ito, T. Interaction of CO₂ with Magnesium Oxide Surfaces: A TPD, FTIR, and Cluster-Model Calculation Study. *J. Phys. Chem.* **99**, 3704–3710 (1995).
- [24] Ito, T., Kobayashi, H. & Tashiro, T. Roles of low-coordinated surface ions in adsorption of gases on MgO. *Nouv. Cim. D* **19**, 1695–1705 (1997).
- [25] McQueen, N., Kelemen, P., Dipple, G., Renforth, P. & Wilcox, J. Ambient weathering of magnesium oxide for CO₂ removal from air. *Nat. Commun.* **11**, 3299 (2020).
- [26] Donat, F. & Müller, C. R. Prospects of MgO-based sorbents for CO₂ capture applications at high temperatures. *Curr. Opin. Green Sustainable Chem.* **36**, 100645 (2022).
- [27] Fu, Y., Zhang, L., Yue, B., Chen, X. & He, H. Simultaneous Characterization of Solid Acidity and Basicity of Metal Oxide Catalysts via the Solid-State NMR Technique. *J. Phys. Chem. C* **122**, 24094–24102 (2018).
- [28] Du, J.-H. *et al.* Identification of CO₂ adsorption sites on MgO nanosheets by solid-state nuclear magnetic resonance spectroscopy. *Nat. Commun.* **13**, 707 (2022).
- [29] Wichtendahl, R., Rodriguez-Rodrigo, M., Härtel, U., Kühlenbeck, H. & Freund, H.-J. Thermodesorption of CO and NO from Vacuum-Cleaved NiO(100) and MgO(100). *Phys. Status Solidi A* **173**, 93–100 (1999).
- [30] Di Valentin, C. *et al.* NO Monomers on MgO Powders and Thin Films. *J. Phys. Chem. B* **106**, 1637–1645 (2002).
- [31] Platero, E. E., Spoto, G. & Zecchina, A. Spectroscopic study of NO adsorption on magnesium oxide, nickel oxide and their solid solutions. *J. Chem. Soc., Faraday Trans. 1* **81**, 1283–1294 (1985).
- [32] Kubas, A. *et al.* Surface Adsorption Energetics Studied with “Gold Standard” Wave-Function-Based Ab Initio Methods: Small-Molecule Binding to TiO₂(110). *J. Phys. Chem. Lett.* **7**, 4207–4212 (2016).
- [33] Sorescu, D. C., Lee, J., Al-Saidi, W. A. & Jordan, K. D. CO₂ adsorption on TiO₂(110) rutile: Insight from dispersion-corrected density functional theory calculations and scanning tunneling microscopy

- experiments. *J. Chem. Phys.* **134**, 104707 (2011).
- [34] Lee, J., Sorescu, D. C., Deng, X. & Jordan, K. D. Diffusion of CO₂ on the Rutile TiO₂(110) Surface. *J. Phys. Chem. Lett.* **2**, 3114–3117 (2011).
- [35] Lin, X. *et al.* Structure and Dynamics of CO₂ on Rutile TiO₂(110)-1×1. *J. Phys. Chem. C* **116**, 26322–26334 (2012).
- [36] Cao, Y., Hu, S., Yu, M., Yan, S. & Xu, M. Adsorption and interaction of CO₂ on rutile TiO₂(110) surfaces: A combined UHV-FTIRS and theoretical simulation study. *Phys. Chem. Chem. Phys.* **17**, 23994–24000 (2015).
- [37] E. Hamlyn, R. C. *et al.* Imaging the ordering of a weakly adsorbed two-dimensional condensate: Ambient-pressure microscopy and spectroscopy of CO₂ molecules on rutile TiO₂ (110). *Phys. Chem. Chem. Phys.* **20**, 13122–13126 (2018).
- [38] Sorescu, D. C., Lee, J., Al-Saidi, W. A. & Jordan, K. D. Coadsorption properties of CO₂ and H₂O on TiO₂ rutile (110): A dispersion-corrected DFT study. *J. Chem. Phys.* **137**, 074704 (2012).
- [39] Scagnelli, A., Valentin, C. D. & Pacchioni, G. Catalytic dissociation of N₂O on pure and Ni-doped MgO surfaces. *Surf. Sci.* **600**, 386–394 (2006).
- [40] Huesges, Z., Müller, C., Paulus, B. & Maschio, L. Dispersion corrected DFT calculations for the adsorption of N₂O on MgO. *Surf. Sci.* **627**, 11–15 (2014).
- [41] Causa, M., Kotomin, E., Pisani, C. & Roetti, C. The MgO(110) surface and CO adsorption thereon. II. CO adsorption. *J. Phys. C: Solid State Phys.* **20**, 4991 (1987).
- [42] Pacchioni, G., Cogliandro, G. & Bagus, P. S. Molecular orbital cluster model study of bonding and vibrations of CO adsorbed on MgO surface. *Int. J. Quantum Chem.* **42**, 1115–1139 (1992).
- [43] Alavi, A. Molecular-dynamics simulation of methane adsorbed on MgO: Evidence for a Kosterlitz-Thouless transition. *Mol. Phys.* **71**, 1173–1191 (1990).
- [44] Todnem, K., Børve, K. J. & Nygren, M. Molecular adsorption of methane and methyl onto MgO(100) An embedded-cluster study. *Surf. Sci.* **421**, 296–307 (1999).
- [45] Drummond, M. L., Sumpter, B. G., Shelton, W. A. & Larese, J. Z. Density functional investigation of the adsorption of a methane monolayer on an MgO(100) surface. *Phys. Rev. B* **73**, 195313 (2006).
- [46] Larese, J. Z., Hastings, J. M., Passell, L., Smith, D. & Richter, D. Rotational tunneling of methane on MgO surfaces: A neutron scattering study. *J. Chem. Phys.* **95**, 6997–7000 (1991).
- [47] Larese, J. Z., y Marero, D. M., Sivia, D. S. & Carlile, C. J. Tracking the Evolution of Interatomic Potentials with High Resolution Inelastic Neutron Spectroscopy. *Phys. Rev. Lett.* **87**, 206102 (2001).
- [48] Tosoni, S. & Sauer, J. Accurate quantum chemical energies for the interaction of hydrocarbons with oxide surfaces: CH₄/MgO(001). *Phys. Chem. Chem. Phys.* **12**, 14330–14340 (2010).
- [49] Sidoumou, M., Angot, T. & Suzanne, J. Ethane adsorbed on MgO(100) single crystal surfaces: A high resolution LEED study. *Surf. Sci.* **272**, 347–351 (1992).
- [50] Hoang, P. N. M., Girardet, C., Sidoumou, M. & Suzanne, J. Structure of ethane monolayers adsorbed on MgO(100): Experiments and calculations. *Phys. Rev. B* **48**, 12183–12192 (1993).
- [51] Trabelsi, M., Saidi, S. & Coulomb, J. P. Structural study of C₂D₆ thin films adsorbed on MgO(100).

- Indian J. Pure Appl. Phys. **53**, 748–752 (2015).
- [52] Alessio, M., Bischoff, F. A. & Sauer, J. Chemically accurate adsorption energies for methane and ethane monolayers on the MgO(001) surface. Phys. Chem. Chem. Phys. **20**, 9760–9769 (2018).
- [53] Bligaard, T. et al. Toward Benchmarking in Catalysis Science: Best Practices, Challenges, and Opportunities. ACS Catal. **6**, 2590–2602 (2016).
- [54] Řezáč, J., Riley, K. E. & Hobza, P. S66: A Well-balanced Database of Benchmark Interaction Energies Relevant to Biomolecular Structures. J. Chem. Theory Comput. **7**, 2427–2438 (2011).
- [55] Goerigk, L. et al. A look at the density functional theory zoo with the advanced GMTKN55 database for general main group thermochemistry, kinetics and noncovalent interactions. Phys. Chem. Chem. Phys. **19**, 32184–32215 (2017).
- [56] Klimeš, J., Kaltak, M., Maggio, E. & Kresse, G. Singles correlation energy contributions in solids. J. Chem. Phys. **143**, 102816 (2015).
- [57] Kaltak, M., Klimeš, J. & Kresse, G. Cubic scaling algorithm for the random phase approximation: Self-interstitials and vacancies in Si. Phys. Rev. B **90**, 054115 (2014).
- [58] Sabatier, P. Hydrogénations et déshydrogénations par catalyse. Ber. Dtsch. Chem. Ges. **44**, 1984–2001 (1911).
- [59] Sauer, J. Ab Initio Calculations for Molecule–Surface Interactions with Chemical Accuracy. Acc. Chem. Res. **52**, 3502–3510 (2019).
- [60] Berger, F., Rybicki, M. & Sauer, J. Molecular Dynamics with Chemical Accuracy–Alkane Adsorption in Acidic Zeolites. ACS Catal. **13**, 2011–2024 (2023).
- [61] Xia, C. et al. Emerging cocatalysts in TiO₂-based photocatalysts for light-driven catalytic hydrogen evolution: Progress and perspectives. Fuel **307**, 121745 (2022).
- [62] Wang, Q. & Domen, K. Particulate Photocatalysts for Light-Driven Water Splitting: Mechanisms, Challenges, and Design Strategies. Chem. Rev. **120**, 919–985 (2020).
- [63] Wang, S. et al. Highly Efficient One-pot Electrosynthesis of Oxime Ethers from NO_x over Ultrafine MgO Nanoparticles Derived from Mg-based Metal-Organic Frameworks. Angewandte Chemie International Edition **63**, e202405553 (2024).
- [64] Campbell, C. T. & Sellers, J. R. V. Enthalpies and Entropies of Adsorption on Well-Defined Oxide Surfaces: Experimental Measurements. Chem. Rev. **113**, 4106–4135 (2013).
- [65] Møller, Chr. & Plesset, M. S. Note on an Approximation Treatment for Many-Electron Systems. Phys. Rev. **46**, 618–622 (1934).
- [66] Raghavachari, K., Trucks, G. W., Pople, J. A. & Head-Gordon, M. A fifth-order perturbation comparison of electron correlation theories. Chem. Phys. Lett. **157**, 479–483 (1989).
- [67] Neese, F., Wennmohs, F., Becker, U. & Riplinger, C. The ORCA quantum chemistry program package. J. Chem. Phys. **152**, 224108 (2020).
- [68] Kállay, M. et al. The MRCC program system: Accurate quantum chemistry from water to proteins. J. Chem. Phys. **152**, 074107 (2020).
- [69] Nagy, P. R., Samu, G. & Kállay, M. Optimization of the Linear-Scaling Local Natural Orbital

- CCSD(T) Method: Improved Algorithm and Benchmark Applications. J. Chem. Theory Comput. **14**, 4193–4215 (2018).
- [70] Nagy, P. R. & Kállay, M. Approaching the Basis Set Limit of CCSD(T) Energies for Large Molecules with Local Natural Orbital Coupled-Cluster Methods. J. Chem. Theory Comput. **15**, 5275–5298 (2019).
- [71] Riplinger, C. & Neese, F. An efficient and near linear scaling pair natural orbital based local coupled cluster method. J. Chem. Phys. **138**, 034106 (2013).
- [72] Riplinger, C., Sandhoefer, B., Hansen, A. & Neese, F. Natural triple excitations in local coupled cluster calculations with pair natural orbitals. J. Chem. Phys. **139**, 134101 (2013).
- [73] Riplinger, C. & Neese, F. An efficient and near linear scaling pair natural orbital based local coupled cluster method. J. Chem. Phys. **138**, 034106 (2013).
- [74] Riplinger, C., Pinski, P., Becker, U., Valeev, E. F. & Neese, F. Sparse maps—A systematic infrastructure for reduced-scaling electronic structure methods. II. Linear scaling domain based pair natural orbital coupled cluster theory. J. Chem. Phys. **144**, 024109 (2016).
- [75] Peterson, K. A. & Dunning, T. H. Accurate correlation consistent basis sets for molecular core-valence correlation effects: The second row atoms Al–Ar, and the first row atoms B–Ne revisited. J. Chem. Phys. **117**, 10548–10560 (2002).
- [76] Balabanov, N. B. & Peterson, K. A. Systematically convergent basis sets for transition metals. I. All-electron correlation consistent basis sets for the 3d elements Sc–Zn. J. Chem. Phys. **123**, 064107 (2005).
- [77] Bistoni, G. *et al.* Treating Subvalence Correlation Effects in Domain Based Pair Natural Orbital Coupled Cluster Calculations: An Out-of-the-Box Approach. J. Chem. Theory Comput. **13**, 3220–3227 (2017).
- [78] Neese, F. & Valeev, E. F. Revisiting the Atomic Natural Orbital Approach for Basis Sets: Robust Systematic Basis Sets for Explicitly Correlated and Conventional Correlated *ab initio* Methods? J. Chem. Theory Comput. **7**, 33–43 (2011).
- [79] Weigend, F., Häser, M., Patzelt, H. & Ahlrichs, R. RI-MP2: Optimized auxiliary basis sets and demonstration of efficiency. Chem. Phys. Lett. **294**, 143–152 (1998).
- [80] Hellweg, A., Hättig, C., Höfener, S. & Klopper, W. Optimized accurate auxiliary basis sets for RI-MP2 and RI-CC2 calculations for the atoms Rb to Rn. Theor. Chem. Acc. **117**, 587–597 (2007).
- [81] Stoychev, G. L., Auer, A. A. & Neese, F. Automatic Generation of Auxiliary Basis Sets. J. Chem. Theory Comput. **13**, 554–562 (2017).
- [82] Lehtola, S. Straightforward and Accurate Automatic Auxiliary Basis Set Generation for Molecular Calculations with Atomic Orbital Basis Sets. J. Chem. Theory Comput. **17**, 6886–6900 (2021).
- [83] Shi, B. X. *et al.* General embedded cluster protocol for accurate modeling of oxygen vacancies in metal-oxides. J. Chem. Phys. **156**, 124704 (2022).
- [84] Shi, B. X. *et al.* Many-Body Methods for Surface Chemistry Come of Age: Achieving Consensus with Experiments. J. Am. Chem. Soc. **145**, 25372–25381 (2023).

- [85] Pacchioni, G., Bagus, P. S. & Parmigiani, F. Cluster Models for Surface and Bulk Phenomena (Springer Science & Business Media, 2013).
- [86] Lu, Y. et al. Multiscale QM/MM modelling of catalytic systems with ChemShell. Phys. Chem. Chem. Phys. **25**, 21816–21835 (2023).
- [87] Drummond, N. D., Needs, R. J., Sorouri, A. & Foulkes, W. M. C. Finite-size errors in continuum quantum Monte Carlo calculations. Phys. Rev. B **78**, 125106 (2008).
- [88] Al-Hamdani, Y. S. Theoretical Approach towards Accurate Molecular Interactions with Low Dimensional Substrates. Doctoral, UCL (University College London) (2016).
- [89] Al-Hamdani, Y. S. et al. Properties of the water to boron nitride interaction: From zero to two dimensions with benchmark accuracy. J. Chem. Phys. **147**, 044710 (2017).
- [90] Bredow, T., Giordano, L., Cinquini, F. & Pacchioni, G. Electronic properties of rutile TiO₂ ultrathin films: Odd-even oscillations with the number of layers. Phys. Rev. B **70**, 035419 (2004).
- [91] Svensson, M. et al. ONIOM: A Multilayered Integrated MO + MM Method for Geometry Optimizations and Single Point Energy Predictions. A Test for Diels-Alder Reactions and Pt(P(t-Bu)₃)₂ + H₂ Oxidative Addition. J. Phys. Chem. **100**, 19357–19363 (1996).
- [92] Pople, J. A. Quantum Chemical Models (Nobel Lecture). Angew. Chem. Int. Ed. **38**, 1894–1902 (1999).
- [93] Shi, B. X., Wales, D. J., Michaelides, A. & Myung, C. W. Going for Gold(-Standard): Attaining Coupled Cluster Accuracy in Oxide-Supported Nanoclusters. J. Chem. Theory Comput. **20**, 5306–5316 (2024).
- [94] Bryenton, K. R., Adeleke, A. A., Dale, S. G. & Johnson, E. R. Delocalization error: The greatest outstanding challenge in density-functional theory. WIREs Comput. Mol. Sci. **13**, e1631 (2023).
- [95] Dkhissi, A., Soulard, P., Perrin, A. & Lacome, N. The NO Dimer. J. Mol. Spectrosc. **183**, 12–17 (1997).
- [96] Wade, E. A., Cline, J. I., Lorenz, K. T., Hayden, C. & Chandler, D. W. Direct measurement of the binding energy of the NO dimer. J. Chem. Phys. **116**, 4755–4757 (2002).
- [97] González-Luque, R., Merchán, M. & Roos, B. O. A theoretical determination of the dissociation energy of the nitric oxide dimer. Theoret. Chim. Acta **88**, 425–435 (1994).
- [98] Sayós, R., Valero, R., Anglada, J. M. & González, M. Theoretical investigation of the eight low-lying electronic states of the cis- and trans-nitric oxide dimers and its isomerization using multiconfigurational second-order perturbation theory (CASPT2). J. Chem. Phys. **112**, 6608–6624 (2000).
- [99] Ivanic, J., Schmidt, M. W. & Luke, B. High-level theoretical study of the NO dimer and tetramer: Has the tetramer been observed? J. Chem. Phys. **137**, 214316 (2012).
- [100] Tobita, M. et al. Critical comparison of single-reference and multireference coupled-cluster methods: Geometry, harmonic frequencies, and excitation energies of N₂O₂. The Journal of Chemical Physics **119**, 10713–10723 (2003).
- [101] Perdew, J. P., Burke, K. & Ernzerhof, M. Generalized Gradient Approximation Made Simple. Phys. Rev. Lett. **77**, 3865–3868 (1996).

- [102] Lee, K., Murray, É. D., Kong, L., Lundqvist, B. I. & Langreth, D. C. Higher-accuracy van der Waals density functional. Phys. Rev. B **82**, 081101 (2010).
- [103] Hamada, I. Van der Waals density functional made accurate. Phys. Rev. B **89**, 121103 (2014).
- [104] Adamo, C. & Barone, V. Toward reliable density functional methods without adjustable parameters: The PBE0 model. J. Chem. Phys. **110**, 6158–6170 (1999).
- [105] Becke, A. D. Density-functional thermochemistry. III. The role of exact exchange. J. Chem. Phys. **98**, 5648–5652 (1993).
- [106] Grimme, S. Semiempirical GGA-type density functional constructed with a long-range dispersion correction. J. Comp. Chem. **27**, 1787–1799 (2006).
- [107] Bučko, T., Lebègue, S., Ángyán, J. G. & Hafner, J. Extending the applicability of the Tkatchenko-Scheffler dispersion correction via iterative Hirshfeld partitioning. The Journal of Chemical Physics **141**, 034114 (2014).
- [108] Ning, J. et al. Workhorse minimally empirical dispersion-corrected density functional with tests for weakly bound systems: r²SCAN+rVV10. Phys. Rev. B **106**, 075422 (2022).
- [109] Heyd, J., Scuseria, G. E. & Ernzerhof, M. Hybrid functionals based on a screened Coulomb potential. J. Chem. Phys. **118**, 8207–8215 (2003).
- [110] Singh, J. P., Lim, W. C., Won, S. O., Song, J. & Chae, K. H. Synthesis and Characterization of Some Alkaline-Earth-Oxide Nanoparticles. J. Korean Phys. Soc. **72**, 890–899 (2018).
- [111] Burdett, J. K., Hughbanks, T., Miller, G. J., Richardson, J. W. & Smith, J. V. Structural-electronic relationships in inorganic solids: Powder neutron diffraction studies of the rutile and anatase polymorphs of titanium dioxide at 15 and 295 K. J. Am. Chem. Soc. **109**, 3639–3646 (1987).
- [112] Kresse, G. & Furthmüller, J. Efficiency of ab-initio total energy calculations for metals and semiconductors using a plane-wave basis set. Comput. Mater. Sci. **6**, 15–50 (1996).
- [113] Kresse, G. & Furthmüller, J. Efficient iterative schemes for ab initio total-energy calculations using a plane-wave basis set. Phys. Rev. B **54**, 11169–11186 (1996).
- [114] Grimme, S. Supramolecular Binding Thermodynamics by Dispersion-Corrected Density Functional Theory. Chem. - Eur. J. **18**, 9955–9964 (2012).
- [115] Li, Y.-P., Gomes, J., Mallikarjun Sharada, S., Bell, A. T. & Head-Gordon, M. Improved Force-Field Parameters for QM/MM Simulations of the Energies of Adsorption for Molecules in Zeolites and a Free Rotor Correction to the Rigid Rotor Harmonic Oscillator Model for Adsorption Enthalpies. J. Phys. Chem. C **119**, 1840–1850 (2015).
- [116] Alfè, D. & Gillan, M. J. Ab initio statistical mechanics of surface adsorption and desorption. II. Nuclear quantum effects. J. Chem. Phys. **133**, 044103 (2010).
- [117] Piccini, G. & Sauer, J. Effect of Anharmonicity on Adsorption Thermodynamics. J. Chem. Theory Comput. **10**, 2479–2487 (2014).
- [118] Rosen, A. S. Quacc – The Quantum Accelerator: <https://zenodo.org/records/13921187>. Zenodo (2024).
- [119] Campbell, C. T. Energies of Adsorbed Catalytic Intermediates on Transition Metal Surfaces: Calori-

- metric Measurements and Benchmarks for Theory. *Acc. Chem. Res.* **52**, 984–993 (2019).
- [120] Schmid, M., Parkinson, G. S. & Diebold, U. Analysis of Temperature-Programmed Desorption via Equilibrium Thermodynamics. *ACS Phys. Chem Au* **3**, 44–62 (2023).
- [121] Dohnálek, Z. *et al.* Physisorption of CO on the MgO(100) Surface. *J. Phys. Chem. B* **105**, 3747–3751 (2001).
- [122] Redhead, P. A. Thermal desorption of gases. *Vacuum* **12**, 203–211 (1962).
- [123] Campbell, C. T. & Sellers, J. R. V. The Entropies of Adsorbed Molecules. *J. Am. Chem. Soc.* **134**, 18109–18115 (2012).
- [124] Boese, A. D. & Sauer, J. Accurate adsorption energies of small molecules on oxide surfaces: CO–MgO(001). *Phys. Chem. Chem. Phys.* **15**, 16481–16493 (2013).
- [125] Alessio, M., Usvyat, D. & Sauer, J. Chemically Accurate Adsorption Energies: CO and H₂O on the MgO(001) Surface. *J. Chem. Theory Comput.* **15**, 1329–1344 (2019).
- [126] Espenson, J. H. *Chemical Kinetics and Reaction Mechanisms* (McGraw-Hill, 1995).
- [127] Wellendorff, J. *et al.* A benchmark database for adsorption bond energies to transition metal surfaces and comparison to selected DFT functionals. *Surf. Sci.* **640**, 36–44 (2015).
- [128] Rangarajan, S. & Mavrikakis, M. A comparative analysis of different van der Waals treatments for molecular adsorption on the basal plane of 2H-MoS₂. *Surf. Sci.* **729**, 122226 (2023).
- [129] Brown, W. A., Kose, R. & King, D. A. Femtomole Adsorption Calorimetry on Single-Crystal Surfaces. *Chem. Rev.* **98**, 797–832 (1998).
- [130] Tait, S. L., Dohnálek, Z., Campbell, C. T. & Kay, B. D. N-alkanes on MgO(100). I. Coverage-dependent desorption kinetics of n-butane. *J. Chem. Phys.* **122**, 164707 (2005).
- [131] Tait, S. L., Dohnálek, Z., Campbell, C. T. & Kay, B. D. N-alkanes on MgO(100). II. Chain length dependence of kinetic desorption parameters for small n-alkanes. *J. Chem. Phys.* **122**, 164708 (2005).
- [132] Lian, J. C. *et al.* N₂O Adsorption on the Surface of MgO(001) Thin Films: An Infrared and TPD Study. *J. Phys. Chem. C* **114**, 3148–3151 (2010).
- [133] Street, S. C., Guo, Q., Xu, C. & Goodman, D. W. Adsorption and Electronic States of Benzene on Ordered MgO and Al₂O₃ Thin Films. *J. Phys. Chem.* **100**, 17599–17605 (1996).
- [134] Arthur, D. A., Meixner, D. L., Boudart, M. & George, S. M. Adsorption, desorption, and surface diffusion kinetics of NH₃ on MgO(100). *J. Chem. Phys.* **95**, 8521–8531 (1991).
- [135] Stirniman, M. J., Huang, C., Scott Smith, R., Joyce, S. A. & Kay, B. D. The adsorption and desorption of water on single crystal MgO(100): The role of surface defects. *J. Chem. Phys.* **105**, 1295–1298 (1996).
- [136] Chen, L., Smith, R. S., Kay, B. D. & Dohnálek, Z. Adsorption of small hydrocarbons on rutile TiO₂(110). *Surf. Sci.* **650**, 83–92 (2016).
- [137] Thompson, T. L., Diwald, O. & Yates, J. T. CO₂ as a Probe for Monitoring the Surface Defects on TiO₂(110)Temperature-Programmed Desorption. *J. Phys. Chem. B* **107**, 11700–11704 (2003).
- [138] Hugenschmidt, M. B., Gamble, L. & Campbell, C. T. The interaction of H₂O with a TiO₂(110) surface. *Surf. Sci.* **302**, 329–340 (1994).

- [139] Dohnálek, Z., Kim, J., Bondarchuk, O., White, J. M. & Kay, B. D. Physisorption of N₂, O₂, and CO on Fully Oxidized TiO₂(110). *J. Phys. Chem. B* **110**, 6229–6235 (2006).
- [140] Li, Z., Smith, R. S., Kay, B. D. & Dohnálek, Z. Determination of Absolute Coverages for Small Aliphatic Alcohols on TiO₂(110). *J. Phys. Chem. C* **115**, 22534–22539 (2011).
- [141] Herman, G. S., Dohnálek, Z., Ruzycki, N. & Diebold, U. Experimental Investigation of the Interaction of Water and Methanol with Anatase-TiO₂(101). *J. Phys. Chem. B* **107**, 2788–2795 (2003).
- [142] Koust, S. *et al.* NH₃ adsorption on anatase-TiO₂(101). *J. Chem. Phys.* **148**, 124704 (2018).
- [143] Trevethan, T. & Shluger, A. L. Building Blocks for Molecular Devices: Organic Molecules on the MgO (001) Surface. *J. Phys. Chem. C* **111**, 15375–15381 (2007).
- [144] Ferrari, A. M., Huber, S., Knözinger, H., Neyman, K. M. & Rösch, N. FTIR Spectroscopic and Density Functional Model Cluster Studies of Methane Adsorption on MgO. *J. Phys. Chem. B* **102**, 4548–4555 (1998).
- [145] Boese, A. D. & Sauer, J. Accurate adsorption energies for small molecules on oxide surfaces: CH₄/MgO(001) and C₂H₆/MgO(001). *J. Comp. Chem.* **37**, 2374–2385 (2016).
- [146] Valero, R., Gomes, J. R. B., Truhlar, D. G. & Illas, F. Good performance of the M06 family of hybrid meta generalized gradient approximation density functionals on a difficult case: CO adsorption on MgO(001). *The Journal of Chemical Physics* **129**, 124710 (2008).
- [147] R. Rehak, F., Piccini, G., Alessio, M. & Sauer, J. Including dispersion in density functional theory for adsorption on flat oxide surfaces, in metal–organic frameworks and in acidic zeolites. *Phys. Chem. Chem. Phys.* **22**, 7577–7585 (2020).
- [148] Ye, H.-Z. & Berkelbach, T. C. Adsorption and vibrational spectroscopy of CO on the surface of MgO from periodic local coupled-cluster theory. *Faraday Discuss.* (2024).
- [149] Mitra, A., Hermes, M. R., Cho, M., Agarawal, V. & Gagliardi, L. Periodic Density Matrix Embedding for CO Adsorption on the MgO(001) Surface. *J. Phys. Chem. Lett.* **13**, 7483–7489 (2022).
- [150] Bajdich, M., Nørskov, J. K. & Vojvodic, A. Surface energetics of alkaline-earth metal oxides: Trends in stability and adsorption of small molecules. *Phys. Rev. B* **91**, 155401 (2015).
- [151] Giordano, L., Goniakowski, J. & Suzanne, J. Partial Dissociation of Water Molecules in the (3x2) Water Monolayer Deposited on the MgO (100) Surface. *Phys. Rev. Lett.* **81**, 1271–1273 (1998).
- [152] Carrasco, J., Illas, F. & Lopez, N. Dynamic Ion Pairs in the Adsorption of Isolated Water Molecules on Alkaline-Earth Oxide (001) Surfaces. *Phys. Rev. Lett.* **100**, 016101 (2008).
- [153] Hu, X. L., Carrasco, J., Klimeš, J. & Michaelides, A. Trends in water monomer adsorption and dissociation on flat insulating surfaces. *Phys. Chem. Chem. Phys.* **13**, 12447–12453 (2011).
- [154] Kebede, G. G., Spångberg, D., Mitev, P. D., Broqvist, P. & Hermansson, K. Comparing van der Waals DFT methods for water on NaCl(001) and MgO(001). *J. Chem. Phys.* **146**, 064703 (2017).
- [155] Karalti, O., Alfè, D., Gillan, M. J. & Jordan, K. D. Adsorption of a water molecule on the MgO(100) surface as described by cluster and slab models. *Phys. Chem. Chem. Phys.* **14**, 7846–7853 (2012).
- [156] Pugh, S. & Gillan, M. J. The energetics of NH₃ adsorption at the MgO(001) surface. *Surf. Sci.* **320**, 331–343 (1994).

- [157] Nakajima, Y. & Doren, D. J. Ammonia adsorption on MgO(100): A density functional theory study. *J. Chem. Phys.* **105**, 7753–7762 (1996).
- [158] Allouche, A., Corà, F. & Girardet, C. Vibrational infrared spectrum of NH₃ adsorbed on MgO(100). I. Ab initio calculations. *Chem. Phys.* **201**, 59–71 (1995).
- [159] Lv, G. *et al.* CO₂ adsorption on a K-promoted MgO surface: A DFT theoretical study. *Surf. Sci.* **749**, 122575 (2024).
- [160] Song, Z., Zhao, B., Xu, H. & Cheng, P. Remarkably Strong Chemisorption of Nitric Oxide on Insulating Oxide Films Promoted by Hybrid Structure. *J. Phys. Chem. C* **121**, 21482–21490 (2017).
- [161] Yanagisawa, Y., Kuramoto, K. & Yamabe, S.-i. Three Types of Adsorptions of Nitric Oxide on the MgO Surface. *J. Phys. Chem. B* **103**, 11078–11085 (1999).
- [162] Rodriguez, J. A., Jirsak, T., Pérez, M., González, L. & Maiti, A. Studies on the behavior of mixed-metal oxides: Adsorption of CO and NO on MgO(100), Ni_xMg_{1-x}O(100), and Cr_xMg_{1-x}O(100). *J. Chem. Phys.* **114**, 4186–4195 (2001).
- [163] Añez, R., Sierraaalta, A. & Soto, L. J. D. NO and NO₂ adsorption on subsurface doped MgO (100) and BaO (100) surfaces. A density functional study. *Appl. Surf. Sci.* **404**, 216–229 (2017).
- [164] Miletic, M., Gland, J. L., Hass, K. C. & Schneider, W. F. First-Principles Characterization of NO_x Adsorption on MgO. *J. Phys. Chem. B* **107**, 157–163 (2003).
- [165] Schneider, W. F., Hass, K. C., Miletic, M. & Gland, J. L. Dramatic Cooperative Effects in Adsorption of NO_x on MgO(001). *J. Phys. Chem. B* **106**, 7405–7413 (2002).
- [166] Schneider, W. F. Qualitative Differences in the Adsorption Chemistry of Acidic (CO₂, SO_x) and Amphiphilic (NO_x) Species on the Alkaline Earth Oxides. *J. Phys. Chem. B* **108**, 273–282 (2004).
- [167] Lu, X., Xu, X., Wang, N. & Zhang, Q. Adsorption and Decomposition of NO on Magnesium Oxide: A Quantum Chemical Study. *J. Phys. Chem. B* **103**, 5657–5664 (1999).
- [168] Lim, J. Y., Kim, K., Kim, E. Y. & Han, J. W. Density functional theory study of NO_x adsorption on alkaline earth metal oxide and transition metal surfaces. *Korean J. Chem. Eng.* **36**, 1258–1266 (2019).
- [169] Rodríguez, A. H., Branda, M. M. & Castellani, N. J. Adsorption of n Methanol Molecules on MgO(100) with n = 1 to 4: A Theoretical Study. *J. Phys. Chem. C* **111**, 10603–10609 (2007).
- [170] Gay, I. D. & Harrison, N. M. A density functional study of water and methanol chemisorption on MgO(110). *Surf. Sci.* **591**, 13–22 (2005).
- [171] Man, I.-C., Soriga, S. G. & Parvulescu, V. Theoretical aspects of methyl acetate and methanol activation on MgO(100) and (501) catalyst surfaces with application in FAME production. *Appl. Surf. Sci.* **392**, 920–928 (2017).
- [172] Hu, X. L., Klimeš, J. & Michaelides, A. Proton transfer in adsorbed water dimers. *Phys. Chem. Chem. Phys.* **12**, 3953–3956 (2010).
- [173] Alvim, R. S., Borges, I. J., Costa, D. G. & Leitão, A. A. Density-Functional Theory Simulation of the Dissociative Chemisorption of Water Molecules on the MgO(001) Surface. *J. Phys. Chem. C* **116**, 738–744 (2012).
- [174] Ding, Z. & Selloni, A. Hydration structure of flat and stepped MgO surfaces. *J. Chem. Phys.* **154**,

- 114708 (2021).
- [175] Stimac, P. J. & Hinde, R. J. Simulating CH₄ physisorption on ionic crystals. *Eur. Phys. J. D* **46**, 69–76 (2008).
- [176] Pisani, C. *et al.* Periodic local MP2 method for the study of electronic correlation in crystals: Theory and preliminary applications. *Journal of Computational Chemistry* **29**, 2113–2124 (2008).
- [177] Tillotson, M. J., Brett, P. M., Bennett, R. A. & Grau-Crespo, R. Adsorption of organic molecules at the TiO₂(110) surface: The effect of van der Waals interactions. *Surf. Sci.* **632**, 142–153 (2015).
- [178] Kovačič, Ž., Likozar, B. & Huš, M. Electronic properties of rutile and anatase TiO₂ and their effect on CO₂ adsorption: A comparison of first principle approaches. *Fuel* **328**, 125322 (2022).
- [179] Liu, L.-M., Zhang, C., Thornton, G. & Michaelides, A. Structure and dynamics of liquid water on rutile TiO₂(110). *Phys. Rev. B* **82**, 161415 (2010).
- [180] Bandura, A. V. *et al.* Adsorption of Water on the TiO₂ (Rutile) (110) Surface: A Comparison of Periodic and Embedded Cluster Calculations. *J. Phys. Chem. B* **108**, 7844–7853 (2004).
- [181] Stefanovich, E. V. & Truong, T. N. Ab initio study of water adsorption on TiO₂(110): Molecular adsorption versus dissociative chemisorption. *Chem. Phys. Lett.* **299**, 623–629 (1999).
- [182] Ye, H.-Z. & Berkelbach, T. C. Ab initio surface chemistry with chemical accuracy. [arXiv:2309.14640](https://arxiv.org/abs/2309.14640) (2024). 2309.14640.
- [183] Schäfer, T., Libisch, F., Kresse, G. & Grüneis, A. Local embedding of coupled cluster theory into the random phase approximation using plane waves. *J. Chem. Phys.* **154**, 011101 (2021).
- [184] Kieu, L., Boyd, P. & Idriss, H. Trends within the adsorption energy of alcohols over rutile TiO₂(110) and (011) clusters. *J. Mol. Catal. A: Chem.* **188**, 153–161 (2002).
- [185] Bates, S. P., Kresse, G. & Gillan, M. J. The adsorption and dissociation of ROH molecules on TiO₂(110). *Surf. Sci.* **409**, 336–349 (1998).
- [186] Lang, X., Wen, B., Zhou, C., Ren, Z. & Liu, L.-M. First-Principles Study of Methanol Oxidation into Methyl Formate on Rutile TiO₂(110). *J. Phys. Chem. C* **118**, 19859–19868 (2014).
- [187] Vittadini, A., Selloni, A., Rotzinger, F. P. & Grätzel, M. Structure and Energetics of Water Adsorbed at TiO₂ Anatase (101) and (001) Surfaces. *Phys. Rev. Lett.* **81**, 2954–2957 (1998).
- [188] Miller, K. L., Musgrave, C. B., Falconer, J. L. & Medlin, J. W. Effects of Water and Formic Acid Adsorption on the Electronic Structure of Anatase TiO₂(101). *J. Phys. Chem. C* **115**, 2738–2749 (2011).
- [189] Onal, I., Soyer, S. & Senkan, S. Adsorption of water and ammonia on TiO₂-anatase cluster models. *Surf. Sci.* **600**, 2457–2469 (2006).
- [190] Zhao, Z., Li, Z. & Zou, Z. Structure and Properties of Water on the Anatase TiO₂(101) Surface: From Single-Molecule Adsorption to Interface Formation. *J. Phys. Chem. C* **116**, 11054–11061 (2012).
- [191] Petersen, T. & Klüner, T. Water Adsorption on Ideal Anatase-TiO₂(101) – An Embedded Cluster Model for Accurate Adsorption Energetics and Excited State Properties. *Z. Phys. Chem.* **234**, 813–834 (2020).
- [192] Wanbayor, R. & Ruangpornvisuti, V. Adsorption of CO, H₂, N₂O, NH₃ and CH₄ on the anatase

- TiO₂(001) and (101) surfaces and their competitive adsorption predicted by periodic DFT calculations. *Mater. Chem. Phys.* **124**, 720–725 (2010).
- [193] Chang, J.-G., Ju, S.-P., Chang, C.-S. & Chen, H.-T. Adsorption Configuration and Dissociative Reaction of NH₃ on Anatase (101) Surface with and without Hydroxyl Groups. *J. Phys. Chem. C* **113**, 6663–6672 (2009).
- [194] Lin, L. Adaptively Compressed Exchange Operator. *J. Chem. Theory Comput.* **12**, 2242–2249 (2016).
- [195] Shi, B. X. Research data supporting: An accurate and efficient framework for predictive insights into ionic surface chemistry. https://github.com/benshi97/Data_autoSKZCAM (2024).
- [196] Günster, J., Liu, G., Stultz, J. & Goodman, D. W. Interaction of methanol and water on MgO(100) studied by ultraviolet photoelectron and metastable impact electron spectroscopies. *J. Chem. Phys.* **110**, 2558–2565 (1999).
- [197] Zhang, Y. & Yang, W. Comment on “Generalized Gradient Approximation Made Simple”. *Phys. Rev. Lett.* **80**, 890–890 (1998).
- [198] Caldeweyher, E. *et al.* A generally applicable atomic-charge dependent London dispersion correction. *J. Chem. Phys.* **150**, 154122 (2019).
- [199] Petitjean, H. *et al.* Quantitative Investigation of MgO Brønsted Basicity: DFT, IR, and Calorimetry Study of Methanol Adsorption. *J. Phys. Chem. C* **114**, 3008–3016 (2010).
- [200] A. Sainna, M. *et al.* A combined periodic DFT and QM/MM approach to understand the radical mechanism of the catalytic production of methanol from glycerol. *Faraday Discuss.* **229**, 108–130 (2021).
- [201] Branda, M. M., Peralta, J. E., Castellani, N. J. & Contreras, R. H. Theoretical study of charge transfer interactions in methanol adsorbed on magnesium oxide. *Surf. Sci.* **504**, 235–243 (2002).
- [202] Trabelsi, M. *et al.* Thermodynamic and structural study of methanol thin films adsorbed on MgO(100). *Surf. Sci.* **566–568**, 789–793 (2004).
- [203] Rudberg, J. & Foster, M. Adsorption of Methanol on the MgO(100) Surface: An Infrared Study at Room Temperature. *J. Phys. Chem. B* **108**, 18311–18317 (2004).
- [204] Ferry, D. *et al.* The properties of a two-dimensional water layer on MgO(001). *Surf. Sci.* **377–379**, 634–638 (1997).
- [205] Ferry, D. *et al.* Water monolayers on MgO(100): Structural investigations by LEED experiments, tensor LEED dynamical analysis and potential calculations. *Surf. Sci.* **409**, 101–116 (1998).
- [206] Meixner, D. L., Arthur, D. A. & George, S. M. Kinetics of desorption, adsorption, and surface diffusion of CO₂ on MgO(100). *Surf. Sci.* **261**, 141–154 (1992).
- [207] Chakradhar, A. & Burghaus, U. Carbon dioxide adsorption on MgO(001)–CO₂ kinetics and dynamics. *Surf. Sci.* **616**, 171–177 (2013).
- [208] Pacchioni, G., Ricart, J. M. & Illas, F. Ab Initio Cluster Model Calculations on the Chemisorption of CO₂ and SO₂ Probe Molecules on MgO and CaO (100) Surfaces. A Theoretical Measure of Oxide Basicity. *J. Am. Chem. Soc.* **116**, 10152–10158 (1994).
- [209] Jensen, M. B., Pettersson, L. G. M., Swang, O. & Olsbye, U. CO₂ Sorption on MgO and CaO Surfaces:

- A Comparative Quantum Chemical Cluster Study. *J. Phys. Chem. B* **109**, 16774–16781 (2005).
- [210] Pacchioni, G. Physisorbed and chemisorbed CO₂ at surface and step sites of the MgO(100) surface. *Surf. Sci.* **281**, 207–219 (1993).
- [211] Hammami, R., Dhouib, A., Fernandez, S. & Minot, C. CO₂ adsorption on (001) surfaces of metal monoxides with rock-salt structure. *Catal. Today* **139**, 227–233 (2008).
- [212] Cornu, D., Guesmi, H., Krafft, J.-M. & Lauron-Pernot, H. Lewis Acido-Basic Interactions between CO₂ and MgO Surface: DFT and DRIFT Approaches. *J. Phys. Chem. C* **116**, 6645–6654 (2012).
- [213] Manae, M. A., Dheer, L., Rai, S., Shetty, S. & Waghmare, U. V. Activation of CO₂ and CH₄ on MgO surfaces: Mechanistic insights from first-principles theory. *Phys. Chem. Chem. Phys.* **24**, 1415–1423 (2022).
- [214] Baltrusaitis, J., Hatch, C. & Orlando, R. Periodic DFT Study of Acidic Trace Atmospheric Gas Molecule Adsorption on Ca- and Fe-Doped MgO(001) Surface Basic Sites. *J. Phys. Chem. A* **116**, 7950–7958 (2012).
- [215] Downing, C. A., Sokol, A. A. & Catlow, C. R. A. The reactivity of CO₂ on the MgO(100) surface. *Phys. Chem. Chem. Phys.* **16**, 184–195 (2013).
- [216] Mazheika, A. & Levchenko, S. V. Ni Substitutional Defects in Bulk and at the (001) Surface of MgO from First-Principles Calculations. *J. Phys. Chem. C* **120**, 26934–26944 (2016).
- [217] Yanagisawa, Y., Takaoka, K., Yamabe, S. & Ito, T. Interaction of CO₂ with Magnesium Oxide Surfaces: A TPD, FTIR, and Cluster-Model Calculation Study. *J. Phys. Chem.* **99**, 3704–3710 (1995).
- [218] Ito, T., Kobayashi, H. & Tashiro, T. Roles of low-coordinated surface ions in adsorption of gases on MgO. *Nouv. Cim. D* **19**, 1695–1705 (1997).
- [219] McQueen, N., Kelemen, P., Dipple, G., Renforth, P. & Wilcox, J. Ambient weathering of magnesium oxide for CO₂ removal from air. *Nat. Commun.* **11**, 3299 (2020).
- [220] Donat, F. & Müller, C. R. Prospects of MgO-based sorbents for CO₂ capture applications at high temperatures. *Curr. Opin. Green Sustainable Chem.* **36**, 100645 (2022).
- [221] Fu, Y., Zhang, L., Yue, B., Chen, X. & He, H. Simultaneous Characterization of Solid Acidity and Basicity of Metal Oxide Catalysts via the Solid-State NMR Technique. *J. Phys. Chem. C* **122**, 24094–24102 (2018).
- [222] Du, J.-H. *et al.* Identification of CO₂ adsorption sites on MgO nanosheets by solid-state nuclear magnetic resonance spectroscopy. *Nat. Commun.* **13**, 707 (2022).
- [223] Wichtendahl, R., Rodriguez-Rodrigo, M., Härtel, U., Kühlenbeck, H. & Freund, H.-J. Thermodesorption of CO and NO from Vacuum-Cleaved NiO(100) and MgO(100). *Phys. Status Solidi A* **173**, 93–100 (1999).
- [224] Di Valentin, C. *et al.* NO Monomers on MgO Powders and Thin Films. *J. Phys. Chem. B* **106**, 1637–1645 (2002).
- [225] Platero, E. E., Spoto, G. & Zecchina, A. Spectroscopic study of NO adsorption on magnesium oxide, nickel oxide and their solid solutions. *J. Chem. Soc., Faraday Trans. 1* **81**, 1283–1294 (1985).
- [226] Kubas, A. *et al.* Surface Adsorption Energetics Studied with “Gold Standard” Wave-Function-Based

- Ab Initio Methods: Small-Molecule Binding to TiO₂(110). *J. Phys. Chem. Lett.* **7**, 4207–4212 (2016).
- [227] Sorescu, D. C., Lee, J., Al-Saidi, W. A. & Jordan, K. D. CO₂ adsorption on TiO₂(110) rutile: Insight from dispersion-corrected density functional theory calculations and scanning tunneling microscopy experiments. *J. Chem. Phys.* **134**, 104707 (2011).
- [228] Lee, J., Sorescu, D. C., Deng, X. & Jordan, K. D. Diffusion of CO₂ on the Rutile TiO₂(110) Surface. *J. Phys. Chem. Lett.* **2**, 3114–3117 (2011).
- [229] Lin, X. et al. Structure and Dynamics of CO₂ on Rutile TiO₂(110)-1×1. *J. Phys. Chem. C* **116**, 26322–26334 (2012).
- [230] Cao, Y., Hu, S., Yu, M., Yan, S. & Xu, M. Adsorption and interaction of CO₂ on rutile TiO₂(110) surfaces: A combined UHV-FTIRS and theoretical simulation study. *Phys. Chem. Chem. Phys.* **17**, 23994–24000 (2015).
- [231] E. Hamlyn, R. C. et al. Imaging the ordering of a weakly adsorbed two-dimensional condensate: Ambient-pressure microscopy and spectroscopy of CO₂ molecules on rutile TiO₂ (110). *Phys. Chem. Chem. Phys.* **20**, 13122–13126 (2018).
- [232] Sorescu, D. C., Lee, J., Al-Saidi, W. A. & Jordan, K. D. Coadsorption properties of CO₂ and H₂O on TiO₂ rutile (110): A dispersion-corrected DFT study. *J. Chem. Phys.* **137**, 074704 (2012).
- [233] Scagnelli, A., Valentin, C. D. & Pacchioni, G. Catalytic dissociation of N₂O on pure and Ni-doped MgO surfaces. *Surf. Sci.* **600**, 386–394 (2006).
- [234] Huesges, Z., Müller, C., Paulus, B. & Maschio, L. Dispersion corrected DFT calculations for the adsorption of N₂O on MgO. *Surf. Sci.* **627**, 11–15 (2014).
- [235] Causa, M., Kotomin, E., Pisani, C. & Roetti, C. The MgO(110) surface and CO adsorption thereon. II. CO adsorption. *J. Phys. C: Solid State Phys.* **20**, 4991 (1987).
- [236] Pacchioni, G., Cogliandro, G. & Bagus, P. S. Molecular orbital cluster model study of bonding and vibrations of CO adsorbed on MgO surface. *Int. J. Quantum Chem.* **42**, 1115–1139 (1992).
- [237] Alavi, A. Molecular-dynamics simulation of methane adsorbed on MgO: Evidence for a Kosterlitz-Thouless transition. *Mol. Phys.* **71**, 1173–1191 (1990).
- [238] Todnem, K., Børve, K. J. & Nygren, M. Molecular adsorption of methane and methyl onto MgO(100) An embedded-cluster study. *Surf. Sci.* **421**, 296–307 (1999).
- [239] Drummond, M. L., Sumpter, B. G., Shelton, W. A. & Larese, J. Z. Density functional investigation of the adsorption of a methane monolayer on an MgO(100) surface. *Phys. Rev. B* **73**, 195313 (2006).
- [240] Larese, J. Z., Hastings, J. M., Passell, L., Smith, D. & Richter, D. Rotational tunneling of methane on MgO surfaces: A neutron scattering study. *J. Chem. Phys.* **95**, 6997–7000 (1991).
- [241] Larese, J. Z., y Marero, D. M., Sivia, D. S. & Carlile, C. J. Tracking the Evolution of Interatomic Potentials with High Resolution Inelastic Neutron Spectroscopy. *Phys. Rev. Lett.* **87**, 206102 (2001).
- [242] Tosoni, S. & Sauer, J. Accurate quantum chemical energies for the interaction of hydrocarbons with oxide surfaces: CH₄/MgO(001). *Phys. Chem. Chem. Phys.* **12**, 14330–14340 (2010).
- [243] Sidoumou, M., Angot, T. & Suzanne, J. Ethane adsorbed on MgO(100) single crystal surfaces: A high resolution LEED study. *Surf. Sci.* **272**, 347–351 (1992).

- [244] Hoang, P. N. M., Girardet, C., Sidoumou, M. & Suzanne, J. Structure of ethane monolayers adsorbed on MgO(100): Experiments and calculations. *Phys. Rev. B* **48**, 12183–12192 (1993).
- [245] Trabelsi, M., Saidi, S. & Coulomb, J. P. Structural study of C₂D₆ thin films adsorbed on MgO(100). *Indian J. Pure Appl. Phys.* **53**, 748–752 (2015).
- [246] Alessio, M., Bischoff, F. A. & Sauer, J. Chemically accurate adsorption energies for methane and ethane monolayers on the MgO(001) surface. *Phys. Chem. Chem. Phys.* **20**, 9760–9769 (2018).
- [247] Bligaard, T. *et al.* Toward Benchmarking in Catalysis Science: Best Practices, Challenges, and Opportunities. *ACS Catal.* **6**, 2590–2602 (2016).
- [248] Řezáč, J., Riley, K. E. & Hobza, P. S66: A Well-balanced Database of Benchmark Interaction Energies Relevant to Biomolecular Structures. *J. Chem. Theory Comput.* **7**, 2427–2438 (2011).
- [249] Goerigk, L. *et al.* A look at the density functional theory zoo with the advanced GMTKN55 database for general main group thermochemistry, kinetics and noncovalent interactions. *Phys. Chem. Chem. Phys.* **19**, 32184–32215 (2017).
- [250] Klimeš, J., Kaltak, M., Maggio, E. & Kresse, G. Singles correlation energy contributions in solids. *J. Chem. Phys.* **143**, 102816 (2015).
- [251] Kaltak, M., Klimeš, J. & Kresse, G. Cubic scaling algorithm for the random phase approximation: Self-interstitials and vacancies in Si. *Phys. Rev. B* **90**, 054115 (2014).
- [252] Sabatier, P. Hydrogénations et déshydrogénations par catalyse. *Ber. Dtsch. Chem. Ges.* **44**, 1984–2001 (1911).
- [253] Sauer, J. Ab Initio Calculations for Molecule–Surface Interactions with Chemical Accuracy. *Acc. Chem. Res.* **52**, 3502–3510 (2019).
- [254] Berger, F., Rybicki, M. & Sauer, J. Molecular Dynamics with Chemical Accuracy–Alkane Adsorption in Acidic Zeolites. *ACS Catal.* **13**, 2011–2024 (2023).
- [255] Xia, C. *et al.* Emerging cocatalysts in TiO₂-based photocatalysts for light-driven catalytic hydrogen evolution: Progress and perspectives. *Fuel* **307**, 121745 (2022).
- [256] Wang, Q. & Domen, K. Particulate Photocatalysts for Light-Driven Water Splitting: Mechanisms, Challenges, and Design Strategies. *Chem. Rev.* **120**, 919–985 (2020).
- [257] Wang, S. *et al.* Highly Efficient One-pot Electrosynthesis of Oxime Ethers from NO_x over Ultrafine MgO Nanoparticles Derived from Mg-based Metal-Organic Frameworks. *Angewandte Chemie International Edition* **63**, e202405553 (2024).
- [258] Campbell, C. T. & Sellers, J. R. V. Enthalpies and Entropies of Adsorption on Well-Defined Oxide Surfaces: Experimental Measurements. *Chem. Rev.* **113**, 4106–4135 (2013).
- [259] Møller, Chr. & Plesset, M. S. Note on an Approximation Treatment for Many-Electron Systems. *Phys. Rev.* **46**, 618–622 (1934).
- [260] Raghavachari, K., Trucks, G. W., Pople, J. A. & Head-Gordon, M. A fifth-order perturbation comparison of electron correlation theories. *Chem. Phys. Lett.* **157**, 479–483 (1989).
- [261] Neese, F., Wennmo, F., Becker, U. & Riplinger, C. The ORCA quantum chemistry program package. *J. Chem. Phys.* **152**, 224108 (2020).

- [262] Kállay, M. *et al.* The MRCC program system: Accurate quantum chemistry from water to proteins. *J. Chem. Phys.* **152**, 074107 (2020).
- [263] Nagy, P. R., Samu, G. & Kállay, M. Optimization of the Linear-Scaling Local Natural Orbital CCSD(T) Method: Improved Algorithm and Benchmark Applications. *J. Chem. Theory Comput.* **14**, 4193–4215 (2018).
- [264] Nagy, P. R. & Kállay, M. Approaching the Basis Set Limit of CCSD(T) Energies for Large Molecules with Local Natural Orbital Coupled-Cluster Methods. *J. Chem. Theory Comput.* **15**, 5275–5298 (2019).
- [265] Riplinger, C. & Neese, F. An efficient and near linear scaling pair natural orbital based local coupled cluster method. *J. Chem. Phys.* **138**, 034106 (2013).
- [266] Riplinger, C., Sandhoefer, B., Hansen, A. & Neese, F. Natural triple excitations in local coupled cluster calculations with pair natural orbitals. *J. Chem. Phys.* **139**, 134101 (2013).
- [267] Riplinger, C. & Neese, F. An efficient and near linear scaling pair natural orbital based local coupled cluster method. *J. Chem. Phys.* **138**, 034106 (2013).
- [268] Riplinger, C., Pinski, P., Becker, U., Valeev, E. F. & Neese, F. Sparse maps—A systematic infrastructure for reduced-scaling electronic structure methods. II. Linear scaling domain based pair natural orbital coupled cluster theory. *J. Chem. Phys.* **144**, 024109 (2016).
- [269] Peterson, K. A. & Dunning, T. H. Accurate correlation consistent basis sets for molecular core-valence correlation effects: The second row atoms Al–Ar, and the first row atoms B–Ne revisited. *J. Chem. Phys.* **117**, 10548–10560 (2002).
- [270] Balabanov, N. B. & Peterson, K. A. Systematically convergent basis sets for transition metals. I. All-electron correlation consistent basis sets for the 3d elements Sc–Zn. *J. Chem. Phys.* **123**, 064107 (2005).
- [271] Bistoni, G. *et al.* Treating Subvalence Correlation Effects in Domain Based Pair Natural Orbital Coupled Cluster Calculations: An Out-of-the-Box Approach. *J. Chem. Theory Comput.* **13**, 3220–3227 (2017).
- [272] Neese, F. & Valeev, E. F. Revisiting the Atomic Natural Orbital Approach for Basis Sets: Robust Systematic Basis Sets for Explicitly Correlated and Conventional Correlated *ab initio* Methods? *J. Chem. Theory Comput.* **7**, 33–43 (2011).
- [273] Weigend, F., Häser, M., Patzelt, H. & Ahlrichs, R. RI-MP2: Optimized auxiliary basis sets and demonstration of efficiency. *Chem. Phys. Lett.* **294**, 143–152 (1998).
- [274] Hellweg, A., Hättig, C., Höfener, S. & Klopper, W. Optimized accurate auxiliary basis sets for RI-MP2 and RI-CC2 calculations for the atoms Rb to Rn. *Theor. Chem. Acc.* **117**, 587–597 (2007).
- [275] Stoychev, G. L., Auer, A. A. & Neese, F. Automatic Generation of Auxiliary Basis Sets. *J. Chem. Theory Comput.* **13**, 554–562 (2017).
- [276] Lehtola, S. Straightforward and Accurate Automatic Auxiliary Basis Set Generation for Molecular Calculations with Atomic Orbital Basis Sets. *J. Chem. Theory Comput.* **17**, 6886–6900 (2021).
- [277] Shi, B. X. *et al.* General embedded cluster protocol for accurate modeling of oxygen vacancies in

- metal-oxides. *J. Chem. Phys.* **156**, 124704 (2022).
- [278] Shi, B. X. *et al.* Many-Body Methods for Surface Chemistry Come of Age: Achieving Consensus with Experiments. *J. Am. Chem. Soc.* **145**, 25372–25381 (2023).
- [279] Pacchioni, G., Bagus, P. S. & Parmigiani, F. *Cluster Models for Surface and Bulk Phenomena* (Springer Science & Business Media, 2013).
- [280] Lu, Y. *et al.* Multiscale QM/MM modelling of catalytic systems with ChemShell. *Phys. Chem. Chem. Phys.* **25**, 21816–21835 (2023).
- [281] Drummond, N. D., Needs, R. J., Sorouri, A. & Foulkes, W. M. C. Finite-size errors in continuum quantum Monte Carlo calculations. *Phys. Rev. B* **78**, 125106 (2008).
- [282] Al-Hamdani, Y. S. *Theoretical Approach towards Accurate Molecular Interactions with Low Dimensional Substrates*. Doctoral, UCL (University College London) (2016).
- [283] Al-Hamdani, Y. S. *et al.* Properties of the water to boron nitride interaction: From zero to two dimensions with benchmark accuracy. *J. Chem. Phys.* **147**, 044710 (2017).
- [284] Bredow, T., Giordano, L., Cinquini, F. & Pacchioni, G. Electronic properties of rutile TiO₂ ultrathin films: Odd-even oscillations with the number of layers. *Phys. Rev. B* **70**, 035419 (2004).
- [285] Svensson, M. *et al.* ONIOM: A Multilayered Integrated MO + MM Method for Geometry Optimizations and Single Point Energy Predictions. A Test for Diels-Alder Reactions and Pt(P(*t*-Bu)₃)₂ + H₂ Oxidative Addition. *J. Phys. Chem.* **100**, 19357–19363 (1996).
- [286] Pople, J. A. Quantum Chemical Models (Nobel Lecture). *Angew. Chem. Int. Ed.* **38**, 1894–1902 (1999).
- [287] Shi, B. X., Wales, D. J., Michaelides, A. & Myung, C. W. Going for Gold(-Standard): Attaining Coupled Cluster Accuracy in Oxide-Supported Nanoclusters. *J. Chem. Theory Comput.* **20**, 5306–5316 (2024).
- [288] Bryenton, K. R., Adeleke, A. A., Dale, S. G. & Johnson, E. R. Delocalization error: The greatest outstanding challenge in density-functional theory. *WIREs Comput. Mol. Sci.* **13**, e1631 (2023).
- [289] Dkhissi, A., Soulard, P., Perrin, A. & Lacome, N. The NO Dimer. *J. Mol. Spectrosc.* **183**, 12–17 (1997).
- [290] Wade, E. A., Cline, J. I., Lorenz, K. T., Hayden, C. & Chandler, D. W. Direct measurement of the binding energy of the NO dimer. *J. Chem. Phys.* **116**, 4755–4757 (2002).
- [291] González-Luque, R., Merchán, M. & Roos, B. O. A theoretical determination of the dissociation energy of the nitric oxide dimer. *Theoret. Chim. Acta* **88**, 425–435 (1994).
- [292] Sayós, R., Valero, R., Anglada, J. M. & González, M. Theoretical investigation of the eight low-lying electronic states of the cis- and trans-nitric oxide dimers and its isomerization using multiconfigurational second-order perturbation theory (CASPT2). *J. Chem. Phys.* **112**, 6608–6624 (2000).
- [293] Ivanic, J., Schmidt, M. W. & Luke, B. High-level theoretical study of the NO dimer and tetramer: Has the tetramer been observed? *J. Chem. Phys.* **137**, 214316 (2012).
- [294] Tobita, M. *et al.* Critical comparison of single-reference and multireference coupled-cluster methods: Geometry, harmonic frequencies, and excitation energies of N₂O₂. *The Journal of Chemical Physics*

- 119**, 10713–10723 (2003).
- [295] Perdew, J. P., Burke, K. & Ernzerhof, M. Generalized Gradient Approximation Made Simple. Phys. Rev. Lett. **77**, 3865–3868 (1996).
- [296] Lee, K., Murray, É. D., Kong, L., Lundqvist, B. I. & Langreth, D. C. Higher-accuracy van der Waals density functional. Phys. Rev. B **82**, 081101 (2010).
- [297] Hamada, I. Van der Waals density functional made accurate. Phys. Rev. B **89**, 121103 (2014).
- [298] Adamo, C. & Barone, V. Toward reliable density functional methods without adjustable parameters: The PBE0 model. J. Chem. Phys. **110**, 6158–6170 (1999).
- [299] Becke, A. D. Density-functional thermochemistry. III. The role of exact exchange. J. Chem. Phys. **98**, 5648–5652 (1993).
- [300] Grimme, S. Semiempirical GGA-type density functional constructed with a long-range dispersion correction. J. Comp. Chem. **27**, 1787–1799 (2006).
- [301] Bučko, T., Lebègue, S., Ángyán, J. G. & Hafner, J. Extending the applicability of the Tkatchenko-Scheffler dispersion correction via iterative Hirshfeld partitioning. The Journal of Chemical Physics **141**, 034114 (2014).
- [302] Ning, J. *et al.* Workhorse minimally empirical dispersion-corrected density functional with tests for weakly bound systems: r²SCAN+rVV10. Phys. Rev. B **106**, 075422 (2022).
- [303] Heyd, J., Scuseria, G. E. & Ernzerhof, M. Hybrid functionals based on a screened Coulomb potential. J. Chem. Phys. **118**, 8207–8215 (2003).
- [304] Singh, J. P., Lim, W. C., Won, S. O., Song, J. & Chae, K. H. Synthesis and Characterization of Some Alkaline-Earth-Oxide Nanoparticles. J. Korean Phys. Soc. **72**, 890–899 (2018).
- [305] Burdett, J. K., Hughbanks, T., Miller, G. J., Richardson, J. W. & Smith, J. V. Structural-electronic relationships in inorganic solids: Powder neutron diffraction studies of the rutile and anatase polymorphs of titanium dioxide at 15 and 295 K. J. Am. Chem. Soc. **109**, 3639–3646 (1987).
- [306] Kresse, G. & Furthmüller, J. Efficiency of ab-initio total energy calculations for metals and semiconductors using a plane-wave basis set. Comput. Mater. Sci. **6**, 15–50 (1996).
- [307] Kresse, G. & Furthmüller, J. Efficient iterative schemes for ab initio total-energy calculations using a plane-wave basis set. Phys. Rev. B **54**, 11169–11186 (1996).
- [308] Grimme, S. Supramolecular Binding Thermodynamics by Dispersion-Corrected Density Functional Theory. Chem. - Eur. J. **18**, 9955–9964 (2012).
- [309] Li, Y.-P., Gomes, J., Mallikarjun Sharada, S., Bell, A. T. & Head-Gordon, M. Improved Force-Field Parameters for QM/MM Simulations of the Energies of Adsorption for Molecules in Zeolites and a Free Rotor Correction to the Rigid Rotor Harmonic Oscillator Model for Adsorption Enthalpies. J. Phys. Chem. C **119**, 1840–1850 (2015).
- [310] Alfè, D. & Gillan, M. J. Ab initio statistical mechanics of surface adsorption and desorption. II. Nuclear quantum effects. J. Chem. Phys. **133**, 044103 (2010).
- [311] Piccini, G. & Sauer, J. Effect of Anharmonicity on Adsorption Thermodynamics. J. Chem. Theory Comput. **10**, 2479–2487 (2014).

- [312] Rosen, A. S. Quacc – The Quantum Accelerator: <https://zenodo.org/records/13921187>. Zenodo (2024).
- [313] Campbell, C. T. Energies of Adsorbed Catalytic Intermediates on Transition Metal Surfaces: Calorimetric Measurements and Benchmarks for Theory. *Acc. Chem. Res.* **52**, 984–993 (2019).
- [314] Schmid, M., Parkinson, G. S. & Diebold, U. Analysis of Temperature-Programmed Desorption via Equilibrium Thermodynamics. *ACS Phys. Chem Au* **3**, 44–62 (2023).
- [315] Dohnálek, Z. *et al.* Physisorption of CO on the MgO(100) Surface. *J. Phys. Chem. B* **105**, 3747–3751 (2001).
- [316] Redhead, P. A. Thermal desorption of gases. *Vacuum* **12**, 203–211 (1962).
- [317] Campbell, C. T. & Sellers, J. R. V. The Entropies of Adsorbed Molecules. *J. Am. Chem. Soc.* **134**, 18109–18115 (2012).
- [318] Boese, A. D. & Sauer, J. Accurate adsorption energies of small molecules on oxide surfaces: CO–MgO(001). *Phys. Chem. Chem. Phys.* **15**, 16481–16493 (2013).
- [319] Alessio, M., Usvyat, D. & Sauer, J. Chemically Accurate Adsorption Energies: CO and H₂O on the MgO(001) Surface. *J. Chem. Theory Comput.* **15**, 1329–1344 (2019).
- [320] Espenson, J. H. *Chemical Kinetics and Reaction Mechanisms* (McGraw-Hill, 1995).
- [321] Wellendorff, J. *et al.* A benchmark database for adsorption bond energies to transition metal surfaces and comparison to selected DFT functionals. *Surf. Sci.* **640**, 36–44 (2015).
- [322] Rangarajan, S. & Mavrikakis, M. A comparative analysis of different van der Waals treatments for molecular adsorption on the basal plane of 2H-MoS₂. *Surf. Sci.* **729**, 122226 (2023).
- [323] Brown, W. A., Kose, R. & King, D. A. Femtomole Adsorption Calorimetry on Single-Crystal Surfaces. *Chem. Rev.* **98**, 797–832 (1998).
- [324] Tait, S. L., Dohnálek, Z., Campbell, C. T. & Kay, B. D. N-alkanes on MgO(100). I. Coverage-dependent desorption kinetics of n-butane. *J. Chem. Phys.* **122**, 164707 (2005).
- [325] Tait, S. L., Dohnálek, Z., Campbell, C. T. & Kay, B. D. N-alkanes on MgO(100). II. Chain length dependence of kinetic desorption parameters for small n-alkanes. *J. Chem. Phys.* **122**, 164708 (2005).
- [326] Lian, J. C. *et al.* N₂O Adsorption on the Surface of MgO(001) Thin Films: An Infrared and TPD Study. *J. Phys. Chem. C* **114**, 3148–3151 (2010).
- [327] Street, S. C., Guo, Q., Xu, C. & Goodman, D. W. Adsorption and Electronic States of Benzene on Ordered MgO and Al₂O₃ Thin Films. *J. Phys. Chem.* **100**, 17599–17605 (1996).
- [328] Arthur, D. A., Meixner, D. L., Boudart, M. & George, S. M. Adsorption, desorption, and surface diffusion kinetics of NH₃ on MgO(100). *J. Chem. Phys.* **95**, 8521–8531 (1991).
- [329] Stirniman, M. J., Huang, C., Scott Smith, R., Joyce, S. A. & Kay, B. D. The adsorption and desorption of water on single crystal MgO(100): The role of surface defects. *J. Chem. Phys.* **105**, 1295–1298 (1996).
- [330] Chen, L., Smith, R. S., Kay, B. D. & Dohnálek, Z. Adsorption of small hydrocarbons on rutile TiO₂(110). *Surf. Sci.* **650**, 83–92 (2016).
- [331] Thompson, T. L., Diwald, O. & Yates, J. T. CO₂ as a Probe for Monitoring the Surface Defects on

- TiO₂(110)Temperature-Programmed Desorption. *J. Phys. Chem. B* **107**, 11700–11704 (2003).
- [332] Hugenschmidt, M. B., Gamble, L. & Campbell, C. T. The interaction of H₂O with a TiO₂(110) surface. *Surf. Sci.* **302**, 329–340 (1994).
- [333] Dohnálek, Z., Kim, J., Bondarchuk, O., White, J. M. & Kay, B. D. Physisorption of N₂, O₂, and CO on Fully Oxidized TiO₂(110). *J. Phys. Chem. B* **110**, 6229–6235 (2006).
- [334] Li, Z., Smith, R. S., Kay, B. D. & Dohnálek, Z. Determination of Absolute Coverages for Small Aliphatic Alcohols on TiO₂(110). *J. Phys. Chem. C* **115**, 22534–22539 (2011).
- [335] Herman, G. S., Dohnálek, Z., Ruzycki, N. & Diebold, U. Experimental Investigation of the Interaction of Water and Methanol with Anatase-TiO₂(101). *J. Phys. Chem. B* **107**, 2788–2795 (2003).
- [336] Koust, S. *et al.* NH₃ adsorption on anatase-TiO₂(101). *J. Chem. Phys.* **148**, 124704 (2018).
- [337] Trevethan, T. & Shluger, A. L. Building Blocks for Molecular Devices: Organic Molecules on the MgO (001) Surface. *J. Phys. Chem. C* **111**, 15375–15381 (2007).
- [338] Ferrari, A. M., Huber, S., Knözinger, H., Neyman, K. M. & Rösch, N. FTIR Spectroscopic and Density Functional Model Cluster Studies of Methane Adsorption on MgO. *J. Phys. Chem. B* **102**, 4548–4555 (1998).
- [339] Boese, A. D. & Sauer, J. Accurate adsorption energies for small molecules on oxide surfaces: CH₄/MgO(001) and C₂H₆/MgO(001). *J. Comp. Chem.* **37**, 2374–2385 (2016).
- [340] Valero, R., Gomes, J. R. B., Truhlar, D. G. & Illas, F. Good performance of the M06 family of hybrid meta generalized gradient approximation density functionals on a difficult case: CO adsorption on MgO(001). *The Journal of Chemical Physics* **129**, 124710 (2008).
- [341] R. Rehak, F., Piccini, G., Alessio, M. & Sauer, J. Including dispersion in density functional theory for adsorption on flat oxide surfaces, in metal–organic frameworks and in acidic zeolites. *Phys. Chem. Chem. Phys.* **22**, 7577–7585 (2020).
- [342] Ye, H.-Z. & Berkelbach, T. C. Adsorption and vibrational spectroscopy of CO on the surface of MgO from periodic local coupled-cluster theory. *Faraday Discuss.* (2024).
- [343] Mitra, A., Hermes, M. R., Cho, M., Agarawal, V. & Gagliardi, L. Periodic Density Matrix Embedding for CO Adsorption on the MgO(001) Surface. *J. Phys. Chem. Lett.* **13**, 7483–7489 (2022).
- [344] Bajdich, M., Nørskov, J. K. & Vojvodic, A. Surface energetics of alkaline-earth metal oxides: Trends in stability and adsorption of small molecules. *Phys. Rev. B* **91**, 155401 (2015).
- [345] Giordano, L., Goniakowski, J. & Suzanne, J. Partial Dissociation of Water Molecules in the (3x2) Water Monolayer Deposited on the MgO (100) Surface. *Phys. Rev. Lett.* **81**, 1271–1273 (1998).
- [346] Carrasco, J., Illas, F. & Lopez, N. Dynamic Ion Pairs in the Adsorption of Isolated Water Molecules on Alkaline-Earth Oxide (001) Surfaces. *Phys. Rev. Lett.* **100**, 016101 (2008).
- [347] Hu, X. L., Carrasco, J., Klimeš, J. & Michaelides, A. Trends in water monomer adsorption and dissociation on flat insulating surfaces. *Phys. Chem. Chem. Phys.* **13**, 12447–12453 (2011).
- [348] Kebede, G. G., Spångberg, D., Mitev, P. D., Broqvist, P. & Hermansson, K. Comparing van der Waals DFT methods for water on NaCl(001) and MgO(001). *J. Chem. Phys.* **146**, 064703 (2017).
- [349] Karalti, O., Alfè, D., Gillan, M. J. & Jordan, K. D. Adsorption of a water molecule on the MgO(100)

- surface as described by cluster and slab models. *Phys. Chem. Chem. Phys.* **14**, 7846–7853 (2012).
- [350] Pugh, S. & Gillan, M. J. The energetics of NH_3 adsorption at the $\text{MgO}(001)$ surface. *Surf. Sci.* **320**, 331–343 (1994).
- [351] Nakajima, Y. & Doren, D. J. Ammonia adsorption on $\text{MgO}(100)$: A density functional theory study. *J. Chem. Phys.* **105**, 7753–7762 (1996).
- [352] Allouche, A., Corà, F. & Girardet, C. Vibrational infrared spectrum of NH_3 adsorbed on $\text{MgO}(100)$. I. Ab initio calculations. *Chem. Phys.* **201**, 59–71 (1995).
- [353] Lv, G. et al. CO_2 adsorption on a K-promoted MgO surface: A DFT theoretical study. *Surf. Sci.* **749**, 122575 (2024).
- [354] Song, Z., Zhao, B., Xu, H. & Cheng, P. Remarkably Strong Chemisorption of Nitric Oxide on Insulating Oxide Films Promoted by Hybrid Structure. *J. Phys. Chem. C* **121**, 21482–21490 (2017).
- [355] Yanagisawa, Y., Kuramoto, K. & Yamabe, S.-i. Three Types of Adsorptions of Nitric Oxide on the MgO Surface. *J. Phys. Chem. B* **103**, 11078–11085 (1999).
- [356] Rodriguez, J. A., Jirsak, T., Pérez, M., González, L. & Maiti, A. Studies on the behavior of mixed-metal oxides: Adsorption of CO and NO on $\text{MgO}(100)$, $\text{Ni}_x\text{Mg}_{1-x}\text{O}(100)$, and $\text{Cr}_x\text{Mg}_{1-x}\text{O}(100)$. *J. Chem. Phys.* **114**, 4186–4195 (2001).
- [357] Añez, R., Sierraalta, A. & Soto, L. J. D. NO and NO_2 adsorption on subsurface doped $\text{MgO}(100)$ and $\text{BaO}(100)$ surfaces. A density functional study. *Appl. Surf. Sci.* **404**, 216–229 (2017).
- [358] Miletic, M., Gland, J. L., Hass, K. C. & Schneider, W. F. First-Principles Characterization of NO_x Adsorption on MgO . *J. Phys. Chem. B* **107**, 157–163 (2003).
- [359] Schneider, W. F., Hass, K. C., Miletic, M. & Gland, J. L. Dramatic Cooperative Effects in Adsorption of NO_x on $\text{MgO}(001)$. *J. Phys. Chem. B* **106**, 7405–7413 (2002).
- [360] Schneider, W. F. Qualitative Differences in the Adsorption Chemistry of Acidic (CO_2 , SO_x) and Amphiphilic (NO_x) Species on the Alkaline Earth Oxides. *J. Phys. Chem. B* **108**, 273–282 (2004).
- [361] Lu, X., Xu, X., Wang, N. & Zhang, Q. Adsorption and Decomposition of NO on Magnesium Oxide: A Quantum Chemical Study. *J. Phys. Chem. B* **103**, 5657–5664 (1999).
- [362] Lim, J. Y., Kim, K., Kim, E. Y. & Han, J. W. Density functional theory study of NO_x adsorption on alkaline earth metal oxide and transition metal surfaces. *Korean J. Chem. Eng.* **36**, 1258–1266 (2019).
- [363] Rodríguez, A. H., Branda, M. M. & Castellani, N. J. Adsorption of n Methanol Molecules on $\text{MgO}(100)$ with $n = 1$ to 4: A Theoretical Study. *J. Phys. Chem. C* **111**, 10603–10609 (2007).
- [364] Gay, I. D. & Harrison, N. M. A density functional study of water and methanol chemisorption on $\text{MgO}(110)$. *Surf. Sci.* **591**, 13–22 (2005).
- [365] Man, I.-C., Soriga, S. G. & Parvulescu, V. Theoretical aspects of methyl acetate and methanol activation on $\text{MgO}(100)$ and (501) catalyst surfaces with application in FAME production. *Appl. Surf. Sci.* **392**, 920–928 (2017).
- [366] Hu, X. L., Klimeš, J. & Michaelides, A. Proton transfer in adsorbed water dimers. *Phys. Chem. Chem. Phys.* **12**, 3953–3956 (2010).
- [367] Alvim, R. S., Borges, I. J., Costa, D. G. & Leitão, A. A. Density-Functional Theory Simulation of

- the Dissociative Chemisorption of Water Molecules on the MgO(001) Surface. *J. Phys. Chem. C* **116**, 738–744 (2012).
- [368] Ding, Z. & Selloni, A. Hydration structure of flat and stepped MgO surfaces. *J. Chem. Phys.* **154**, 114708 (2021).
- [369] Stimac, P. J. & Hinde, R. J. Simulating CH₄ physisorption on ionic crystals. *Eur. Phys. J. D* **46**, 69–76 (2008).
- [370] Pisani, C. *et al.* Periodic local MP2 method for the study of electronic correlation in crystals: Theory and preliminary applications. *Journal of Computational Chemistry* **29**, 2113–2124 (2008).
- [371] Tillotson, M. J., Brett, P. M., Bennett, R. A. & Grau-Crespo, R. Adsorption of organic molecules at the TiO₂(110) surface: The effect of van der Waals interactions. *Surf. Sci.* **632**, 142–153 (2015).
- [372] Kovačič, Ž., Likozar, B. & Huš, M. Electronic properties of rutile and anatase TiO₂ and their effect on CO₂ adsorption: A comparison of first principle approaches. *Fuel* **328**, 125322 (2022).
- [373] Liu, L.-M., Zhang, C., Thornton, G. & Michaelides, A. Structure and dynamics of liquid water on rutile TiO₂(110). *Phys. Rev. B* **82**, 161415 (2010).
- [374] Bandura, A. V. *et al.* Adsorption of Water on the TiO₂ (Rutile) (110) Surface: A Comparison of Periodic and Embedded Cluster Calculations. *J. Phys. Chem. B* **108**, 7844–7853 (2004).
- [375] Stefanovich, E. V. & Truong, T. N. Ab initio study of water adsorption on TiO₂(110): Molecular adsorption versus dissociative chemisorption. *Chem. Phys. Lett.* **299**, 623–629 (1999).
- [376] Ye, H.-Z. & Berkelbach, T. C. Ab initio surface chemistry with chemical accuracy. [arXiv:2309.14640](https://arxiv.org/abs/2309.14640) (2024). 2309.14640.
- [377] Schäfer, T., Libisch, F., Kresse, G. & Grüneis, A. Local embedding of coupled cluster theory into the random phase approximation using plane waves. *J. Chem. Phys.* **154**, 011101 (2021).
- [378] Kieu, L., Boyd, P. & Idriss, H. Trends within the adsorption energy of alcohols over rutile TiO₂(110) and (011) clusters. *J. Mol. Catal. A: Chem.* **188**, 153–161 (2002).
- [379] Bates, S. P., Kresse, G. & Gillan, M. J. The adsorption and dissociation of ROH molecules on TiO₂(110). *Surf. Sci.* **409**, 336–349 (1998).
- [380] Lang, X., Wen, B., Zhou, C., Ren, Z. & Liu, L.-M. First-Principles Study of Methanol Oxidation into Methyl Formate on Rutile TiO₂(110). *J. Phys. Chem. C* **118**, 19859–19868 (2014).
- [381] Vittadini, A., Selloni, A., Rotzinger, F. P. & Grätzel, M. Structure and Energetics of Water Adsorbed at TiO₂ Anatase (101) and (001) Surfaces. *Phys. Rev. Lett.* **81**, 2954–2957 (1998).
- [382] Miller, K. L., Musgrave, C. B., Falconer, J. L. & Medlin, J. W. Effects of Water and Formic Acid Adsorption on the Electronic Structure of Anatase TiO₂(101). *J. Phys. Chem. C* **115**, 2738–2749 (2011).
- [383] Onal, I., Soyer, S. & Senkan, S. Adsorption of water and ammonia on TiO₂-anatase cluster models. *Surf. Sci.* **600**, 2457–2469 (2006).
- [384] Zhao, Z., Li, Z. & Zou, Z. Structure and Properties of Water on the Anatase TiO₂(101) Surface: From Single-Molecule Adsorption to Interface Formation. *J. Phys. Chem. C* **116**, 11054–11061 (2012).
- [385] Petersen, T. & Klüner, T. Water Adsorption on Ideal Anatase-TiO₂(101) – An Embedded Cluster

- Model for Accurate Adsorption Energetics and Excited State Properties. Z. Phys. Chem. **234**, 813–834 (2020).
- [386] Wanbayor, R. & Ruangpornvisuti, V. Adsorption of CO, H₂, N₂O, NH₃ and CH₄ on the anatase TiO₂(001) and (101) surfaces and their competitive adsorption predicted by periodic DFT calculations. Mater. Chem. Phys. **124**, 720–725 (2010).
- [387] Chang, J.-G., Ju, S.-P., Chang, C.-S. & Chen, H.-T. Adsorption Configuration and Dissociative Reaction of NH₃ on Anatase (101) Surface with and without Hydroxyl Groups. J. Phys. Chem. C **113**, 6663–6672 (2009).
- [388] Lin, L. Adaptively Compressed Exchange Operator. J. Chem. Theory Comput. **12**, 2242–2249 (2016).